UNIVERSITY OF CALIFORNIA, SAN DIEGO

Investigation of Bit Patterned Media, Thermal Flying Height Control Sliders and Heat Assisted Magnetic Recording in Hard Disk Drives

A dissertation submitted in partial satisfaction of the
requirements for the degree
Doctor of Philosophy

in

Engineering Sciences (Mechanical Engineering)

by

Hao Zheng

Committee in charge:

Professor Frank E. Talke, Chair
Professor David J. Benson
Professor Eric Fullerton
Professor Philip E. Gill
Professor Hidenori Murakami

2011

This dissertation of Hao Zheng is approved, and it is acceptable in quality and form for publication on microfilm and electronically:

_____

_____

_____

_____

_____
Chair

University of California, San Diego

2011

to my parents Yanping Duan and Guangyuan Zheng

TABLE OF CONTENTS

LIST OF FIGURES

LIST OF TABLES

ACKNOWLEDGEMENTS

First of all, I would like to express my sincere gratitude to Professor Frank E. Talke for his guidance and support during my Ph.D. research. I am very grateful to be able to work with him. He motivated my interest in engineering and research and has been a great teacher and guide in many aspects during my Ph.D. study. It is his valuable advice and continual encouragement that have made me a better-trained graduate student. I greatly enjoyed working with him.

I am very grateful to Dr. Hui Li from Hitachi Asia Ltd. for discussion and motivation on my research. He has been a good labmate and an invaluable colleague. Countless communications and fruitful conversations with him have contributed greatly to the dissertation in the present form.

I wish to thank Dr. Melanie Gauvin and Benjamin Suen for discussion and cooperation on the experimental work. I would like to thank Professor Ho-Jong Kang and his group members for their support, discussions and for supplying the advanced lubricants for our experiments.

I am also grateful to Dr. Ladislav Pust, Dr. Wentao Yan, Dr. Shuyu Zhang and Dr. David Fowler for their help and supportive suggestions throughout my summer internship at Western Digital Corporation.

I wish to thank Professor Izhak Estion from Technion Israel Institute of Technology, Professor Lin Wu from the University of Science and Technology of China, Professor Vlado A. Lubarda and Dr. Fred Spada from University of California, San Diego for investing helpful discussions and advice into my research.

Special thanks to all the current and former members of Professor Talke's group, who were extremely helpful and provided me with a nice working environment. They are not only excellent colleagues but also great friends. I am very lucky to be able to meet and work with them and I really enjoy the time being together with them.

Many thanks to Betty Manoulian, Iris Villanueva, Jan Neumann James, Ray Descoteaux, Lauren Coleman and Kevin Ngo Wang for their help with many different administrative matters.

I would like to thank our industry partners for many helpful discussions, motivations and supplements. In particular, I wish to thank Edmund B. Fanslau Jr., Dr. Hui Li and Dr. Kensuke Amemiya.

I am especially grateful to Dr. Pablo A. Salas-mendez and Wenping Song for their supportive suggestions and Benjamin Suen and Eva Kozachenko for their great efforts in proof reading some parts of this dissertation.

Last but not the least, I would like to thank my family and all my friends for being a strong support in many different ways throughout the years. My parents, my uncle and aunt, and my extended family back in China have supported me mentally and have been a great source of encouragement during my stay in San Diego.

Acknowledgement for published work:

Chapter 3, in part, is a reprint of the material as it appears in "Air bearing simulation for bit patterned media," Hui Li, Hao Zheng, Yeoungchin Yoon, and Frank E. Talke, Tribology Letters, 2009, pp. 199 – 204. The dissertation author was one of the investigators and coauthors of this paper.

Chapter 3, in part, is a reprint of the material as it appears in "Numerical simulation of a "spherical pad" slider flying over bit patterned media," Hui Li, Hao Zheng, Kensuke Amemiya, and Frank E. Talke, IEEE Transactions on Magnetics, Vol. 45, No. 10, Oct. 2009, pp. 3616 – 3619. The dissertation author was one of the investigators and coauthors of this paper.

Chapter 5, in part, is a reprint of the material as it appears in "The effect of thermal radiation on thermal flying height control sliders," Hao Zheng, Shuyu Zhang, Wentao Yan, Ladislav Pust, David Fowler, and Frank E. Talke, IEEE Transactions on Magnetics, Vol. 46, No. 6, Jun. 2010, pp. 2376 – 2378. The dissertation author was the primary investigator and author of this paper.

Chapter 6, in part, is a reprint of the material as it appears in "Numerical simulation of a thermal flying height control slider with dual heater and insulator elements," Hao Zheng, Hui Li, and Frank E. Talke, IEEE Transactions on Magnetics, Vol. 45, No. 10, Oct. 2009, pp. 3628 – 3631. The dissertation author was the primary investigator and author of this paper.

Chapter 6, in part, is a reprint of the material as it appears in "The effect of write current on thermal flying height control sliders with dual heater/insulator elements," Hao Zheng, Hui Li, Kensuke Amemiya, and Frank E. Talke, Microsystem Technologies, Vol. 17, 2011, pp. 959 – 964. The dissertation author was the primary investigator and author of this paper.

Chapter 7, in part, is a reprint of the material as it appears in "Numerical simulation of thermal flying height control sliders in heat-assisted magnetic recording,"

Hao Zheng, Hui Li, and Frank E. Talke, submitted to Microsystem Technologies, 2011. The dissertation author was the primary investigator and author of this paper.

Chapter 8, in part, is a reprint of the material as it appears in "Enhanced photo-thermal stability of modified PFPE lubricants under laser beam exposure," Melanie Gauvin, Hao Zheng, Benjamin Suen, Ho-Jong Kang, Jihye Lee, and Frank E. Talke, IEEE Transactions on Magnetics, Vol. 46, No. 7, Jul. 2011, pp. 1849 – 1854. The dissertation author was one the investigators and coauthors of this paper.

VITA

2002-2006	Bachelor of Mechanical Engineering, Beijing University of Technology
2006-2010	Research and Teaching Assistant, Center for Magnetic Recording Research, Department of Mechanical and Aerospace Engineering, University of California, San Diego
Summer 2009	Research Position, Western Digital Inc., Fremont, California
2008	Master of Science, University of California, San Diego
2011	Doctor of Philosophy, University of California, San Diego

PUBLICATIONS

H. Zheng, A. N. Murthy, E. B. Fanslau Jr., and F. E. Talke, "Effect of suspension design on the non-operational shock response in a load/unload hard disk drive," Microsystem Technologies, Vol. 16, No. 1 – 2, May 2009, pp. 267 – 271.

H. Li, H. Zheng, Y. Yoon, and F. E. Talke, "Air bearing simulation for bit patterned media," Tribology Letters, Vol. 33, No. 3, 2009, pp. 199 – 204.

H. Li, H. Zheng, K. Amemiya, and F. E. Talke, "Numerical simulation of a "spherical pad" slider flying over bit patterned media," IEEE Transactions on Magnetics, Vol. 45, No. 10, Oct. 2009, pp. 3616 – 3619.

H. Zheng, H. Li, and F. E. Talke, "Numerical simulation of a thermal flying height control slider with dual heater and insulator elements," IEEE Transactions on Magnetics, Vol. 45, No. 10, Oct. 2009, pp. 3628 – 3631.

H. Zheng, S. Zhang, W. Yan, L. Pust, D. Fowler, and F. E. Talke, "The effect of thermal radiation on thermal flying height control sliders," IEEE Transactions on Magnetics, Vol. 46, No. 6, Jun. 2010, pp. 2376 – 2378.

L. Li, H. Zheng, E. B. Fanslau, and F. E. Talke, "A numerical study of dimple/gimbal interface in hard disk drive," Microsystem Technologies, Vol. 17, No. 5 – 7, 2010, pp. 869 – 873.

J. Fritzsche, H. Li, H. Zheng, K. Amemiya, and F. E. Talke, "The effect of air bearing contour design on thermal pole-tip protrusion," Microsystem Technologies, Vol. 17, No. 5 – 7, 2010, pp. 813 – 820.

H. Zheng, H. Li, K. Amemiya, and F. E. Talke, "The effect of write current on thermal flying height control sliders with dual heater/insulator elements," Microsystem Technologies, Vol. 17, No. 5 – 7, 2011, pp. 959 – 964.

M. Gauvin, H. Zheng, B. Suen, J. Lee, H. J. Kang, and F. E. Talke, "Enhanced photo-thermal stability of modified PFPE lubricants under laser beam exposure," IEEE Transactions on Magnetics, Vol. 47, No. 7, Jul. 2011, pp. 1849 – 1854.

H. Zheng, H. Li, and F. E. Talke, "Numerical simulation of thermal flying height control sliders in heat-assisted magnetic recording," submitted to Microsystem Technologies, 2011.

ABSTRACT OF THE DISSERTATION

Investigation of Bit Patterned Media, Thermal Flying Height Control Sliders and Heat Assisted Magnetic Recording in Hard Disk Drives

by

Hao Zheng

Doctor of Philosophy in Engineering Sciences (Mechanical Engineering)

University of California, San Diego, 2011

Professor Frank E. Talke, Chair

Many advanced technologies in the field of magnetic disk recording are being studied in order to achieve areal densities in excess of 1.6 gigabits per square millimeter (1 terabits per square inch). Bit patterned media (BPM) is one of these promising technologies. By using disks with physically separated magnetic patterns instead of conventional continuous media, bit patterned media avoid magnetic interference between adjacent bits and improve the thermal stability of the media. Currently, thermal flying height control (TFC) sliders are commonly used to compensate thermal effects during reading and writing and to maintain a stable and ultra-low head/disk spacing during drive operation. Heat assisted magnetic recording (HAMR) has been introduced in order to address difficulties in writing of information on magnetic media with high coercivity. By using a laser beam to locally heat the media above its Curie temperature, the magnetic material momentarily reduces its

coercivity and permits writing of information on the disk. However, the method raises concerns about the stability of the lubricants on the disk.

In this dissertation, we focus on the investigation of the head/disk interface for bit patterned media, the design of thermal flying height control sliders, and the implementation of heat assisted magnetic recording. In particular, we use a finite-element-based air bearing simulator to study the steady-state flying characteristics of sliders flying over bit patterned media. This air bearing simulator is then combined with a thermo-mechanical model of a slider in order to analyze thermal flying height control sliders featuring dual heater/insulator elements. Next, a finite element model of a thermal flying height control slider with an integrated heat assisted magnetic recording optical system is developed to study the effect of heat dissipation along the laser delivery path on the performance of the HAMR-TFC slider. The design parameters of the dual thermal flying height control heaters are optimized in order to minimize the dependence of the head/disk spacing on laser induced thermal effects. Finally, experimental techniques are developed to investigate the photo-thermo stability and tribological properties of HAMR-type lubricants which are designed to be resistant to the high temperatures experienced under laser exposure.

Chapter 1

Introduction

This chapter provides a short introduction on the principles of magnetic recording and the history of hard disk drives. The head/disk interface and the major mechanical components of a hard drive are explained and illustrated. This chapter also provides an overview of current and promising approaches that may increase the capacity of hard disk drives. The content of this dissertation is summarized at the end of this chapter.

1.1 History of Hard Disk Drives

It has been over four decades since the term "information age" was first coined in the 1970s [1]. As digital devices, laptops, personal computers and the internet have become an important part of people's lives, a huge amount of data has been produced from the use of digital documentation, emailing, messaging, images, social networking, and other data devices. The International Data Cooperation (IDC) [2] reported that over 280 exabytes (1 EB = 10^{18} bytes; 1 byte = 8 bits) of digital data was processed worldwide in 2007. It was predicted that the data usage would be larger than Avogadro's number (the number of carbon-12 atoms in 12 grams of carbon-12, which is approximately 6.022×10^{23}) in 2022, following a growth factor of 10 every 5 years [2][199][200]. According to researchers from the Global Information Industry Center

at the University of California, San Diego [3], both analog and digital information consumed by American household amounted to approximately 3.6 zettabytes (1 ZB = 10^{21} bytes) in 2008. The data was from a gamut of sources such as traditional radio, TV, phone, newspaper, and computers [3]. In addition, they reported that roughly 9.57 ZB of data was processed by 27 million enterprise servers over the world in 2008. This amount of information can fill in a stack of books reaching from the earth to Neptune (approximately 4.4 billion kilometers) and back twenty times [4][198].

The explosion of the amount of data generated and consumed boosts demand for storage capacity at low costs. Information can be stored on various devices such as paper, tapes, disks, and volatile and nonvolatile memory devices [5]. Among all these devices, magnetic hard disks are the most widely used in digital storage due to the best cost to storage ratio, the fast speed of access data, power efficiency, and the ease of information interchangeability [6]. The market share of hard disk drives with respect to the shipped capacity of storage was over 50% in 2007, compared to other storage devices (Figure 1.1) [2] .

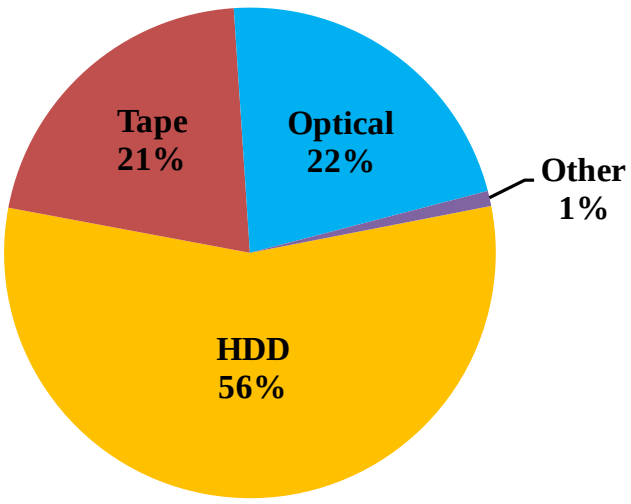

Figure 1.1 Storage capacity shipped in 2007 (after [2])

The concept of magnetic recording was first introduced by Oberlin Smith in 1878 [7]. Figure 1.2 shows a diagram of the recording part of an electrical phonograph proposed by Smith [8]. Part A is an ordinary telephone used to collect sounds. A current is generated by the diaphragm in part A and passes through the coil in part B. This causes changes in the magnetic field of the coil. The sound is then recorded onto part C, the steel cord. The steel cord continuously runs between the two wheels of part D and part E. The audio is recorded in the form of alternating magnetization patterns on the cord. Part F is a battery in the circuit that allows for the generation of a strong current. Part J is used to keep the cord in tension. When the magnetized steel cord moves through the coil, the recorded sound could be replayed from the induced current.

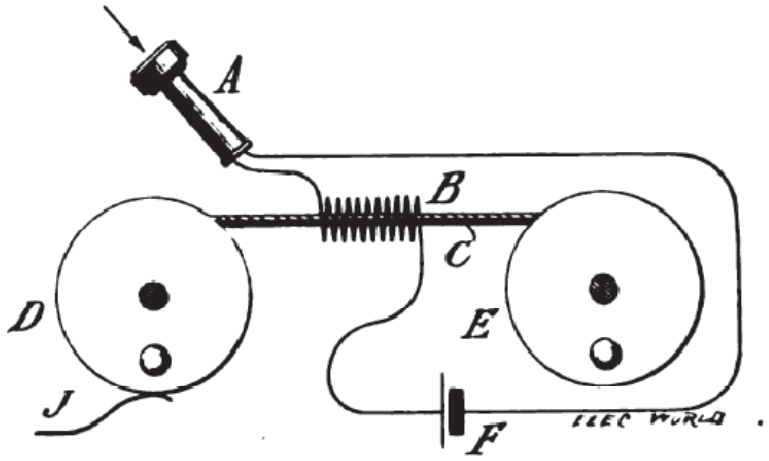

Figure 1.2 Schematic of magnetic sound recorder by Oberlin Smith (courtesy of [8])

Though Smith's idea of magnetic recording was remarkable, he did not succeed in creating a working model. The first working magnetic recorder, named "Telegraphone", was developed by the Danish engineer Valdemar Poulsen and

consisted of a drum and a recording head, as shown in Figure 1.3 [9-11]. It was designed for recording messages from phones. The sound was recorded on a steel wire wrapping around the drum. The magnetic data was recorded by a moving head along the wire. The invention of the Telegraphone was a milestone of magnetic recording. However, the signal of Telegraphone was very weak due to lack of electronic amplification [11].

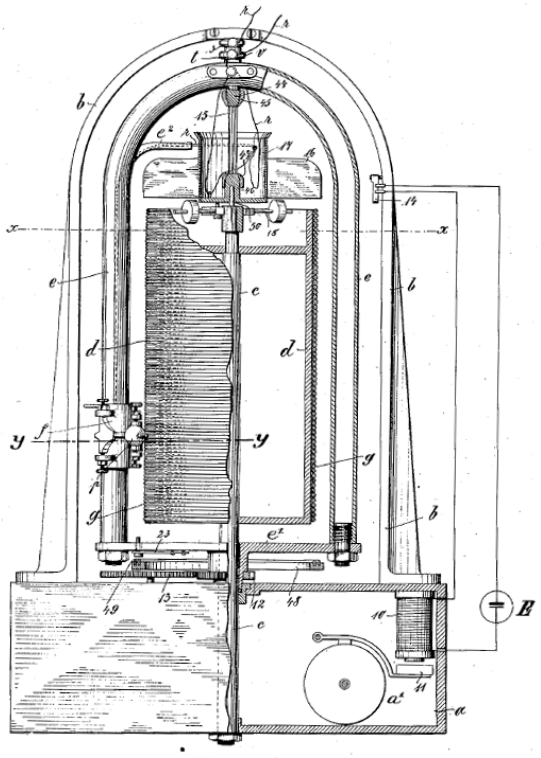

Figure 1.3 Magnetic wire reorder from Poulsen (courtesy of [12])

The Magnetophon audio tape recorder (Figure 1.4) was exhibited at the German Radio Exhibition in 1935 and drew great attention. It was the first time that coated magnetic recording tape was implemented in a magnetic recording device. The tape was developed by the BASF (Badische Anilin-und Soda-Fabrik) group in

Ludwigshafen. The tape transport, ring-shaped magnetic heads [13], electronics and loudspeakers were designed by AEG (Allgemeine Elektricit¨ats-Gesellschaft) group in Berlin [9]. The invention of the Magnetophon resulted in the rapid development of magnetic tape recording.

Figure 1.4 Magnetophon exhibited at German Radio Exhibition in 1935 (courtesy of [13])

Following the birth of the Ampex Quadruplex videotape recorders in 1956 and the Universal Automatic Computer I (UNIVAC I) in 1951, magnetic tapes have been used as the recording medium of audio, video, and digital data storage [14-16].

With the implementation of new materials, advanced process procedures, and novel techniques, such as servo track writing and low-friction giant magnetoresistive (GMR) read/write head assembly, the areal density of tape recording has reached 46 Mb/mm² (29.5 Gb/in²; 1 Mb = 10^6 bits; 1 Gb = 10^9 bits) in 2010 [17][18]. Although

the access times are relatively slow, magnetic tapes are reliable, energy efficient, and very cost effective. Tapes are still the preferred medium for backup, archive and long term data storage [18].

Not long after the magnetic tape was implemented in computers, the so-called "Random Access Method of Accounting and Control (RAMAC)" device became the first commercial device to implement magnetic disk storage. RAMAC was announced by IBM in 1956 [19]. This was a remarkable milestone that indicated the beginning of magnetic disk data storage. The storage system of the RAMAC was composed of magnetic disk memory units, access mechanisms with electronic and pneumatic controls, and an air compressor, as shown in Figure 1.5 [19][20]. The images of 5 billion characters were stored in a stack of fifty 610-mm (24-inch)-diameter disks rotating at 1200 RPM (rotations per minute). The areal density was around 3 bit/mm² (2000 bit/in²). The total capacity of the storage system was less than 5 megabytes (1 MB = 10^6 bytes; 1 byte = 8 bits) [19]. The maximum access time for reading and writing onto the disk stack was less than one second [21]. The typical spacing between the slider and the disk was around 20 μm. Even with only 5 MB of storage capacity, the lease of IBM's RAMAC 350 was $3200 per month [19].

The IBM 1301 (Figure 1.6), produced in 1962, was the next generation of hard disk drives. The drives implemented self-acting air bearing sliders and used the concept of one flying head per disk surface [22]. These novel techniques allowed for a small head/disk spacing of approximately 6 μm and increased the areal density to

approximately 13 times than that of the RAMAC [20]. The access time was reduced to 0.1 second [22].

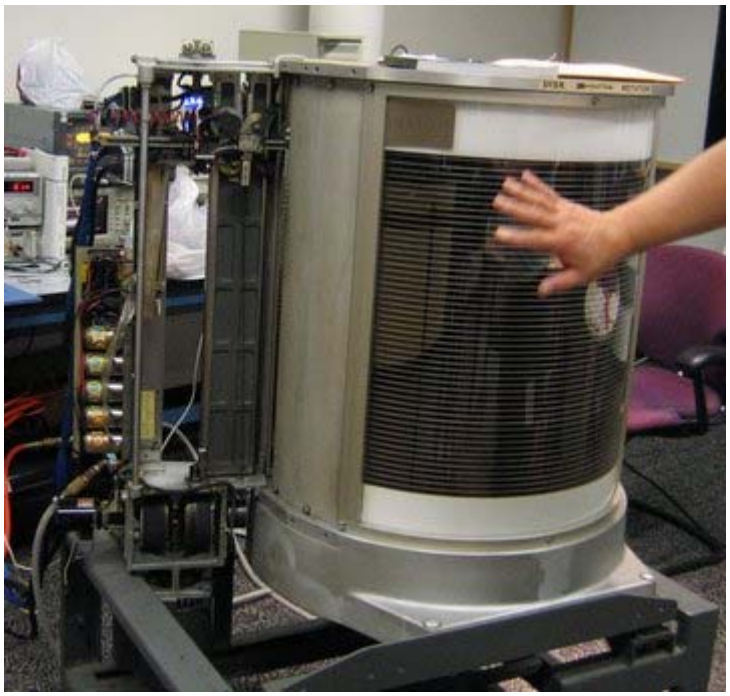

Figure 1.5 The Storage System of IBM RAMAC exhibited at Computer History Museum in Mountain View, CA (courtesy of [19])

Right after the IBM 1301, the IBM 1311 was announced in 1963. The IBM 1311 introduced the idea of exchangeable and portable disk pack between drives [20]. The concept of low cost removable disk packs (Figure 1.7) led to smaller sizes and reduced price hard disk drives. The areal density of the IBM 1311 increased by a factor of two compared to that of the IBM 1301. The spacing between the head and disk was approximately 3 μm, which was half that of the IBM 1301 [19].

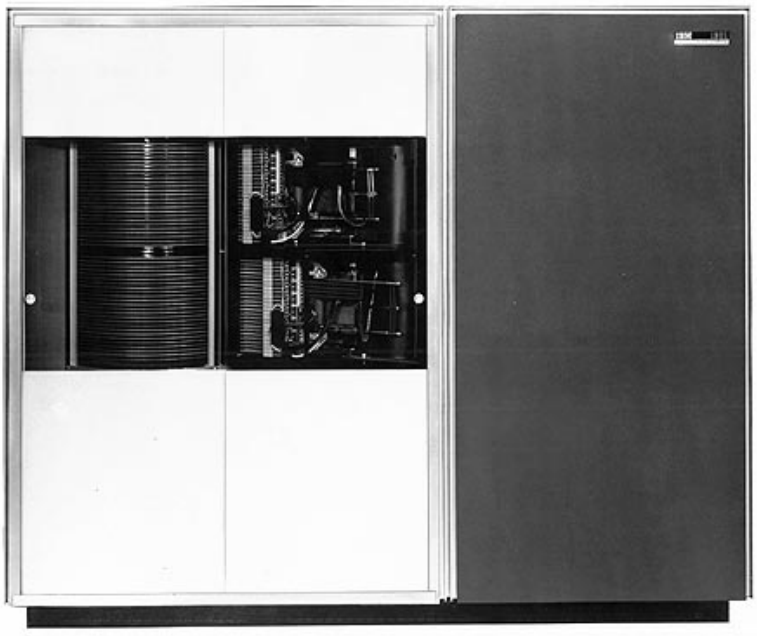

Figure 1.6 IBM 1301 disk storage unit (courtesy of [20])

Figure 1.7 IBM 1311 disk storage drive (courtesy of [23])

The introduction of the IBM 3340 (Figure 1.8) in 1973 was another historic landmark of hard disk drives. IBM 3340 implemented the "Winchester" technology. The technology was an advanced head/disk system that featured low cost, low mass, low load (< 196 mN), low flying height (~ 0.5 μm) sliders [22] along with lubricated media. The IBM 3340 drives are regarded as the first model of modern hard drives [24]. The areal density was increased to 2635 b/mm² (1.7 Mb/in²) with a reduced access time of 25 milliseconds.

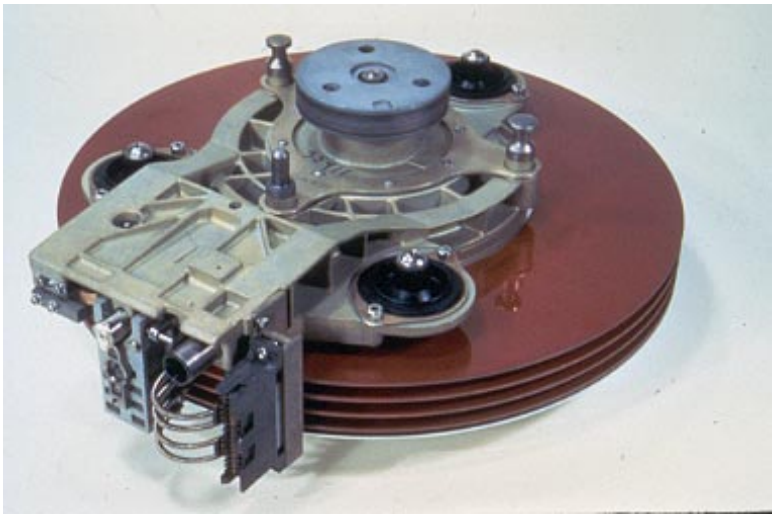

Figure 1.8 IBM 3340 disk unit (courtesy of [20])

With the continuous adoption of innovations such as thin film techniques and anti-ferromagnetic coupling enhanced magnetic media, the size and the cost of hard disk drives has been reduced significantly. Figure 1.9 shows the evolution of magnetic hard disk drives from the 1980s to the present [25]. The form factor of hard disk drives has decreased from the old 203-mm (8-inch) disks to 46-mm (1.8-inch) hard disks. The latter are widely used for storage in global positioning systems (GPS), MP3 players, personal digital assistants (PDA), digital cameras, and mobile computers [26].

Currently, the most commonly used hard disk drives for laptops and personal computers are 64-mm (2.5-in) and 89-mm (3.5-inch) disks. These disks are less than 15% of the diameter of disks in the RAMAC. As of the writing of this dissertation, the storage capacity of a typical 89-mm (3.5-inch) hard disk drive is 3 terabytes (1 TB = 10^{12} bytes). This is 600,000 times larger than the capacity of the RAMAC. In contrast to the expensive cost of the RAMAC, the cost of storage in a modern drive is less than 5 cents per gigabyte.

Figure 1.9 Evolution of size of hard disk drive (courtesy of [25])

1.2 Evolution of Areal Density

The increase in capacity of hard disk drives is highly related to the increase of areal density. Areal density indicates how much information (measured in bits) can be stored in a unit area of the disk surface [27][28]. The areal density has increased dramatically since the RAMAC was introduced in 1956. The areal density of the

RAMAC was approximate 3 b/mm² (2000 b/in²). Currently, the areal density of a typical hard disk drive is over 775 Mb/mm² (500 Gb/in²), which is more than 250-million times that of the RAMAC. In August 2011, Toshiba announced its first 1 terabyte 64-mm (2.5-inch) hard disk drive. It uses 500 GB per platter technology and features an industry-leading areal density of 1.2 Gb/mm² (744 Gb/in²) [29].

The evolution of areal density since the 1950s can be found in Figure 1.10 [48][57]. The compound annual growth rate (CAGR) measures the annualized gain of the areal density. For the first three decades, it is approximately 39% [31]. The introduction of magnetoresistive (MR), giant magnetoresistive (GMR), tunneling magnetoresistive (TMR), and anti-ferromagnetic coupling (AFC) enhanced magnetic media technologies resulted in a 60% – 100% CAGR during the 1990s. The growth rate slowed down in the early 2000s. New techniques such as perpendicular magnetic recording (PMR), two-dimensional magnetic recording, energy assisted magnetic recording, and patterned media are being investigated in order to push the areal density even higher. Currently, the rate of areal density increase is about 25 – 40% per year [30].

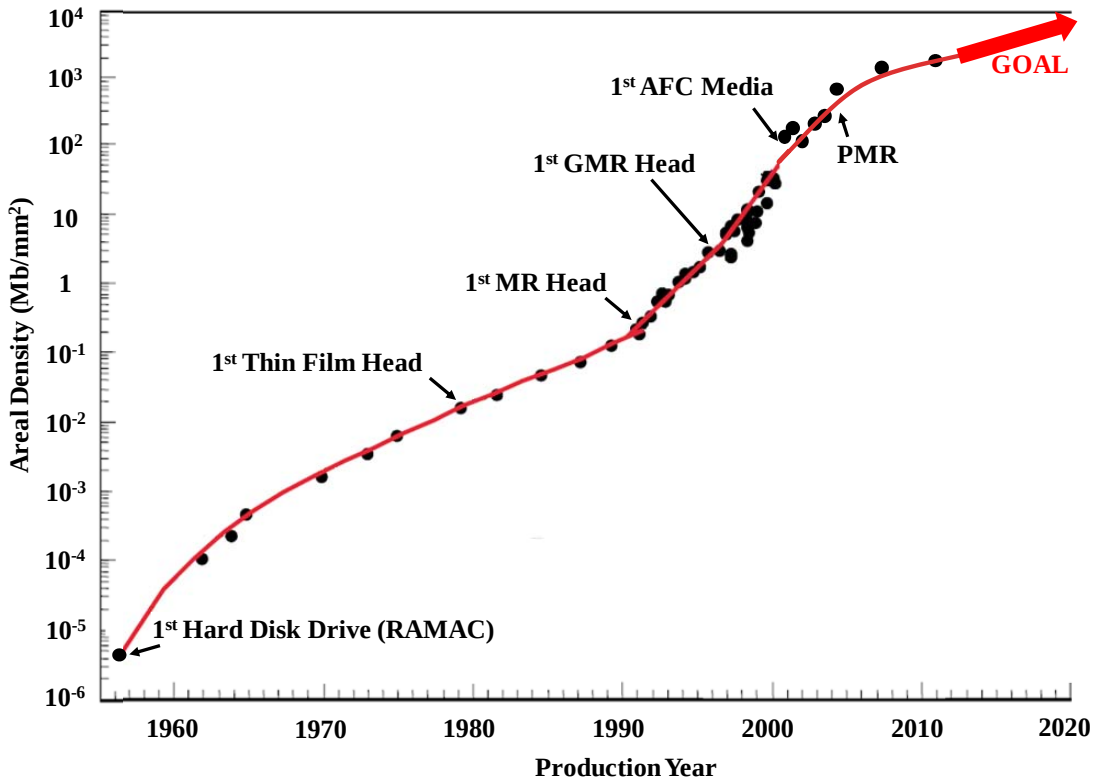

Figure 1.10 Evolution of areal density (after [48][157])

In order to increase areal density, a decrease of the size of magnetic bits and a reduction of the form factors of magnetic recording heads are required. Reliable recording on increasingly smaller magnetic bits is a continuing challenge for magnetic recording [27]. Optimizing magnetic spacing, the distance between the bottom surface of the magnetic recording head and the top surface of the magnetic recording layer, is the key to accomplish this requirement. The read-back signal decays exponentially as the magnetic spacing increases. In addition, the magnetic field becomes too weak to change the magnetic orientations of the media when the inductive write element is moved away from the disk. Thus, it is of great importance to reduce the magnetic spacing in order to increase areal density. Improving the smoothness of the slider and

disk surfaces and reducing the thickness of the protective diamond-like carbon (DLC) overcoat, lubricant films, and flying height are means of reducing the magnetic spacing [76].

1.3 Principle of Magnetic Recording

In this section, the principles of magnetic recording are introduced. The aspects of magnetic materials, the read and write process, and the evolution of the read and write elements will be discussed.

1.3.1 Magnetic Materials [32] [33]

When a magnetic material is exposed to an external magnetic field, the resulting magnetic field is a superposition of the applied field and the induced magnetic field within the material. Materials respond differently under externally applied magnetic field. According to the induced magnetic fields, they can be categorized as diamagnetic, paramagnetic, and ferromagnetic materials.

Diamagnetism results from the effect of external magnetic fields on the molecular current loops. The current loops are generated by the orbital movement of electrons. In general, diamagnetism is a very weak phenomenon in most materials, except for superconductors, and is an inherent property for all materials. The magnetic field generated by diamagnetic materials is opposite to the applied field, leading to a slightly smaller total magnetic field than the external field. Typical diamagnetic materials are copper, silver, lead, mercury and most organic compounds, such as petroleum and some plastics [34].

Paramagnetism is a stronger form of magnetism than diamagnetism. When a magnetic field is present, the net magnetic dipoles of the constituent atoms or molecules align to the applied field, leading to a stronger total magnetic field than the imposed field. Typical paramagnetic materials are tungsten, aluminum, lithium and manganese.

The magnetization of diamagnetic and paramagnetic materials cannot be sustained when the applied magnetic field drops to zero. On the other hand, ferromagnetic materials, such as iron, nickel, gadolinium, and cobalt, retain a considerable degree of magnetization when the applied field is removed. The retained field can be stronger than the imposed field.

Ferromagnetism is related to the crystalline structure, the microscopic organization, and the chemical makeup of the material [35]. The phenomenon of ferromagnetism can be explained by the hypothetical concept of ferromagnetic domains as proposed by P. Weiss and illustrated schematically in Figure 1.11 [36][37]. The strong inter-atomic interactions of ferromagnetic materials have a tendency to keep the spins of adjacent atoms parallel. This forms small ferromagnetic domains that are spontaneously magnetized. Since the magnetization of each domain is randomly oriented, the bulk substance, which is composed of a great numbers of ferromagnetic domains, exhibits zero net magnetization in the absence of an external field, as shown in Figure 1.11 (a). When a magnetic field is applied, domains that are oriented in a favorable magnetization direction along the applied field will expand. This is at the expense of reducing the size of domains that are directed opposite to the applied field. As the external magnetic field increases, the magnetization direction of the domains

will rotate to align with the direction of applied field, as illustrated in Figure 1.11 (b) and (c). When the external field is removed, the boundaries of the ferromagnetic domains will not be in their initial positions. This leads to the residual magnetization of the material. Additional energy is needed to demagnetize the ferromagnetic material.

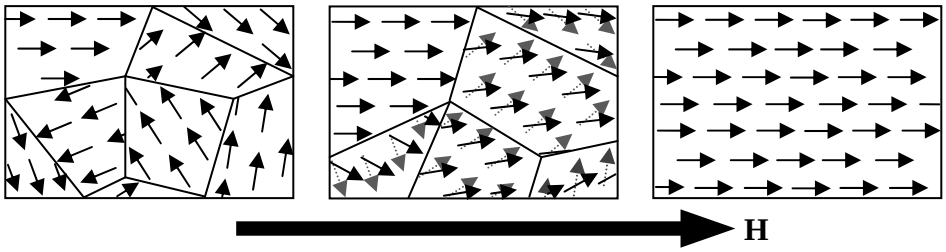

Figure 1.11 Schematic of magnetization of ferromagnetism: (a) the magnetization of each ferromagnetic domain is randomly oriented at the initially unmagnetized state; (b) domains expand along with a rotation of magnetization direction when exposed to an external magnetic field; and (c) the magnetization orientation is aligned with the applied field (after [32])

The process of demagnetizing ferromagnetic materials is not the inverse of the magnetization process. The irreversibility of ferromagnetic material is referred as hysteresis. Figure 1.12 is a typical hysteresis loop showing the magnetization of a ferromagnetic material when passing through an altering magnetic field. When the magnetic field strength $\mathbf{H}$ increases from zero, the magnetization of the material $\mathbf{M}$ follows a non-linear magnetization curve (OA) and saturates at M_s. As the driving magnetic field drops to zero, the magnetization decreases along curve (AB) and a remanent magnetization M_r is retained. A reversed magnetic field is needed to

demagnetize the material. The field required to drive the magnetization back to zero is called "coercivity" (denoted by H_c). If the opposing field further increases, the material will be magnetized to the negative saturation point (point D) along curve CD. A negative residual magnetization (point E) is sustained without an external field until an increasing positive field drives the magnetization back to M_s. This forms a closed loop along the trace FA. The two remanent magnetizations of ferromagnetic materials play a key role in magnetic recording by providing magnetic "memory" at two stable states.

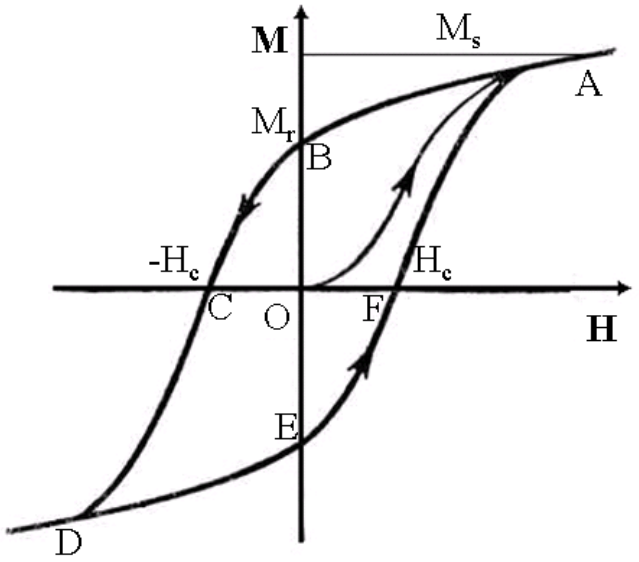

Figure 1.12 Hysteresis loop of ferromagnetism

1.3.2 Write Process

Figure 1.13 (a) and (b) show the schematics of the write process in longitudinal magnetic recording (LMR) and in perpendicular magnetic recording (PMR), respectively. A magnetic core surrounded by an inductive coil flies above the rotating

magnetic disk. The information to be recorded on the disk is received by the data channel and is converted into alternating currents flowing through the write coil [37][38]. A magnetic field is produced by the write current. In longitudinal magnetic recording, the fringing field at the pole tip passes through the magnetic medium, magnetizes it, and creates magnetization patterns parallel to the disk surface. In perpendicular magnetic recording, the magnetic flux passes through the recording layer and the soft magnetic under layer. The magnetic patterns generated in the recording layer are perpendicular to the disk surface. The soft under layer (SUL) serves as a flux return path to enhance the writing field [39][40]. A more detailed description of perpendicular magnetic recording will be given in Section 1.7. We observe from Figure 1.13 that the geometry of the write head for perpendicular magnetic recording is different from that in longitudinal magnetic recording. Perpendicular recording heads have a larger return pole so that the magnetic flux density in the return pole is small enough to prevent the erasure of the recorded information.

The orientation of the magnetic bits on the disk can be influenced by the direction of the write current. A magnetic transition is produced when there is a change in the direction of magnetization. The transition corresponds to the recording of a binary “1” on the disk. When the direction of the magnetization stays the same, there is no transition created. Thus, a binary “0” is recorded on the disk.

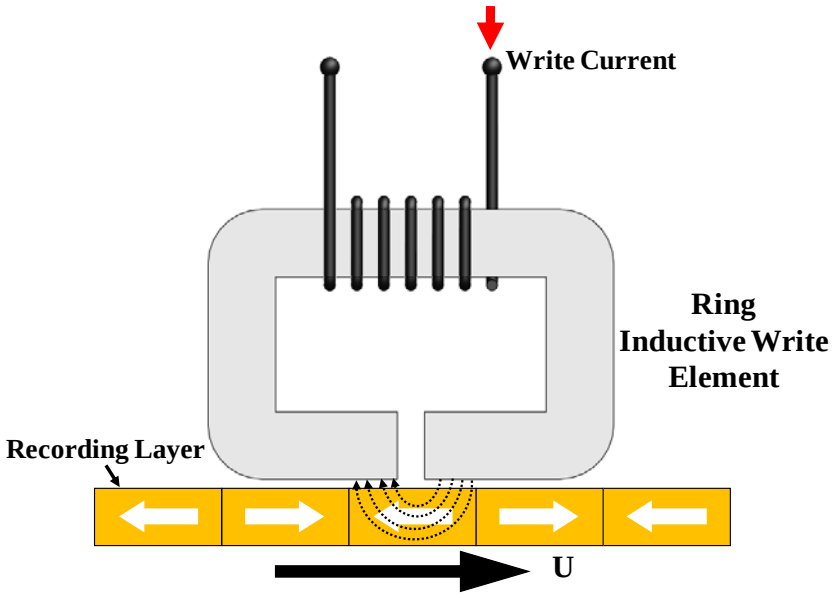

(a) Longitudinal Magnetic Recording

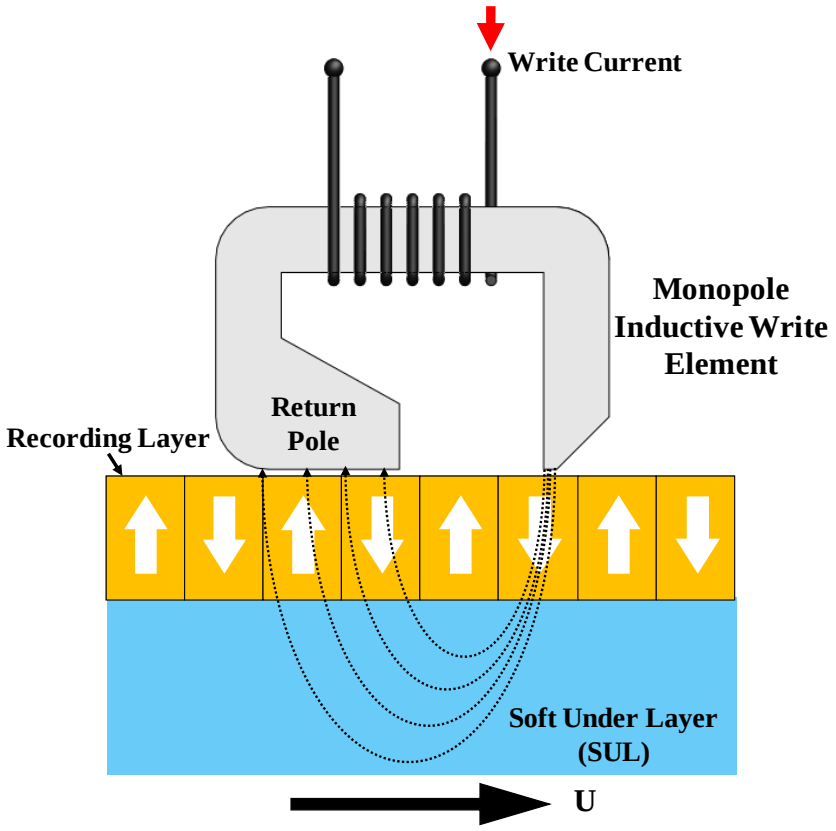

(b) Perpendicular Magnetic Recording

Figure 1.13 Schematic of read and write process for (a) longitudinal magnetic recording and (b) perpendicular magnetic recording (after [41])

1.3.3 Read Process

Information can be recorded as magnetic transitions that correspond to binary digits. The procedure of reading information involves the read head detecting magnetic flux at the magnetic transitions.

The ferrite inductive read/write heads used in early magnetic hard disk drives are pieces of C-shaped ferrite wound with a fine wire coil [41][46] (Figure 1.14). The inductive read/write head is used for both writing and reading magnetic information. The reading process of the inductive read head is conceptually opposite of the recording process [42]. As the magnetized disk is rotating under the read/write head, a voltage is induced across the induction coil. The induced voltage pulse is related to the magnetic flux by Faraday's Law [42]:

$$V = -N\frac{d\phi}{dt} = -NU\frac{d\phi}{dx} \tag{1.1}$$

where N is the number of loops of the coil, ϕ is the magnetic flux detected by the read head, U is the disk velocity, $\frac{d\phi}{dx}$ denotes the change of flux along the track.

The magnetic flux flowing through the coil of a read/write head can be expressed by the reciprocity integral [37][42][43][209]:

$$\phi = \mu_0 \iiint \mathbf{M}\left(x - \bar{x}\right)\frac{\mathbf{H}(\mathbf{x})}{i}dxdydz \tag{1.2}$$

where μ_0 is the magnetic permeability of free space, $\mathbf{M}$ and $\mathbf{H}$ are the magnetization of the media and the magnetic field produced by the head, respectively. $\bar{x} = Ut$ with U

and t being the disk velocity and time, respectively. Defining the head sensitivity function $\mathbf{h} \equiv \mathbf{H} / i$ yields [209]:

$$\phi = \mu_0 \iiint \mathbf{M}\left(x - \bar{x}\right)\mathbf{h}\left(\mathbf{x}\right) dxdydz \tag{1.3}$$

A magnetic transient can be approximated by [209]:

$$M_0 \exp\left(-jkx\right) \tag{1.4}$$

where M_0 is the amplitude of magnetization and k is the wave number. Substituting Equation (1.4) into Equation (1.3) and assuming uniform magnetization and head filed components across the track and through the thickness of the recording medium [209], we obtain:

$$\phi = \mu_0 w M_0 \int_d^{d+\delta} \exp\left(jk\bar{x}\right) dy \int_{-\infty}^{+\infty} \left[\exp\left(-jkx\right) M_x\left(x - \bar{x}\right) h_x\left(\mathbf{x}\right)\right] dx \tag{1.5}$$

where w is the track width, d is the head/disk spacing. The thickness of the magnetic film is δ. The term in the bracket indicates the Fourier transform of h_x [209]. Substitution of h_x, the Karlqvist head field [44], into Equation (1.5) gives [209]:

$$\phi = \mu_0 w M_0 \frac{H_g g}{i} \delta\left[e^{-kd}\right]\left[\frac{1 - e^{-k\delta}}{k\delta}\right]\left[\frac{\sin\left(kg/2\right)}{kg/2}\right] \exp\left(jk\bar{x}\right) \tag{1.6}$$

where H_g is the field of the gap, g is the gap width. The first term in the bracket $\left[e^{-kd}\right]$ is called spacing loss term and shows that the read-back signal decays exponentially with the magnetic spacing. The second term in the bracket $\left[\frac{1 - e^{-k\delta}}{k\delta}\right]$ is the thickness loss term showing the signal loss due to an increase of the thickness of

the magnetic medium. The third bracket $\left[\frac{\sin(kg/2)}{kg/2}\right]$ is the gap loss term and becomes zero when $kg/2 = n\pi$ with $n = 1, 2, 3, \ldots$.

Applying Faraday's Law (Equation (1.1)) in Equation (1.6), the output voltage can be expressed as:

$$V(\bar{x}) = -NU\mu_0 wM_0 \frac{H_g g}{i} k\delta\left[e^{-kd}\right]\left[\frac{1-e^{-k\delta}}{k\delta}\right]\left[\frac{\sin(kg/2)}{kg/2}\right] j\exp(jk\bar{x}) \qquad (1.7)$$

Since longitudinal and perpendicular fields are Hilbert transform pairs [209][211], the magnetic flux and the output voltage for perpendicular magnetization are of the same magnitude as longitudinal magnetization with a phase shift [209].

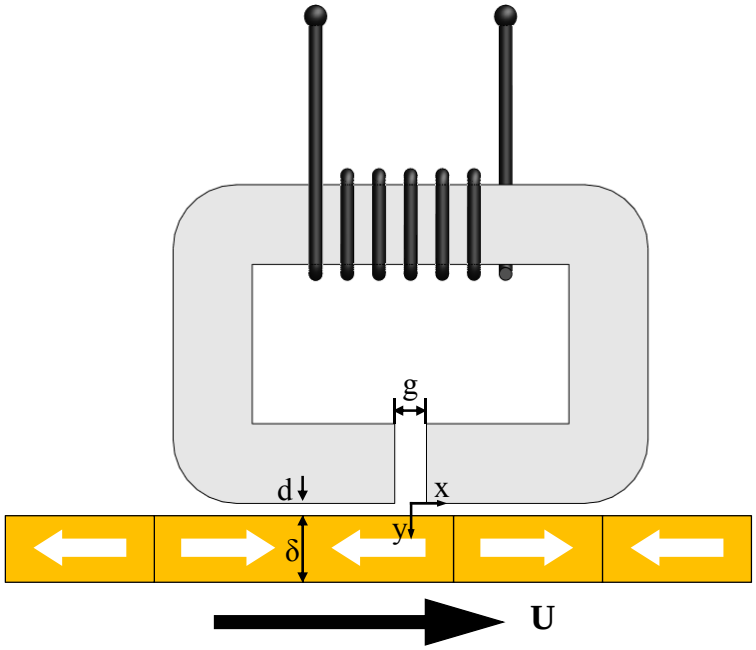

Figure 1.14 Schematics of inductive read/write head and definition of symbols and dimensions for analysis of read-back signal

The inductive read/write head was improved in the 1980s with the implementation of thin film heads. The heads were produced by advanced photolithography techniques. This process enabled a higher resolution that allowed information to be recorded on smaller bits. In addition, the photolithography techniques reduced the manufacturing cost of the read/write head.

The inductive head was used until the 1990s. Magnetoresistive (MR) technology was introduced in 1991 by IBM [47]. The magnetoresistive read element is separated from the inductive write element such that the read and write elements can be optimized independently (Figure 1.15). The magnetoresistive read sensor is made of materials such as nickel-iron alloy. The materials have the properties such that the electrical resistance of the material depends on the alignment between the direction of the current and the magnetic orientation. Changes to the applied external magnetic field lead to variations of the electrical resistance in the MR sensor. This is used as the read-back signal [48]. The areal density of hard disk drives using magnetoresistive technology is more than four times that of inductive read heads [49]. However, the maximum change in the resistivity caused by the magnetoresistive effect is relatively small [49][50].

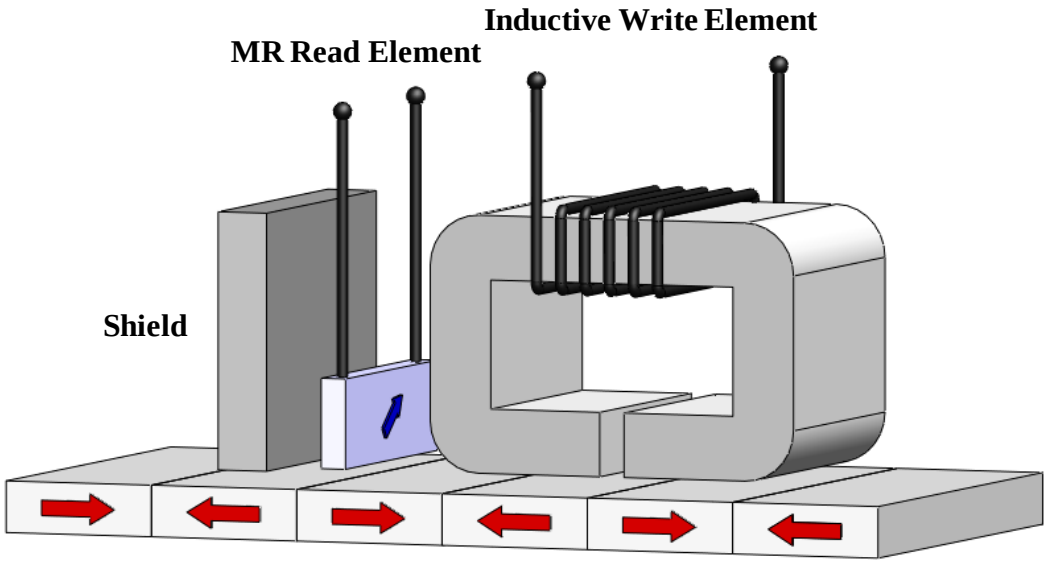

Figure 1.15 Schematic of the reproducing process of magnetoresistive read element

The giant magnetoresistive (GMR) effect was discovered by Fert and Grünberg in 1988. Both were jointly awarded the Nobel Prize in Physics in 2007 for this outstanding discovery. In the presence of changing magnetic fields, large resistance changes are observed in materials consisting of alternating thin layers of ferromagnetic and non-magnetic materials due to the giant magnetoresistive effect. This leads to a higher signal-to-noise (SNR) ratio in the giant magnetoresistive head. A typical giant magnetoresistive head consists of a sensing layer that detects the changes in the magnetic field of the disk and a thin spacer layer of a non-magnetic material. The head also contains a pinned layer with fixed magnetic direction, and an exchange layer of antiferromagnetic material that holds the magnetic orientation of the pinned layer [47][51]. These features are shown in Figure 1.16. When the magnetic direction changes, the electrons of the free layer rotate and become misaligned with

the pinned layer. This significantly increases the resistance of the giant magnetoresistive head. The giant magnetoresistive read element replaced the magnetoresistive read element in late 1990s. This implementation has led to an areal density increase by a factor of three compared to a magnetoresistive head.

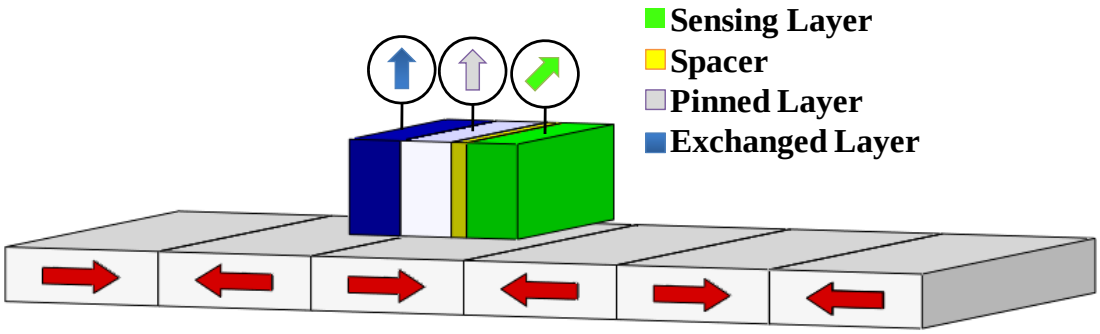

Figure 1.16 Schematics of the giant magnetoresistive sensor (after [51])

Tunnel magnetoresistance (TMR) is the next technology used in the read heads. The technology came with the advent of perpendicular recording and was announced by Seagate in 2005. The tunnel magnetoresistive effect occurs when two ferromagnetic layers are separated by an ultra-thin insulating layer with a thickness smaller than 2 nm. Electrons pass from one ferromagnetic electrode to the other by quantum mechanical tunneling through the ultra-thin insulator barrier [52][53]. In the presence of magnetic fields, the magnetizations of the ferromagnetic layers change individually. The relative orientation of the two magnetic layers results in the change of the resistance in the tunneling current.

The output voltage for (giant/tunnel) magnetoresistive read signal is sensitive to the magnetic flux. Considering a soft under layer which is separated from the

magnetic layer by an intermediate layer (Figure 1.17) and assuming the soft under layer is infinitely thick with infinite permeability [210], we obtain the magnetic flux detected by the read head in perpendicular magnetic recording [210][212][213]:

$$\phi \propto M_0 \frac{\sinh k(\delta + s) - \sinh(ks)}{\sinh k(d + \delta + s)} \tag{1.8}$$

For extremely high density, i.e., $k \to \infty$, $\sinh(kx) \to \exp(kx)/2$, we obtain [210]:

$$\phi(k \to \infty) \propto M_0 \left(1 - e^{-k\delta}\right) e^{-kd} \tag{1.9}$$

Similar to Equation (1.6), Equation (1.9) shows that the read-back signal decays with the magnetic spacing. Thus, it is of great importance to reduce the magnetic spacing in order to increase areal density.

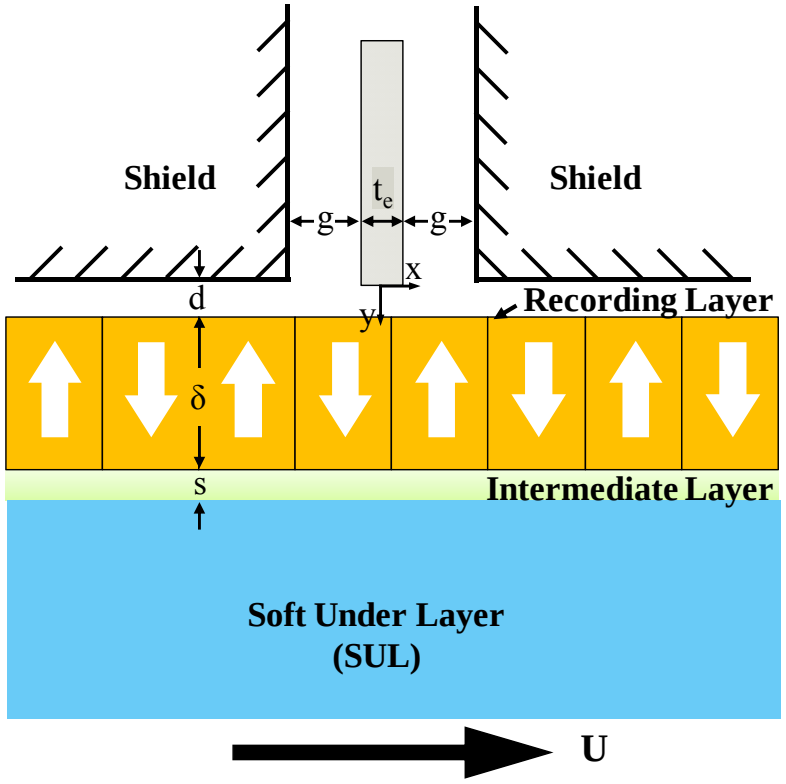

Figure 1.17 Schematics of (giant/tunnel) magnetoresistive head and definition of symbols and dimensions for analysis of read-back signal

1.4 Mechanical Structure of Hard Disk Drives

The mechanical structure of a modern hard disk drive is shown in Figure 1.18. Information is stored along concentric tracks on one or more of the magnetic disk platters mounted on the spindle motor. The spindle rotates at a speed of 5400 to 15000 rpm [54]. The disk is a multilayer structure made of glass or aluminum substrate and is covered with thin film layers. The layers include the underlayer, magnetic layer, and protective layers. The structure of magnetic disks will be introduced in the next section.

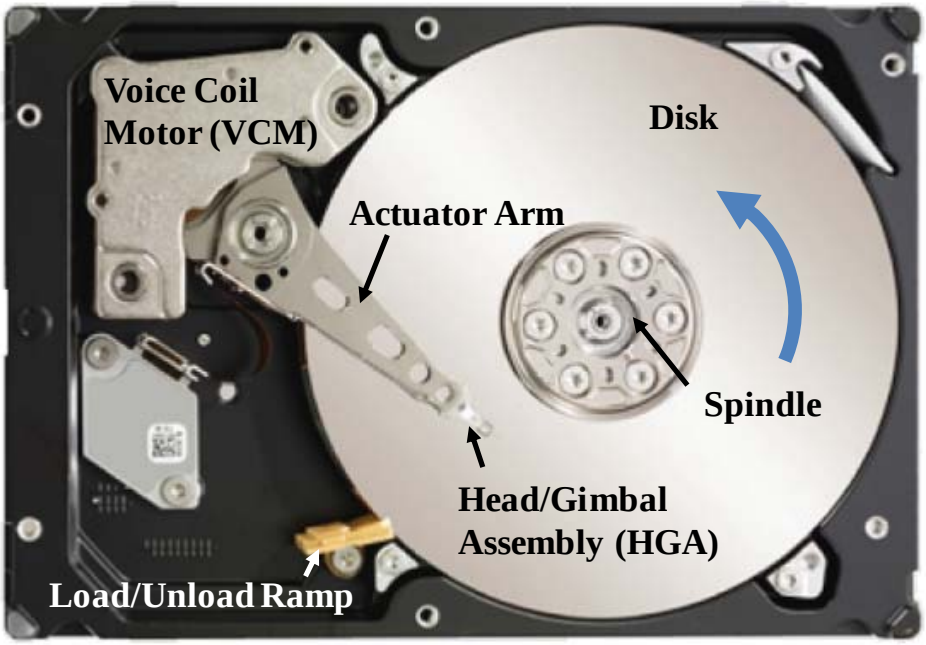

Figure 1.18 Mechanical structure of hard disk drive (after [54])

The slider, carrying the integrated thin film read and write elements, flies over the rotating disk. The surface of the slider facing the disk is etched with patterns and is called the “air bearing surface (ABS)”. A converging channel is formed between the slider and the fast rotating disk. As the slider flies over the disk, a self-acting air

bearing is generated as a result of the viscous air flow in the channel and keeps the slider at a constant distance from the surface. The slider is attached to the suspension through the gimbal, as shown in Figure 1.19, and moves around the dimple. The dimple is stamped into the suspension. The suspension exerts a preload on the slider. The preload is balanced by the air bearing. The mathematical description of forces on the slider by the suspension and the air bearing will be presented in Chapter 2.

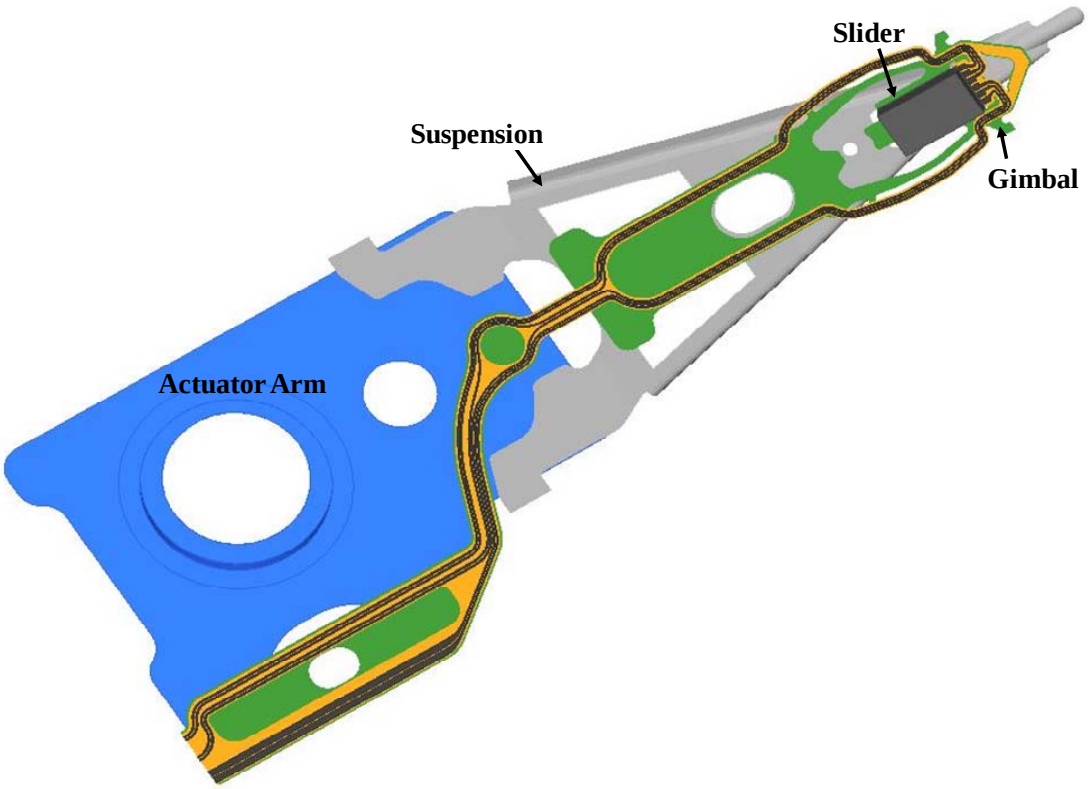

Figure 1.19 Schematic of head/gimbal assembly (HGA)

The head/gimbal assembly (HGA) is attached to the actuator arm and is driven by the voice coil motor (VCM). The voice coil motor provides accurate position of the slider on the tracks in order to read and write information. When the power is off, the

actuator arm and the HGA are moved away from the disk and rest on the load/unload ramp [38][55].

1.5 Head/Disk Interface

As described in Section 1.2, the slider should be as close as possible to the magnetic media in order to decrease the magnetic spacing and increase the areal density. However, with respect to friction and wear during slider-disk contacts, this will adversely affect the reliability and performance of the hard disk drive from a tribological point of view. Thus, an ultra-low but stable interface between the slider and disk is required for all operating conditions. A schematic of the head/disk interface with exaggerating roughness is shown in Figure 1.20. Since the magnetic spacing should be as small as possible, the surface of the disk and the slider should be sufficiently smooth in order to minimize the possibility of slider-disk contacts and to improve the reliability and durability of the hard disk drive. The root mean square (RMS) roughness of the slider is around 0.4 nm. The disk is much smoother than the slider with a RMS roughness smaller than 0.2 nm [38][214]. The flying height is defined as the distance between the top surface of the disk and the bottom surface of the slider. In the case that surface roughness must be considered, a fictitious surface through the mean of the surface roughness of slider and disk is used (Figure 1.20). Flying height is one of the most important parameters in magnetic recording.

The substrate of the slider is made of Al_2O_3-TiC. Advanced techniques such as line photolithography and additive or subtractive processing have been used to develop the multilayer thin film head structure at the trailing edge of the substrate [56].

The air bearing surface at the bottom of the slider facing the disk surface is designed to create a self-acting air bearing. The air bearing maintains a stable head/disk interface and reduces contact, friction and wear between the surfaces of slider and disk [57]. The air bearing design is critical to ensure a steady and low flying height that is independent of the radial position and rotating speed of the disk.

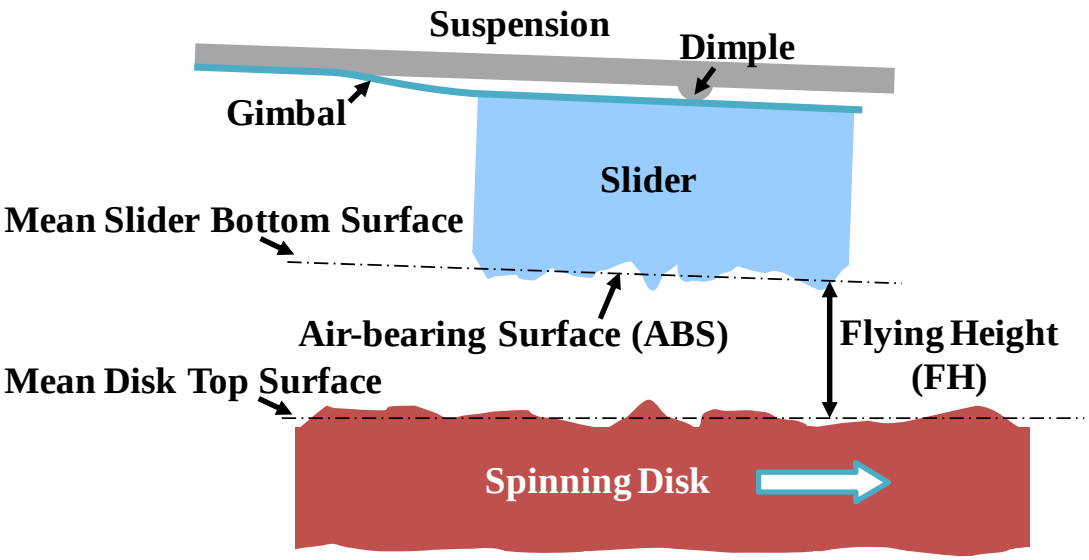

Figure 1.20 Schematic of the head/disk interface

As introduced in Section 1.1, the IBM 1301 implemented the first slider with a curved air bearing surface. The slider flew over the disk at a distance of approximately 6 μm.

Mini-Winchester sliders implemented the first rail-type air bearing surface design [58], as shown in Figure 1.21. The dimension of the "mini" ferrite slider was 4 mm by 3.2 mm by 0.86 mm with the mass of 55 milligram. The read and write elements were supported by the center rail. Air bearing surfaces with two side rails compress the air flow and form positive air bearing pressure distributions over the

whole air bearing surface. The distance between the slider and the disk for this design was around 0.46 μm [58].

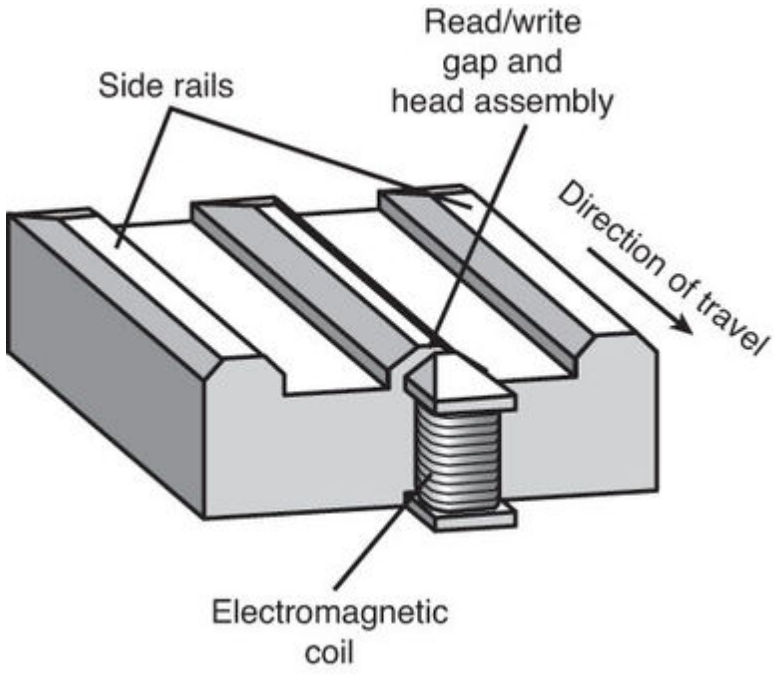

Figure 1.21 Typical "mini" form factor slider (courtesy of [59])

The sliders presently used are sub-ambient air bearing sliders which were first introduced in the early 1990s [60]. Figure 1.22 shows the schematic and the pressure distribution of a sub-ambient air bearing designs. The air bearing surface has several height levels (■ and ■). The maximum pressure occurs at the trailing edge of the slider where the spacing between the slider and the disk is the smallest. A recessed area (■) is formed by an increase in the air bearing spacing. Here, the compressed air flow expands suddenly and causes a pressure distributions below ambient pressure [55][123][124]. The sub-ambient air bearing design requires less load, allows for a constant flying height, and is less sensitive to disk velocity and ambient pressure when compared to positive air bearing designs [55][58].

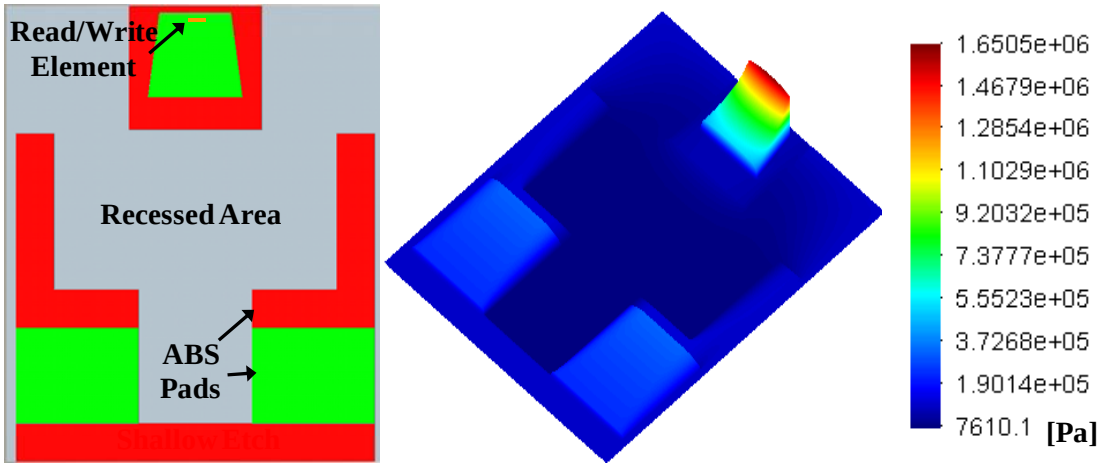

Figure 1.22 Schematic and pressure distribution of sub-ambient air bearing design

In addition to the evolution of ABS design, the size and the mass of the sliders have been dramatically reduced due to increasing areal density and due to reduced form factor disks. The evolution of the size and mass of sliders is shown in Figure 1.23. The sliders in current use are femto and pico sliders. Femto sliders are only 20% of the size and 1% of the mass of a mini ferrite slider used in 1975, while pico sliders are 30% of the size and 3% of the mass of the mini sliders.

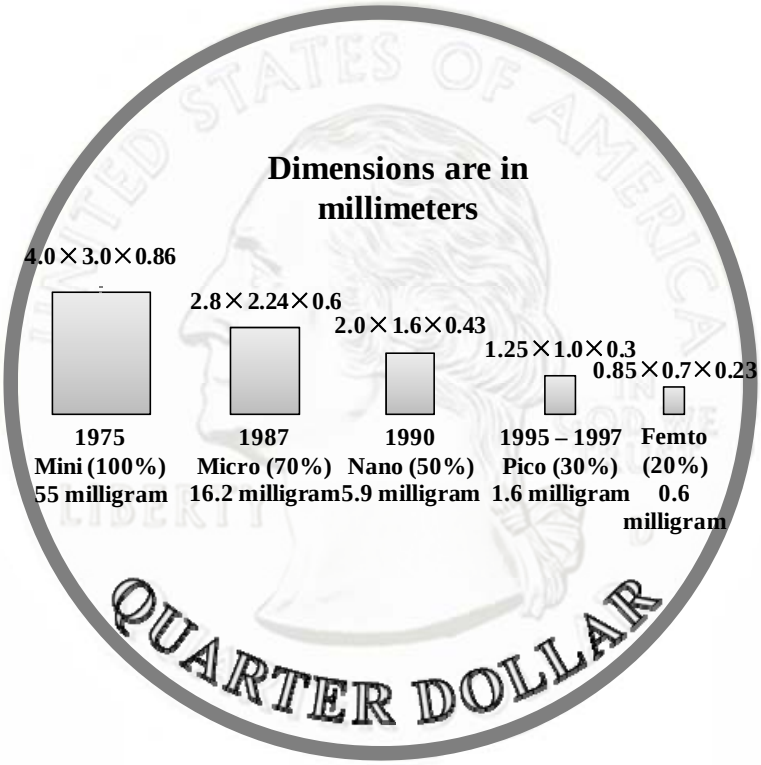

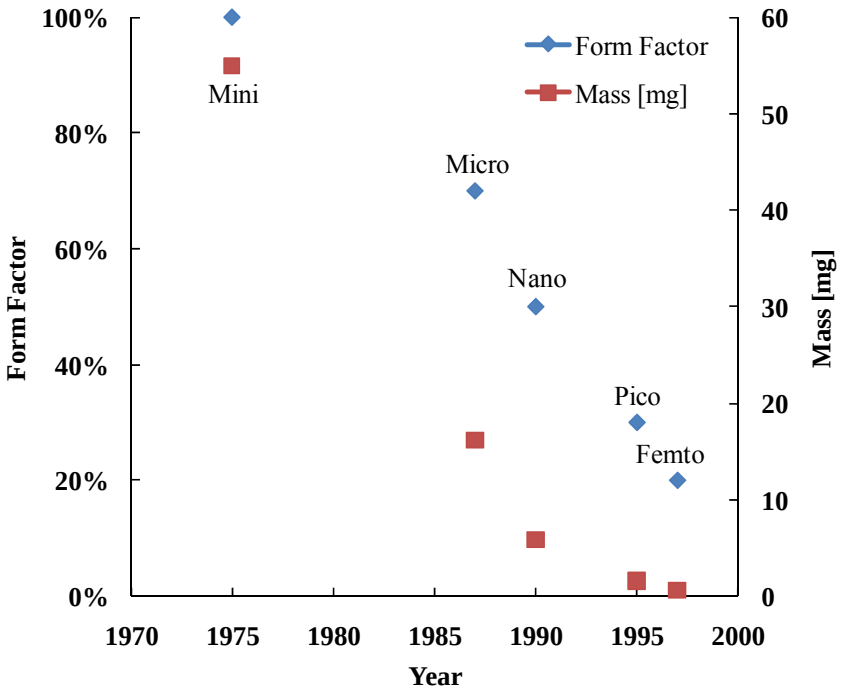

Figure 1.23 Evolution of size and mass of the slider (after [58])

Magnetic disks are multilayer structures. The cross-section view of typical magnetic disks, for longitudinal magnetic recording, is shown in Figure 1.24 (a). The substrate of the disks used in longitudinal magnetic recording is made of aluminum or glasses. For aluminum disks, a nickel phosphorous (NiP) under layer is deposited on the substrate in order to prevent corrosion and to increase the hardness of the disk [61]. A magnetic layer is deposited by sputtering or chemical vapor deposition. For perpendicular magnetic recording disks, as shown in Figure 1.24 (b), soft magnetic under layers (SUL) are applied on top of the substrate. An intermediate layer is sputtered before the magnetic layer in order to reduce the interaction between the soft magnetic under layers and the recording layer. A thin diamond-like carbon (DLC) overcoat film and a lubricant film are applied on top of the magnetic layer in both longitudinal and perpendicular magnetic recording disks in order to protect the magnetic layer from wear and corrosion [39][62].

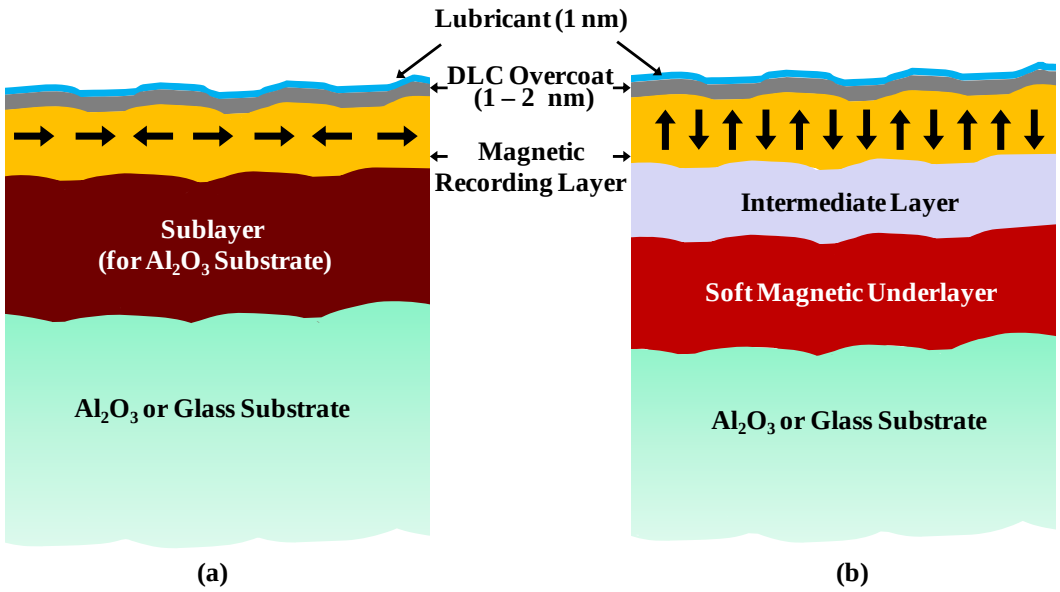

Figure 1.24 Schematic view of cross-section of magnetic disks for (a) longitudinal magnetic recording and (b) perpendicular magnetic recording

1.6 Magnetic Trilemma

Further advancements in the areal density require a reduction in the size of magnetic bits. Likewise, the decrease in the form factor of magnetic recording systems requires a decrease of the geometry of the slider, the magnetic spacing at the head/disk interface and the thickness of the disk. This results in a degraded signal-to-noise ratio (SNR). The signal-to-noise ratio of the head is defined as $SNR_{\text{head}} \propto P_{\text{head}} \left(\Delta R / R\right)^2 / 4k_B TB$, where P_{head} is the power dissipated in the head, $\Delta R / R$ is the fractional head sensitivity. $k_B T$ represents the thermal energy and is defined as the product of the Boltzmann's constant k_B and the absolute temperature T. B is the bandwidth. The signal-to-noise ratio of the head is proportional to the power dissipated in the head, which is limited by the thermal conductance [63]. The signal-to-noise ratio of the media, $SNR_{\text{media}} \propto V_{\text{bit}} / V_{\text{grain}}$, is proportional to the ratio of the volume of the bit V_{bit} to the volume of the magnetic grains V_{grain}. At very high densities, the form factor of the recording system goes down and the degradation of signal-to-noise ratio of the media will be the dominant factor limiting the performance of the system [64]. Since the signal-to-noise ratio of the media is strongly related to the number of grains per bit [63][65], the magnetic grains need to be reduced in order to maintain a reasonable signal-to-noise ratio for a smaller bit.

As grain sizes get smaller and smaller, the energy barrier separating the two magnetization states reaches approximately the same value as the thermal energy. The magnetization of grains becomes unstable and the magnetic polarity is easily switched

due to temperature fluctuations. This leads to signal decay at a rate proportional to $\exp\left(-K_u V_{\text{grain}} / k_B T\right)$ [64][66][67]. $K_u V_{\text{grain}}$ is the energy barrier for reversal of magnetization directions and is the product of the anisotropy constant of the material K_u and the volume of magnetic grain V_{grain}. $k_B T$ is the thermal energy. This thermal instability is referred as the superparamagnetic effect and is the fundamental limiting factor for the density growth in magnetic recording [63][68].

Increasing the coercivity of the magnetic material will increase the anisotropy energy density, which is approximated by the product of the coercivity and magnetization in the medium [63]. High coercively can counter the superparamagnetic effect [66][69]. The coercivity is defined as the field necessary to change the magnetization to zero (Section 1.3.1) and is determined by $H_c = 2\alpha K_u / M_S - N_{eff} M_s$ [70][71]. α is the micro-structural parameter. M_s is the saturation magnetization, as defined in Section 1.3.1. N_{eff} is an averaged local effective demagnetization factor, which depends on the grain shapes, exchange interactions etc.

A high coercivity demands a stronger writing field. On the other hand, the capabilities of inductive write heads are limited by materials, fabrication technologies, and the form factor of write elements [72].

The tradeoff between signal-to-noise ratio (SNR), writing capability and thermal stability forms the "magnetic recording trilemma" (Figure 1.25) [69][72]. The trilemma constrains the further increase of areal density in magnetic hard disk drives. Bertram [73] estimated in 1998 the density limit for conventional longitudinal magnetic recording to be 155 Mb/mm² (100 Gb/in²). This density limit has been

exceeded by almost one order of magnitude in present disk drives. Innovations such as perpendicular magnetic recording, energy assisted magnetic recording, and patterned media have been introduced in order to push the areal density even higher. Current and future technologies for magnetic hard disk drives will be presented in the next section.

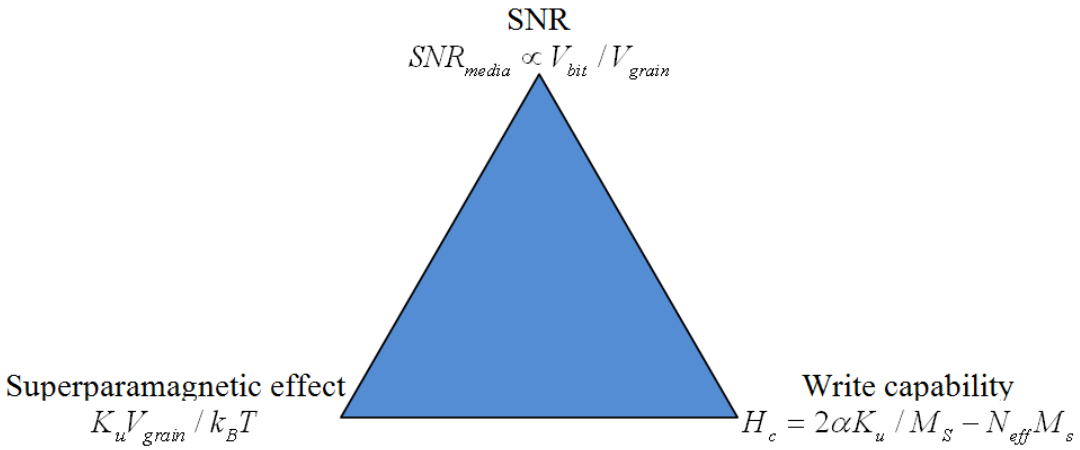

Figure 1.25 Magnetic recording trilemma (after [72])

1.7 Current and Future Technologies under Consideration to Achieve Higher Storage Density

The driving force for research and development in the field of magnetic recording is to increase areal density. However, the magnetic trilemma shows serious limitations for the growth of areal density. Current and promising new technologies that push the areal density beyond the constrains are introduced in this section.

1.7.1 Perpendicular Magnetic Recording (PMR)

The introduction of perpendicular magnetic recording (PMR) led to an increase in the compound annual growth rate of the areal density. It can be seen in Figure 1.13 that the magnetization of the bits in longitudinal magnetic recording (LMR) is parallel to the disk surface. A magnetic transition can be detected when the adjacent magnetic bits are pointing north-pole to north-pole ($\boxed{S \rightarrow N}\boxed{N \leftarrow S}$) or south-pole to south-pole ($\boxed{N \leftarrow S}\boxed{S \rightarrow N}$). On the other hand, the magnetic orientation of bits in perpendicular magnetic recording points up and down. Magnetic transition in perpendicular magnetic recording occurs when the neighboring bits stand with north-pole to south-pole ($\boxed{\uparrow}\boxed{\downarrow}$). This is more stable, since it is less prone to thermal fluctuations compared to longitudinal magnetic recording, and allows the bits to be stacked closer [74][75].

The magnetically soft under layer (SUL) deposited underneath the magnetic recording layer serves as a mirror and generates a magnetic image of the inductive write element [38][75]. A schematic of perpendicular magnetic recording is shown in Figure 1.26. The writing field produced between the trailing poles of the write element and of its image is approximately twice that of the fringing field generated at the write gap in longitudinal magnetic recording. The gradient of the magnetic field is higher than that of conventional longitudinal magnetic recording heads [39]. This enables the use of magnetic materials with higher coercivity that are resistant to temperature variations. In addition, since the stray field from the magnetic transitions in

perpendicular magnetic recording is larger than the longitudinal magnetic recording, the signal-to-noise ratio is improved [75].

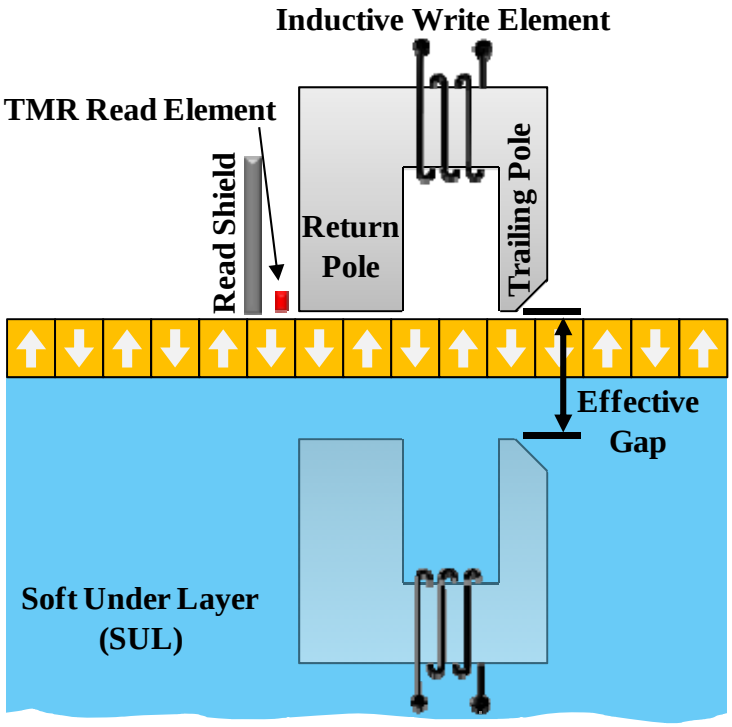

Figure 1.26 Principle of perpendicular magnetic recording (after [39])

1.7.2 Thermal Flying Height Control (TFC) Slider

Flying height reduction is one of the key considerations in reducing the magnetic spacing for the purpose of increasing areal density. In order to achieve an areal density in excess of 1.6 Gb/mm² (1 Tb/in²), the head/disk spacing should approach the sub-2 nm region [76]. Thus, effective control of the spacing between the read/write element and the disk is crucial for achieving high areal density in hard disk drives [77]. Manufacturing tolerances, surface roughness and variations of flying height caused by changes in operating conditions should be minimized in order to

ensure a stable and ultra-low head/disk spacing and reliable performance of hard disk drives.

The idea of using thermal flying height control comes from the observation of pole-tip protrusion caused by Joule heating of the write element. The trailing part of a slider consists of a number of components such as the read element, the read shields, the write coil, and the write element (write pole in perpendicular magnetic recording), as shown in Figure 1.27. Each component is made of different materials. When the temperature increases due to energizing the write coil, the region near the read and write elements deforms thermally due to localized heating and due to differences in the thermal expansion coefficients of the different head materials. The thermal protrusion induced by the temperature increase due to the write current can adversely affect the stability of the slider.

In thermal flying height control sliders, a thermal resistor, the so-called "heater", is integrated into the slider in proximity to the read/write element. If the heater is energized by a current, a thermal protrusion at the read/write element is observed due to heat dissipated in the heater. Using this effect, one can control the flying height at the read and write elements effectively. A schematic of the trailing part of a typical TFC slider is shown in Figure 1.27.

Thermal flying height control sliders are presently in use to compensate thermal effects during reading and writing and are used to effectively maintain a stable and ultra-low spacing between the head and the magnetic disk [78]. In addition, when the heater is energized, the thermal deformation will move the read and write element towards the disk, thereby reducing the local flying height at the read/write element.

The implementation of thermal flying height control techniques allows the reduction of flying height at the read and write elements to the sub-2 nm region.

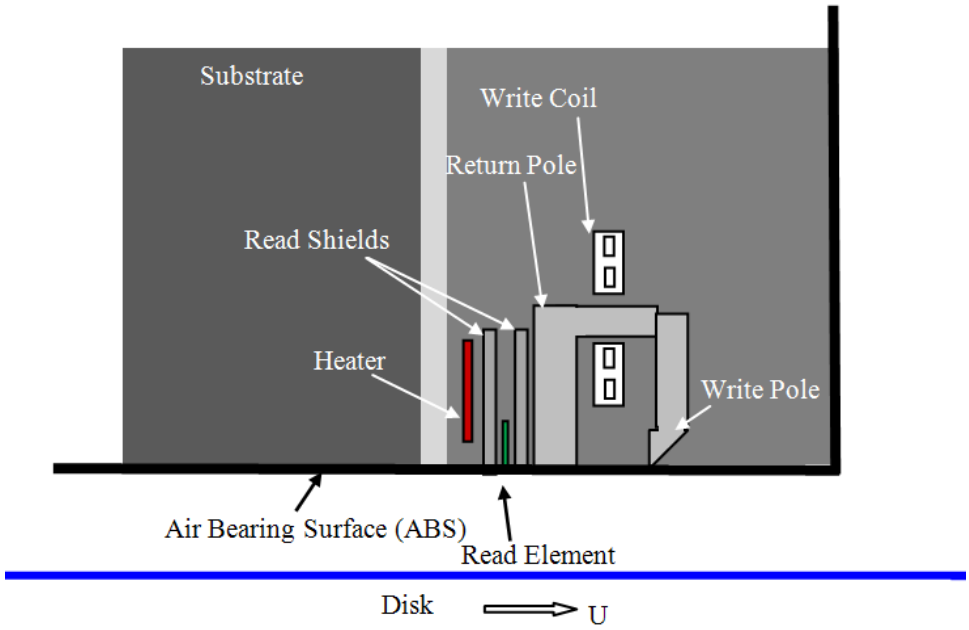

(a)

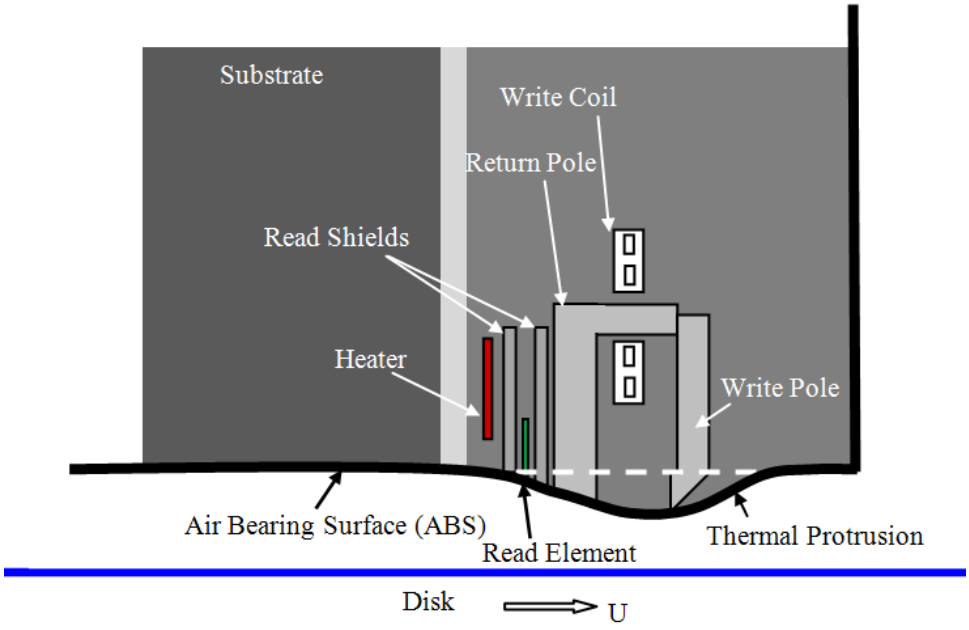

(b)

Figure 1.27 Schematic of thermal flying height control slider with (a) heater is deactivated and (b) heater is energized

Thermo-mechanical modeling of a thermal flying height control slider featuring two separate thermal flying height control heaters and two individual insulator elements will be presented in Chapter 6 as a function of design parameters.

1.7.3 Two Dimensional Magnetic Recording (TDMR)

The implementation of perpendicular recording technology has greatly increased the areal density of disks but is reaching a limit at an areal density around 1.6 – 2.3 Gb/mm² (1 – 1.5 Tb/in²) [27][79]. New technologies are needed to keep the fast growth rate (~40% per year) [27] of areal density for future storage devices.

Two-dimensional magnetic recording (TDMR) is based on so-called "shingle writing" and "two-dimensional read-back processing". Two-dimensional magnetic recording can achieve higher areal density without a substantial redesign of current read/write system [68][80]. Shingle magnetic recording is regarded as a necessary step in achieving higher areal densities of approximately 3.1 – 7.8 Gb/mm² (2 – 5 Tb/in²) before more advanced technologies such as energy assisted magnetic recording or patterned media will be implemented [79][81]. As shown in Figure 1.28, during shingle writing, the corner of a write head records information on tracks that are wider than the desired width. After the track has been written, the head is incremented and a new track is written leaving a narrow portion of the initial track. This allows the width of the write element be larger than the desired track width and eliminates adjacent track erasure. In addition, the magnetic field generated in shingle recording is much stronger than that of a conventional write element, with high field gradient in both down-track and cross track directions [68][80]. However, implementation of shingle

magnetic recording loses the “update-in-place” feature of conventional magnetic recording, which means that the information on a track cannot be updated until the data on the sequentially overlapping tracks has been recovered and rewritten onto the disk. This causes a longer writing time [81] and requires new technologies such as adaption of firmware similar to solid-state disks (SSD) [82].

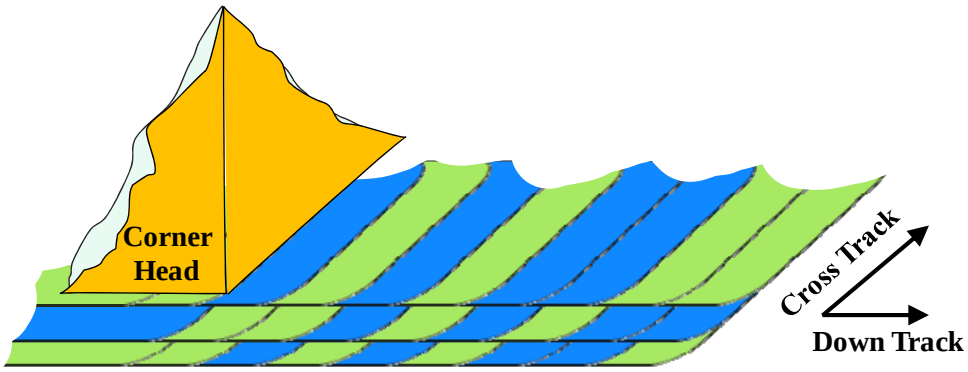

Figure 1.28 Schematic of shingle magnetic recording (after [68])

Two-dimensional (2-D) read-back techniques are among the most promising approaches to achieve higher areal density compared to conventional continuous magnetic media [68]. In two-dimensional read-back processing, an array head detects magnetic transitions from several neighboring tracks at the same time and forms a two-dimensional read-back signal with high resolution in both down-track and cross-track directions. Advanced coding and signal-processing techniques must be used to recover the read-back signals. Since the two-dimensional signal detection process takes into consideration the interference between adjacent tracks, the read process is more complicated and impacted by a low signal-to-noise ratio. The signal detection

procedure can also be achieved by a single read element by reading information from several sequentially passes. However, this will delay the read time [80].

1.7.4 Heat Assisted Magnetic Recording (HAMR)

Magnetic materials with high coercivity have good resistance to thermal fluctuation. Using a high coercivity magnetic material enables a reduced grain size and results in an increase of areal density. However, switching the magnetic orientation with high coercivity materials requires strong magnetic fields which cannot be achieved with write elements presently used. Additional energy must be used to assist the reversal of magnetization. Energy assisted magnetic recording has been proposed to address the difficulties of writing information on small and tightly packed bits of high coercivity media [27].

One promising approach is heat assisted magnetic recording (HAMR). Heat assisted magnetic recording uses the phenomenon that the coercivity H_c of magnetic material decreases with temperature [6]. This enables information recording on high coercivity magnetic material at elevated temperature, with a lower field than at room temperature. As can be seen in Figure 1.29, in heat assisted magnetic recording the temperature is increased until the coercivity of the magnetic material is lower than the available head writing filed. Writing can be performed as long as the coercivity of the material is lower than the available write field. The medium magnetization becomes "frozen" when the temperature decreases to room temperature [83].

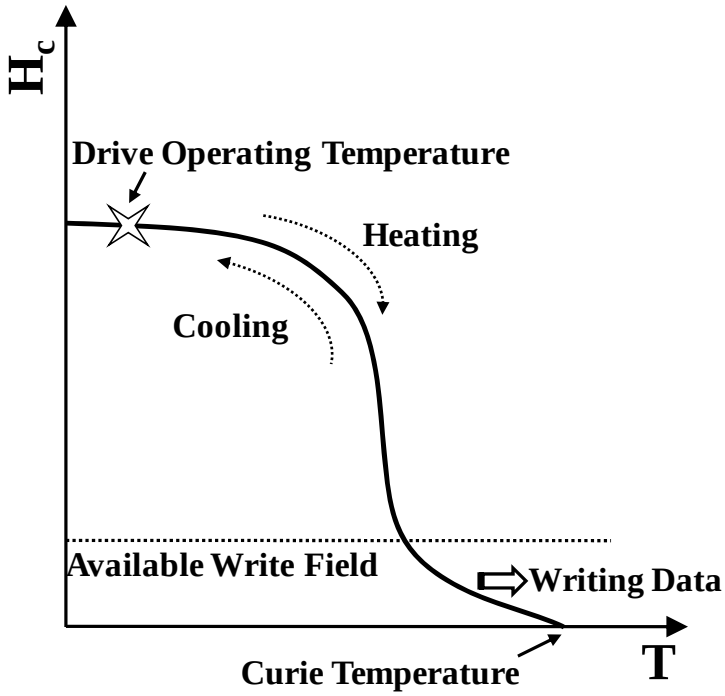

Figure 1.29 Principle of write process in heat assisted magnetic recording (after [6])

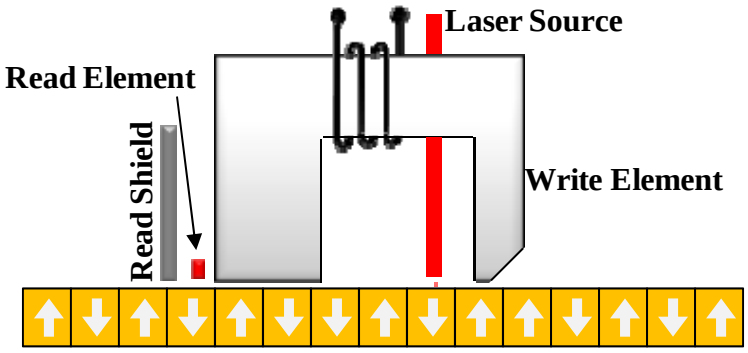

Figure 1.30 Schematic of heat assisted magnetic recording head/disk interface

A schematic of the head/disk interface for heat assisted magnetic recording is shown in Figure 1.30. A thermo-mechanical model incorporating a heat assisted magnetic recording optical system into a thermal flying height control slider with dual

heater/insulator elements will be presented in Chapter 6. There, we explore the effect of heat dissipated along the laser delivery path on the thermal deformation and flying characteristics of a HAMR-TFC slider.

The high temperature experienced by the magnetic media raises concerns about the stability and tribological properties of the lubricant layer on the disk surface. Experimental evaluations on advanced HAMR-type lubricants with improved photo-thermal stability and tribological properties will be present in Chapter 7.

1.7.5 Microwave Assisted Magnetic Recording (MAMR)

Another possible option for recording information on a high coercivity magnetic material may be achieved by applying a microwave field during writing. This is known as “microwave assisted magnetic recording”.

As seen in Figure 1.31, an ac field generator is incorporated into the slider in order to produce a localized ac field in the microwave frequency regime. The amplitude of this ac field is on the order of kilo-Oersted (kOe) and its frequency is on the order of Gigahertz (GHz), matching the “ferromagnetic resonance frequency” [80][85]. The reversal field of the magnetic media is significantly reduced by the presence of microwaves. The information can be recorded with a write field that normally would be too small to cause the reversal.

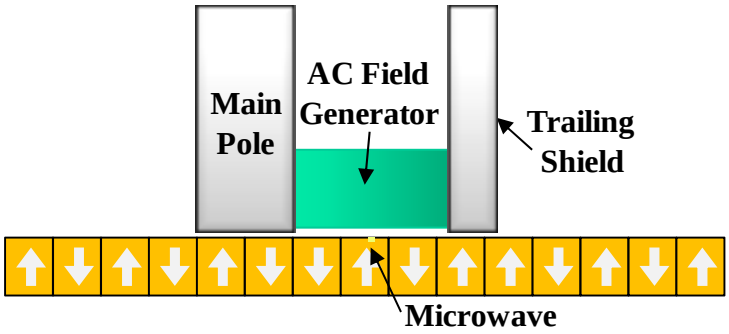

Figure 1.31 Schematic of microwave assisted recording

1.7.6 Patterned Media

One of the main challenges for hard disk drive designers is to increase the areal density while maintaining the stability and reliability of the recorded information at the same time. In order to increase the areal density, the magnetic bits need to be made smaller and more tightly packed, which may introduce thermal instability and magnetic "cross talk" between bits.

Patterned media is one of the most promising technologies that assure continual areal density growth. Instead of a continuous granular recording layer, in patterned media the magnetic bits are physically separated in order to reduce interference between neighboring bits. This improves the signal-to-noise ratio and allows a reduction of the number of grains per bit [86][87].

A schematic of continuous media and patterned media is shown in Figure 1.32. In discrete track recording (DTR), individual tracks are etched on the disk surface. This is to avoid the "cross talk" between bits in the radial direction. In bit patterned media (BPM), arrays of tiny well-defined magnetic islands are produced on the disk surface with one bit of information stored in a single island [68].

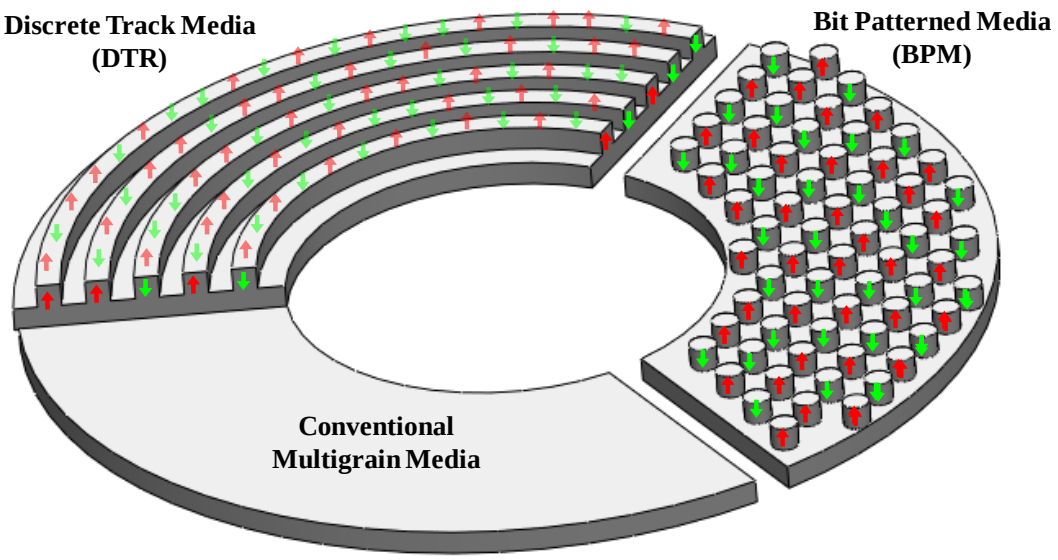

Figure 1.32 Comparison of conventional disks and patterned media

One of the challenges in patterned media recording is the manufacturing of the patterned media. Fabrication procedures such as electron beam lithography, ion beam lithography, immersion lithography, and nanoimprinting [88-90] have been investigated for high resolution patterned media. Yang et al. fabricated bit patterned media using high-resolution electron beam lithography followed by the deposition of a magnetic film in order to avoid resolution degradation due to etching or lift off. They have demonstrated a 5.1 Gb/mm² (3.3 Tb/in²) areal density [86]. In addition to the difficulties of disk fabrication, writing must be synchronized so that the write field is coincident with the location of patterned bits. This adds huge challenges to the development of patterned media technology [80].

A numerical investigation of the steady-state flying characteristics of sliders flying over bit patterned media will be presented in Chapter 3.

1.8 Organization of the Dissertation

This dissertation focuses on (a) investigation of the head/disk interface for bit patterned media (BPM), (b) the design of thermal flying height control (TFC) sliders, and (c) the implementation and tribology of heat assisted magnetic recording (HAMR).

Chapter 1 provides a short introduction on the history of magnetic recording and the principles of the reading and writing process. The mechanical structure in a hard disk drive is explained and illustrated. In addition, an overview of current approaches and potential technological improvements in hard disk drives is presented.

Chapter 2 presents an overview of the theoretical background of hydrodynamic lubrication for air bearing simulations of the head/disk interface. The derivation of the governing equations that are used to obtain the pressure distribution and flying characteristics of a slider is presented along with a derivation of the finite element formulation of the Reynolds equation.

Chapter 3 investigates the steady-state flying behavior of conventional and spherical-pad sliders over bit patterned media. A finite-element-based air bearing simulator, described in Chapter 2, is used to study the effect of design parameters on the flying characteristics of sliders.

Chapter 4 provides an overview of the theoretical background for the thermo-mechanical analysis of a slider with an internal heat source. The derivation of heat flux at the head/disk interface is presented. An integrated simulator combining the air

bearing simulation and the thermo-mechanical modeling of a slider is introduced. This integrated simulator is used for the numerical studies presented in Chapters 5, 6 and 7.

Chapter 5 investigates numerically the effect of enhanced thermal radiation for thermal flying height control sliders at very small flying heights.

Chapter 6 presents a numerical investigation of a thermal flying height control slider featuring two heater and insulator elements. The effect of design parameters of the heater/insulator elements is studied to optimize the performance of thermal flying height control sliders.

Chapter 7 introduces a finite element model that incorporates a heat assisted magnetic recording optical system into a thermal flying height control slider. The effect of heat dissipation along the laser path on the thermal deformation and flying characteristics of a HAMR-TFC slider is investigated. The design parameters of a slider with two thermal flying height control heaters, the so-called “dual TFC slider”, are optimized in order to minimize the dependence of the head/disk interface spacing on laser induced thermal effects.

Chapter 8 experimentally estimates the photo-thermal stability and tribological properties of perfluoropolyether (PFPE) lubricants modified with photo stabilizer end groups under laser beam exposure for heat assisted magnetic recording applications. The reflectance change due to exposure of the modified PFPE lubricant films to laser light and the friction force at the head/disk interface of sliders flying over modified PFPE lubricants are evaluated.

Chapter 9 summarizes this thesis.

Chapter 2

Hydrodynamic Lubrication of the Head/Disk Interface

As described in Chapter 1, a stable head/disk interface is critical to the functionality and reliability of hard disk drives. The surfaces of the slider and disk are "conformal" since the spacing between the slider and disk is much smaller than the dimensions of the slider and disk [91]. A hydrodynamic air bearing is formed between the flying slider and the rotating disk. Viscous forces generated within the air bearing create a pressure distribution that supports the normal load exerted on the slider by the suspension. This enables a constant spacing between the read/write element and the magnetic medium. Pressure distribution in the hydrodynamic lubricating layer formed in the converging gap between the slider and disk can be described by the Reynolds equation [91].

In this chapter, the compressible Reynolds equation is derived. A modified form of the Reynolds equation accounting for rarefaction effects is used to describe the ultra-thin hydrodynamic air bearing in hard disk drives. The finite element solution of the governing equations presented in this chapter will be used in Chapter 3 for the predictions of pressure distribution and flying characteristics of sliders flying over bit patterned media.

2.1 Reynolds Equation

The Reynolds equation is derived from the Navier-Stokes equations [91]. It is based on the continuum theory of fluid mechanics. In particular, the fluid is considered to be a Newtonian fluid with constant viscosity [92][128]. The flow is assumed to be laminar and isothermal. The viscous force is dominant over the body forces [93].

A typical converging channel simulating the head/disk interface is shown in Figure 2.1. The spacing between the slider and the disk is a function of the position (x, y) and is denoted by $h(x, y)$. The minimum head/disk spacing is $h_{\min}$. B is the length of the slider while L is the width of the slider. U and V are the disk velocities in the x and y direction, respectively. $\mathbf{u} = (u \quad v \quad w)$ is the velocity of air flow with $u, \quad v, \quad w$ being the velocity components in the x, y and z directions, respectively.

For dimensions used in current hard disk drives, the minimum spacing between the slider and the disk is on the order of a few nanometers. On the other hand, the length and width of a typical femto slider are 850 and 700 μm, respectively. Thus, $h_{\min} << B, L$.

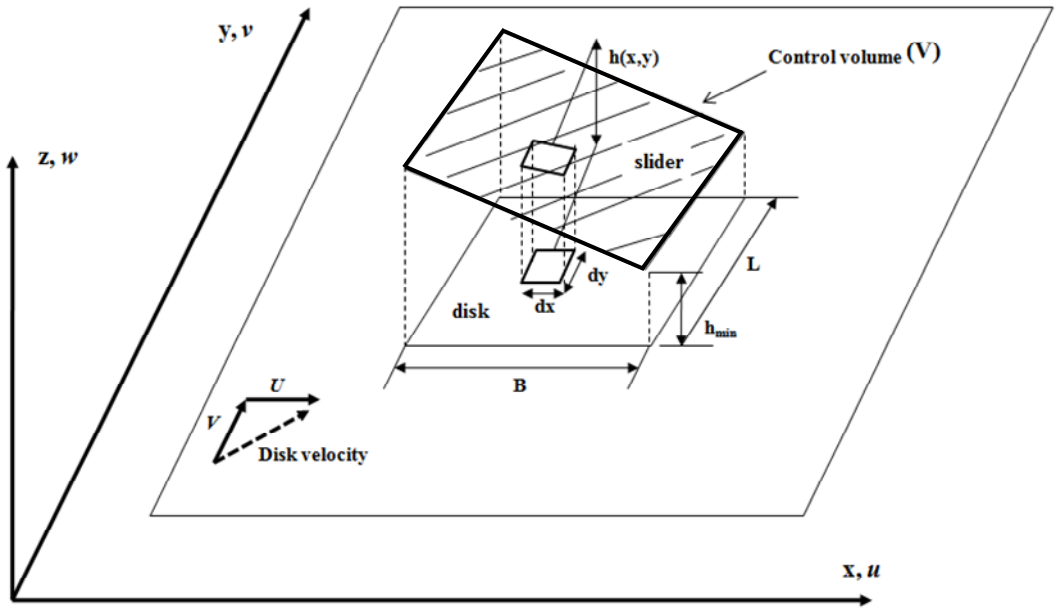

Figure 2.1 Control volume in pivoted slider bearing (courtesy of [92])

According to Newton's law of motion, the rate of change of momentum inside a control volume and the net flux of momentum across the boundary equals the surface force exerted at the boundary of the volume (neglecting the body forces which are mainly due to gravity) [94], i.e.,

$$\int_V \frac{\partial}{\partial t}(\rho \mathbf{u})\, dV + \int_S \rho \mathbf{u}\mathbf{u} \cdot \mathbf{n} dS = \int_S \boldsymbol{\tau} \cdot \mathbf{n} dS \tag{2.1}$$

where ρ is the density of the air, $\boldsymbol{\tau}$ denotes the stress tensor, $\mathbf{n}$ is the unit outward normal to the boundary surface S, and V is the volume.

The rate of change of mass within a control volume should be equal to the net flux across the boundary:

$$\int_V \frac{\partial \rho}{\partial t} dV + \int_S \rho \mathbf{u} \cdot \mathbf{n} dS = 0 \tag{2.2}$$

The general Gauss' theorem relates the behavior of a physical field **A** in the domain to the flux of the field across the boundary [95][96] and is expressed as:

$$\int_V \nabla \cdot \mathbf{A} dV = \int_S \mathbf{n} \cdot \mathbf{A} dS \tag{2.3}$$

Applying the Gauss' theorem to Equation (2.1), and noting that the integrand in Equation (2.1) is independent of the choice of the control volume [92][94], we obtain the momentum equation in the form:

$$\rho\left(\frac{\partial \mathbf{u}}{\partial t} + \mathbf{u} \cdot \nabla \mathbf{u}\right) = \nabla \cdot \boldsymbol{\tau} \tag{2.4}$$

The constitutive equation for a Newtonian fluid describing the relation between the deformation and the stress is [94]:

$$\boldsymbol{\tau} = -\left(p + \frac{2}{3}\mu \nabla \cdot \mathbf{u}\right)\boldsymbol{\delta} + \mu\left[\nabla \mathbf{u} + (\nabla \mathbf{u})^T\right] \tag{2.5}$$

where p is the pressure, μ is the viscosity of the fluid and $\boldsymbol{\delta}$ is a second-order isotropic tensor. The negative sign in front of the pressure is because the normal components of the stress $\boldsymbol{\tau}$ are negative when indicating compression [94].

An "order of magnitude" analysis is needed to determine the relevant terms in Equation (2.4) and (2.5). The coordinates and the velocity can be normalized by the characteristic dimensions of the slider and the velocity of the disk, i.e.,

$$\begin{aligned} x^* &= \frac{x}{B}, y^* = \frac{y}{L}, z^* = \frac{z}{h_{\min}} \\ u^* &= \frac{u}{U}, v^* = \frac{v}{V}, w^* = \frac{w}{W} \end{aligned} \tag{2.6}$$

where W is the velocity scale in the z direction. The normalized density and pressure are given by:

$$\rho^* = \frac{\rho}{\rho_a}, p^* = \frac{p}{P} \tag{2.7}$$

where ρ_a and P are the ambient density and the pressure scale of the air, respectively.

The velocity scale W can be determined from the steady-state continuity equation:

$$\frac{\rho_a U}{B}\frac{\partial \rho^* u^*}{\partial x^*} + \frac{\rho_a V}{L}\frac{\partial \rho^* v^*}{\partial y^*} + \frac{\rho_a W}{h_{\min}}\frac{\partial \rho^* w^*}{\partial z^*} = 0 \tag{2.8}$$

Since all the terms in Equation (2.8) should be of the same order, W is given by:

$$W = \frac{h_{\min}}{B}U = \frac{h_{\min}}{L}V \tag{2.9}$$

The pressure scale can be determined from the momentum equation in the x direction:

$$\begin{aligned} \mathrm{Re}^*\left[\frac{\partial}{\partial x^*}\left(\rho^* u^{*2}\right) + \frac{\partial}{\partial y^*}\left(\rho^* u^* v^*\right) + \frac{\partial}{\partial z^*}\left(\rho^* u^* w^*\right)\right] = -\frac{P h_{\min}^2}{\mu U B}\frac{\partial p^*}{\partial x^*} + \\ \left(\frac{h_{\min}}{B}\right)^2\left[\frac{4}{3}\frac{\partial^2 u^*}{\partial x^{*2}} + \frac{1}{3}\frac{\partial^2 v^*}{\partial x^* \partial y^*} + \frac{1}{3}\frac{\partial^2 w^*}{\partial x^* \partial z^*}\right] + \left(\frac{h_{\min}}{L}\right)^2\frac{\partial^2 u^*}{\partial y^{*2}} + \frac{\partial^2 u^*}{\partial z^{*2}} \end{aligned} \tag{2.10}$$

where Re^* is the modified Reynolds number defined by:

$$\mathrm{Re}^* \equiv \frac{\rho_a U B}{\mu}\left(\frac{h_{\min}}{B}\right)^2 = \mathrm{Re}\left(\frac{h_{\min}}{B}\right)^2 \tag{2.11}$$

For a typical head/disk interface and standard air properties, ρ_a is approximately 1.21 kg/m³ and μ is 1.82×10^{-5} kg/(m·s) [107]. The length of the slider B is on the order of 10^{-3} m. We assume that the spacing between the slider and the disk h is 5×10^{-9} m, and that the disk velocity is 20 m/s. With these assumptions, Re^* is approximately 3.3×10^{-8}. Clearly, the ratio of inertia terms on the left hand side of Equation (2.10) to

viscous terms on the right hand side of Equation (2.10) is much smaller than 1, i.e., inertia terms can be neglected relative to viscous terms.

Since $h_{\min} << B, L$ and $\mathrm{Re}^* << 1$, the momentum equation in the x direction can be simplified as:

$$-\frac{P{h_{\min}}^2}{\mu UB}\frac{\partial p^*}{\partial x^*}+\frac{\partial^2 u^*}{\partial {z^*}^2}=0 \tag{2.12}$$

The terms in Equation (2.12) have to be of the same order; thus, the pressure scale P can be written as:

$$P=\frac{\mu UB}{h_{\min}^2} \tag{2.13}$$

Substituting the dimensionless variables defined above into the momentum equation in the y and z directions, we obtain:

$$\begin{aligned}\mathrm{Re}^*&\left[\frac{\partial}{\partial x^*}\left(\rho^* u^* v^*\right)+\frac{\partial}{\partial y^*}\left(\rho^* {v^*}^2\right)+\frac{\partial}{\partial z^*}\left(\rho^* v^* w^*\right)\right]=-\frac{P{h_{\min}}^2}{\mu VL}\frac{\partial p^*}{\partial y^*}\\&+\left(\frac{h_{\min}}{L}\right)^2\left[\frac{4}{3}\frac{\partial^2 v^*}{\partial {y^*}^2}+\frac{1}{3}\frac{\partial^2 u^*}{\partial x^*\partial y^*}+\frac{1}{3}\frac{\partial^2 v^*}{\partial y^*\partial z^*}\right]+\left(\frac{h_{\min}}{B}\right)^2\frac{\partial^2 v^*}{\partial {x^*}^2}+\frac{\partial^2 v^*}{\partial {z^*}^2}\end{aligned} \tag{2.14}$$

$$\begin{aligned}\mathrm{Re}^*&\left(\frac{h_{\min}}{B}\right)^2\left[\frac{\partial}{\partial x^*}\left(\rho^* u^* w^*\right)+\frac{\partial}{\partial y^*}\left(\rho^* v^* w^*\right)+\frac{\partial}{\partial z^*}\left(\rho^* {w^*}^2\right)\right]=-\frac{\partial p^*}{\partial z^*}\\&+\left(\frac{h_{\min}}{B}\right)^2\left[\frac{4}{3}\frac{\partial^2 w^*}{\partial {z^*}^2}+\frac{1}{3}\frac{\partial^2 u^*}{\partial x^*\partial z^*}+\frac{1}{3}\frac{\partial^2 v^*}{\partial y^*\partial z^*}+\left(\frac{h_{\min}}{B}\right)^2\frac{\partial^2 w^*}{\partial {x^*}^2}+\left(\frac{h_{\min}}{L}\right)^2\frac{\partial^2 w^*}{\partial {y^*}^2}\right]\end{aligned} \tag{2.15}$$

Since $h_{\min} << B, L$ and $\mathrm{Re}^* << 1$, the momentum equation in the y and z direction are simplified as:

$$-\frac{P{h_{\min}}^2}{\mu VL}\frac{\partial p^*}{\partial y^*}+\frac{\partial^2 v^*}{\partial {z^*}^2}=0 \tag{2.16}$$

and

$$\frac{\partial p^*}{\partial z^*} = 0 \tag{2.17}$$

Rewriting Equation (2.12), (2.16) and (2.17) in dimensional forms, we obtain:

$$\frac{\partial p}{\partial x} = \frac{\partial}{\partial z}\left(\mu \frac{\partial u}{\partial z}\right) \tag{2.18}$$

$$\frac{\partial p}{\partial y} = \frac{\partial}{\partial z}\left(\mu \frac{\partial v}{\partial z}\right) \tag{2.19}$$

$$\frac{\partial p}{\partial z} = 0 \tag{2.20}$$

From Equation (2.18-2.20), it can be seen that the pressure forces are balanced by the viscous forces. This statement reveals the fundamental principle of lubrication theory. In addition, we notice that the pressure is only a function of x and y and does not vary across the thickness of the fluid film (Equation (2.20)).

The non-slip boundary conditions state that the velocity of the fluid at the disk surface ($z = 0$) equals the disk velocity, i.e. $u = U$ and $v = V$ and that the velocity of the fluid attached to the air bearing surface of the slider ($z = h$) is 0.

Applying the non-slip boundary conditions to the integrated equations of (2.18) and (2.19), we obtain the velocity distribution of the flow in the x and y directions as:

$$\begin{aligned} u &= \frac{1}{2\mu}\frac{\partial p}{\partial x}\left(z^2 - zh\right) + U\left(1 - \frac{z}{h}\right) \\ v &= \frac{1}{2\mu}\frac{\partial p}{\partial y}\left(z^2 - zh\right) + V\left(1 - \frac{z}{h}\right) \end{aligned} \tag{2.21}$$

The continuity equation in integral form can be written as:

$$\int_0^h \left[\frac{\partial \rho}{\partial t} + \frac{\partial}{\partial x}(\rho u) + \frac{\partial}{\partial y}(\rho v) + \frac{\partial}{\partial z}(\rho w) \right] dz = 0 \tag{2.22}$$

Rearranging Equation (2.22) results in:

$$\int_0^h \frac{\partial}{\partial z}(\rho w)\, dz = -\int_0^h \left[\frac{\partial \rho}{\partial t} + \frac{\partial}{\partial x}(\rho u) + \frac{\partial}{\partial y}(\rho v) \right] dz \tag{2.23}$$

Since the vertical velocity w at the disk surface, i.e., at $z = 0$, equals zero, the term on the left hand side of Equation (2.23) can be written as:

$$\int_0^h \frac{\partial}{\partial z}(\rho w)\, dz = \rho w\Big|_0^h = \rho w\Big|_{z=h} = \rho \frac{\partial h}{\partial t} + \rho u\Big|_{z=h} \frac{\partial h}{\partial x} + \rho v\Big|_{z=h} \frac{\partial h}{\partial y} \tag{2.24}$$

Substituting Equation (2.24) into Equation (2.23), we obtain:

$$\rho \frac{\partial h}{\partial t} + \rho u\Big|_{z=h} \frac{\partial h}{\partial x} + \rho v\Big|_{z=h} \frac{\partial h}{\partial y} = -\int_0^h \left[\frac{\partial \rho}{\partial t} + \frac{\partial}{\partial x}(\rho u) + \frac{\partial}{\partial y}(\rho v) \right] dz \tag{2.25}$$

The integration and differentiation of terms on the right hand side of in Equation (2.25) can be exchanged by the Leibnitz rule, which states that:

$$\int_0^h \frac{\partial}{\partial x} F(x, y, z)\, dz = -\frac{\partial}{\partial x} \int_0^h F(x, y, z)\, dz + \frac{\partial h}{\partial x} F(x, y, z = h) \tag{2.26}$$

Applying Equation (2.26) to Equation (2.25) yields:

$$\begin{aligned} &\rho \frac{\partial h}{\partial t} + \rho u\Big|_{z=h} \frac{\partial h}{\partial x} + \rho v\Big|_{z=h} \frac{\partial h}{\partial y} = \\ &-\frac{\partial}{\partial t} \int_0^h \rho\, dz + \rho \frac{\partial h}{\partial t} - \frac{\partial}{\partial x} \int_0^h (\rho u)\, dz + \rho u\Big|_{z=h} \frac{\partial h}{\partial x} - \frac{\partial}{\partial y} \int_0^h (\rho v)\, dz + \rho v\Big|_{z=h} \frac{\partial h}{\partial y} \end{aligned} \tag{2.27}$$

After rearranging, Equation (2.27) becomes:

$$\frac{\partial \rho h}{\partial t} + \frac{\partial}{\partial x} \int_0^h (\rho u)\, dz + \frac{\partial}{\partial y} \int_0^h (\rho v)\, dz = 0 \tag{2.28}$$

Substituting the velocity distribution (Equation (2.21)) into Equation (2.28), the last two terms in Equation (2.28) can be written as:

$$\begin{aligned}
\frac{\partial}{\partial x}\int_0^h (\rho u)\,dz &= \frac{\partial}{\partial x}\int_0^h \left\{\rho\left[\frac{1}{2\mu}\frac{\partial p}{\partial x}\left(z^2 - zh\right) + U\left(1-\frac{z}{h}\right)\right]\right\} dz \\
&= \frac{\partial}{\partial x}\rho\left[\frac{1}{2\mu}\frac{\partial p}{\partial x}\left(\frac{z^3}{3} - \frac{z^2 h}{2}\right) + U\left(z - \frac{z^2}{2h}\right)\right]_0^h \\
&= \frac{\partial}{\partial x}\left[\frac{1}{2\mu}\frac{\partial p}{\partial x}\left(-\frac{\rho h^3}{6}\right) + U\left(\frac{\rho h}{2}\right)\right] \\
\frac{\partial}{\partial y}\int_0^h (\rho v)\,dz &= \frac{\partial}{\partial y}\int_0^h \left\{\rho\left[\frac{1}{2\mu}\frac{\partial p}{\partial y}\left(z^2 - zh\right) + V\left(1-\frac{z}{h}\right)\right]\right\} dz \\
&= \frac{\partial}{\partial y}\rho\left[\frac{1}{2\mu}\frac{\partial p}{\partial y}\left(\frac{z^3}{3} - \frac{z^2 h}{2}\right) + V\left(z - \frac{z^2}{2h}\right)\right]_0^h \\
&= \frac{\partial}{\partial y}\left[\frac{1}{2\mu}\frac{\partial p}{\partial y}\left(-\frac{\rho h^3}{6}\right) + V\left(\frac{\rho h}{2}\right)\right]
\end{aligned} \tag{2.29}$$

This results in:

$$\frac{\partial \rho h}{\partial t} - \frac{1}{12\mu}\frac{\partial}{\partial x}\left(\rho h^3 \frac{\partial p}{\partial x}\right) + \frac{U}{2}\frac{\partial}{\partial x}(\rho h) - \frac{1}{12\mu}\frac{\partial}{\partial y}\left(\rho h^3 \frac{\partial p}{\partial y}\right) + \frac{V}{2}\frac{\partial}{\partial y}(\rho h) = 0 \tag{2.30}$$

Assuming that air is an ideal gas following the perfect gas law $p = RT\rho$, we obtain the Reynolds equation for compressible gases in the form:

$$\frac{\partial}{\partial x}\left(ph^3 \frac{\partial p}{\partial x}\right) + \frac{\partial}{\partial y}\left(ph^3 \frac{\partial p}{\partial y}\right) = 6\mu U \frac{\partial}{\partial x}(ph) + 6\mu V \frac{\partial}{\partial y}(ph) + 12\mu \frac{\partial}{\partial t}(ph) \tag{2.31}$$

Using standard vector notations, Equation (2.31) can be expressed as:

$$\nabla \cdot \left(ph^3 \nabla p\right) = 6\mu \mathbf{U} \cdot \nabla (ph) + 12\mu \frac{\partial}{\partial t}(ph) \tag{2.32}$$

where $\mathbf{U} = \begin{bmatrix} U & V \end{bmatrix}$ is the velocity vector of the disk.

2.2 Rarefaction Effects for Ultra-Low Head/Disk Interface

An areal density beyond 1.6 Gb/mm² (1 Tb/in²) requires a reduction of the spacing between the slider and the disk to a few nanometers. This is much smaller than the mean free path of the air ($\lambda \approx 65$ nm at standard temperature and pressure). The so-called "Knudsen number" is a dimensionless quantity that is used to determine the degree of rarefaction and is defined by $\mathrm{Kn} = \lambda / h$. As the head/disk spacing becomes smaller, the Knudsen number Kn becomes increasingly larger [97]. Whenever $\mathrm{Kn} > 0.01$, the continuum description of a fluid in a hydrodynamic bearing breaks down. The layer directly adjacent to the solid surface has a finite slip velocity. Slip flow boundary conditions at the interface between the solid and the gas need to be considered in order to represent the rarefaction effect [55]. Several slip correction models have been derived to describe the slip velocity boundary conditions [98] at the head/disk interface in a hard disk drive.

A first-order slip flow correction was introduced by Burgdorfer [99], which enforces the boundary conditions:

$$\begin{aligned} z = 0: \quad & u = U + \frac{2-\sigma_M}{\sigma_M}\lambda \left.\frac{\partial u}{\partial z}\right|_{z=0} \qquad v = V + \frac{2-\sigma_M}{\sigma_M}\lambda \left.\frac{\partial v}{\partial z}\right|_{z=0} \\ z = h: \quad & u = -\frac{2-\sigma_M}{\sigma_M}\lambda \left.\frac{\partial u}{\partial z}\right|_{z=h} \qquad v = -\frac{2-\sigma_M}{\sigma_M}\lambda \left.\frac{\partial v}{\partial z}\right|_{z=h} \end{aligned} \tag{2.33}$$

where λ is the mean free path of the air, and σ_M is the so-called "surface accommodation coefficient" of momentum representing the tendency of a gas to

accommodate to the state of the wall [100]. The velocity profile corresponding to the first-order slip boundary condition is:

$$\begin{aligned} u &= \frac{1}{2\mu}\frac{\partial p}{\partial x}\left(z^2 - zh - a\lambda h\right) + U\left(1 - \frac{z + a\lambda}{h + 2a\lambda}\right) \\ v &= \frac{1}{2\mu}\frac{\partial p}{\partial y}\left(z^2 - zh - a\lambda h\right) + V\left(1 - \frac{z + a\lambda}{h + 2a\lambda}\right) \end{aligned} \tag{2.34}$$

where $a \equiv \left(2 - \sigma_M\right)/\sigma_M$.

The first-order slip theory is applicable for Knudsen numbers $0.01 < \mathrm{Kn} < 0.1$ [101]. A more accurate second-order slip model suitable for head/disk spacing below 100 nm [55] was developed by Hsia and Domoto [101], with the slip flow boundary conditions of:

$$\begin{aligned} z = 0: \quad & u = U + \lambda\left.\frac{\partial u}{\partial z}\right|_{z=0} - \frac{\lambda}{2}\left.\frac{\partial^2 u}{\partial z^2}\right|_{z=0} \qquad v = V + \lambda\left.\frac{\partial v}{\partial z}\right|_{z=0} - \frac{\lambda}{2}\left.\frac{\partial^2 v}{\partial z^2}\right|_{z=0} \\ z = h: \quad & u = -\lambda\left.\frac{\partial u}{\partial z}\right|_{z=h} - \frac{\lambda}{2}\left.\frac{\partial^2 u}{\partial z^2}\right|_{z=h} \qquad v = -\lambda\left.\frac{\partial v}{\partial z}\right|_{z=h} - \frac{\lambda}{2}\left.\frac{\partial^2 v}{\partial z^2}\right|_{z=h} \end{aligned} \tag{2.35}$$

The velocity distribution of the flow in the x and y directions is:

$$\begin{aligned} u &= \frac{1}{2\mu}\frac{\partial p}{\partial x}\left(z^2 - zh - \lambda h - \lambda^2\right) + U\left(1 - \frac{z + \lambda}{h + 2\lambda}\right) \\ v &= \frac{1}{2\mu}\frac{\partial p}{\partial y}\left(z^2 - zh - \lambda h - \lambda^2\right) + V\left(1 - \frac{z + \lambda}{h + 2\lambda}\right) \end{aligned} \tag{2.36}$$

For ultra-low head/disk spacings as in modern hard disk drives, a more complicated “Boltzmann correction” is generally in use. It was derived by Gans [102] from the linearized Boltzmann equations [102]. Fukui and Kaneko [103] generalized all three models in one general form as:

$$\nabla\cdot\left(\bar{Q}ph^3\nabla p\right) = 6\mu\mathbf{U}\cdot\nabla\left(ph\right) + 12\mu\frac{\partial}{\partial t}\left(ph\right) \tag{2.37}$$

where the correction term $\bar{Q}$ is the ratio of the Poiseuille flow rate $Q_p(D)$ to the continuum flow rate $Q_c(D)$, and D is the modified inverse Knudsen number defined by $D = \sqrt{\pi}/2Kn$. The correction term for the first-order, second-order and Boltzmann equations are expressed by Equation (2.38-2.40), respectively:

$$Q_{p1} = \frac{D}{6} + \frac{\sqrt{\pi}}{2} \tag{2.38}$$

$$Q_{p2} = \frac{D}{6} + \frac{\sqrt{\pi}}{2} + \frac{\pi}{4D} \tag{2.39}$$

$$Q_{p\mathrm{B}} = \begin{cases} \frac{D}{6} + 1.0162 + \frac{1.0653}{D} - \frac{2.1354}{D^2} & (5 \le D) \\ 0.13852D + 1.25087 + \frac{0.15653}{D} - \frac{0.00969}{D^2} & (0.15 \le D \le 5) \\ -2.22919\mathrm{D} + 2.10673 + \frac{0.01653}{D} - \frac{0.0000694}{D^2} & (0.01 \le D \le 0.15) \end{cases} \tag{2.40}$$

2.3 Finite Element Formulation of Reynolds Equation

It can be seen from Equation (2.37) that the Reynolds equation is a non-linear partial differential equation. Only a few limiting cases of this equation are available in closed form solution. For most cases of practical importance, numerical analysis is needed. At the Center for Magnetic Recording Research (CMRR) an air bearing simulator was developed in the last decade based on the finite element solution of the slip-corrected Reynolds equation. This simulator is described in the following section

and is used for the numerical investigation of the head/disk interface described in this thesis.

The finite element method is one of the most common numerical approaches to find the solution of a partial differential equation or an integral equation predicting the system behavior in a global sense. The idea of the finite element method is to discretize a domain posed by mathematically defined statements into a finite numbers of small, non-overlapping sub-domains, the so-called "elements" [55][104][105]. Solutions are obtained at the nodal points and are interpolated by shape functions within the elements.

Multiplying Equation (2.37) by weight functions w satisfying the essential boundary conditions, and integrating over the air bearing surface, Equation (2.37) can be written as:

$$\int_V w\left\{\nabla\cdot\left(\bar{Q}ph^3\nabla p\right)-6\mu\mathbf{U}\cdot\nabla\left(ph\right)-12\mu\frac{\partial}{\partial t}\left(ph\right)\right\}dV=0 \tag{2.41}$$

Using integration by parts, i.e.,

$$\int_V\left(\nabla\cdot\mathbf{v}\right)wdV=\int_V\nabla\cdot\left(\mathbf{v}w\right)dV-\int_V\mathbf{v}\cdot\nabla wdV \tag{2.42}$$

one can write Equation (2.41) as:

$$\begin{aligned}&\int_V\left\{\nabla\cdot\left(\bar{Q}ph^3\nabla pw\right)-\left(\bar{Q}ph^3\nabla p\right)\cdot\nabla w\right.\\&\left.-6\mu\mathbf{U}\cdot\nabla\left(ph\right)w-12\mu\frac{\partial}{\partial t}\left(ph\right)w\right\}dV=0\end{aligned} \tag{2.43}$$

Implementing the Gauss' theorem (Equation (2.3)), the first term in Equation (2.43) becomes:

$$\int_V\nabla\cdot\left(\bar{Q}ph^3\nabla pw\right)dV=\int_S\mathbf{n}\cdot\left(\bar{Q}ph^3\nabla pw\right)dS \tag{2.44}$$

Choosing the arbitrary weight functions w to be zero at the boundaries where the pressure is known as the ambient pressure, Equation (2.44) equals zero and Equation (2.43) is reduced to:

$$\int_V \left\{ -\left(\bar{Q} p h^3 \nabla p\right) \cdot \nabla w - 6\mu \mathbf{U} \cdot \nabla\left(ph\right) w - 12\mu \frac{\partial}{\partial t}\left(ph\right) w \right\} dV = 0 \tag{2.45}$$

The steady-state equation is obtained by neglecting the time-dependent term in Equation (2.45):

$$\int_V \left\{ -\left(\bar{Q} p h^3 \nabla p\right) \cdot \nabla w - 6\mu \mathbf{U} \cdot \nabla\left(ph\right) w \right\} dV = 0 \tag{2.46}$$

The pressure p is nonlinear and can be linearized using a Taylor series expansion around the initial guess of pressure p_0:

$$p = p_0 + \frac{\partial p}{\partial p} dp + \frac{1}{2} \frac{\partial^2 p}{\partial p^2} \left(dp\right)^2 + \ldots \approx p_0 + dp \tag{2.47}$$

where dp is a small variation of p from p_0. dp can be considered as the variation in the pressure between consecutive iterations. In this case, the pressure p can be improved through a recursive iteration procedure [92][128]:

$$p^{k+1} = p^k + dp \tag{2.48}$$

where "k" is the iteration number. Iteration continues until the convergence criterion is satisfied, i.e., until dp approaches zero.

The nonlinear terms in Equation (2.46) can be rewritten as follows [92][128]:

$$p \nabla p = \left(p_0 + dp\right) \nabla \left(p_0 + dp\right) = p_0 \nabla p_0 + p_0 \nabla dp + dp \nabla p_0 + dp \nabla dp \tag{2.49}$$

$$\nabla\left(ph\right) = \nabla\left(\left[p_0 + dp\right] h\right) = p_0 \nabla h + h \nabla p_0 + h \nabla dp + dp \nabla h \tag{2.50}$$

Since $dp\nabla dp$ is of higher order than the other terms, it can be neglected. Substituting Equation (2.49) and (2.50) into Equation (2.46), we can write the linearized equation as:

$$\begin{aligned}&\int_V \left\{\bar{Q}h^3\left(dp\nabla p_0 + p_0\nabla dp\right)\cdot\nabla W + 6\mu\mathbf{U}\cdot\left(h\nabla dp + dp\nabla h\right)W\right\}dV = \\ &-\int_V \left\{\bar{Q}h^3 p_0\nabla p_0\cdot\nabla W + 6\mu\mathbf{U}\cdot\left(h\nabla p_0 + p_0\nabla h\right)W\right\}dV\end{aligned} \tag{2.51}$$

Equation (2.51) can be rearranged so that the left-hand terms are dependent on the unknown quantity dp while the right-hand terms are only dependent on the known values obtained from the precious iteration step.

For a single element, the pressure within the element can be interpolated by:

$$p\left(\mathbf{x}\right) = \sum_{i=1}^{n} N_i\left(\mathbf{x}\right) p_i \tag{2.52}$$

where n is the number of nodes per element, N_i is the shape functions at the i^{th} node and p_i is the i^{th} nodal pressure.

The shape of elements is often distorted in order to achieve reasonable discretization of a complicated geometry, such as the air bearing surface used in hard disk drives. Isoparametric elements are developed in finite element analysis to map the distorted elements in the global Cartesian coordinate system into a simple standard geometry so that the analysis of elements can be performed numerically using the same normalized isoparametric elements.

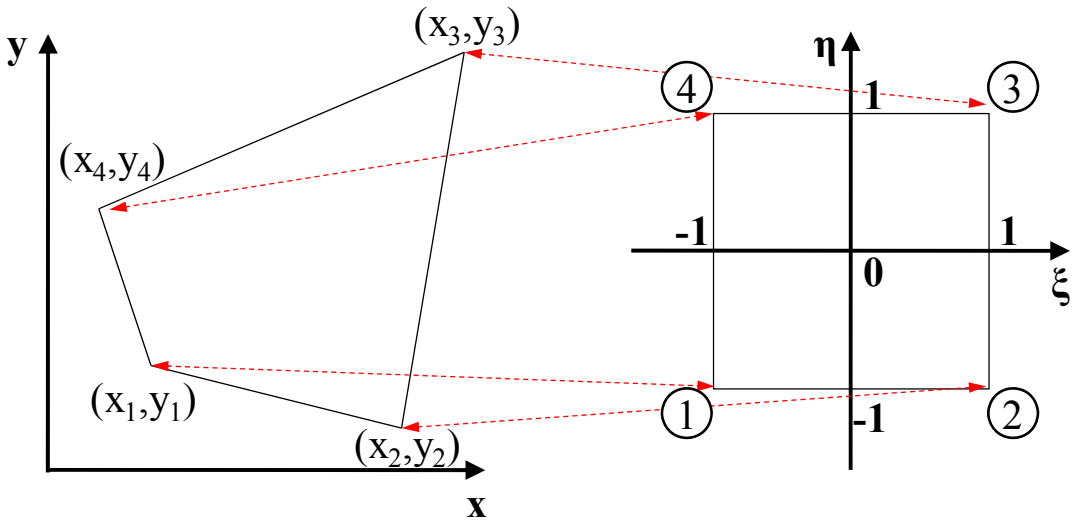

Figure 2.2 Transformation between distorted elements and isoparametric elements

The "one" to "one" transformation of coordinates between the standard isoparametric elements and quadrilateral elements in the (x, y)-plane is given by:

$$x = \sum_{i=1}^{n} N_i(\xi)\, x_i \quad \text{and} \quad y = \sum_{i=1}^{n} N_i(\xi)\, y_i \tag{2.53}$$

where x_i and y_i are the coordinates of node i. The form of the shape functions $\mathbf{N}(\xi)$ of the quadrilateral bilinear elements implemented in CMRR/Talke Lab air bearing simulator can be found in [55] and [108]. The pressure within the isoparametric elements is then given by:

$$p(\xi) = \sum_{i=1}^{n} N_i(\xi)\, p_i \tag{2.54}$$

The transformation of infinitesimal elements between the (x, y)-space and the (ξ, η)-space is:

$$\begin{Bmatrix} dx \\ dy \end{Bmatrix} = \begin{bmatrix} \dfrac{\partial x}{\partial \xi} & \dfrac{\partial x}{\partial \eta} \\ \dfrac{\partial y}{\partial \xi} & \dfrac{\partial y}{\partial \eta} \end{bmatrix} \begin{Bmatrix} d\xi \\ d\eta \end{Bmatrix} = \mathbf{J} \begin{Bmatrix} d\xi \\ d\eta \end{Bmatrix} \tag{2.55}$$

where $\mathbf{J} \equiv \begin{bmatrix} \dfrac{\partial x}{\partial \xi} & \dfrac{\partial x}{\partial \eta} \\ \dfrac{\partial y}{\partial \xi} & \dfrac{\partial y}{\partial \eta} \end{bmatrix}$ is the Jacobian matrix. Correspondingly,

$$\begin{Bmatrix} d\xi \\ d\eta \end{Bmatrix} = inv\mathbf{J} \begin{Bmatrix} dx \\ dy \end{Bmatrix} = \frac{1}{\det \mathbf{J}} \begin{bmatrix} \dfrac{\partial y}{\partial \eta} & -\dfrac{\partial x}{\partial \eta} \\ -\dfrac{\partial y}{\partial \xi} & \dfrac{\partial x}{\partial \xi} \end{bmatrix} \begin{Bmatrix} dx \\ dy \end{Bmatrix} = \begin{bmatrix} \dfrac{\partial \xi}{\partial x} & \dfrac{\partial \xi}{\partial y} \\ \dfrac{\partial \eta}{\partial x} & \dfrac{\partial \eta}{\partial y} \end{bmatrix} \begin{Bmatrix} dx \\ dy \end{Bmatrix} \tag{2.56}$$

where $\det \mathbf{J}$ is the determinant of the Jacobian matrix and can be expressed as:

$$\begin{aligned} &\det \mathbf{J} = \frac{\partial x}{\partial \xi}\frac{\partial y}{\partial \eta} - \frac{\partial x}{\partial \eta}\frac{\partial y}{\partial \xi} = \\ &\left(\sum_{i=1}^{n} \frac{\partial N_i}{\partial \xi} x_i\right)\left(\sum_{i=1}^{n} \frac{\partial N_i}{\partial \eta} y_i\right) - \left(\sum_{A=1}^{n} \frac{\partial N_i}{\partial \eta} x_i\right)\left(\sum_{A=1}^{n} \frac{\partial N_i}{\partial \xi} y_i\right) \end{aligned} \tag{2.57}$$

Equation (2.55) and (2.56) yields the relationship between partial derivatives as:

$$\begin{aligned} \frac{\partial \xi}{\partial x} &= \frac{1}{\det \mathbf{J}} \frac{\partial y}{\partial \eta} \\ \frac{\partial \xi}{\partial y} &= -\frac{1}{\det \mathbf{J}} \frac{\partial x}{\partial \eta} \\ \frac{\partial \eta}{\partial x} &= -\frac{1}{\det \mathbf{J}} \frac{\partial y}{\partial \xi} \\ \frac{\partial \eta}{\partial y} &= \frac{1}{\det \mathbf{J}} \frac{\partial x}{\partial \xi} \end{aligned} \tag{2.58}$$

The first derivative of a function $f = f(\mathbf{x})$ with respect to isoparametric coordinates can be obtained from Equation (2.58) and the chain rule of differentiation:

$$\frac{\partial f}{\partial x}=\frac{\partial f}{\partial \xi}\frac{\partial \xi}{\partial x}+\frac{\partial f}{\partial \eta}\frac{\partial \eta}{\partial x}=\frac{1}{\det \mathbf{J}}\left(\frac{\partial f}{\partial \xi}\frac{\partial y}{\partial \eta}-\frac{\partial f}{\partial \eta}\frac{\partial y}{\partial \xi}\right)$$
$$\frac{\partial f}{\partial y}=\frac{\partial f}{\partial \xi}\frac{\partial \xi}{\partial y}+\frac{\partial f}{\partial \eta}\frac{\partial \eta}{\partial y}=\frac{1}{\det \mathbf{J}}\left(-\frac{\partial f}{\partial \xi}\frac{\partial x}{\partial \eta}+\frac{\partial f}{\partial \eta}\frac{\partial x}{\partial \xi}\right) \tag{2.59}$$

Substituting Equation (2.53) into Equation (2.59), the first derivative of $f=f\left(\mathbf{x}\right)$ in matrix form can be written as:

$$\begin{Bmatrix}\frac{\partial f}{\partial x}\\ \frac{\partial f}{\partial y}\end{Bmatrix}=\frac{1}{\det \mathbf{J}}\begin{bmatrix}\sum_{i=1}^{n}\frac{\partial N_i}{\partial \eta}y_i & -\sum_{i=1}^{n}\frac{\partial N_i}{\partial \xi}y_i\\ -\sum_{i=1}^{n}\frac{\partial N_i}{\partial \eta}x_i & \sum_{i=1}^{n}\frac{\partial N_i}{\partial \xi}x_i\end{bmatrix}\begin{Bmatrix}\frac{\partial f}{\partial \xi}\\ \frac{\partial y}{\partial \eta}\end{Bmatrix} \tag{2.60}$$

Similarly, the first derivatives of the pressure are:

$$\frac{\partial p}{\partial x}=\sum_{A=1}^{n}\frac{\partial N_A}{\partial x}p_A \quad \text{and} \quad \frac{\partial p}{\partial y}=\sum_{A=1}^{n}\frac{\partial N_A}{\partial x}p_A \tag{2.61}$$

where the derivative of the shape functions are in the forms of:

$$\begin{Bmatrix}\frac{\partial N_i}{\partial x}\\ \frac{\partial N_i}{\partial y}\end{Bmatrix}=\frac{1}{\det \mathbf{J}}\begin{bmatrix}\sum_{k=1}^{n}\frac{\partial N_k}{\partial \eta}y_k & -\sum_{k=1}^{n}\frac{\partial N_k}{\partial \xi}y_k\\ -\sum_{k=1}^{n}\frac{\partial N_k}{\partial \eta}x_k & \sum_{k=1}^{n}\frac{\partial N_k}{\partial \xi}x_k\end{bmatrix}\begin{Bmatrix}\frac{\partial N_i}{\partial \xi}\\ \frac{\partial N_i}{\partial \eta}\end{Bmatrix} \tag{2.62}$$

Gauss quadrature is used to obtain the integration of Equation (2.51), in which the integral is estimated by the sum of function evaluations at integration points. The Gauss quadrature formula over the normalized 2-D domains is defined as:

$$\int_{-1}^{1}\int_{-1}^{1} f\left(\xi,\eta\right)d\xi d\eta=\sum_{m=1}^{ngp}\sum_{n=1}^{ngp} f\left(\xi_m,\eta_n\right)W_m W_n \equiv \underset{ngp\times ngp}{\mathbf{I}} f\left(\xi,\eta\right) \tag{2.63}$$

where (ξ_m, η_n) are the Gauss points and ngp is the number of selected Gauss points. The polynomial of order s can be integrated exactly with $ngp \geq (s+1)/2$ Gauss points. W are the weights depending on how many Gauss points have been used [109].

The element equation for every element can be written as:

$$[\mathbf{k}]^e \{\mathbf{dp}\}^e = \{\mathbf{r}\}^e \tag{2.64}$$

where $[\mathbf{k}]^e$ is the stiffness matrix of the element with:

$$k_{ij} = \underset{ngp \times ngp}{\mathbf{I}} \left\{ \bar{Q} h^3 \left(N_j \nabla p_0 + p_0 \nabla N_j \right) \cdot \nabla N_i + 6\mu \mathbf{u} \cdot \left(h \nabla N_j + N_j \nabla h \right) N_i \right\} \det \mathbf{J} \tag{2.65}$$

$\{\mathbf{dp}\}^e$ is the unknown vector of each element indicating the improvement of pressure. The components of the right-hand side vector of Equation (2.51) $\{\mathbf{r}\}^e$ for individual elements can be expressed as:

$$r_i = - \underset{ngp \times ngp}{\mathbf{I}} \left\{ \bar{Q} h^3 p_0 \nabla p_0 \cdot \nabla N_i + 6\mu \mathbf{u} \cdot \left(h \nabla p_0 + p_0 \nabla h \right) N_i \right\} \det \mathbf{J} \tag{2.66}$$

The global equation of the system is obtained by assembling the equations of individual elements (2.64) according to the numbering of the global degrees of freedom associate with each element [92] and is given by:

$$\underset{N \times N}{[\mathbf{K}]} \underset{N \times 1}{\{\mathbf{dp}\}} = \underset{N \times 1}{\{\mathbf{r}\}} \tag{2.67}$$

where $[\mathbf{K}]$ is the global stiffness matrix and N is the number of unknown finite element nodes in the model. The nodes on the boundaries are enforced essential boundary conditions and the related components in the stiffness matrix are not

assembled. Equation (2.67) is solved repeatedly to obtain the change of pressure $\{\mathbf{dp}\}$ between consecutive iterations.

2.4 Equilibrium Equations of the Slider

As described in Section 2.2, the pressure distribution p of the air bearing can be obtained by the Reynolds equation (Equation (2.37)), with a given spacing between the slider and the disk h. However, the spacing in a hard disk drive is a function of additional parameters such as the disk velocity, the position of the slider, and the exerted load. It is difficult to determine the spacing ahead of time.

In the equilibrium position, the slider is balanced by the opposing forces of the air bearing and the suspension. The flying characteristics and the pressure distribution of the slider can be determined by simultaneously solving the equilibrium equations and the Reynolds equation for the slider.

Figure 2.3 shows the schematic of a pivoted slider bearing. The slider is glued to the gimbal and moves around the pivot point of the slider. The gimbal is attached to the suspension and constrains the following three degrees of freedom of the slider: (a) yaw motion, (b) off-track motion, and (c) down-track motion. The suspension allows vertical translation (h), pitch (α), and roll (β) around the pivot points of the slider, which are associated with the suspension stiffness (k_z), and gimbal stiffness (k_α) and (k_β), respectively. The slider is held in flight by the force and momentum of the air bearing and the suspension. The equilibrium equations of the slider for small perturbations can be written as:

$$\begin{bmatrix} k_z & 0 & 0 \\ 0 & k_\alpha & 0 \\ 0 & 0 & k_\beta \end{bmatrix} \begin{Bmatrix} dh \\ d\alpha \\ d\beta \end{Bmatrix} = \begin{Bmatrix} F_z^{air} - F_z^{ext} \\ M_\alpha^{air} - M_\alpha^{ext} \\ M_\beta^{air} - M_\beta^{ext} \end{Bmatrix} \tag{2.68}$$

The air bearing force can be obtained by integrating the air bearing pressure over the air bearing surface and is given by:

$$F_z^{air} = \iint_A p(x,y)\, dA \tag{2.69}$$

The momentum of the air bearing in the pitch and roll directions can be obtained from:

$$\begin{aligned} M_\alpha^{air} &= \iint_A p(x,y)\left(x - x_p\right) dA \\ M_\beta^{air} &= \iint_A p(x,y)\left(y - y_p\right) dA \end{aligned} \tag{2.70}$$

Equation (2.68) can be written as:

$$\begin{bmatrix} k_z & 0 & 0 \\ 0 & k_\alpha & 0 \\ 0 & 0 & k_\beta \end{bmatrix} \begin{Bmatrix} dh \\ d\alpha \\ d\beta \end{Bmatrix} = \begin{Bmatrix} \iint_A p(x,y)\, dA - F_z^{ext} \\ \iint_A p(x,y)\left(x - x_p\right) dA - M_\alpha^{ext} \\ \iint_A p(x,y)\left(y - y_p\right) dA - M_\beta^{ext} \end{Bmatrix} \tag{2.71}$$

The steady-state air bearing pressure distribution and the flying characteristics of the slider can be calculated by simultaneously solving the Reynolds equation (Equation (2.37)) and the equilibrium equation for the slider (Equation (2.71)).

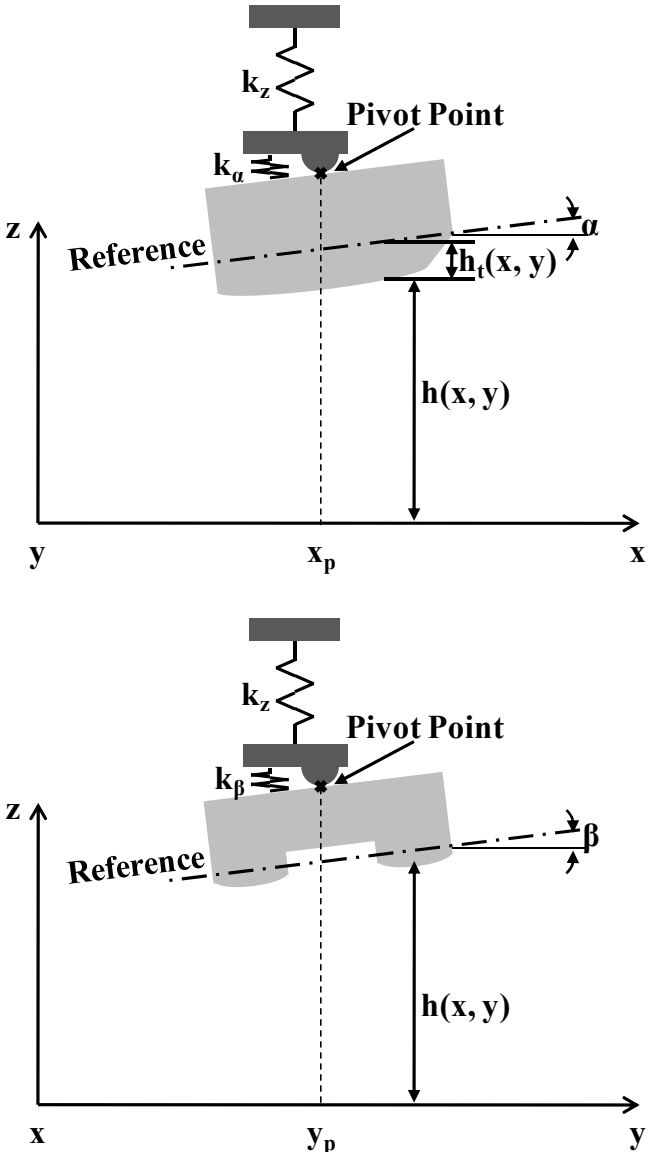

Figure 2.3 Schematic of pivoted slider bearing (after [92])

The CMRR/Talke Lab air bearing simulator uses the Newton-Raphson method in order to obtain the finite element solution of the simultaneously solved Reynolds equation and the equilibrium equations. The Newton-Raphson method is one of the most commonly used numerical methods in applications were one needs to solve for the roots of a real-valued function [110]. The method provides second-order accuracy

with successively improved approximations. The implementation of the simultaneous Newton-Raphson method to the Reynolds equation and the equilibrium equations of a slider is described in the Appendix A.

This chapter describes the theoretical background behind the simulation of the air bearing in the head/disk interface. The numerical investigation of a slider is conducted based on the finite element solution for the Reynolds equation and the equilibrium equation. We use this solution in order to study the steady-state flying characteristics and the pressure distribution of the slider when flying over bit patterned media. Further details will be presented in the next chapter.

Chapter 3

Slider Design and Air Bearing Simulation of Bit Patterned Media

The steady-state characteristics of sliders flying over bit patterned media are investigated in this chapter. The finite element method that is used to solve the Reynolds and equilibrium equations of the slider was described in the previous chapter. This method is used to simulate the behavior of sliders flying on bit patterned media. The discrete bits of bit patterned media are modeled as isolated protrusions on the disk surface. The effects of variations in the designs of bit patterns and air bearing surfaces on the flying characteristics of sliders are investigated. We observe air bearing pressure peaks at each bit. The flying height of the slider is a function of the disk and slider design parameters.

3.1 Introduction

As introduced in Chapter 1, discrete track recording (DTR) and bit patterned media (BPM) are presently being investigated as promising approaches that reduce the "cross-talk" between adjacent bits, improve the thermal stability of the media, and have the potential to increase the areal density beyond 1.6 Gb/mm² (1 Tb/in²) [111-114]. In discrete track recording, individual tracks are etched on the disk surface. In bit

patterned media, bits are contained within individual island-like protrusions on the disk surface.

A number of studies have investigated the flying characteristic of magnetic recording sliders over patterned media. Kawazoe et al. [115], Mitsuya et al. [116-118], and Ohkubo and Mitsuya [119] have used the averaged Reynolds equation to study the effects of two-dimensional surface textures on the flying characteristics of magnetic recording sliders. This approach allowed the prediction of global flying characteristics for magnetic recording sliders over textured media. However, it did not reveal local variations in pressure due to the texture. Tagawa and Bogy used a deterministic rectangular micro-texture model to analyze the air film dynamics of micro-textured slider bearings [120]. Murthy et al. studied the steady-state characteristics of femto sliders flying over bit patterned media by transferring the bit pattern from the disk surface to the slider surface. In their study, the bit patterns were represented by uniform cylindrical protrusions [121]. A similar approach was also pursued by Li et al. Li simulated the head/disk interface on a discrete track disk by transferring the grooves from the disk to the air-bearing surface (ABS) of the slider [122]. In order to study the flying characteristics of a slider over discrete track recording disks, Duwensee et al. investigated four different slider designs. They derived an empirical equation for flying height loss as a function of groove width, track pitch, and groove depth. They also observed that the design of the discrete track recording media had no effect on the pitch angle of the slider [123][124]. Peng et al. used an averaged flow model to predict the flying height loss of discrete track recording media and verified their predictions through touchdown pressure measurements [125]. Yoon and Talke

found that discrete track recording disks exhibit a larger hysteresis between touch-down and take-off compared to smooth disks. In particular, they found that the touch-down velocity and pressure on discrete track recording disks was higher than the smooth disks [126].

This chapter presents numerical models and air bearing simulations for femto sliders flying over bit patterned media and investigates the effect of disk and slider design parameters on steady-state flying performance.

3.2 Numerical Model

The bit patterned media is modeled as an array of islands evenly spaced over the disk surface. A model of the head/disk interface for bit patterned media is shown in Figure 3.1. In order to simulate the effect of etching, we assume that the shape of the individual islands are either cylindrical (Figure 3.1 (a)) or cuboidal (Figure 3.1 (b)) and have a flat upper surface. The bits on the disk surface are modeled by changing the local flying height at each step. The spacing between slider and disk surface at each step is calculated by determining whether the node of interest in the discretized air bearing surface is located on a recessed area or on top of a land in the bit patterned media. The bit design parameters (Figure 3.1) considered in our study are the bit height (h), the bit diameter (d), and the pitch (p), respectively.

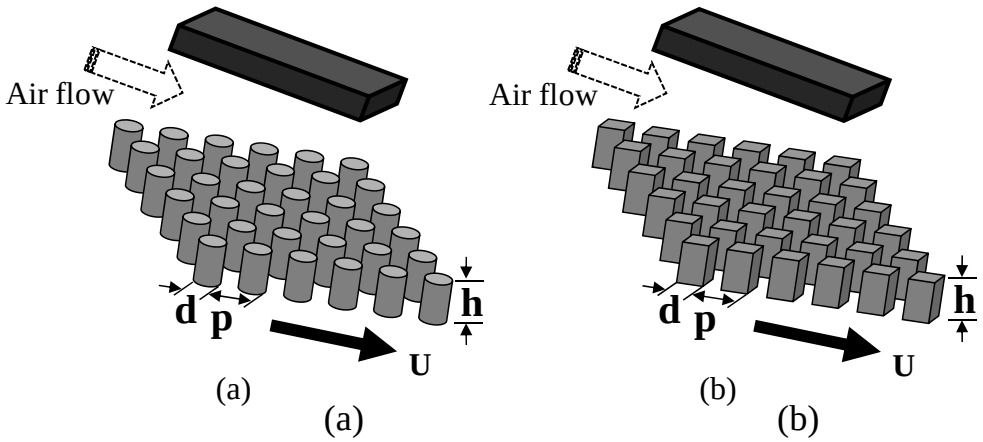

Figure 3.1 Schematic of the head/disk interface of bit patterned media with (a) cylindrical and (b) Cuboidal bits

We assume that the air flow between the head/disk interface is quasi-steady, i.e., time-dependent effects of the moving protrusions on the flying characteristics of the slider are neglected. In this case, the air flow between the slider and the bit patterned media is governed by the steady-state Reynolds equation [127]. Simultaneously solving the Reynolds and equilibrium equations for the slider, we obtain the air bearing pressure distribution over the air bearing surface and the steady-state flying characteristics of the slider. The finite element solutions to the Reynolds and equilibrium equations for a slider were presented in Chapter 2 and are solved with the CMRR/Talke Lab air bearing simulator [128].

The design of the femto sliders used in our simulation is shown in Figure 3.2 (a). The simulated steady-state flying height of the slider is 24.4 nm on a smooth (non-patterned) disk. The dimensions of the small trailing pad are 30 μm in length and 50 μm in width. The recession depths of each layer are 0 (), 0.15 (), 0.2 () and 1 μm (). The finite element mesh on the surface of the slider must be very fine in order to

achieve results for the air bearing pressure distribution with sufficient resolution. Figure 3.2 (b) shows the unstructured triangular mesh over the air bearing surface. In our calculations, the mesh size on the trailing pad of is 50 nm. The mesh size is 20 μm on the side-pads and 40 μm on the leading pad.

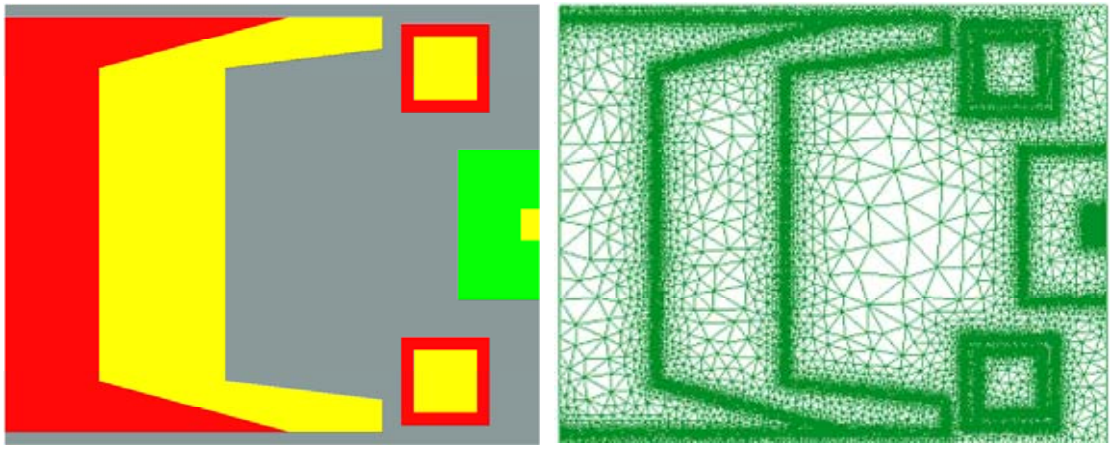

(a) (b)

Figure 3.2 (a) Femto slider design and (b) unstructured triangular mesh on air bearing surface used in simulation

3.3 Simulation Results

3.3.1 Air Bearing Pressure Distribution

Figure 3.3 shows a typical air bearing pressure profile for the femto slider flying over a bit patterned disk. The following bit parameters are chosen in this case: p = 600 nm, d = 300 nm, and h = 20 nm. Peaks in the air bearing pressure distribution over each island are clearly visible.

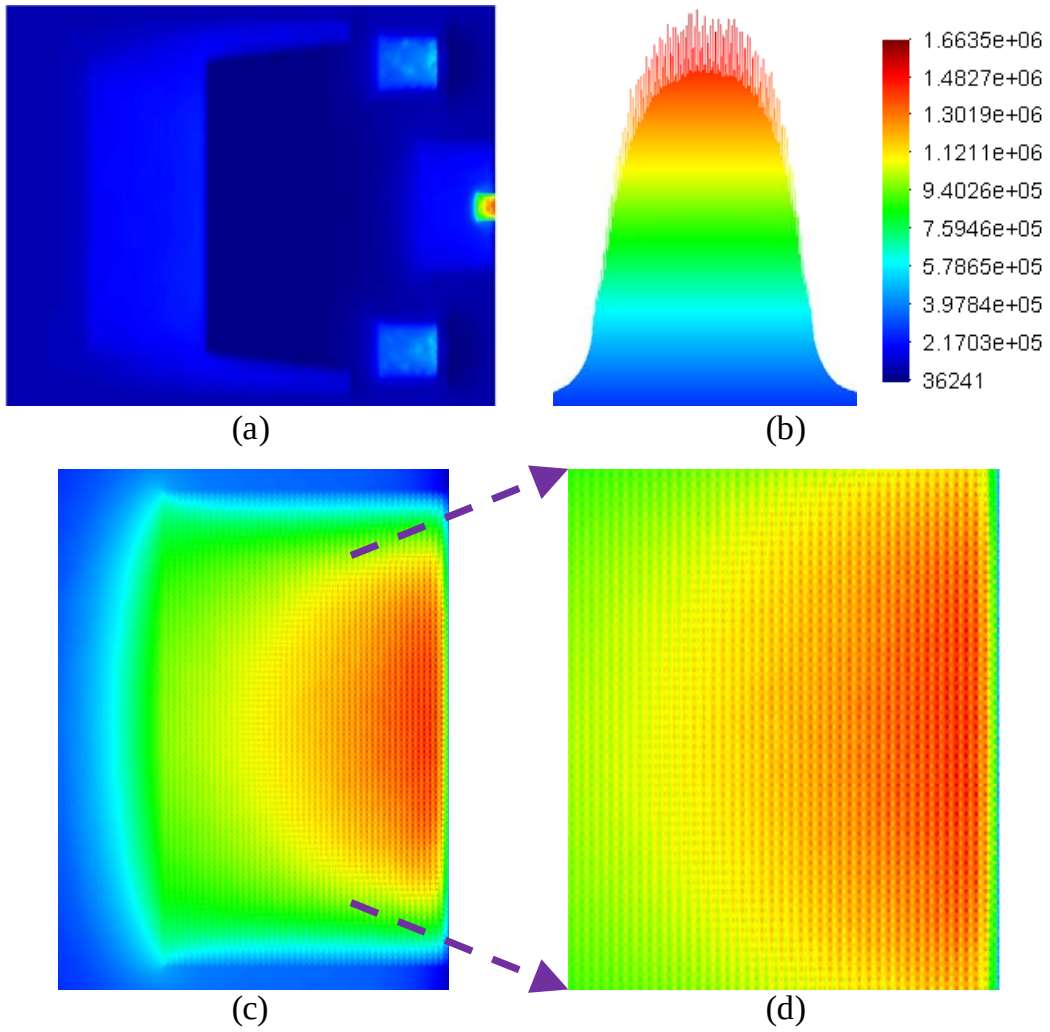

Figure 3.3 Pressure distribution of a femto slider on bit patterned media (a) whole air bearing surface, (b) side view of trailing pad, (c) top view of trailing pad and (d) large magnification of trailing pad

The resolution of the pressure distribution is an important part of bit patterned media air bearing simulations due to the small dimension of each individual bit. In order to validate the chosen mesh, we re-meshed the trailing pad of the slider with different element sizes while keeping the mesh on the other surface unchanged. Figure 3.4 shows the top views of air bearing pressure distributions with 50 nm, 100

nm, and 150 nm mesh sizes. We observe that the surface of an individual bit, which creates the pressure peaks, is not discretized sufficiently when the mesh is scaled to 100 nm and 150 nm per element. When the mesh is too coarse, it does not accurately calculate the pressure distribution over the bit patterns. Figure 3.5 shows the numerically calculated flying height of the slider as a function of the mesh size at the trailing pad. We observe that the flying height converges to a constant value as the mesh size decreases. From our simulation results, we have observed that the ratio of mesh size to bit diameter (d = 300 nm) should be smaller than 1 : 6 in order to guarantee sufficiently high resolution in the pressure distribution. Using a mesh size of 50 nm, we obtained the air bearing pressure profiles on the trailing pad in the cross-track direction, as shown in Figure 3.6. One arbitrarily chosen bit is marked. It indicates that approximately 12 nodes are generated.

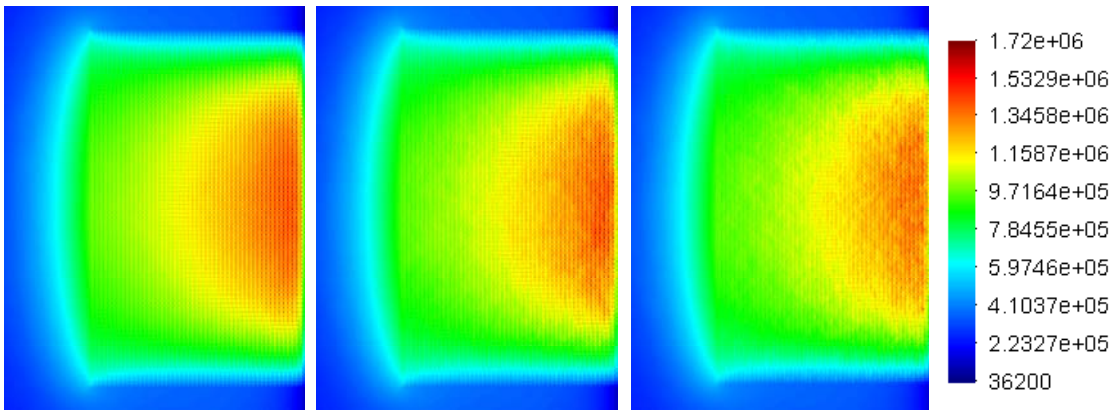

(a) 50 nm (b) 100 nm (c) 150 nm

Figure 3.4 Pressure distribution on the trailing pad of the femto slider as a function of mesh size

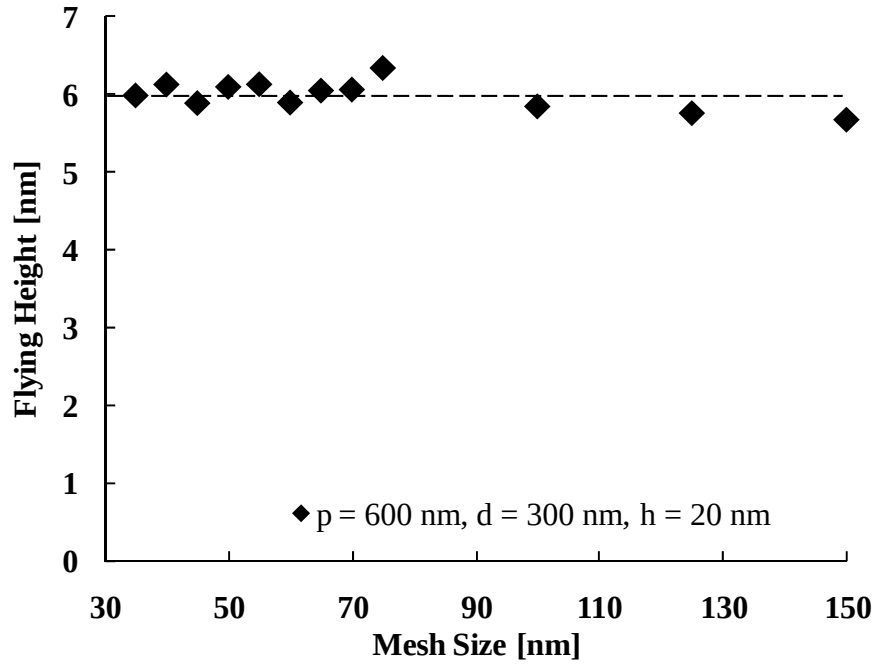

Figure 3.5 Flying height as a function of mesh size

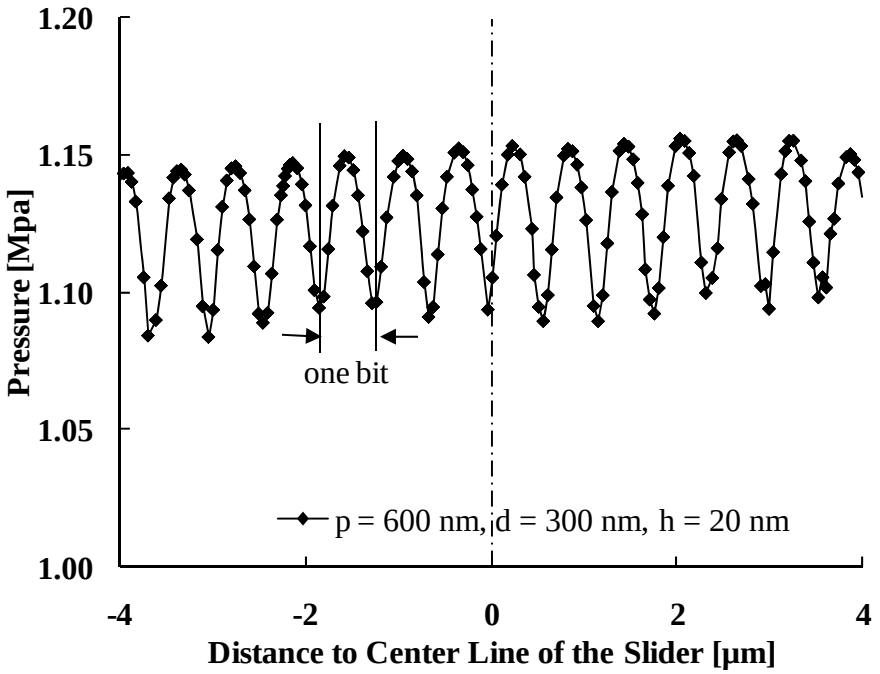

Figure 3.6 Air bearing pressure profiles on trailing pad of the femto slider in the cross track of the slider

3.3.2 Effect of Design of Bit Patterned Media

A slider discretized with a 50 nm mesh on the trailing pad is used to investigate the effect of design parameters on flying characteristics. Figure 3.7 shows the flying height as a function of the bit height. When the bit height is increased from 0 nm to 25 nm, the flying height of the slider is reduced by approximately 20 nm. The ratio of flying height reduction to bit height is about 0.8.

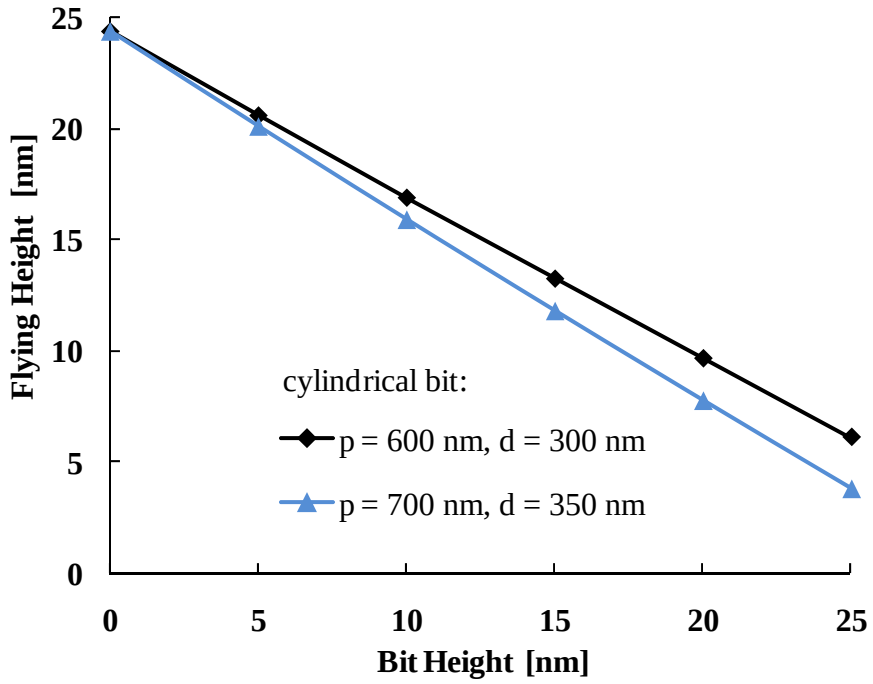

Figure 3.7 Flying height loss as a function of cylindrical bit height

Previous simulation results for discrete track media have indicated that the reduction of flying height due to changes in the groove depth is proportional to the ratio of groove width to groove pitch ([122-124]). The relationship is described by the following equation: $\Delta FH = h \times \frac{w}{p}$, where h is the groove depth, w and p are the

groove width and groove pitch respectively. That is, for a groove width of 300 nm and a groove pitch of 600 nm, the ratio of the reduction in flying height to groove depth is around 0.5. This value is much smaller than the value found for our simulation for bit patterned media. The reason for this result is that the ratio of land area to recessed area for discrete track media is larger than that of bit pattern media.

For a bit spacing of 700 nm and diameter of 350 nm, the calculated flying height loss is larger than the case where a bit spacing of 600 nm and diameter of 300 nm is used. This occurs despite a similar ratio between the bit diameter and pitch. On the other hand, we observe that the pitch angle of the slider changes with an increase in bit height (Figure 3.8). A 4% reduction of the original pitch angle (387.83 μrad) is observed.

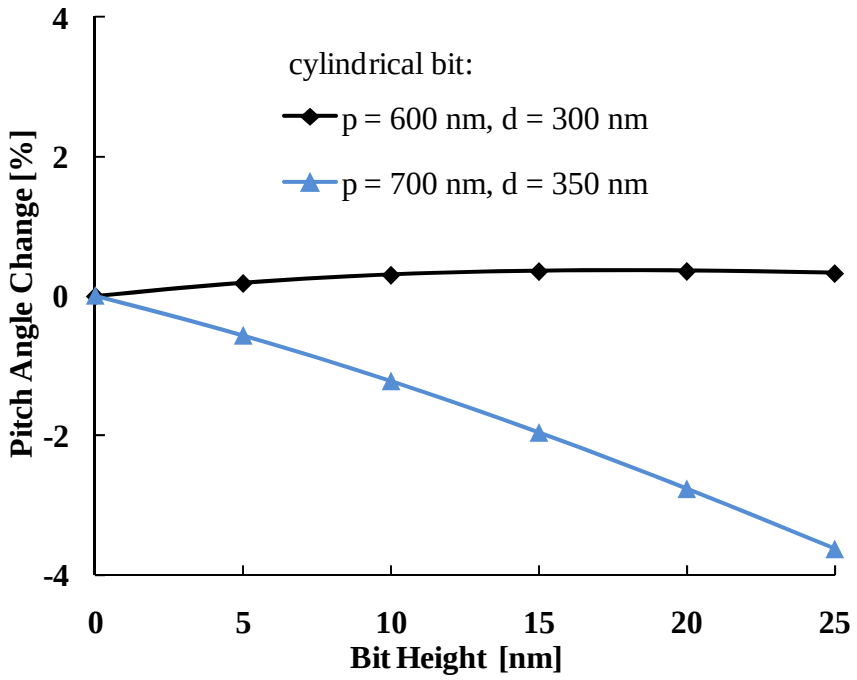

Figure 3.8 Pitch angle as a function of cylindrical bit height

Figure 3.9 and 3.10 shows the flying characteristics of the femto slider flying over bit patterned disks with cylindrical and cuboidal protrusions. Here, we have chosen the diameter of the cylinders to be equal to the length and width of cuboidal bits as illustrated in Figure 3.1. From Figure 3.9, we observe that the flying height loss of the cylindrical bit pattern is larger than that of the cuboidal bit pattern. On the other hand, the pitch angle remains almost constant.

Figure 3.11 shows the slider flying height change as a function of the skew angle. Compared to the smooth media, the flying height of the slider becomes more sensitive to skew angle when flying over bit patterned media. We note that the difference in flying height between the inner diameter (ID) and outer diameter (OD) increases when the bit height increases.

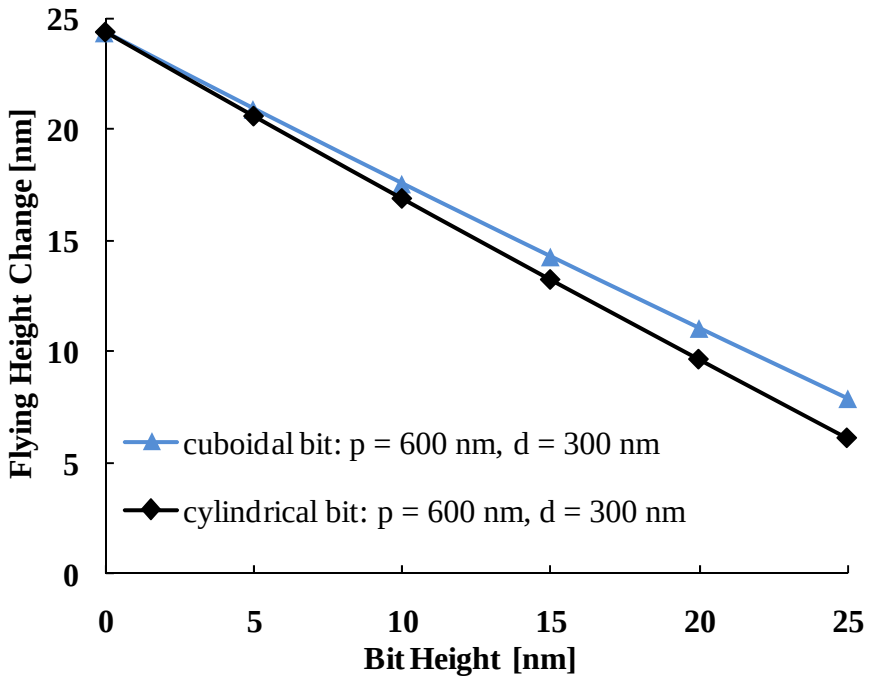

Figure 3.9 Flying height as a function of design of bit patterned media

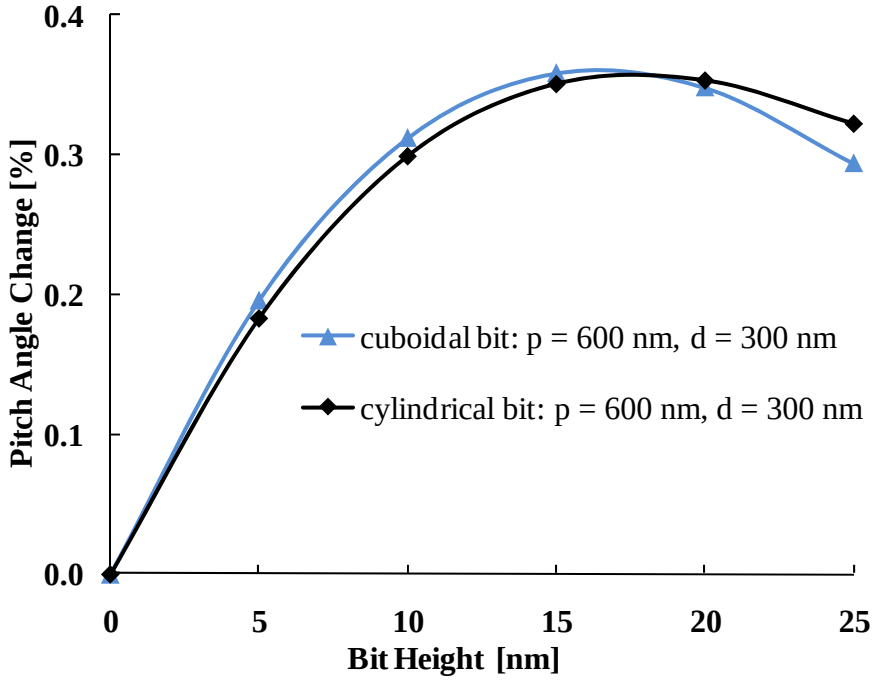

Figure 3.10 Pitch angle as a function of design of bit patterned media

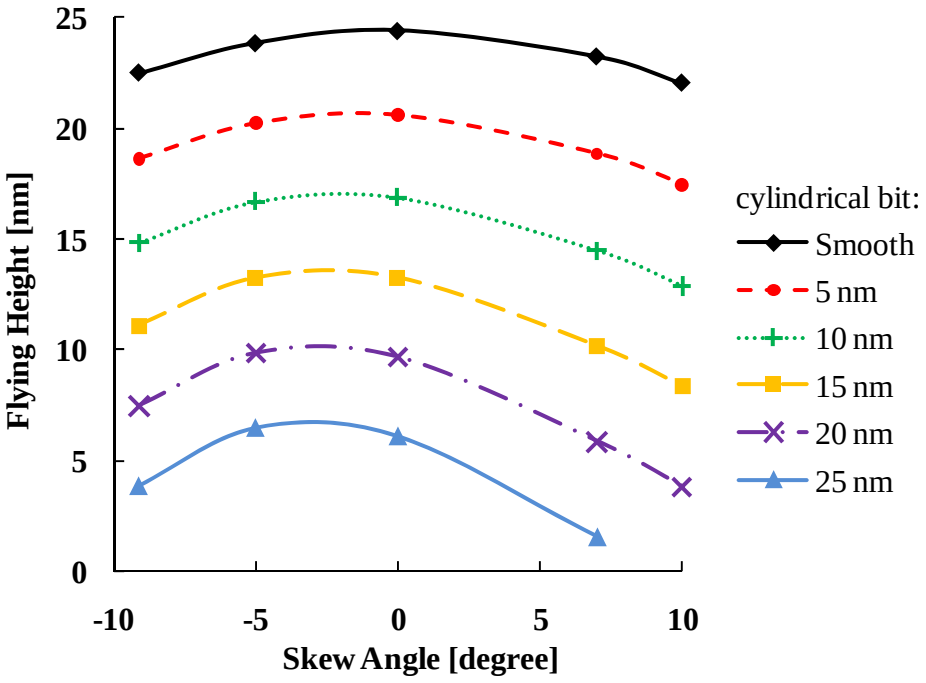

Figure 3.11 Slider flying height as a function of skew angle

3.3.3 Spherical-Pad Slider Flying over Bit Patterned Media

In order to achieve a stable head/disk interface and ultra-low spacing, a spherical-pad slider was created as an alternative to conventional air bearing surface designs. The spherical-pad slider was found to exhibit less spacing loss due to pitch and roll motion than a conventional slider. In addition, because of the curved contour, meniscus forces were found to be smaller than those found in conventional designs [129-131].

A schematic of a slider with a spherical pad flying over bit patterned media is shown in Figure 3.12. The spherical-pad slider exhibits a spherical protrusion, known as the "spherical pad", on the top of the surface of the trailing pad. The height of the spherical pad is denoted by H_p. If H_p is equal to zero, the slider is the same as a traditional slider. The radii of the spherical pad are R_x and R_y along the length and width of the slider, respectively.

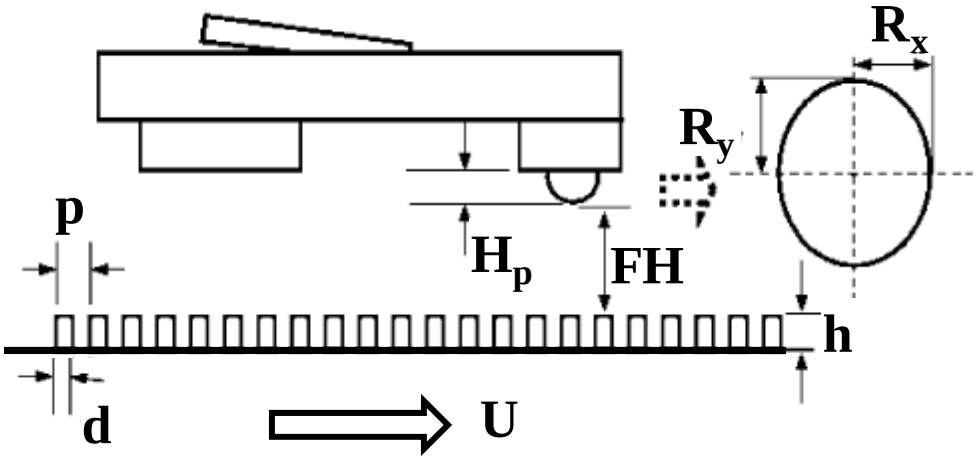

Figure 3.12 Spherical pad slider flying over bit patterned media

A typical spherical-pad slider, as used in our simulations, is shown in Figure 3.13. Again, the finite element mesh on the surface of the slider must be refined in order to obtain an air bearing pressure distribution with sufficiently high resolution. In this investigation, meshes with the size of 10 nm, 30 nm, and 50 nm are generated on the spherical and trailing pad (Figure 3.14). These are the surfaces that are closest to the disk surface when the slider is flying. The mesh size on the side-pads and the leading pad is the same as the femto slider described in Section 3. 2.

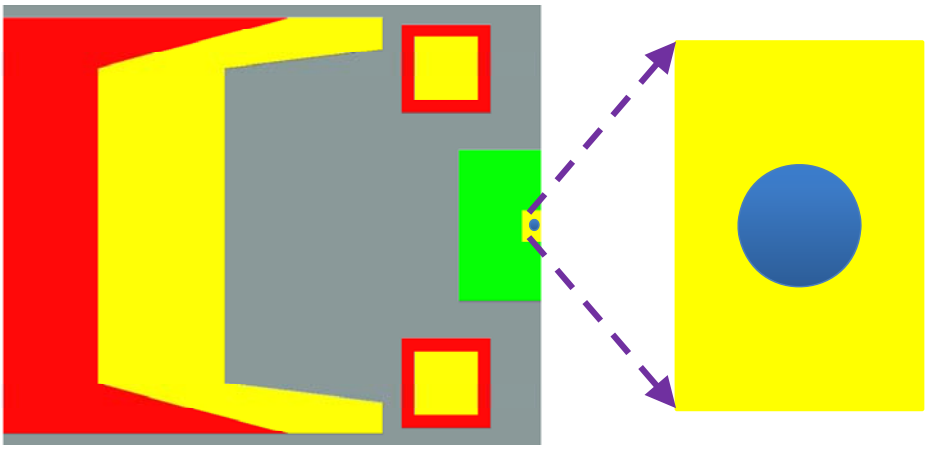

Figure 3.13 Air bearing surface of spherical pad slider design

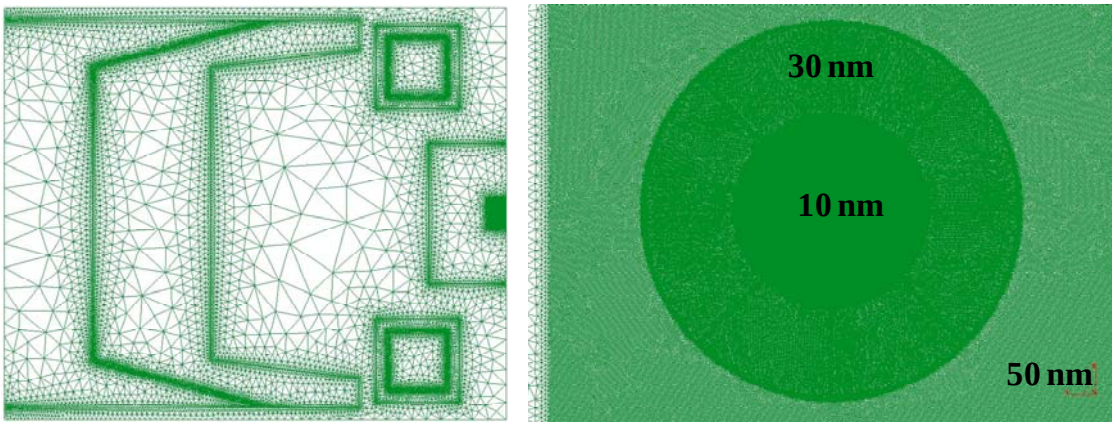

(a) (b)

Figure 3.14 (a) Unstructured triangular mesh on air bearing surface (1.73×10^6 elements and 8.6×10^5 nodes) and (b) mesh around the spherical

3.3.3.1 Air Bearing Pressure Distribution

Figure 3.15 shows the air bearing pressure distributions on the air bearing surface of (a) the traditional slider and (b) the spherical-pad slider ($R_x = R_y = 12.5$ μm, and H_p = 10 nm). In addition, the spherical-pad slider flying over bit patterned media is shown in (c) for comparison. The design parameters for the bit patterned media are p = 1200 nm, d = 600 nm and h = 10 nm.

It can be observed from Figure 3.15 that the spherical pad changes the pressure distribution pattern. The maximum air bearing pressure occurs at the trailing edge of the top pad for a traditional slider design, as shown in Figure 3.15 (a). It is shifted away from the trailing edge in the case of the spherical-pad design. Compared to the traditional slider, we observe that there is a 0.21 MPa increase in the peak value of the air bearing pressure (Figure 3.15 (b)). This value further increases to 1.6 MPa (Figure 3.15 (c)) when the slider is flying over bit patterned media.

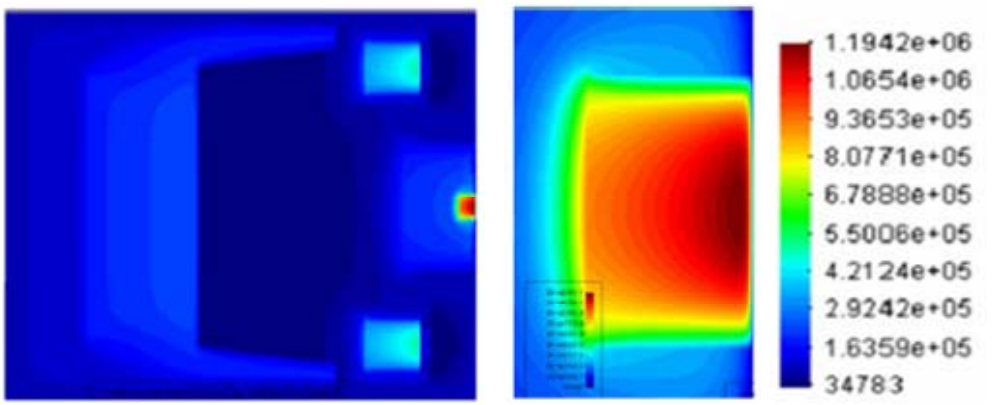

(a)

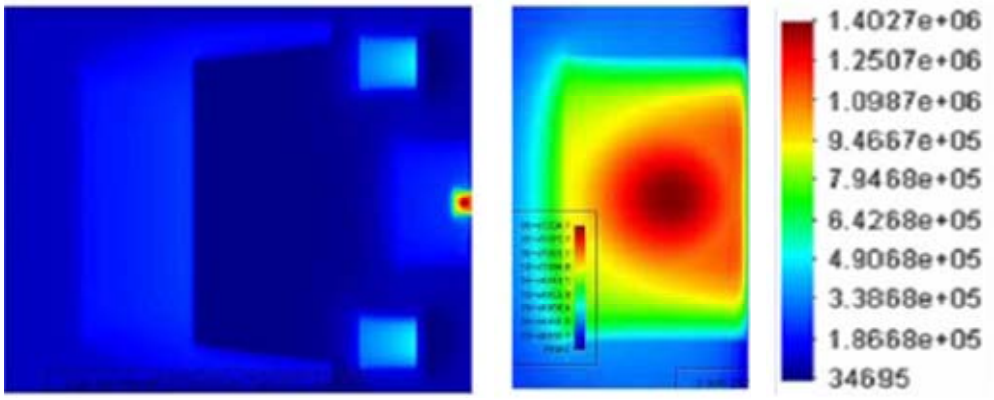

(b)

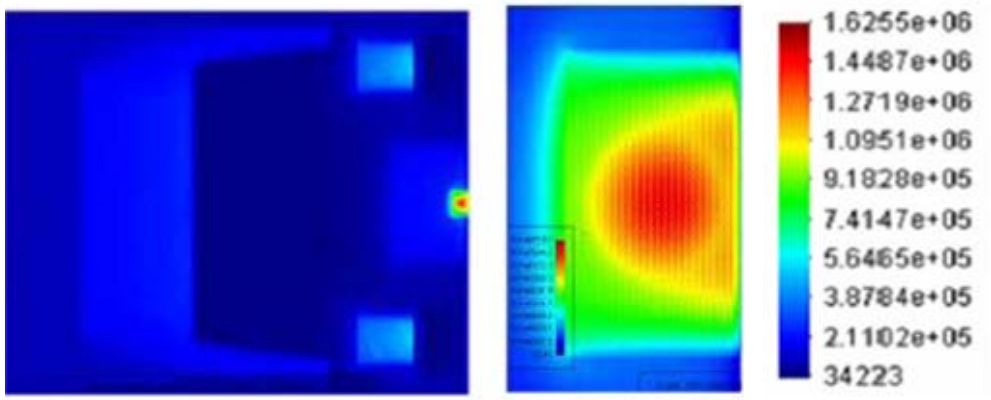

(c)

Figure 3.15 Air bearing pressure distribution (a) a traditional slider flying over a smooth disk, (b) spherical-pad slider flying over a smooth disk and (c) spherical-pad slider flying over a bit patterned disk

3.3.3.2 Comparison of Spherical-Pad Slider and Traditional Slider

Figure 3.16 and Figure 3.17 show the flying height of both the spherical-pad slider and the traditional sliders as a function of the cylindrical bit height. Three types of bit patterned media with the same bit diameter to bit pitch ratio are studied. The ratios of bit diameter to bit pitch are set to 0.5. The values of the bit pitches are chosen to be 600 nm, 900 nm, and 1200 nm.

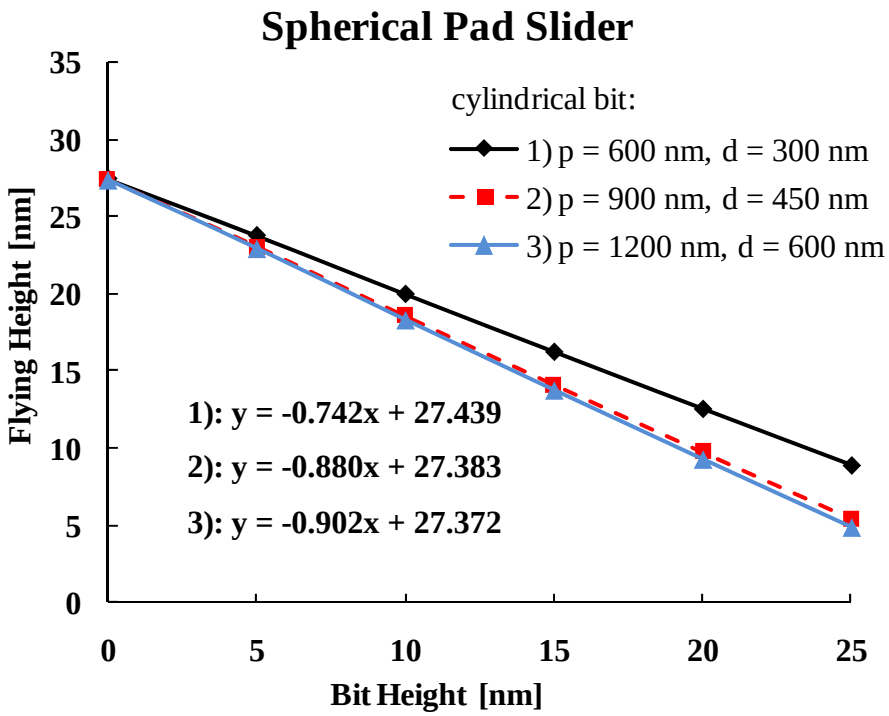

Figure 3.16 Flying height of a spherical-pad slider as a function of bit height

For both the spherical-pad slider and the traditional slider, it can be observed that the flying height is a function of the dimensions of the bit pattern. For the spherical-pad slider ($R_x = R_y = 10$ μm, and H_p = 10 nm), the ratios of the flying height reduction to the bit height for the 600nm, 900nm, and 1200nm cases are 0.742,

0.880, and 0.902, respectively. For the traditional slider, the ratios are 0.730, 0.857 and 0.915, respectively. The results show that the effect of bit patterned media on the flying characteristics of the spherical-pad and the traditional slider are similar.

Figure 3.18 shows the flying height of the slider as a function of skew angle. Over skew angles ranging from -20 to 20 degrees, the variation in flying height is 10.4 nm for a traditional slider and is 7.47 nm for a spherical-pad slider. For a range of skew angles from -5 to 5 degrees, the variation in flying height of a traditional slider is 1.96 nm and is 0.46 nm for a spherical-pad slider. There is a significant reduction in flying height variation for a spherical-pad slider compared to a traditional slider. The reason is that the spherical pad has a smaller effective surface area that interacts with the air flow compared to the effective surface area of a traditional slider. The result shown in the previous section (Figure 3.13) indicates that the dependence of the flying performance, of a traditional slider, on the skew angle increases when flying over bit patterned media compared to flying over smooth media. In other words, a spherical-pad slider has better flying characteristics for flying over bit patterned media than a traditional slider.

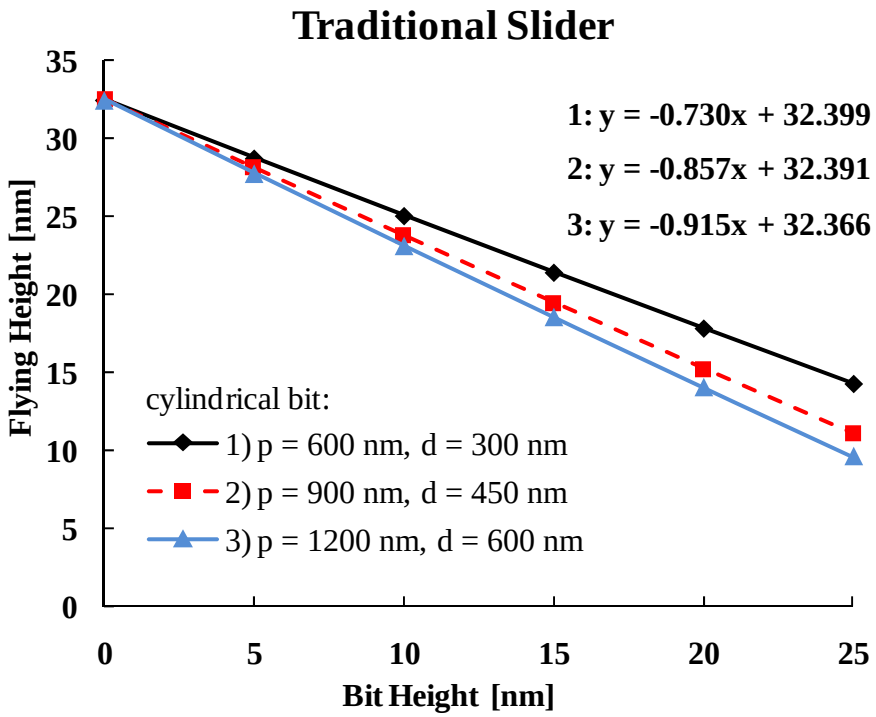

Figure 3.17 Flying height of a traditional slider as a function of bit height

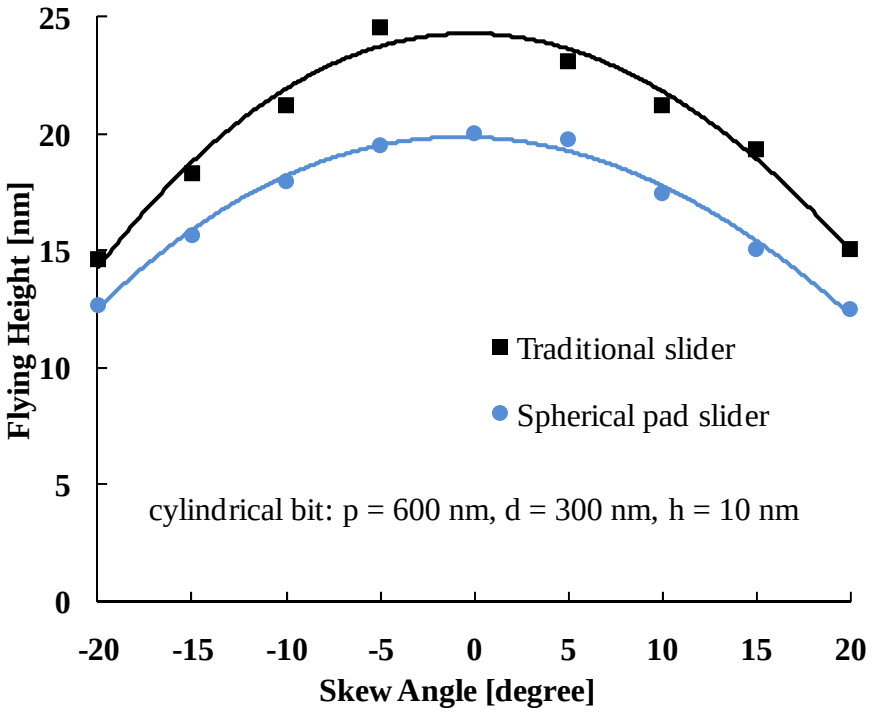

Figure 3.18 Flying height of slider as a function of skew angle

3.3.3.3 Parametric Study of Spherical Pad

Figure 3.19 and Figure 3.20 show the flying performance of the spherical-pad slider as a function of the spherical-pad height H_p. It can be observed that the flying height of the spherical-pad slider is linearly reduced by an increase in H_p. In addition, the ratio of flying height reduction to bit height is similar for the four different spherical-pad heights. Furthermore, the variation of the pitch angle is minimal even when the height of bit pattern is increased to 25 nm (Figure 3.20).

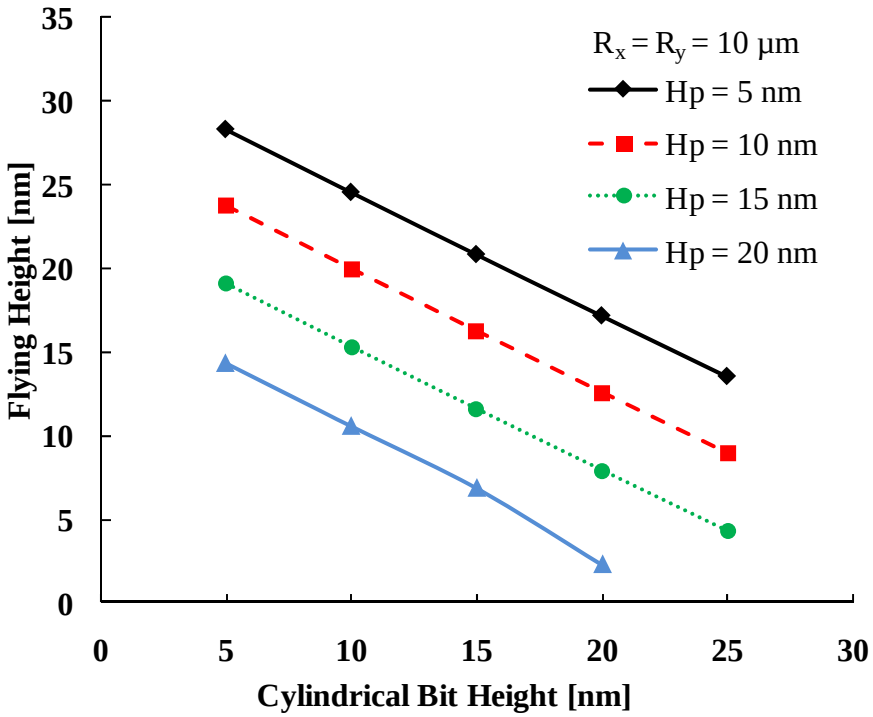

Figure 3.19 Variation of flying height of slider with height of spherical pad

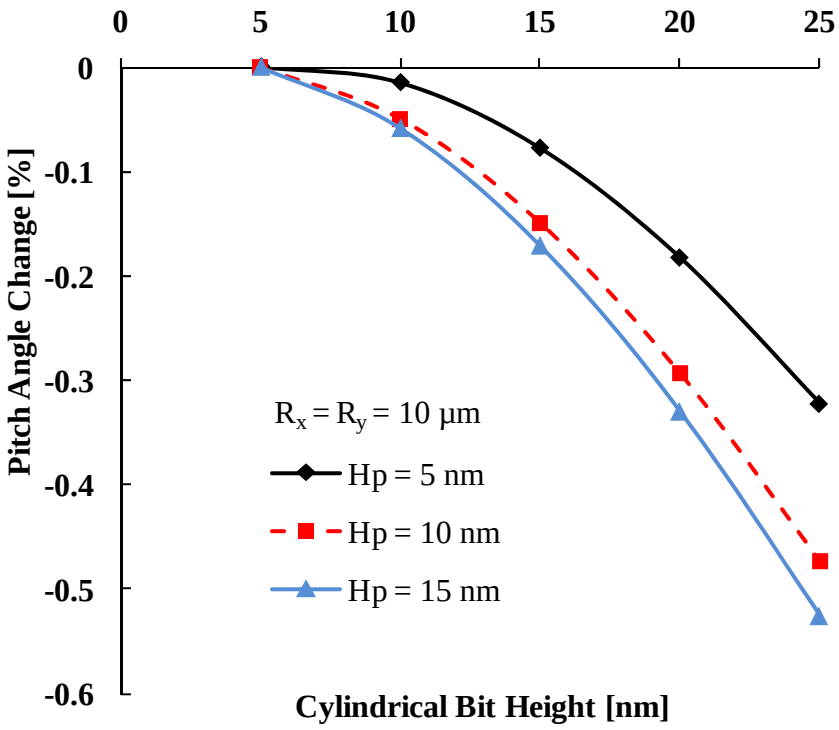

Figure 3.20 Variation of pitch angle of slider with height of spherical pad

Figure 3.21 shows the effect of the radii of spherical pad on the flying height. It can be observed that when flying over bit patterned media there is negligible difference in the flying height for all simulated radii of the spherical pad. Thus, the flying height of the spherical-pad slider is a function of the height of the spherical pad (Figure 3.19) but is not sensitive to the radii of the spherical pad (Figure 3.21).

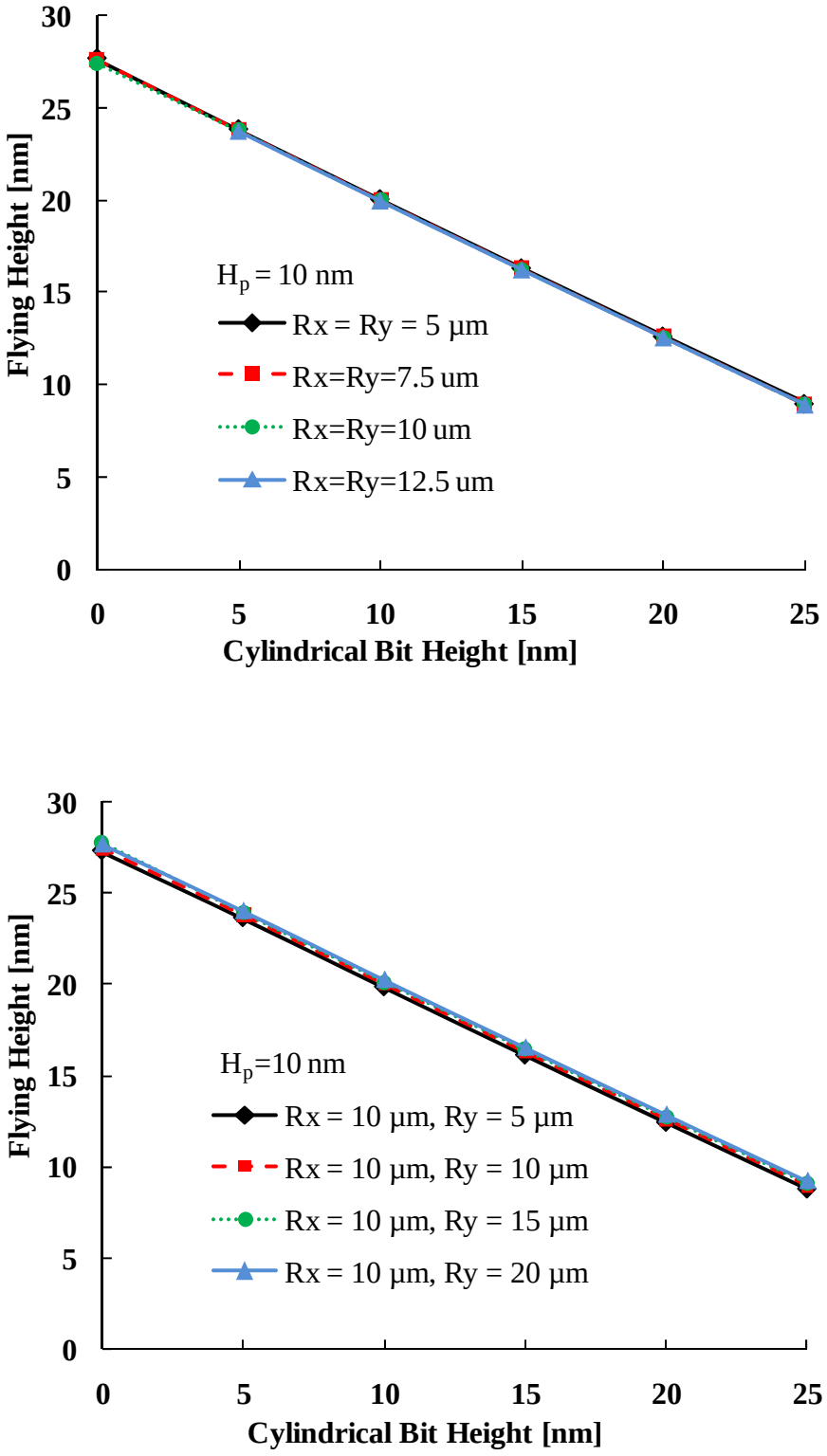

Figure 3.21 Variation of flying height of slider with radius of spherical pad

3.4 Summary and Conclusions

This chapter describes numerical simulations of the changes in the flying characteristics of femto and spherical-pad sliders due to variations in the design parameters of bit patterned media. The discrete bits are modeled as isolated islands on the disk surface. The peaks in the air bearing pressure distribution over each island are clearly visible from simulation results. When a spherical-pad slider is used, the maximum pressure shifts towards the spherical pad of the slider. The flying characteristics of both femto and spherical-pad sliders flying over bit patterned media are different from sliders flying over smooth media. The reduction in the flying height of a slider is a function of the bit design parameters. These parameters include the bit height, the ratio of bit diameter to bit pitch, and the bit shape. The flying height reduction is approximately linear to the increase in bit pattern height. The ratio of the reduction in flying height to bit pattern height is larger than that observed in sliders flying over a discrete track media. The flying height of the femto slider is more sensitive to skew angle when flying over bit patterned media than when flying over ‘‘smooth’’ media. On the other hand, the flying height of a spherical-pad slider is less sensitive to the skew angle than that of a traditional slider. The flying height of a spherical-pad slider is linearly reduced with an increasing spherical-pad height. However, the ratio of the flying height reduction to bit height remains the same regardless of the height of spherical pads. In addition, the flying height of a spherical-pad slider is not sensitive to the radii of the spherical pad.

3.5 Acknowledgement

Chapter 3, in part, is a reprint of the material as it appears in “Air bearing simulation for bit patterned media,” Hui Li, Hao Zheng, Yeoungchin Yoon and Frank E. Talke, Tribology Letters, 2009, pp. 199 – 204. The dissertation author was one of the investigators and coauthors of this paper.

Chapter 3, in part, is a reprint of the material as it appears in “Numerical simulation of a “spherical pad” slider flying over bit patterned media,” Hui Li, Hao Zheng, Kensuke Amemiya and Frank E. Talke, IEEE Transactions on Magnetics, Vol. 45, No. 10, Oct. 2009, pp. 3616 – 3619. The dissertation author was one of the investigators and coauthors of this paper.

Chapter 4

Thermo-Mechanical Modeling of Sliders with Heat Source

The trailing region of a slider consists of several components including the read/write element, the write coil, and the shields. Each of these components is made of different material with unique thermal/mechanical properties. The heat generated in a slider, due to heat dissipation in the write head and the heaters, or due to heat dissipation in the light delivery system of a heat assisted magnetic recording head, can cause a thermal protrusion near the read/write element. This protrusion is also a function of the thermal expansion coefficients of the different materials.

In this chapter, the theoretical background for modeling the thermal protrusions of a slider is described. A numerical simulation tool is developed to investigate the thermal deformation and flying characteristics of a slider when the heater or the write coil are energized. This simulation tool combines the CMRR/Talke Lab air bearing simulator (Chapter 2) with a finite element solution of the thermo-mechanical model of a slider. Numerical simulations of thermal flying height control sliders and sliders used in heat assisted magnetic recording will be presented in Chapter 5, 6 and 7.

4.1 Theoretical Background of Thermo-Mechanical Simulation

The heat generated by a heat source in a slider can be expressed as $Q = I^2_{HeatSource} R_{HeatSource}$, where $I_{HeatSource}$ and $R_{HeatSource}$ are the current and the resistance of the heat source, respectively. ANSYS is used in our numerical analysis in order to determine the temperature distribution and the thermal deformation of the slider when the heat source is energized. In ANSYS, the thermo-mechanical analysis proceeds sequentially, i.e., the temperature distribution of the slider is first calculated from the thermal analysis and is then read into the database to provide a thermal load for the mechanical simulation [134].

4.1.1 Thermal Analysis

The temperature distribution of the slider caused by a heat source is obtained from the finite element solution of the heat transfer equation. The governing equation for steady heat transfer is based on Fourier's law and the conservation of energy.

For a differential control volume [132]:

$$\nabla \cdot \mathbf{q} = \Phi \tag{4.1}$$

where Φ is the volumetric heat generation and $\mathbf{q}$ is the heat flux vector. $\mathbf{q}$ is related to the gradient of temperature T by Fourier's law [105]:

$$\mathbf{q} = -\mathbf{k}\nabla T \tag{4.2}$$

where $\mathbf{k}$ is the thermal conductivity matrix. The negative sign in front of $\mathbf{k}\nabla T$ indicates heat flows from high temperature to low temperature.

Substitution of Equation (4.2) into Equation (4.1) yields [132]:

$$\nabla \cdot \left(\mathbf{k} \nabla T \right) + \Phi = 0 \tag{4.3}$$

Assuming that the material is isotropic, $\mathbf{k} = \begin{bmatrix} k & 0 & 0 \\ 0 & k & 0 \\ 0 & 0 & k \end{bmatrix}$, Equation (4.3) can be written as:

$$\frac{\partial}{\partial x}\left(k \frac{\partial T}{\partial x} \right) + \frac{\partial}{\partial y}\left(k \frac{\partial T}{\partial y} \right) + \frac{\partial}{\partial z}\left(k \frac{\partial T}{\partial z} \right) + \Phi = 0 \tag{4.4}$$

In order to solve Equation (4.3), boundary conditions must be prescribed. Typical boundary conditions that could apply are shown in Figure 4.1. These are [108]:

1) Prescribed temperatures T^* on boundary S_t:

$$T = T^* \text{ at } S_t \tag{4.5}$$

This is a so-called “essential boundary condition”;

2) Prescribed heat flux on boundary S_q:

$$\mathbf{n} \cdot \mathbf{q} = -q^* \text{ at } S_q \tag{4.6}$$

where q^* is the specified heat flux over the surface S_q and **n** is the unit normal vector of the surface pointing outwards;

3) Prescribed convection, i.e., Newton’s law of cooling over boundary S_c:

$$\mathbf{n} \cdot \mathbf{q} = -h_c (T_f - T_s) \text{ at } S_c \tag{4.7}$$

where h_c is the heat transfer coefficient. T_s and T_f are the temperatures at the surface and the surrounding fluid, respectively [132].

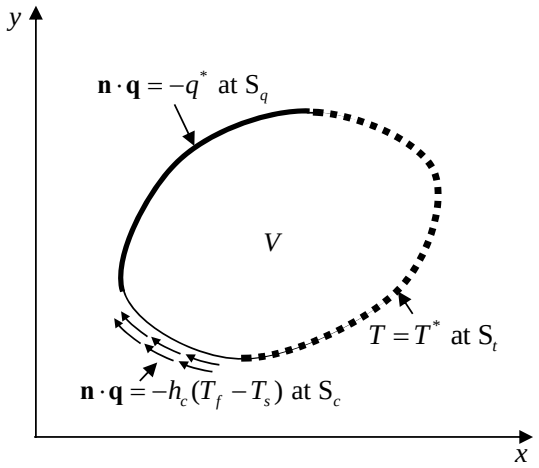

$S_t \cup S_q \cup S_c = S;\ S_t, S_q$ and S_c are not overlapped

Figure 4.1 Problem domain and boundary conditions (after [109])

In order to obtain a finite element formulation of Equation (4.3), we first multiply Equation (4.3) by the weight function w and integrate over the volume of the element V^e:

$$\int_{V^e} w\left\{\nabla\cdot\left(\mathbf{k}\nabla T\right)+\Phi\right\}dV^e = 0 \tag{4.8}$$

Using integration by part (Equation (2.42)), we obtain:

$$\int_{V^e}\left\{\nabla\cdot\left(w\mathbf{k}\nabla T\right)-\nabla w\cdot\left(\mathbf{k}\nabla T\right)+w\Phi\right\}dV^e = 0 \tag{4.9}$$

Applying the general Gauss' theorem (Equation (2.3)) to Equation (4.9), one can write the first term in Equation (4.9) as:

$$\int_{V^e}\nabla\cdot\left(w\mathbf{k}\nabla T\right)dV^e = \int_{S^e}\mathbf{n}\cdot\left(w\mathbf{k}\nabla T\right)dS^e \tag{4.10}$$

Applying the boundary conditions (Equation (4.5-4.7)) to Equation (4.10) and choosing the arbitrary weight functions w to be zero at the essential boundaries (i.e., $w = 0$ at S_t), the first term in Equation (4.9) becomes:

$$\int_{V^e} \nabla \cdot \left(w\mathbf{k}\nabla T \right) dV^e = \int_{S_q^e} wq^* dS_q^e + \int_{S_c^e} wh_c \left(T_f - T \right) dS_c^e \tag{4.11}$$

Substituting Equation (4.11) into Equation (4.9), we obtain:

$$\int_{V^e} \nabla w \cdot \left(\mathbf{k}\nabla T \right) dV^e = \int_{V^e} w\Phi dV^e + \int_{S_q^e} wq^* dS_q^e + \int_{S_c^e} wh_c \left(T_f - T \right) dS_c^e \tag{4.12}$$

For a single element, the temperature distribution within the element can be interpolated by:

$$T\left(\mathbf{x}\right) = \mathbf{N}\left(\mathbf{x}\right)\mathbf{T}^e \tag{4.13}$$

where $\mathbf{N}\left(\mathbf{x}\right) = \begin{bmatrix} N_1\left(\mathbf{x}\right) & N_2\left(\mathbf{x}\right) & \ldots & N_n\left(\mathbf{x}\right) \end{bmatrix}$ are the element shape functions, with n denoting the number of nodes per element, $\mathbf{T}^e = \begin{bmatrix} T_1 & T_2 & \ldots & T_n \end{bmatrix}^T$ is the nodal temperature vector. The gradient of temperature can be obtained by:

$$\nabla T\left(\mathbf{x}\right) = \nabla \mathbf{N}\left(\mathbf{x}\right)\mathbf{T}^e = \mathbf{B}\left(\mathbf{x}\right)\mathbf{T}^e \tag{4.14}$$

where $\mathbf{B}\left(\mathbf{x}\right) \equiv \nabla \mathbf{N}\left(\mathbf{x}\right) = \begin{bmatrix} \frac{\partial N_1}{\partial x} & \frac{\partial N_2}{\partial x} & \ldots & \frac{\partial N_n}{\partial x} \\ \frac{\partial N_1}{\partial y} & \frac{\partial N_2}{\partial y} & \ldots & \frac{\partial N_n}{\partial y} \\ \frac{\partial N_1}{\partial z} & \frac{\partial N_2}{\partial z} & \ldots & \frac{\partial N_n}{\partial z} \end{bmatrix}$. w can be written using the same shape functions as for the temperature fields:

$$\begin{aligned} w\left(\mathbf{x}\right) &= \mathbf{N}\left(\mathbf{x}\right)\mathbf{w}^e \\ \nabla w\left(\mathbf{x}\right) &= \nabla \mathbf{N}\left(\mathbf{x}\right)\mathbf{w}^e = \mathbf{B}\left(\mathbf{x}\right)\mathbf{w}^e \end{aligned} \tag{4.15}$$

where $\mathbf{w}^e$ is an arbitrary virtual term satisfying the zero-temperature boundary conditions. A superscript e represents element-wise quantities.

Substituting Equation (4.13-4.15) into Equation (4.12) yields:

$$\begin{aligned}&\mathbf{w}^{eT}\int_{V^e}\mathbf{B}^T\mathbf{k}\mathbf{B}dV^e\mathbf{T}^e = \\ &\mathbf{w}^{eT}\int_{V^e}\mathbf{N}^T\Phi dV^e+\mathbf{w}^{eT}\int_{S_q^e}\mathbf{N}^T q^* dS_q^e+\mathbf{w}^{eT}\int_{S_c^e}h_c\mathbf{N}^T\left(T_F-\mathbf{N}\mathbf{T}^e\right)dS_c^e\end{aligned} \tag{4.16}$$

Equation (4.16) holds for an arbitrary $\mathbf{w}^e$. Thus, we have:

$$\begin{aligned}&\left(\int_{V^e}\mathbf{B}^T\mathbf{k}\mathbf{B}dV^e\mathbf{T}^e+\int_{S_c^e}h_c\mathbf{N}^T\mathbf{N}dS_c^e\right)\mathbf{T}^e = \\ &\int_{V^e}\mathbf{N}^T\Phi dV^e+\int_{S_q^e}\mathbf{N}^T q^* dS_q^e+\int_{S_c^e}h_c\mathbf{N}^T T_F dS_c^e\end{aligned} \tag{4.17}$$

Equation (4.17) is rearranged so that the left hand terms are dependent on the unknown quantity $\mathbf{T}^e$ while the right hand terms are the known values.

Defining the element conductivity matrix and heat flow vector as:

$$\begin{aligned}\left[\mathbf{K}\right]^e &\equiv \int_{V^e}\mathbf{B}^T\mathbf{k}\mathbf{B}dV^e+\int_{S_c^e}h_c\mathbf{N}^T\mathbf{N}dS_c^{e'} \\ \left\{\mathbf{Q}\right\}^e &\equiv \int_{V^e}\mathbf{N}^T\Phi dV^e+\int_{S_q^e}\mathbf{N}^T q^* dS_q^e+\int_{S_c^e}h_c\mathbf{N}^T T_F dS_c^e\end{aligned} \tag{4.18}$$

we can write the finite element equation for each element as:

$$\left[\mathbf{K}\right]^e\left\{\mathbf{T}\right\}^e=\left\{\mathbf{Q}\right\}^e \tag{4.19}$$

After assembling the elements, the global finite element equation for the system becomes:

$$\left[\mathbf{K}_{th}\right]\left\{\mathbf{T}\right\}=\left\{\mathbf{Q}\right\} \tag{4.20}$$

where $\left[\mathbf{K}_{th}\right]$ is the global conductivity matrix. The temperature distribution can be obtained from Equation (4.20). Figure 4.2 shows a typical temperature distribution inside the thermal flying height control slider. The heater is energized and a temperature increase near the read/write element will occur.

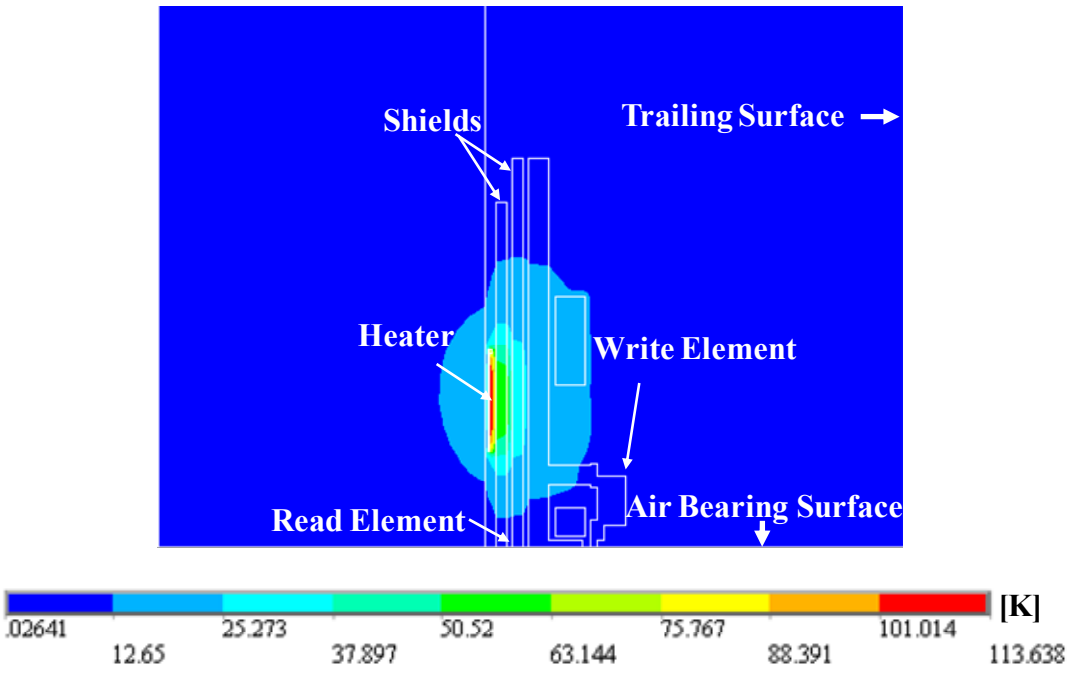

Figure 4.2 Typical temperature distribution inside the slider caused by a thermal flying height heater

4.1.2 Mechanical Analysis

A change of temperature results in a thermal deformation of the slider. The deformation can be calculated from the mechanical analysis of the slider. The governing equation of mechanical analysis can be obtained by the principle of virtual work stating that a virtual variation of the internal strain energy must be equal to the virtual change in external work done by the applied load [108][132], i.e.,

$$\int_{V^e} \boldsymbol{\delta\varepsilon}^T \boldsymbol{\sigma} dV^e = \int_{V^e} \boldsymbol{\delta u}^T \mathbf{f}_b dV^e + \int_{S_t^e} \boldsymbol{\delta u}^T \mathbf{t} dS^e \qquad (4.21)$$

where $\boldsymbol{\delta\varepsilon}$ and $\boldsymbol{\delta u}$ are the virtual strain and virtual displacement, respectively. $\mathbf{f}_b$ and $\mathbf{t}$ are the prescribed body forces and surface traction, respectively.

$\boldsymbol{\sigma} = \begin{bmatrix} \sigma_x & \sigma_y & \sigma_z & \sigma_{xy} & \sigma_{yz} & \sigma_{xz} \end{bmatrix}^T$ is the stress vector and is related to the strain by the generalized Hooke's Law:

$$\boldsymbol{\sigma} = \mathbf{D}\boldsymbol{\varepsilon}_{el} \tag{4.22}$$

where $\mathbf{D}$ is the elasticity matrix [109][132], $\boldsymbol{\varepsilon}_{el} = \boldsymbol{\varepsilon} - \boldsymbol{\varepsilon}_{th}$ is the elastic strain vector. $\boldsymbol{\varepsilon} = \begin{bmatrix} \varepsilon_x & \varepsilon_y & \varepsilon_z & \gamma_{xy} & \gamma_{yz} & \gamma_{zx} \end{bmatrix}^T$ is the total strain vector and is related to the displacement $\mathbf{u}$ by:

$$\boldsymbol{\varepsilon} = \mathbf{L}\mathbf{u} \tag{4.23}$$

where $L = \begin{bmatrix} \frac{\partial}{\partial x} & 0 & 0 & \frac{\partial}{\partial y} & \frac{\partial}{\partial z} & 0 \\ 0 & \frac{\partial}{\partial y} & 0 & \frac{\partial}{\partial x} & 0 & \frac{\partial}{\partial z} \\ 0 & 0 & \frac{\partial}{\partial z} & 0 & \frac{\partial}{\partial x} & \frac{\partial}{\partial y} \end{bmatrix}^T$.

$\boldsymbol{\varepsilon}_{th}$ is the thermal strain vector induced by the change of temperature. It is defined by $\boldsymbol{\varepsilon}_{th} = \Delta T \begin{bmatrix} \alpha_x & \alpha_y & \alpha_z & 0 & 0 & 0 \end{bmatrix}^T = \boldsymbol{\alpha}_T \Delta T$ [132], where ΔT is the temperature change caused by the heat source and is obtained from thermal analysis, $\boldsymbol{\alpha}_T$ is the thermal expansion coefficient of material with α_x, α_y and α_z are the thermal expansion coefficient in the x, y and z directions.

Substituting Equation (4.22) and (4.23) into Equation (4.21), one obtains:

$$\int_{V^e} \boldsymbol{\delta}\mathbf{u}^T \mathbf{L}^T \mathbf{D}\left(\mathbf{L}\mathbf{u} - \boldsymbol{\varepsilon}_{th}\right) dV^e = \int_{V^e} \boldsymbol{\delta}\mathbf{u}^T \mathbf{f}_b dV^e + \int_{S_t^e} \boldsymbol{\delta}\mathbf{u}^T \mathbf{t} dS^e \tag{4.24}$$

For a single element, the displacement vector within the element can be interpolated by:

$$\mathbf{u}(\mathbf{x}) = \mathbf{N}(\mathbf{x})\mathbf{u}^e \tag{4.25}$$

where $\mathbf{N}(\mathbf{x}) = \begin{bmatrix} N_1 & 0 & 0 & N_2 & 0 & 0 & \dots & N_n & 0 & 0 \\ 0 & N_1 & 0 & 0 & N_2 & 0 & \dots & 0 & N_n & 0 \\ 0 & 0 & N_1 & 0 & 0 & N_2 & \dots & 0 & 0 & N_n \end{bmatrix}$ are the element shape functions, with n denoting the number of nodes per element, and $\mathbf{u}^e = \begin{bmatrix} u_1 & v_1 & w_1 & u_2 & v_2 & w_2 & \dots & u_n & v_n & w_n \end{bmatrix}^T$ is the nodal displacement vector. Substituting Equation (4.25) into (4.23), we obtain:

$$\boldsymbol{\varepsilon} = \mathbf{L}\mathbf{u} = \mathbf{L}\mathbf{N}\mathbf{u}^e = \mathbf{B}\mathbf{u}^e \tag{4.26}$$

where $\mathbf{B} \equiv \mathbf{L}\mathbf{N}$ is the strain-displacement matrix. The virtual displacement $\boldsymbol{\delta}\mathbf{u}$ and virtual strain $\boldsymbol{\delta\varepsilon}$ can be written in a similar way, i.e.,

$$\begin{aligned} \boldsymbol{\delta}\mathbf{u} &= \mathbf{N}\boldsymbol{\delta}\mathbf{u}^e \\ \boldsymbol{\delta\varepsilon} &= \mathbf{L}\mathbf{N}\boldsymbol{\delta}\mathbf{u}^e = \mathbf{B}\boldsymbol{\delta}\mathbf{u}^e \end{aligned} \tag{4.27}$$

Substituting Equation (4.25-4.27) into Equation (4.24) yields:

$$\int_{V^e} \boldsymbol{\delta}\mathbf{u}^{eT}\mathbf{B}^T\mathbf{D}\left(\mathbf{B}\mathbf{u}^e - \boldsymbol{\varepsilon}_{th}\right)dV^e = \int_{V^e} \boldsymbol{\delta}\mathbf{u}^{eT}\mathbf{N}^T\mathbf{f}_b dV^e + \int_{S_t^e} \boldsymbol{\delta}\mathbf{u}^T\mathbf{N}^T\mathbf{t}dS^e \tag{4.28}$$

Again, $\boldsymbol{\varepsilon}_{th}$ is the thermal strain vector induced by the change of temperature. The above expression must hold for all values of $\boldsymbol{\delta}\mathbf{u}^e$. Thus, Equation (4.28) becomes:

$$\int_{V^e} \mathbf{B}^T\mathbf{D}\left(\mathbf{B}\mathbf{u}^e - \boldsymbol{\varepsilon}_{th}\right)dV^e = \int_{V^e} \mathbf{N}^T\mathbf{f}_b dV^e + \int_{S_t^e} \mathbf{N}^T\mathbf{t}dS^e \tag{4.29}$$

or, after rearranging:

$$\int_{V^e} \mathbf{B}^T\mathbf{D}\mathbf{B}dV^e\mathbf{u}^e = \int_{V^e} \mathbf{N}^T\mathbf{f}_b dV^e + \int_{S_t^e} \mathbf{N}^T\mathbf{t}dS^e + \int_{V^e} \mathbf{B}^T\mathbf{D}\boldsymbol{\varepsilon}_{th}dV^e \tag{4.30}$$

The last term on the right hand side is the element thermal load vector.

We define the element stiffness matrix and load vector as:

$$\begin{aligned} \left[\mathbf{K}\right]^e &\equiv \int_{V^e} \mathbf{B}^T \mathbf{D}\mathbf{B} dV^e \\ \left\{\mathbf{F}\right\}^e &\equiv \int_{V^e} \mathbf{N}^T \mathbf{f}_b dV^e + \int_{S_t^e} \mathbf{N}^T \mathbf{t} dS^e + \int_{V^e} \mathbf{B}^T \mathbf{D}\boldsymbol{\varepsilon}_{th} dV^e \end{aligned} \tag{4.31}$$

The finite element equation for each element can then be written as:

$$\left[\mathbf{K}\right]^e \left\{\mathbf{u}\right\}^e = \left\{\mathbf{F}\right\}^e \tag{4.32}$$

After assembling all individual elements, the global finite element equation for the system becomes:

$$\left[\mathbf{K}_{st}\right]\left\{\mathbf{u}\right\} = \left\{\mathbf{F}\right\} \tag{4.33}$$

where $\left[\mathbf{K}_{st}\right]$ is the global stiffness matrix.

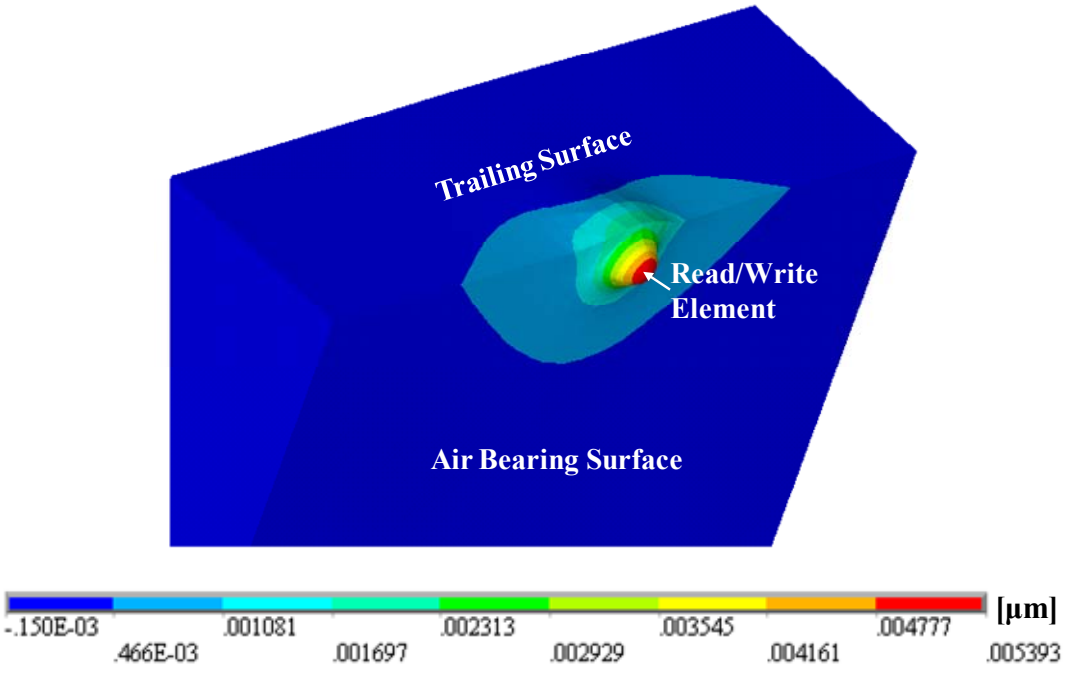

Figure 4.3 Thermal protrusion of the slider caused by the thermal flying height control heater

Figure 4.3 shows the thermal protrusion caused by the heater element of the thermal flying height control slider. We observe that the maximum protrusion occurs near the read/write element.

4.2 Heat Transfer at the Head/Disk Interface [106][204]

The heat transfer between the slider and the air bearing serves as the boundary conditions for the thermal analysis of a slider with internal heat sources. The heat transfer plays an important role in determining the temperature distribution, and correspondingly, the thermal deformation and flying characteristics of the slider. In this section, we present the derivation of a heat transfer model following the procedures in [106] and [204]. The models are in good agreement with experimental results [202-204] and have been widely used in the thermo-mechanical modeling of sliders to account for the thermal effects of air bearings [147-151]. In calculating the heat transfer at the head/disk interface, the momentum equations (described in Chapter 2) and energy equation are solved separately, based on the assumption that the physical properties of air are constant. In order to take into account rarefaction effects at ultra-low head/disk spacings, the first-order boundary conditions for both the velocity and the temperature are used [106][204].

For steady-state conditions, the energy equation for a Newtonian fluid is:

$$\rho c_p \mathbf{u} \cdot \nabla T = k_{air} \nabla^2 T + \mathbf{u} \cdot \nabla p + \phi \tag{4.34}$$

where ρ is the air density, $\mathbf{u} = \begin{pmatrix} u & v & w \end{pmatrix}$ is the velocity of air flow as defined in Chapter 2, c_p is the specific heat at constant pressure, T is the temperature of the air, k_{air} is the thermal conductivity of air, and p is the pressure. ϕ is the viscous dissipation function defined as [135]:

$$\begin{aligned} \phi = 2\mu & \left[\left(\frac{\partial u}{\partial x} \right)^2 + \left(\frac{\partial v}{\partial y} \right)^2 + \left(\frac{\partial w}{\partial z} \right)^2 - \frac{1}{3} \left(\nabla \cdot \mathbf{u} \right)^2 \right] \\ & + \mu \left[\left(\frac{\partial u}{\partial y} + \frac{\partial v}{\partial x} \right)^2 + \left(\frac{\partial v}{\partial z} + \frac{\partial w}{\partial y} \right)^2 + \left(\frac{\partial u}{\partial z} + \frac{\partial w}{\partial x} \right)^2 \right] \end{aligned} \tag{4.35}$$

where μ is the viscosity of air.

The relevant terms in Equation (4.34) and (4.35) can be determined following an "order-of-magnitude" analysis similar to the one described in Section 2.1. This analysis is shown in Appendix B. As a result, the energy equation can be simplified as:

$$k_{air} \frac{\partial^2 T}{\partial z^2} + u \frac{\partial p}{\partial x} + v \frac{\partial p}{\partial y} + \mu \left(\frac{\partial u}{\partial z} \right)^2 + \mu \left(\frac{\partial v}{\partial z} \right)^2 = 0 \tag{4.36}$$

The temperature distribution in the air bearing can be obtained by integrating Equation (4.36) twice:

$$T = -\frac{z^2}{2k_{air}} \left[u \frac{\partial p}{\partial x} + v \frac{\partial p}{\partial y} + \mu \left(\frac{\partial u}{\partial z} \right)^2 + \mu \left(\frac{\partial v}{\partial z} \right)^2 \right] + C_1 z + C_2 \tag{4.37}$$

where u and v are velocity distributions obtained from Equation (2.18) and (2.19). C_1 and C_2 are constants and can be determined from the boundary conditions of the temperature.

In this derivation, we use the first-order boundary conditions for both the velocity and the temperature [106][204]. As was shown in Chapter 2, the velocity profile obtained for the first-order slip flow correction is given by:

$$\begin{aligned} u &= \frac{1}{2\mu}\frac{\partial p}{\partial x}\left(z^2 - zh - a\lambda h\right) + U\left(1 - \frac{z + a\lambda}{h + 2a\lambda}\right) \\ v &= \frac{1}{2\mu}\frac{\partial p}{\partial y}\left(z^2 - zh - a\lambda h\right) + V\left(1 - \frac{z + a\lambda}{h + 2a\lambda}\right) \end{aligned} \tag{4.38}$$

where $a \equiv \left(2 - \sigma_M\right)/\sigma_M$. Using these expressions in Equation (4.37), we can rewrite Equation (4.37) as:

$$\begin{aligned} T = &-\frac{z^4}{2k_{air}}\left\{\frac{1}{8\mu}\left(\left[\frac{\partial p}{\partial x}\right]^2 + \left[\frac{\partial p}{\partial y}\right]^2\right)\right\} \\ &-\frac{z^3}{2k_{air}}\left\{-\left[\frac{h}{4\mu}\left(\left[\frac{\partial p}{\partial x}\right]^2 + \left[\frac{\partial p}{\partial y}\right]^2\right) + \frac{1}{2\left(h + 2a\lambda\right)}\left(U\frac{\partial p}{\partial x} + V\frac{\partial p}{\partial y}\right)\right]\right\} \\ &-\frac{z^2}{2k_{air}}\left\{\frac{a\lambda + 2h}{2\left(h + 2a\lambda\right)}\left(U\frac{\partial p}{\partial x} + V\frac{\partial p}{\partial y}\right) + \frac{h\left(h - 2a\lambda\right)}{8\mu}\left(\left[\frac{\partial p}{\partial x}\right]^2 + \left[\frac{\partial p}{\partial y}\right]^2\right)\right\} \\ &-\frac{z^2}{2k_{air}}\left\{\frac{\mu\left(U^2 + V^2\right)}{2\left(h + 2a\lambda\right)^2}\right\} + C_1 z + C_2 \end{aligned} \tag{4.39}$$

In addition to the slip velocity, a temperature jump at the interface between a solid and a gas needs to be considered when the continuum description breaks down. The temperature-jump condition due to rarefaction effects can be expressed as [106][204]:

$$\begin{aligned} z = 0: &\quad T = T_d + b\lambda\left.\frac{\partial T}{\partial z}\right|_{z=0} \\ z = h: &\quad T = T_s - b\lambda\left.\frac{\partial T}{\partial z}\right|_{z=h} \end{aligned} \tag{4.40}$$

where λ is the mean free path of air and $b \equiv 2(2-\sigma_T)\gamma / \{\sigma_T(\gamma+1)\Pr\}$. In this equation, σ_T is the thermal accommodation coefficient. γ is the ratio of specific heat at constant pressure c_p and constant volume c_v, respectively. Pr is the Prandtl number defined by $\Pr = \mu c_p / k$ [136]. Applying Equation (4.40) to Equation (4.39), we obtain:

$$\begin{aligned} C_1 = \frac{T_s - T_d}{h+2b\lambda} + \frac{1}{2k_{air}}\left\{\frac{h^3 + a\lambda h^2 + b\lambda h^2 + 2ab\lambda^2 h}{2(h+2a\lambda)(h+2b\lambda)}\left(U\frac{\partial p}{\partial x} + V\frac{\partial p}{\partial y}\right)\right\} \\ + \frac{1}{2k_{air}}\left\{-\frac{a\lambda h^2}{4\mu}\left(\left[\frac{\partial p}{\partial x}\right]^2 + \left[\frac{\partial p}{\partial y}\right]^2\right) + \frac{\mu(U^2+V^2)}{2(h+2a\lambda)^2}h\right\} \\ C_2 = T_d + b\lambda C_1 \end{aligned} \tag{4.41}$$

Applying Fourier's law (Equation (4.2)) at the surface of the slider, i.e., at $z = h$, we obtain the heat transfer at the air bearing surface:

$$\begin{aligned} q = -k_{air}\left.\frac{\partial T}{\partial z}\right|_{z=h} = -k_{air}\frac{T_s - T_d}{h+2b\lambda} - \frac{a\lambda h^2}{8\mu}\left[\left(\frac{\partial p}{\partial x}\right)^2 + \left(\frac{\partial p}{\partial y}\right)^2\right] \\ + \frac{\mu h}{2}\frac{U^2+V^2}{(h+2a\lambda)^2} + \frac{(ah^2\lambda + bh^2\lambda + 2abh\lambda^2)}{2(h+2a\lambda)(h+2b\lambda)}\left(U\frac{\partial p}{\partial x} + V\frac{\partial p}{\partial y}\right) \end{aligned} \tag{4.42}$$

Equation (4.42) can be written as:

$$q = q_{conduct} + q_{visocus} \tag{4.43}$$

where the first term $-k_{air}(T_s - T_d)/(h+2b\lambda)$ corresponds to heat conduction $q_{conduct}$ between slider and disk. It has been demonstrated in [106][203][204] that this term is several orders of magnitude larger than the other terms for a typical head/disk interface in present use. Thus,

$$q = -\frac{k_{air}}{h + 2b\lambda}\left(T_s - T_d\right) \tag{4.44}$$

can been used as a simplified boundary condition at the air bearing surface for the thermo-mechanical analysis. We note that the heat conduction is modified by a factor of $1/\left(1+2b\lambda/h\right)$ as a consequence of the temperature-jump boundary condition [106][204]. In the absence of a temperature jump, the heat conduction between the slider and the disk is $q = -k_{air}\left(T_s - T_d\right)/h$.

The typical heat flux calculated from Equation (4.44) is shown in Figure 4.4. The maximum heat transfer occurs at the trailing edge of the slider, where the head/disk spacing is smallest.

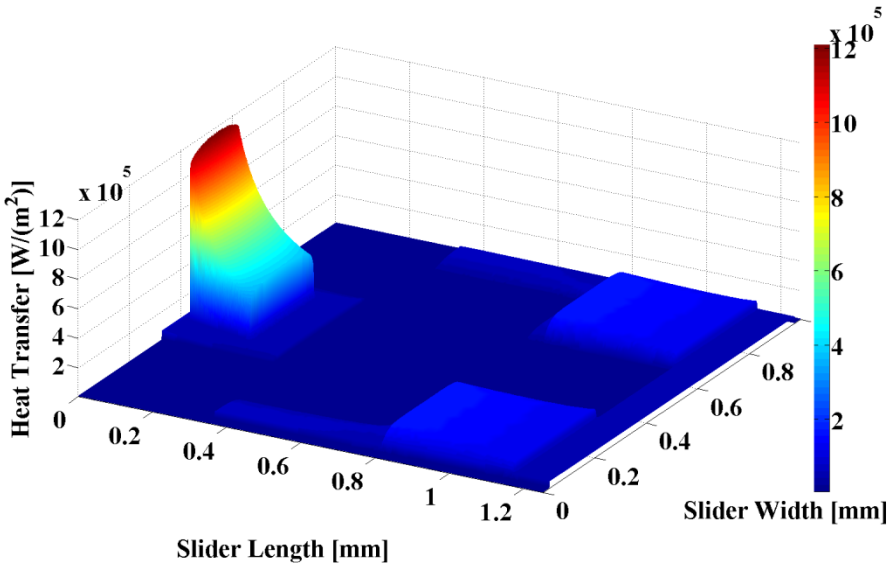

Figure 4.4 Heat transfer between the slider and the air bearing for a temperature difference $T_s - T_d = 1\,\mathrm{K}$

4.3 Integrated Simulation Tool for Thermo-Mechanical Modeling of Sliders

An iterative solution is required in order to obtain the temperature distribution, thermal protrusion and the flying height change of a slider, when the embedded heat source is energized. The flow chart of the iterative procedure is shown in Figure 4.5 and is as follows. First, the air bearing pressure and the flying height of the slider are obtained by solving simultaneously the equations of motion of the slider and the Reynolds equation (CMRR air bearing simulator). Then, the heat transfer coefficient between the slider and the air bearing is determined (Equation (4.44)) and used as boundary conditions at the air bearing surface for the thermal analysis. The thermal deformation causes a protrusion of the read/write element, which, in turn, alters the geometry of the air bearing surface. A new air bearing calculation is needed to obtain the updated pressure distribution and flying height. Iteration continues until convergence is reached.

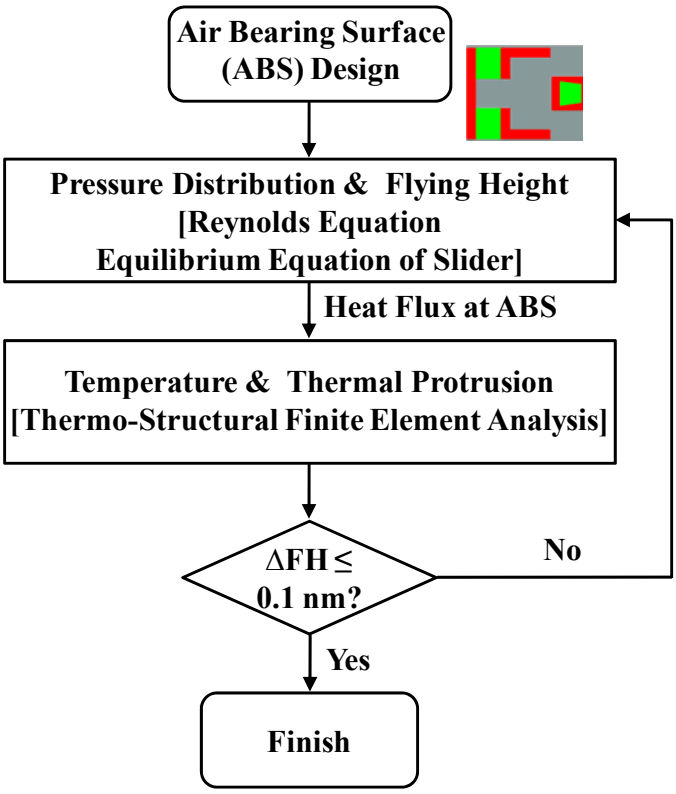

Figure 4.5 Flow chart of simulation procedure of thermo-mechanical-ABS modeling of the slider

The simulation procedure described above is a complicated process and involves the air bearing simulation, the heat flux calculation and the thermo-mechanical modeling of the slider. The issue of compatibility of different software programs provides a challenge in the numerical solution. A large number of manual steps is needed to transfer files back and forth. To simplify the calculation, an integrated simulator was developed to efficiently reduce both time cost and human power cost. The modules in the integrated simulator include: (a) CMRR/Talke Lab air bearing simulator, (b) Module of heat flux calculation, (c) ANSYS and (d) Module of interpolation. The CMRR/Talke Lab air bearing simulator is used to calculate the

steady-state pressure distribution and flying height for a given air bearing surface design. These values are needed in (b) to obtain the heat transfer at the air bearing surface. ANSYS is used for the thermo-mechanical simulation of the slider with a heat source. Interpolation plays an important role in the iterations because the discretization of the air bearing surface is generally different from that of the finite element model. The thermal protrusion obtained from (c) needs to be “mapped” onto the meshed file for the air bearing simulation to iterate the procedure. A detailed description of the interpolation scheme is presented in Appendix C.

Chapter 5

Effect of Thermal Radiation on Thermal Flying Height Control Sliders

Thermal flying height control (TFC) sliders are presently in common use in magnetic recording hard disk drives to control the flying height at the read/write element during drive operation. In calculating the thermal deformation caused by the resistance heater, radiation as predicted by Plank's blackbody radiation law is usually neglected because of its small magnitude compared to conduction. Experimental investigations have shown that Planck's law breaks down in a small gap of nano-scale dimensions and that the heat transfer coefficient at distances on the order of nanometers can exceed Plank's blackbody radiation by more than three orders of magnitude. In this chapter, we numerically investigate the effect of enhanced thermal radiation for thermal flying height control sliders at very small flying heights.

5.1 Introduction

Thermal flying height control sliders are presently in common use in order to compensate thermal effects during reading and writing and to maintain an ultra-low spacing between the head and the magnetic disk [78]. Dietzel et al. demonstrated the feasibility of dynamic flying height control by integrating a microresistor into a slider

and observing a local protrusion near the read/write element [144]. Suk et al. reported experimental data showing a change of flying height as a function of thermal actuation [145]. Many numerical investigations have been performed to study thermal flying height control and air bearing cooling of magnetic recording slider. Kurita et al. developed a finite element model to investigate the heat transfer and thermal deformation of a thermal flying height slider. They proposed a prototype design of a thermal flying height control slider with a build-in thermal actuator fabricated with thin-film processing techniques [146]. Juang and Bogy investigated the effect of air bearing surface (ABS) design on thermal deformation and proposed an air bearing design to improve the efficiency of thermal flying height control slider [147]. Fritzsche et al. compared different air bearing surface designs to investigate the relationship between air bearing surface and flying characteristics of thermal flying height control sliders [148]. Liu et al. studied the effect of heat transfer on the air bearing surface and investigated the design of the heaters and the effect of material properties on the response time of a typical thermal protrusion [149]. In these investigations, the assumption was made that the heat flux due to radiation is negligible compared to the heat conduction. This assumption is justifiable since the temperature difference between the slider and the disk is small.

A study by Narayanaswamy et al. has demonstrated that diffraction and near-field effects can become important in radiative heat transfer if the gap between objects is on the order of less than 100 nanometers [152]. In addition, experimental investigations by Shen et al. have shown that Planck's blackbody radiation law breaks down in a small gap of nanometer dimensions [153]. In Figure 5.1 experimental

results from [153] are shown (courtesy of Shen et al.) for the near-field heat transfer coefficient as a function of spacing. We observe from Figure 5.1 that increasingly larger deviations from the classical blackbody radiation law occur as the gap between two adjacent surfaces decreases below 100 nm.

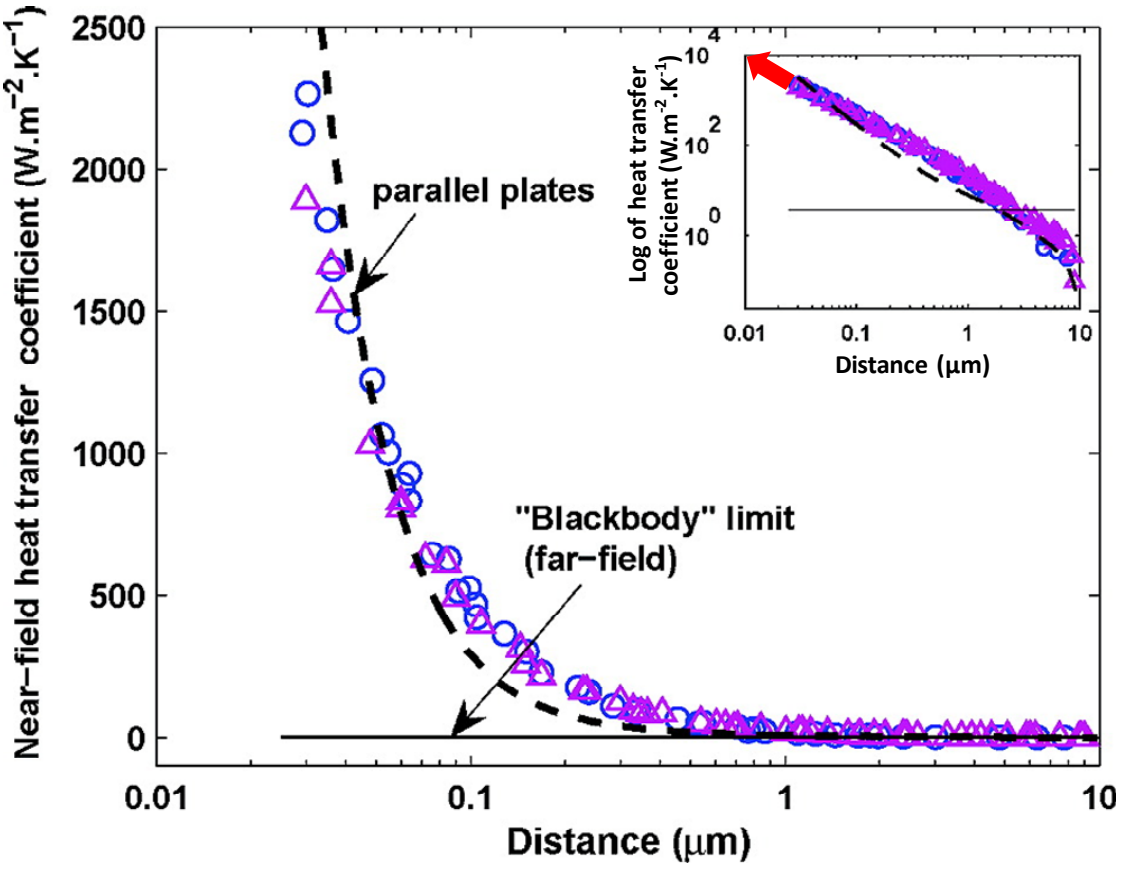

Figure 5.1 Experimental results of near-field heat transfer coefficient (courtesy of [153])

This novel result appears to be of potential interest in the head/disk interface of a hard disk drive, where the gap between the read/write element and the disk is on the order of nanometers. Clearly, thermal flying height control of magnetic recording

sliders, which is a function of the heat transfer in the air bearing, could be affected by increased near-field radiation.

This chapter evaluates the effect of near-field radiation by varying the value of the near-field heat transfer coefficient over a range of values that could potentially be encountered in the head/disk interface.

5.2 Heat Transfer between Head and Disk Interface

In order to investigate the effect of radiation in the limit of extremely small spacing of the head/disk interface, we assume that conduction and radiation effects can be superimposed. As discussed in Chapter 4, the heat transfer in an air bearing [106][155] in the absence of radiation is given by (5.1), i.e.,

$$q = \frac{k_{air} p}{h + 2b\lambda_0 p_0}\left(T_d - T_s\right) \tag{5.1}$$

where k_{air} is the thermal conductivity of air; h is the flying height; p_0 and λ_0 are the reference pressure and the mean free path of air at the reference pressure p_0, respectively; p is the air bearing pressure; T_s is the absolute temperature on the air bearing surface and T_d is the temperature of the disk surface. The coefficient b is a function of the air properties and is given by:

$$b = 2\frac{\left(2-\sigma_T\right)\gamma}{\sigma_T\left(\gamma+1\right)\mathrm{Pr}} \tag{5.2}$$

where σ_T is the thermal accommodation coefficient; γ is the ratio of specific heat at constant pressure c_p and constant volume c_v, respectively, and Pr is the Prandtl number defined by $\Pr = \mu c_p / k$.

To determine the effect of radiation at the slider/disk interface, we apply the Stefan-Boltzmann equation [156] for heat transfer between two plane surfaces, i.e.,

$$q = \varepsilon\sigma\left(T_d^4 - T_s^4\right) \tag{5.3}$$

where ε is the emissivity of a black body and σ is the Stefan-Boltzmann constant, given by $5.6704\times10^{-8} kg/\left(s^3\cdot \mathrm{K}^4\right)$.

Adding both heat transfer terms, we obtain the total heat flux due to conduction and radiation as:

$$q = \frac{k_{air}\, p}{h + 2b\lambda_0 p_0}\left(T_d - T_s\right) + \mathrm{C}\varepsilon\sigma\times\left(T_d{}^4 - T_s{}^4\right) \tag{5.4}$$

It can be observed from Equation (5.4) that a factor C is introduced in front of the radiation term. This factor accounts for the effect of near-field radiation in a small gap. It should be noted that C is a function of the local flying height, i.e., the factor C changes with x and y position on the slider. As a first approximation, we assumed that C is constant over the whole surface of the slider. To determine the effect of increased radiation at the head/disk interface, the value of C was varied from 0 to 5×10^4 and the heat flux was determined for the full slider using Equation (5.4). When C equals 0, the total heat flux (Equation (5.4)) is the same as the conductive heat flux (Equation (5.1)), i.e., the radiative heat transfer is neglected and conduction is the only contributor to the heat transfer between slider and disk. From an extrapolation of the inset of Figure

5.1 (from ref. [153]), we observe that the near-field radiative heat transfer coefficient can exceed 10^4 at 0.01 μm (10 nm). Assuming that the near-field radiation increases as the distance decreases, we extrapolate from Figure 5.1 that C may reach an extreme value of 5×10^4.

5.3 Discussion and Analysis

For a typical head/disk interface and standard air properties, k_{air} is approximately 0.03 W/(m·K). We assume that the flying height h is 10 nm, that λ_0 ~ 65 nm, $p/p_0 \sim 20$, $\gamma \sim 1.4$ and that the Prandtl number Pr is approximately 0.707. A thermal accommodation coefficient σ_T = 0.35 gives good agreement between numerical and experimental results [142]. Therefore, this latter value was used in this work, although other authors have used values of the thermal accommodation coefficient closer to one. For the present "order of magnitude" investigation the exact value of the thermal accommodation coefficient is immaterial. Assuming that the maximum temperature difference between slider and disk is 40 Kelvin, we obtain that the heat flux in the absence of radiation is approximately 2×10^7 W/m².

Assuming that the disk temperature is 300 Kelvin, we obtain that the heat flux from Plank's blackbody radiation law is approximately 3×10^2 W/m². Clearly, for this situation the heat transfer due to radiation is five orders of magnitude smaller than that due to conduction.

Considering enhanced radiation by assuming that C increases to 10^3 [153], we observe that the magnitude of the heat flux due to conduction is still two orders of

magnitude larger than the heat flux due to radiation. On the other hand, if the radiative heat transfer approaches 10^5 as the distance between the slider and the disk decreases, the effect of near-field radiation becomes increasingly more important.

5.4 Numerical Model

In order to numerically evaluate the effect of radiation on thermal protrusion and flying height reduction, a finite element model for a typical thermal flying height control slider with air bearing cooling was developed. Figure 5.2 shows a schematic of the thermal flying height control slider. The heater element is integrated into the slider in proximity to the read/write element. When the heater is energized by a current, a thermal protrusion at the read/write element is observed.

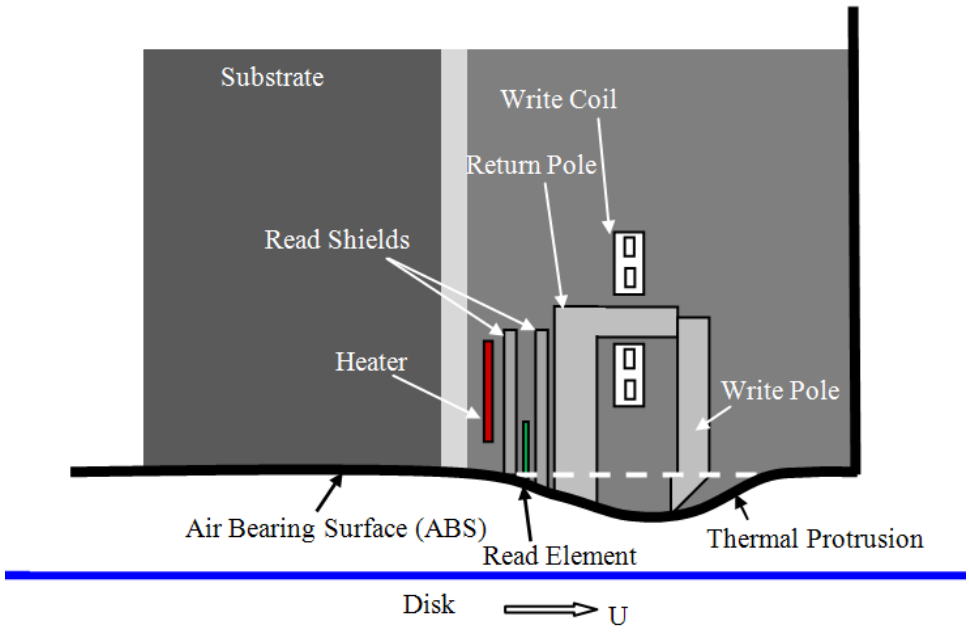

Figure 5.2 Schematic of thermal flying height control slider

In Chapter 4, an integrated simulation tool consisting of air bearing simulation and thermo-mechanical modeling of a slider with a heat source was introduced. In this chapter, the simulation tool is used to determine the thermal actuation caused by the temperature increase due to the heater. It consists of the following steps: First, the Reynolds equation and equilibrium equations of a thermal flying height control slider is solved numerically to determine the pressure and flying height of the slider. Then, the heat flux between slider and disk is calculated and used as boundary condition for calculating the temperature distribution and thermal deformation of the slider. The thermal deformation of the slider changes the flying height and pressure distribution of the slider, which, in turn, changes the heat flux and, consequently, the temperature and thermal displacement of the slider. To evaluate the effect of near-field radiation, the iteration procedure was used with the heat flux calculated from Equation (5.4) for various values of C. This iteration is continued until convergence is obtained.

5.5 Simulation Results

Figure 5.3 shows values of the heat flux coefficient (ratio of heat flux q divided by the temperature difference between slider and disk) along the center line of the slider for the cases of (a) conduction only (C = 0) and (b) the combined effect of conduction and radiation. In calculating the heat flux coefficient, the value of C was assumed to be 10^3, 10^4 and 5×10^4, respectively. It is apparent that the effect of near-field radiation on the heat flux coefficient is small for a value of C equal to 10^3. However, the value of near-field radiation becomes increasingly more important if C increases and takes values in excess of 10^4.

From the thermal analysis we observe that the maximum temperature increase occurs near the read/write element and is approximately 33.2 Kelvin for the case that radiation is neglected (C = 0). If the combined effect of conduction and radiation is considered, the maximum temperature increase is approximately 32.2 Kelvin for the case that C is 10^3, 30.9 Kelvin for the case that C is 10^4 and 26.1 Kelvin for the case that C is 5×10^4. Clearly, the effect of radiation on the maximum temperature increases with increasing values of C.

In Figure 5.4, the thermal protrusion profile along the center line of the slider is shown. The inset in the upper left corner of Figure 5.4 shows a magnification of the thermal protrusion in the area of the read/write element. The difference in the maximum thermal protrusion for (a) conduction only and (b) the combined effect of conduction and radiation is less than 0.2 nm (1%) for C = 10^3. If C is increased to 10^4, a decrease in the thermal protrusion of 0.4 nm (3%) is observed. When C reaches 5×10^4, the decrease in the thermal protrusion is 2.0 nm (17%). Clearly, the effect of near-field radiation becomes increasingly more important if the factor C becomes larger than 10^4.

Figure 5.5 compares the flying height reduction as a function of the magnification factor C. It is apparent that the effect of near-field radiation on flying height reduction is small as long as C < 10^4. On the other hand, the change in flying height becomes substantial (0.9 nm) when C equals 5×10^4. This result agrees well with our previous "order of magnitude" analysis, i.e., the effect of near-field radiation on the flying height change is small but increases as C increases.

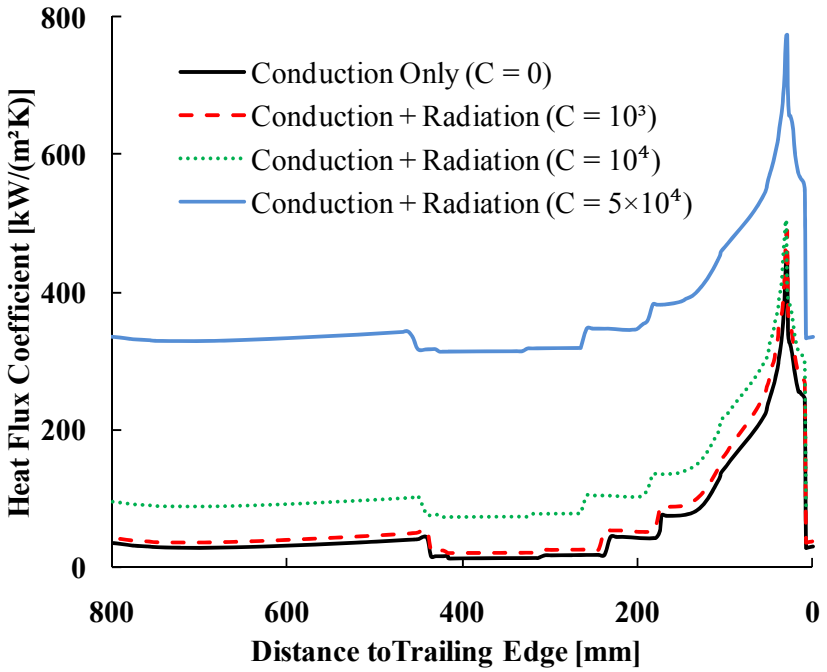

Figure 5.3 Heat flux coefficient along the center line of slider

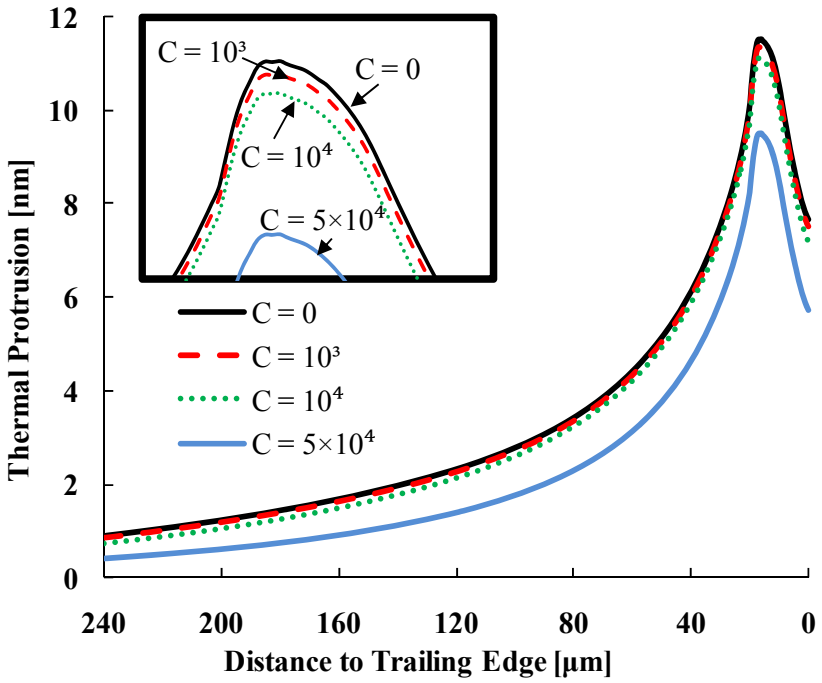

Figure 5.4 Thermal actuation along the center line of slider

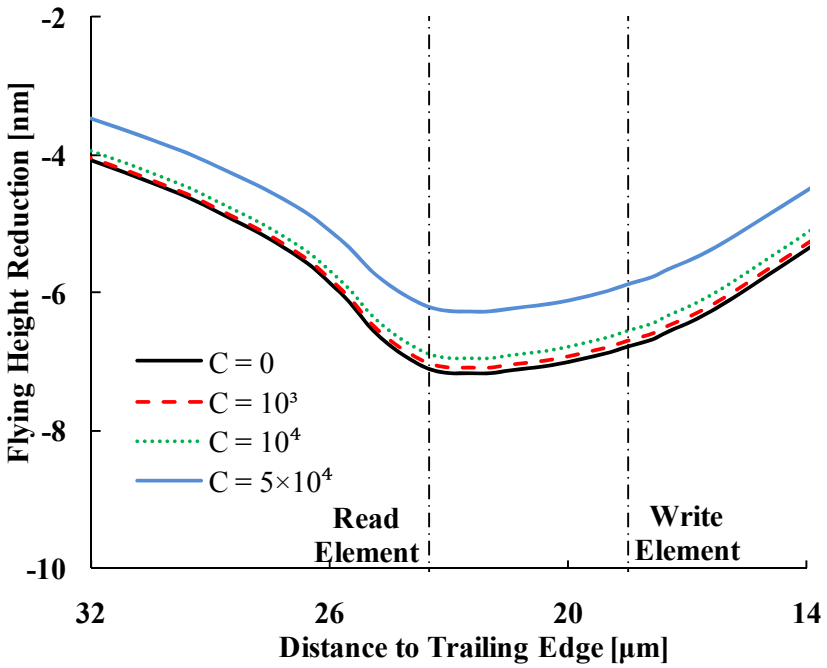

Figure 5.5 Flying height reduction along the center line of slider

5.6 Summary and Conclusions

A scale factor C was introduced to account for the effect of near-field radiation in a small gap. This factor C was assumed to be constant for the whole slider. Numerical results show that the effect of radiation due to near-field effects is small up to values of C = 10^4. However, if the coefficient C is increased to 5×10^4, the effect of radiation becomes important and should be considered. For the head/disk spacing and materials used in current hard disk drives, it is unlikely that such high values of C will be encountered. Thus, we conclude that near-field heat transfer effects are negligible for head/disk interfaces in present use.

5.7 Acknowledgement

Chapter 5, in part, is a reprint of the material as it appears in "The effect of thermal radiation on thermal flying height control sliders," Hao Zheng, Shuyu Zhang, Wentao Yan, Ladislav Pust, David Fowler, and Frank E. Talke, IEEE Transactions on Magnetics, Vol. 46, No. 6, Jun. 2010, pp. 2376 – 2378. The dissertation author was the primary investigator and author of this paper.

Chapter 6

Optimization of Thermal Flying Height Control Sliders with Dual Heater/Insulator Elements

In this chapter, we numerically investigate a thermal flying height control slider design with two separate heaters and two individual insulator elements. The thermo-mechanical simulation described in Chapter 4 is used to study the thermal protrusion and the flying characteristics of a thermal flying height control slider. Simulation results are shown for situations where the write current is ‘‘on’’ and where the write current is ‘‘off’’. The effect of design parameters for a thermal flying height control slider with two heater/insulator elements is studied to optimize the performance of the slider. The goal of the optimization is to achieve low flying height, high thermal actuation efficiency, and reduced dependence of the write current on flying height changes at the read and write elements. Here, thermal actuation efficiency is defined as the ratio of flying height reduction to the maximum thermal protrusion. One of the goals of this study is to maximize this ratio.

6.1 Introduction

In order to achieve areal densities beyond 1.6 Gb/mm² (1 Tb/in²), a stable head/disk interface at an ultra-low magnetic spacing is required for magnetic hard disk drives. Thermal deformation induced by the write current, though on the order of several nanometers, must be taken into consideration in calculating the flying height of a slider. Imamura et al. developed an experimental measurement scheme to evaluate the temperature distribution at the air bearing surface (ABS). They found that a high temperature distribution occurred near the read/write element if a write current was present [137]. Pust et al. developed an isothermal three-dimensional finite element model with detailed write coil geometry in order to simulate the temperature-induced pole-tip protrusion and the write-induced pole-tip protrusion of the slider. The effect of material properties of the photoresist and the design layout of the slider on the thermal stress and the thermal deformation was investigated [138]. Li et al. implemented an unstructured adaptive triangular mesh method and the Voronoi polygon control volume method to numerically study thermal effects caused by Joule heating of the write element. They found that the heat transfer at the head/disk interface plays an important role in the thermal deformation and flying height variation of a slider [139]. Kurita et al. optimized several design parameters, such as the thickness of the base coat and the size of the pole and the shields, to compensate the flying height loss caused by write-induced pole tip protrusion [140]. Song et al. simulated the write-induced pole tip protrusion in both longitudinal magnetic recording and perpendicular magnetic recording. Their simulation results are in good

agreement with their experimental measurements [141][142]. Xu et al. used Laser Doppler Vibrometry (LDV) to perform parametric studies of the dynamic behavior of sliders during contact caused by write-induced pole tip protrusion and disk surfaces with different roughness. One of the results of this study showed that an increase in vibration amplitude was observed when the write channel was engaged [143].

Thermal flying height control sliders are presently in common use in order to compensate thermal effects during reading and writing and to maintain an ultra-low spacing between the head and the magnetic disk [78][144-149]. Boettcher et. al. proposed a computational scheme to optimize the heater input power so that the repeatable flying height variations can be minimized. This scheme is based on the dynamic model of the thermal flying height control heater and convex optimization techniques [201]. In a recent investigation, Hui et al. investigated a typical thermal flying height control heater element in combination with a separate thermal insulator. They observed that the flying height of the read/write element could be further reduced by placing a single thermal insulator element adjacent to the thermal flying height control heater element [150].

In this chapter, the simulation tool described in Chapter 4 is used to investigate the performance of a thermal flying height control slider with two separate heaters and two individual insulator elements. The performance of this so-called “dual TFC slider” is compared with a thermal flying height control slider using a single heater. In addition, the flying characteristics of a thermal flying height control slider with dual heater/insulator element are evaluated for situations where the write current is ‘‘on’’ and where the write current is ‘‘off’’. The design parameters for the dual

heater/insulator elements are optimized to achieve low flying height, high thermal efficiency, and reduced dependence of the write current on flying height variations at the read and write elements.

6.2 Numerical Model

Figure 6.1 (a) shows a schematic of a thermal flying height control slider with dual heater/insulator elements. The heater elements with individual insulators are depicted in Figure 6.1 (b).

Heater 1 with the insulator on the left is located near the read element, while heater 2 with the insulator on the right hand side is located close to the write element. The thermal insulator is used to control the temperature distribution inside the slider. This gives a larger flying height reduction than obtained with a thermal flying height control slider without insulators. The thickness of the insulators of heater 1 and 2 is denoted as T_1 and T_2 respectively. In our numerical simulation, a value of 0.16 μm is used. The distance between heater 1 and heater 2 to the air bearing surface (ABS) is denoted by D_1 and D_2 respectively.

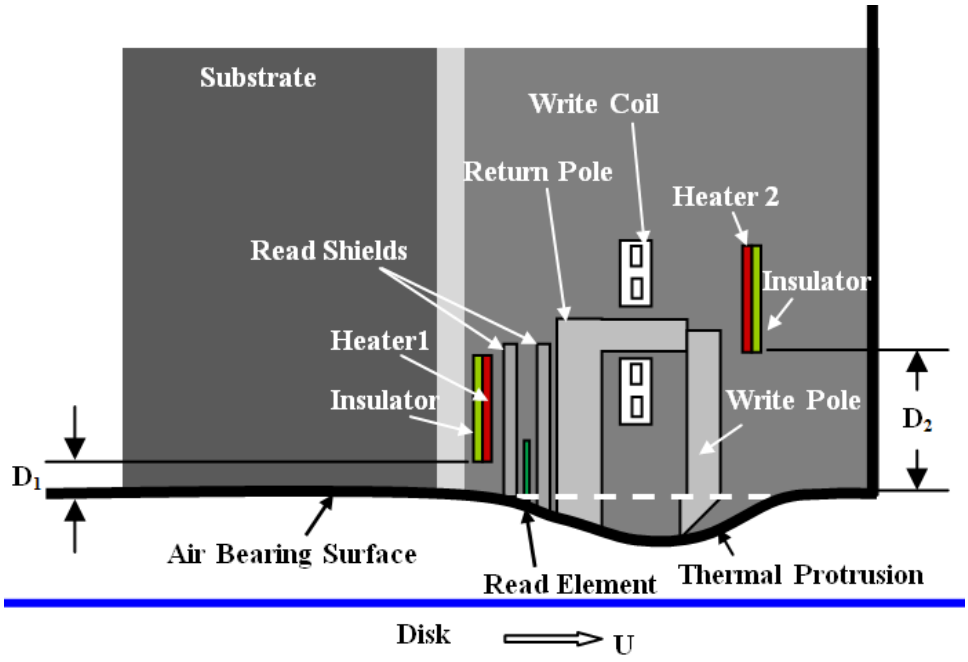

(a)

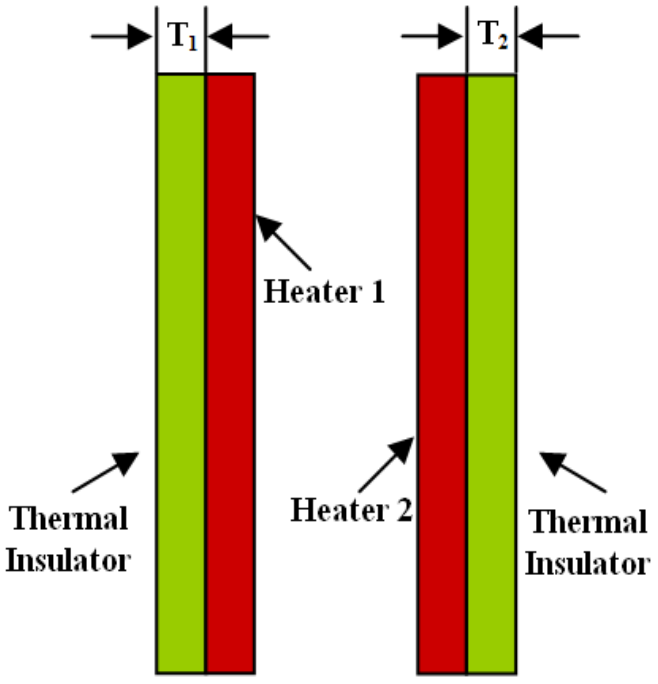

(b)

Figure 6.1 (a) Schematic of the dual TFC slider and (b) blow-up of heaters with thermal insulators

6.3 Comparison between Single Heater and Dual Heaters

A previous investigation by Hui et al. has shown that the implementation of a thermal insulator resulted in a reduced flying height at the read/write element by 20% and 22%, respectively [150].

In this section, two types of thermal flying height control slider designs are investigated. In the first design, a single thermal flying height control heater with one insulator is used. The distance between the heater and the air bearing surface is 17 μm. In the second design, two thermal flying height control heaters and insulators are used, as shown in Figure 6.1. The distance of the heaters to the air bearing surface D_1 and D_2 is chosen to be 12 μm and 23μm, respectively. In the following investigations, a constant heater power P_T is applied to both sliders with a single heater and with dual heaters, i.e.,

$$P_{single} = P_1 + P_2 = P_T$$

where P_{single} is the heater power of the single heater in the first design, while P_1 and P_2 are the power input of heater 1 and heater 2 in the dual TFC design, respectively.

The design of the femto slider used in the simulation is shown in Figure 6.2 (a). The recession depths of each air bearing level are 0 (■), 0.2 (■) and 1.4 μm (■). Figure 6.2 (b) shows the unstructured triangular mesh over the air bearing surface. In our calculations, the mesh size on the trailing pad is 1 μm. The mesh size is 10 μm on the side-pads and 20 μm on the leading pad. The simulated steady-state flying heights

are 10.5 and 9.9 nm at the read and write elements, respectively, in the absence of heat input into the slider.

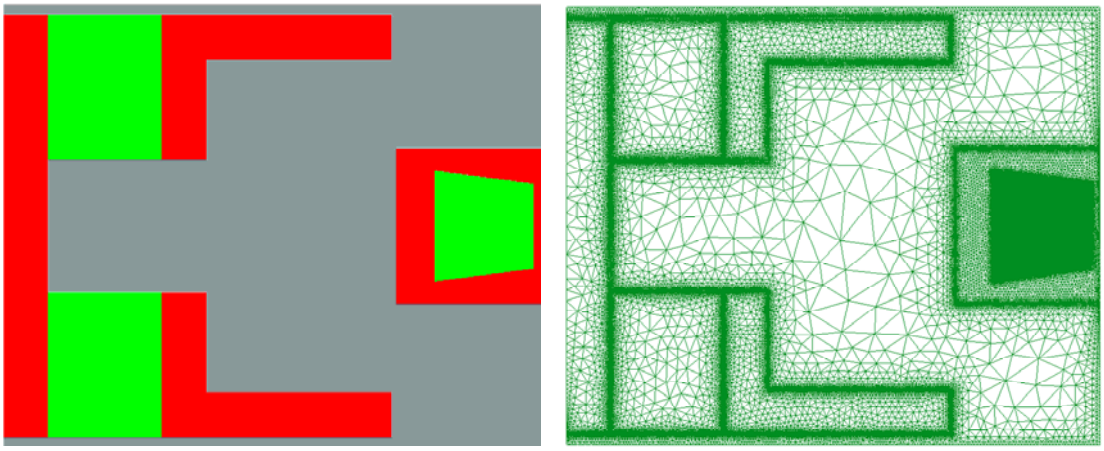

(a) (b)

Figure 6.2 (a) Femto slider design and (b) unstructured triangular mesh on air bearing surface used in simulation

Figure 6.3 compares the thermal protrusion profiles along the center line of both slider designs. A larger thermal protrusion is observed in the dual TFC slider due to the concentration of thermal energy near the read/write element. For the dimensions used in the simulation the peak protrusion occurs near the read/write element and attains values of 9.2 nm and 8.9 nm, respectively, for each model.

Figure 6.4 shows the flying height profiles for the two thermal flying height control slider designs and the original slider without thermal flying height control heater elements. We observe that the design of dual TFC slider exhibits a lower flying height at the read/write element than the single TFC slider.

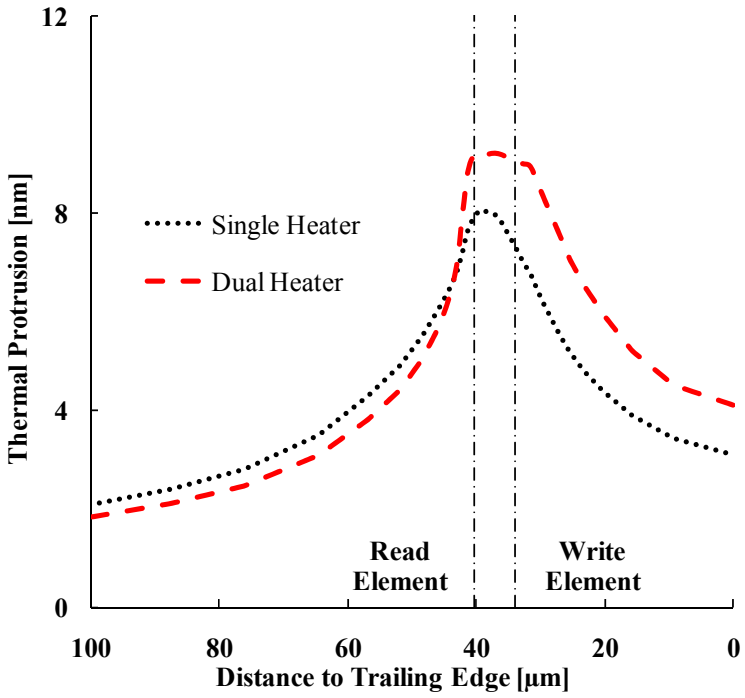

Figure 6.3 Thermal protrusion profiles along the center line of the slider with one and two heater elements, respectively

A summary of flying height (FH) and thermal actuation efficiency (TAE) is given in Table 6.1. Comparing the single TFC slider with the dual heater design, we observe that the dual TFC slider shows an additional flying height reduction of 11% (1.0 nm) and 14% (1.4 nm), at the write and read elements, respectively. In addition, an improvement of approximately 5% and 9% is obtained for the thermal actuation efficiency of the write and read elements, respectively.

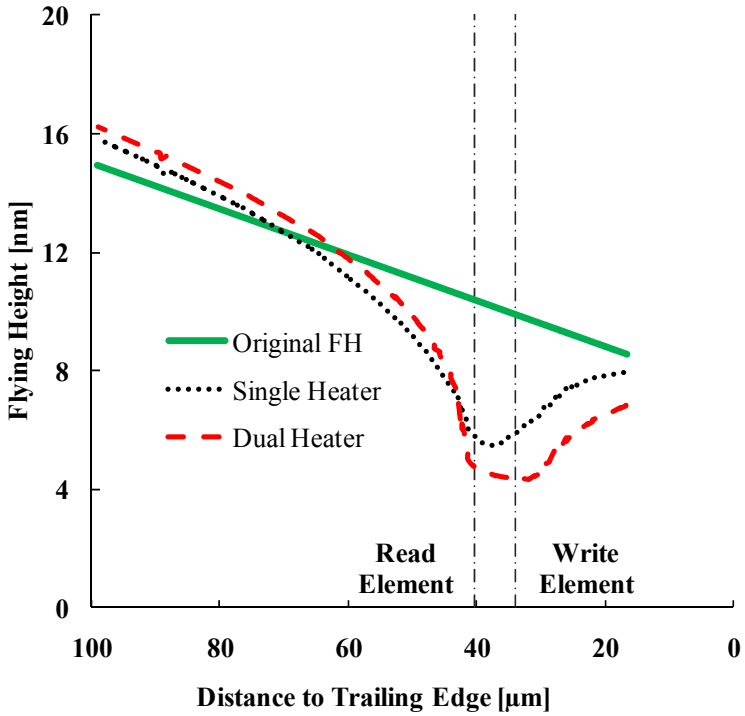

Figure 6.4 Flying height profiles along the center line of the slider with no heater, one and two heater elements, respectively

Table 6.1 Summary of the simulation results for thermal flying height control sliders

Model	Max. Thermal Protrusion [nm]	Flying Height [nm]		Thermal Acutation Efficiency [%]	
		Write Element	Read Element	Write Element	Read Element
No TFC Heater		9.9	10.4		
Single TFC Heater	8.1	5.8	5.8	50.6	56.8
Dual TFC Heaters	9.2	4.8	4.4	55.9	65.4

6.4 Effect of Write Current

Figure 6.5 shows the thermal protrusion profile along the center line of the slider with two thermal flying height control heaters for the cases that (a) only the write current is “on”, (b) the write current is turned “off” but the two heaters are “on” with equal heat input (i.e., $P_1 : P_2 = 1 : 1$, where P_1 and P_2 are the power inputs of

heater 1 and heater 2, respectively), and (c) both the write current and the two heaters are "on". The curve "WE + DH" is displayed in Figure 6.5 by adding the values of thermal protrusions of case (a) and (b). Figure 6.6 shows the corresponding flying height profiles along the center line of the slider for the above four cases. In addition, the "original" flying height profile of a conventional slider without any heat input is shown in Figure 6.6 for comparison.

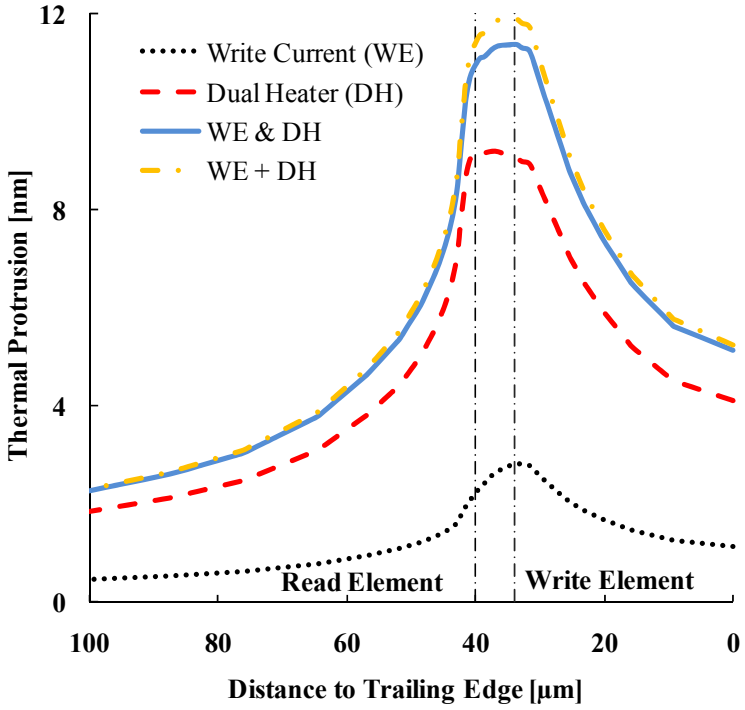

Figure 6.5 Thermal protrusion profile along the center line of slider

We observe from Figure 6.5 that a small thermal protrusion is present if the write current is turned "on" without the heaters. A much larger thermal protrusion is obtained if the heaters are "on" without the write element operating. The thermal protrusion is the largest among the three cases when both the write element and the heaters are turned "on". However, this result ("WE & DH") does not agree exactly

with the mathematical sum of the thermal protrusion profiles of case (a) and (b), which is indicated as “WE + DH”. This is due to the nonlinearity of the air bearing. The maximum difference between the two profiles is 0.5 nm.

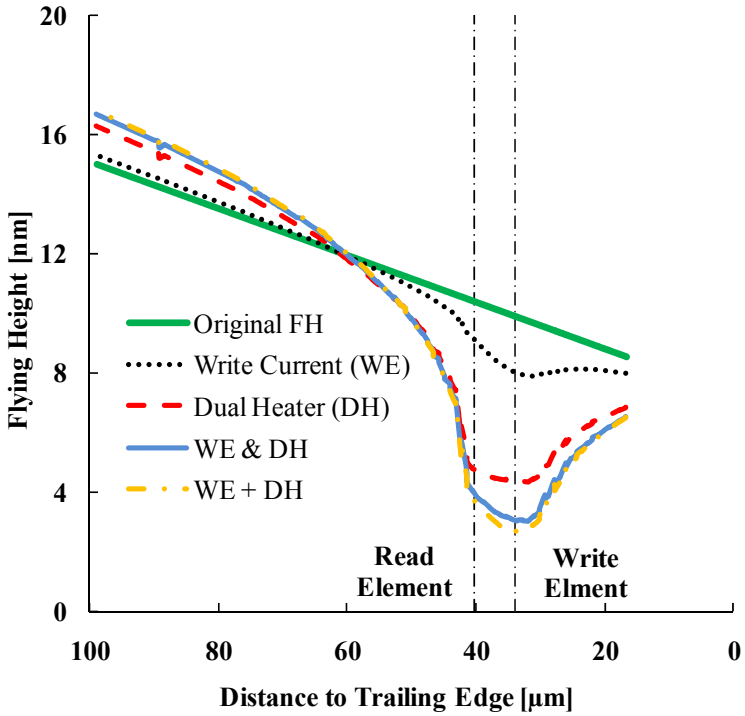

Figure 6.6 Flying height profile along the center line of slider

Figure 6.6 shows that a small decrease in flying height occurs if the write current is turned “on”. A much larger decrease is observed if the dual heater elements are “on”. The largest decrease in flying height is observed for the case that both the heaters and the write element are under operation. This case leads to an additional decrease in flying height of 0.7 nm and 1.3 nm at the read/write element, respectively, compared to the case that only the heaters are turned on. However, the thermal actuation efficiency at the read element reduces from 61%, when both the heater and the write current are “on”, to 56%, when only the two heaters are “on” and the write

current is “off”. It can also be seen from Figure 6.6 that the flying height prediction for the case that both the write current and the heaters are “on” (“WE & DH”) does not equal to the flying height calculated from the air bearing surface with the thermal protrusion profile as the case “WE + DH”. The difference at the read and write elements is 12% (0.4 nm) and 8% (0.2 nm), respectively.

6.5 Effect of Location of Dual Heaters

Figure 6.7 and Figure 6.8 show the thermal protrusion and flying height profiles along the center line of the slider as the distance between heater 1 and the air bearing surface (i.e., D_1) is increased from 12 μm to 28 μm. It can be observed that the change in the thermal protrusion and flying height at the write element is smaller than the change at the read element. This is because heater 1 is located near the read element and therefore the distance between heater 1 and the air bearing surface is more sensitive to the thermal protrusion and flying height reduction at the read element than at the write element.

Figure 6.9 shows the flying height at the read/write element as a function of D_1. We observe that when D_1 increases, the flying height at the read element increases rapidly (from 4 nm to 6.3 nm, when the write current is “on”) while the flying height change at the write element is less than 0.2 nm. A similar trend occurs in the case that the write current is turned “off”. In addition, Figure 6.9 shows that the flying height difference for the write current being “on” or “off” is smaller for the read element than for the write element, i.e., the write current has a smaller effect on the flying height change of the read element than of the write element.

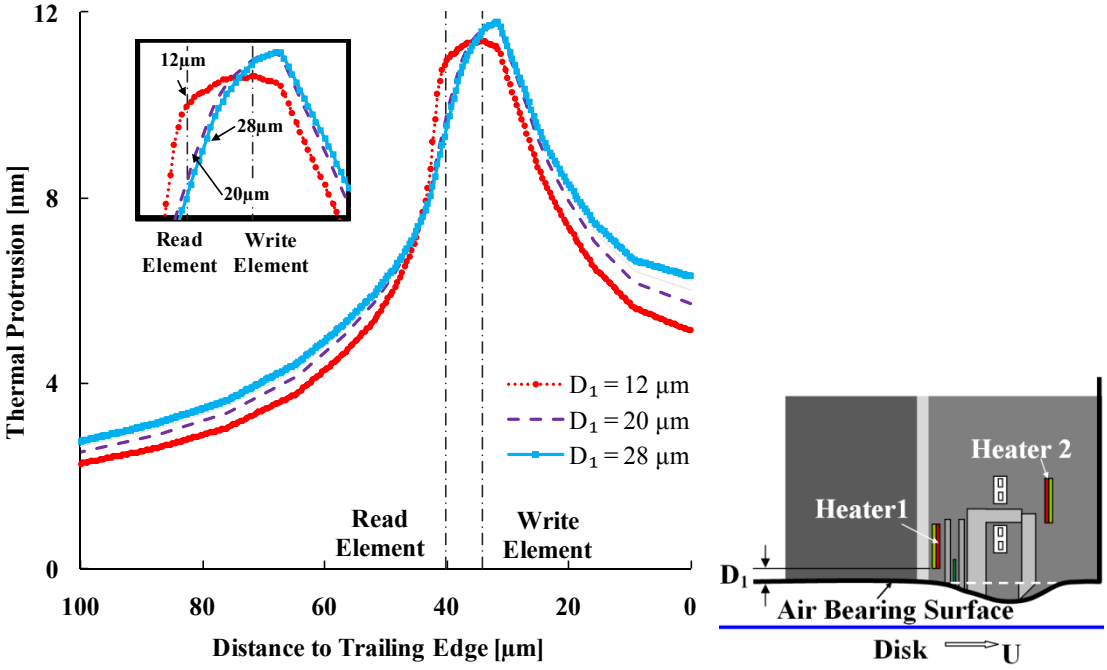

Figure 6.7 Thermal protrusion profile along the center line of slider as a function of the distance between heater 1 and the air bearing surface (D_1)

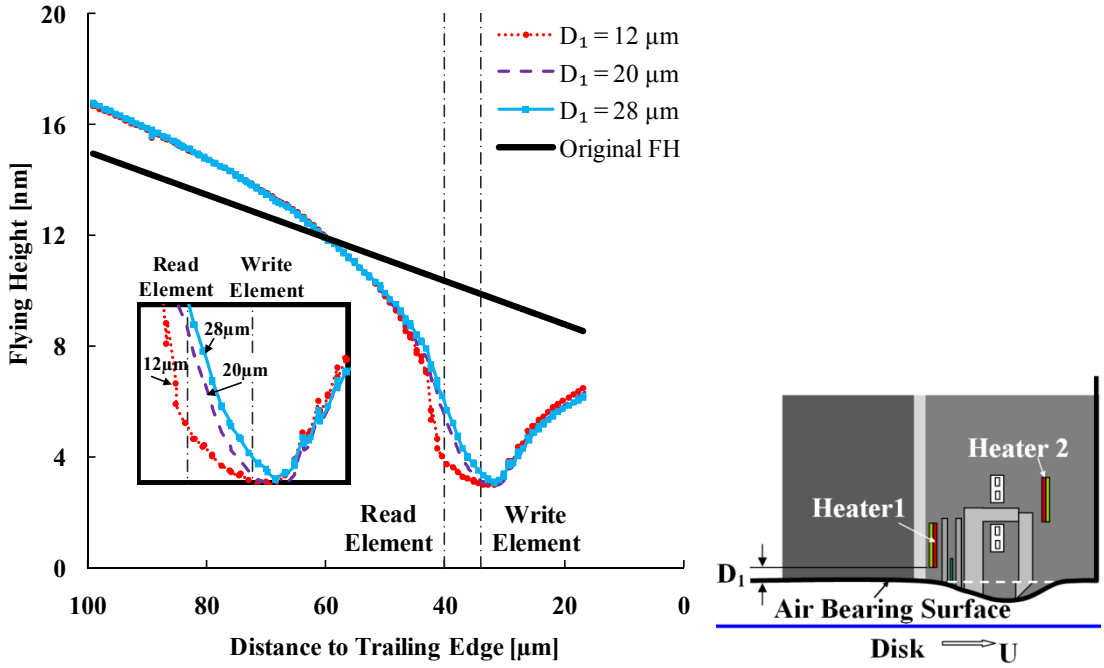

Figure 6.8 Flying height profile along the center line of slider as a function of the distance between Heater 1 and the air bearing surface (D_1)

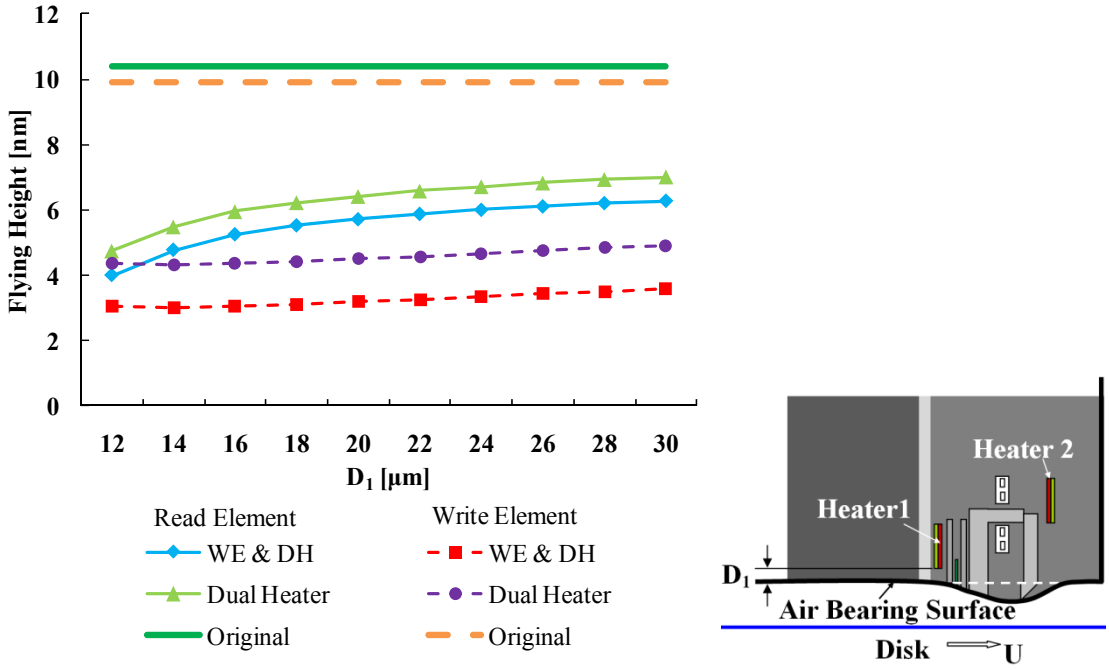

Figure 6.9 Effect of D_1 on flying height at the read and write elements

Thermal actuation efficiency at the read element reduces from 61% to 35% as the distance between heater 1 and air bearing surface increases from 12 μm to 30 μm. The effect of D_1 on the thermal actuation efficiency at the write element is smaller than 7% as shown in Figure 6.10.

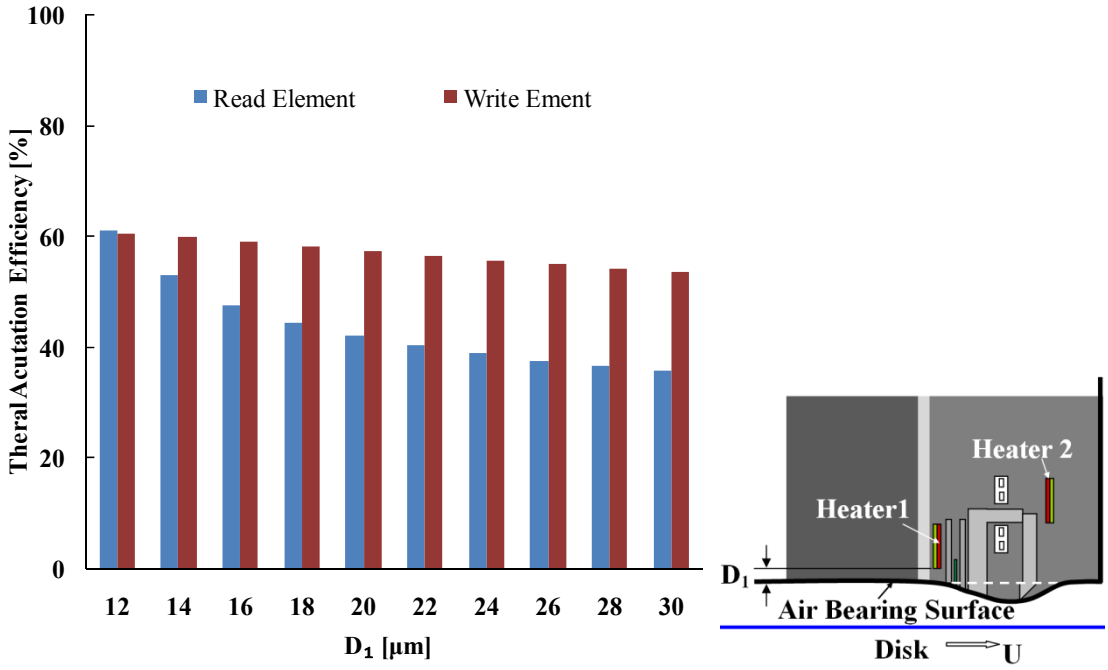

Figure 6.10 Thermal actuation efficiency as a function of the distance between heater 1 and the air bearing surface (D_1)

Figure 6.11 and Figure 6.12 show the flying height and the thermal actuation efficiency at the read and write element as a function of the distance between heater 2 and the air bearing surface (D_2). It can be seen that the flying height reduction and thermal actuation efficiency at both the read and the write element decreases as D_2 decreases. A similar trend for the effect of the write current on the flying height of the read/write element can be observed. In particular, the flying height difference for the case that the write current is “on” and “off” is smaller for the read element than for the write element, i.e., the write current has a smaller effect on the flying height change at the read element than that at the write element.

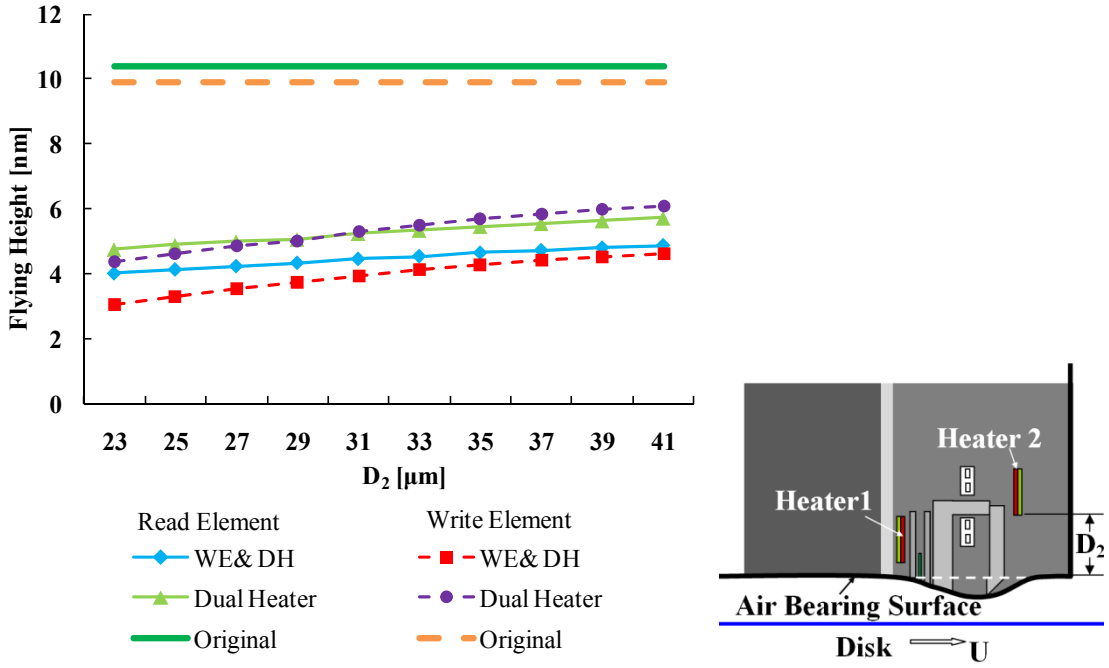

Figure 6.11 Effect of the distance between heater 2 and the air bearing surface (D_2) on flying height at the read and write elements

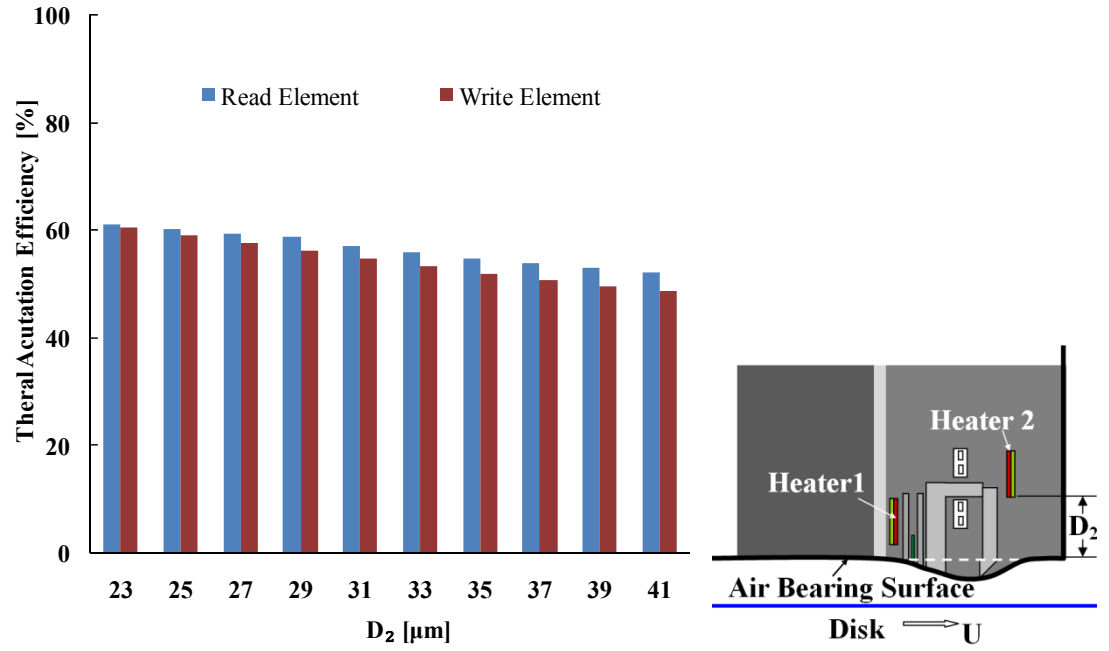

Figure 6.12 Thermal actuation efficiency as a function of the distance between heater 2 and the air bearing surface (D_2)

Figure 6.13 shows the temperature increase ΔT at the read element as heater 1 and heater 2 moving away from the air bearing surface. The results are normalized for the reference case where both dual heaters and write current are "on", and the distance between air bearing surface to heater 1 and heater 2 are 12 μm and 23 μm, respectively. The temperature rise at the read element decreases as the heaters move away from the air bearing surface. In addition, the distance between heater 1 and air bearing surface, i.e., D_1, contributes more to the temperature variation at the read element than D_2.

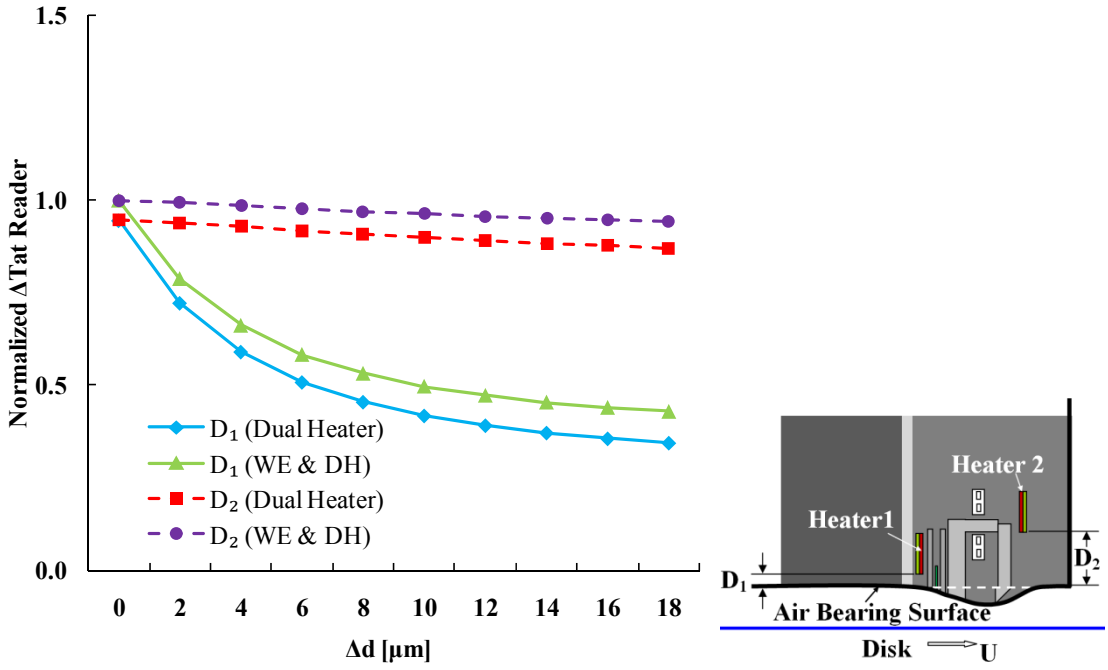

Figure 6.13 Effect of the distance between heater1 and heater 2 to the air bearing surface (Δd) on temperature increase at the read element

6.6 Effect of the Power Ratio of Dual Heaters

Figure 6.14 and Figure 6.15 show the effect of power partitioning between heater 1 and heater 2 in a slider with two thermal flying height control heaters. The

total power input P_T was kept constant. The ratios investigated varied from 1:3 to 3:1. We observe that an increase in the power input of heater 1 (i.e., P_1) leads to an increase of the thermal protrusion at the read element. This causes a decrease in the flying height at the read element. A similar relationship is found between heater 2 and the write element.

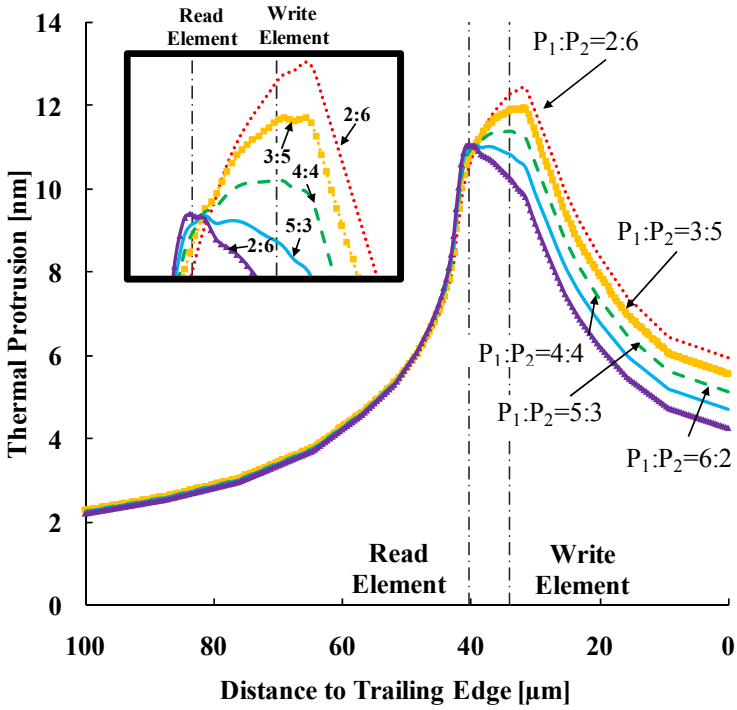

Figure 6.14 Thermal protrusion profile along the center line of slider as a function of power ratio between heater 1 and heater 2

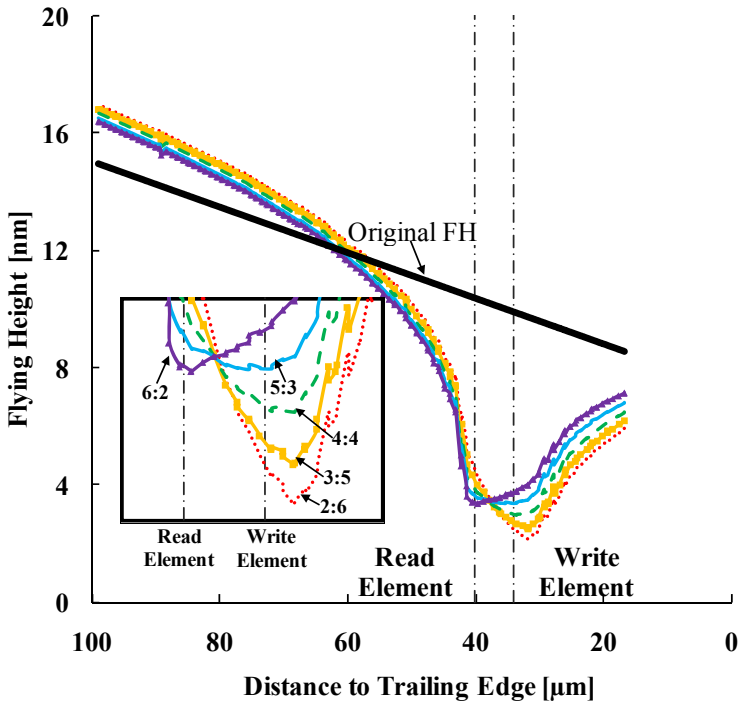

Figure 6.15 Flying height profile along the center line of slider as a function of power ratio between heater 1 and heater 2

Figure 6.16 compares the flying height profiles for different input power to the dual heaters, with the write current being "on" and "off". In particular, Figure 6.17 plots the flying height difference between the read element and the write element as the power ratio of heater 1 increases. It can be observed that for the particular thermal flying height control slider design under consideration (D_1 = 12 μm and D_2 = 23 μm), partitioning of approximately 40% of the heat input for heater 1 achieves a high flying height reduction while keeping the flying height difference at the read element and write element approximately equal to the original air bearing surface design without any protrusion considered. When the write current is "on", however, the power ratio of heater 1 should be increased to 55% to compensate for the effect of the write current.

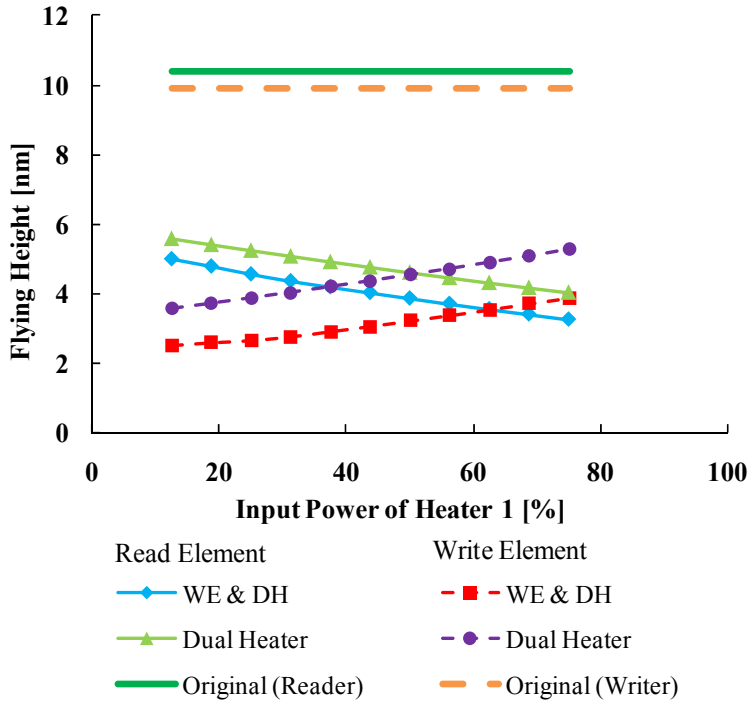

Figure 6.16 Effect of power partitioning on flying height

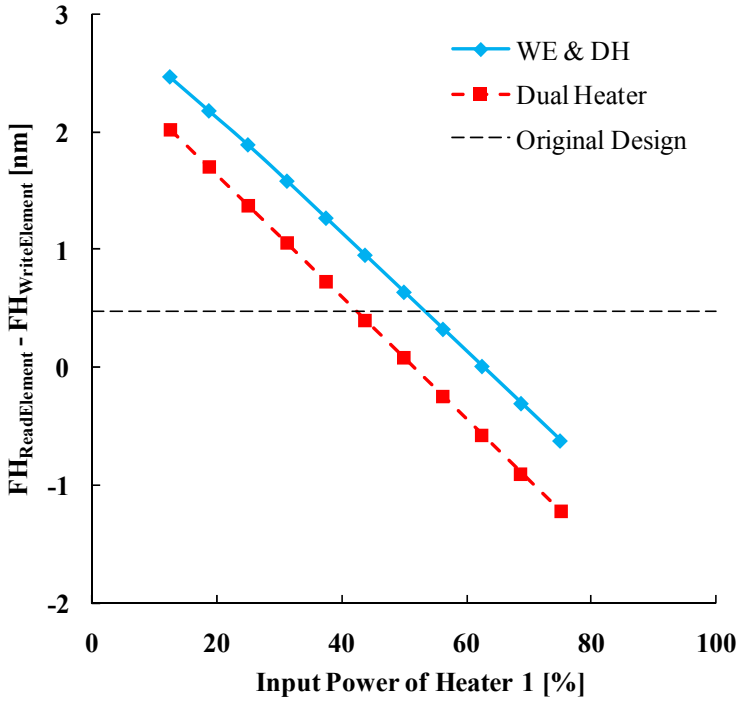

Figure 6.17 Effect of power partitioning on flying height difference between read element and write element

Thus, it is very important to carefully select the input power of the heaters to optimize the flying characteristics of thermal flying height control sliders during drive operations.

6.7 Summary and Conclusions

A thermal flying height control (TFC) slider with two separate heaters and two individual insulator elements was investigated numerically and was compared with a thermal flying height control slider using single heater. It was found that the reduction in flying height at the read/write element of a dual TFC slider was larger than that obtained for single TFC design. In addition, the thermal actuation efficiency was found to be improved.

A write-induced thermal protrusion is observed when the write current is turned “on”. The write current has a smaller effect on the flying height change at the read element than at the write element. In order to reduce the flying height and improve the thermal actuation efficiency of the read/write element, both heater elements of a dual TFC slider must be positioned in close proximity to the air bearing surface. For a given position of heater 1 and heater 2, the power ratio of the heaters must be carefully selected to achieve low flying height, high thermal efficiency, and reduced dependence of the write current on spacing changes at the read/write elements.

6.8 Acknowledgement

Chapter 6, in part, is a reprint of the material as it appears in "Numerical simulation of a thermal flying height control slider with dual heater and insulator elements," Hao Zheng, Hui Li, and Frank E. Talke, IEEE Transactions on Magnetics, Vol. 45, No. 10, Oct. 2009, pp. 3628 – 3631. The dissertation author was the primary investigator and author of this paper.

Chapter 6, in part, is a reprint of the material as it appears in "The effect of write current on thermal flying height control sliders with dual heater/insulator elements," Hao Zheng, Hui Li, Kensuke Amemiya, and Frank E. Talke, Microsystem Technologies, Vol. 17, 2011, pp. 959 – 964. The dissertation author was the primary investigator and author of this paper.

Chapter 7

Numerical Simulation of Thermal Flying Height Control Sliders in Heat-Assisted Magnetic Recording

Heat assisted magnetic recording (HAMR) is one of the most promising techniques to extend the recording density in hard disk drives beyond 1.6 Gb/mm² (1Tb/inch²). Although the diameter of the spot on the disk that is heated by the laser beam is very small, on the order of nanometers, high local temperatures on the disk and the heat dissipated in the slider during the light delivery process can cause thermal deformations of both the disk and the slider, thereby affecting the flying characteristics at the head/disk interface. In this chapter, a finite element model is developed which incorporates a heat assisted magnetic recording optical system into a thermal flying height control (TFC) slider with dual heater/insulator elements to study the effect of heat dissipation in the wave guide on the thermal deformation and flying characteristics of a HAMR-TFC slider. In addition, the power input of the laser and design parameters of the heaters are investigated.

7.1 Introduction

As introduced in previous chapters, thermal flying height control sliders are presently in common use to compensate thermal effects during reading and writing and to maintain ultra-low spacing between the head and the magnetic disk. Investigations in Chapter 6 have shown that the thermal protrusion profile and flying characteristics at the read and write elements can be optimized by incorporating two heaters and adjusting the position and power ratio of the two heaters.

Heat assisted magnetic recording (HAMR) is one of the most promising techniques to extend the recording density in hard disk drives beyond 1.6 Gb/mm² (1Tb/inch²) [83][158][159]. Many investigations have been conducted to better understand heat assisted magnetic recording technology. Challener et al. proposed a near-field transducer (NFT) which achieves a track width of 70 nm [160]. Stipe et al. integrated a plasmonic E-antenna with a heat assisted magnetic recording head to improve the track width and optical efficiency [161]. Wu and Talke numerically investigated lubricant depletion in heat assisted magnetic recording systems due to heating by a moving laser. They observed a strong dependence of the temperature distribution and lubricant depletion of the disk on the thickness and material properties of thin-film heat assisted magnetic recording disks [62]. Peng et al. developed boundary element and finite element models for the analysis of the head/disk interface including thermal, magnetic and mechanical effects. They found that a highly localized heat source on the disk will lead to severe stress concentrations and that the heat distributed at the heat assisted magnetic recording head will cause changes of the

flying height [162]. Li et al. investigated the effect of heating-induced pressure and contour changes on the flying stability of a slider. They observed a strong influence of the laser-writing operations on the protrusion and proposed an optimized slider design to improve flying stability of the slider [163]. Erden et al. modulated the laser power to compensate the spacing variation between the slider and the disk in heat assisted magnetic recording systems [164]. Gauvin et al. investigated the thermal stability and tribological properties of Zdol lubricants modified with benzophenone compounds under laser beam exposure [165].

The local temperature that the magnetic media can reach in heat assisted magnetic recording is likely in excess of 900 K. The heat dissipated in the slider during the light delivery process can cause thermal deformations of the slider which, in turn, can affect the flying characteristics of the slider. Thus, thermal flying height control sliders used in heat assisted magnetic recording systems need to take account of the additional thermal deformation caused by the heat dissipated along the laser delivery path.

In this chapter, a finite element model of a HAMR-TFC slider is developed by incorporating a heat assisted magnetic recording optical structure for the laser light delivery with a thermal flying height control slider featuring dual heater/insulator elements. The design parameters of the dual heaters are optimized to minimize the dependence of the laser induced thermal effects on the spacing variation of the head/disk interface.

7.2 Numerical Model

A schematic model of a typical HAMR-TFC slider and a blow up image of a heat assisted magnetic recording optical path are shown in Figure 7.1 (a) and Figure 7.1 (b). The HAMR-TFC slider consists of a regular dual TFC slider as described in Chapter 6 and an additional heat assisted magnetic recording optical system based on the design proposed by Challener et al. [160]. The incident laser light is coupled into the parabolic wave guide and the near-field transducer (NFT) to heat the media and reduce the coercivity of the media for writing. The wave guide is a three-layered structure, including a planar solid immersion mirror (PSIM) core layer and top and bottom "cladding" layers. The distance between heater 1 and heater 2 to the air bearing surface (ABS) is denoted by D_1 and D_2, respectively. The total power of the dual heaters is denoted as P_H, while the power input for heater 1 and heater 2 is denoted as P_{H1} and P_{H2}, respectively. The dissipated energy in the wave guide is P_{WG}.

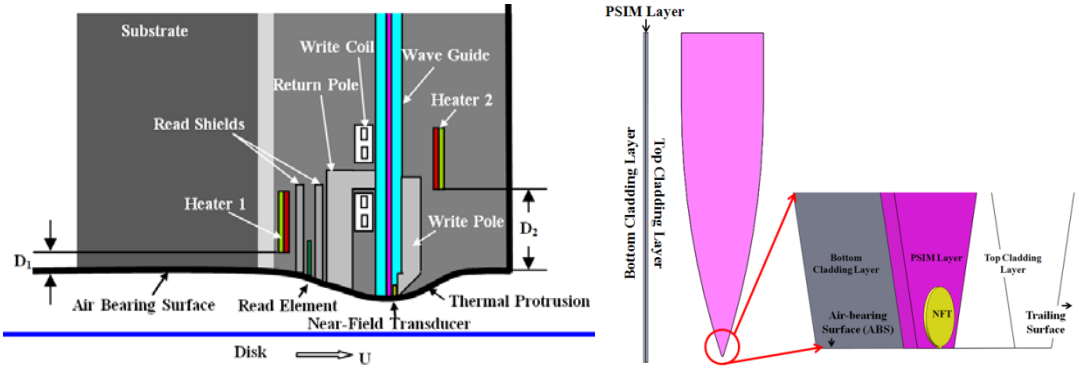

(a) (b)

Figure 7.1 (a) Schematic of HAMR-TFC slider and (b) Diagram of heat assisted magnetic recording optical system, including near-field transducer (NFT) and wave guide

An iterative solution is required to obtain the flying height change of a HAMR-TFC slider as a function of the thermal protrusion. A detailed description of the simulation procedure was present in Chapter 4.

7.3 Simulation Results

7.3.1 Comparison between Dissipated Heat in the Wave Guide and Heat Input of the Heaters

Figure 7.2 shows the thermal deformation near the read/write element for the cases of (a) 32 mW heat power input to the dual heaters ($P_{H1} = P_{H2} = 16$ mW) and (b) 32 mW heat dissipation in the wave guide [163]. The corresponding thermal protrusion profiles along the center line of the slider are shown in Figure 7.3. We observe from Figures 7.2 and Figure 7.3 that the thermal deformation due to the heat dissipation of the optical system is of similar magnitude as the thermal deformation due to the heaters. In particular, we note that the thermal deformation due to the dissipated heat in the wave guide has a smaller radius at the read/write element than the thermal deformation due to an equal power input to the heaters. A protrusion with small radius seems undesirable from a tribological point of view with respect to wear during slider/disk contacts. In addition, the thermal deformation induced by the dissipated power in the wave guide causes a deformation at the trailing edge of the slider approximately 7 nm larger than that due to the power input into the heaters. Thus, the flying characteristics of a HAMR-TFC slider are likely to be influenced by the power dissipation in the light delivery system.

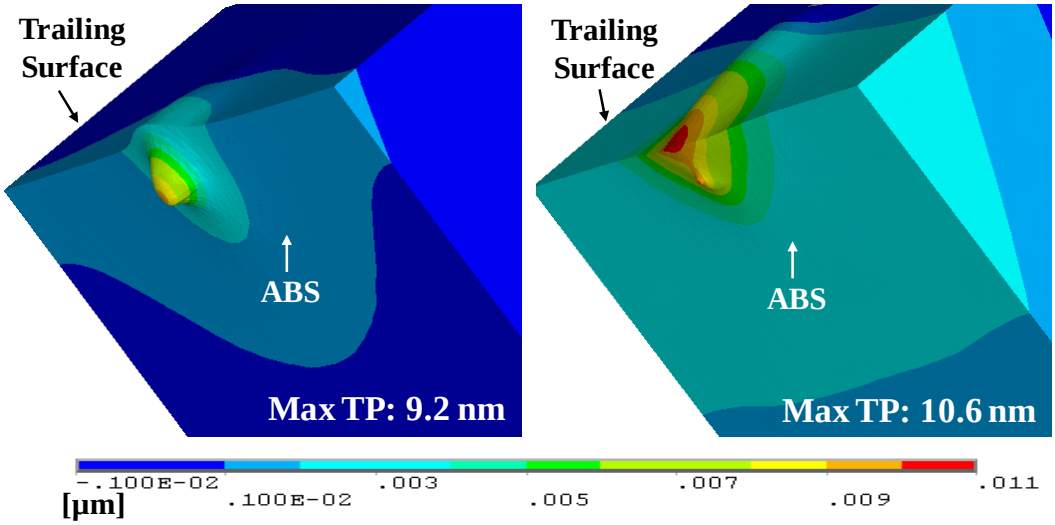

(a) (b)

Figure 7.2 Thermal protrusion near the read and write elements for cases of (a) Dual Heaters: 32 mW power input to the dual heaters and (b) Wave Guide: 32 mW residual heat dissipation in the wave guide

For typical heat assisted magnetic recording optical systems under current investigations, the dissipated heat along the laser delivery path is likely to be on the order of 20 ~ 50 mW [162][163][166]. Thus, the additional thermal deformation due to the heat dissipation in the wave guide is of great importance and must be considered in the design of HAMR-TFC heads. The effect of dissipated heat on the thermal protrusion and flying characteristics of a typical HAMR-TFC slider will be described in the next section.

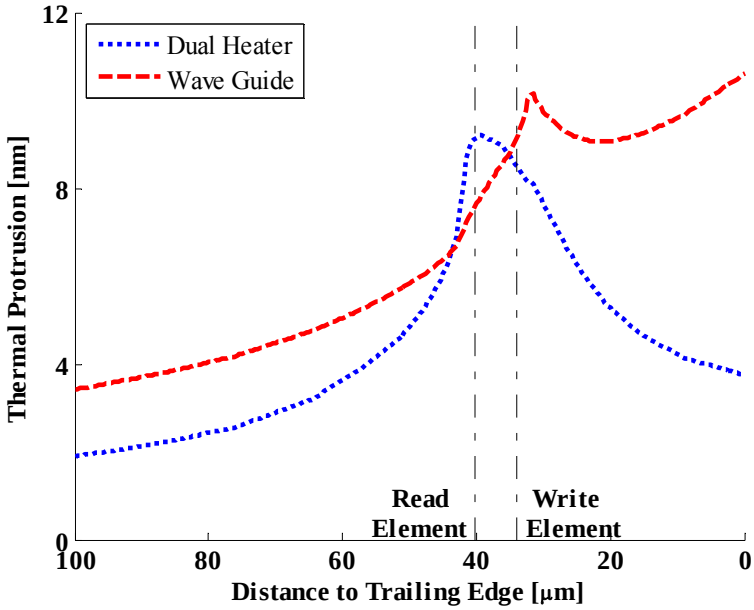

Figure 7.3 Thermal protrusion profile along the center line of slider

The pressure distribution at the air bearing surface (ABS) for the two cases studied in Figure 7.3 is shown in Figure 7.4. In addition, the original pressure distribution at the air bearing surface of the slider without heat input is shown for comparison. We observe from Figure 7.4 that the maximum pressure occurs at the trailing edge of the trailing pad in the absence of heat input to the slider ("Original"). If the heaters are energized, the maximum pressure increases and the pressure peak shifts towards the read/write element ("Dual Heater"). If an equal amount of heat is dissipated in the wave guide, a high pressure region appears at both the read/write element and the trailing edge of the trailing pad ("Wave Guide").

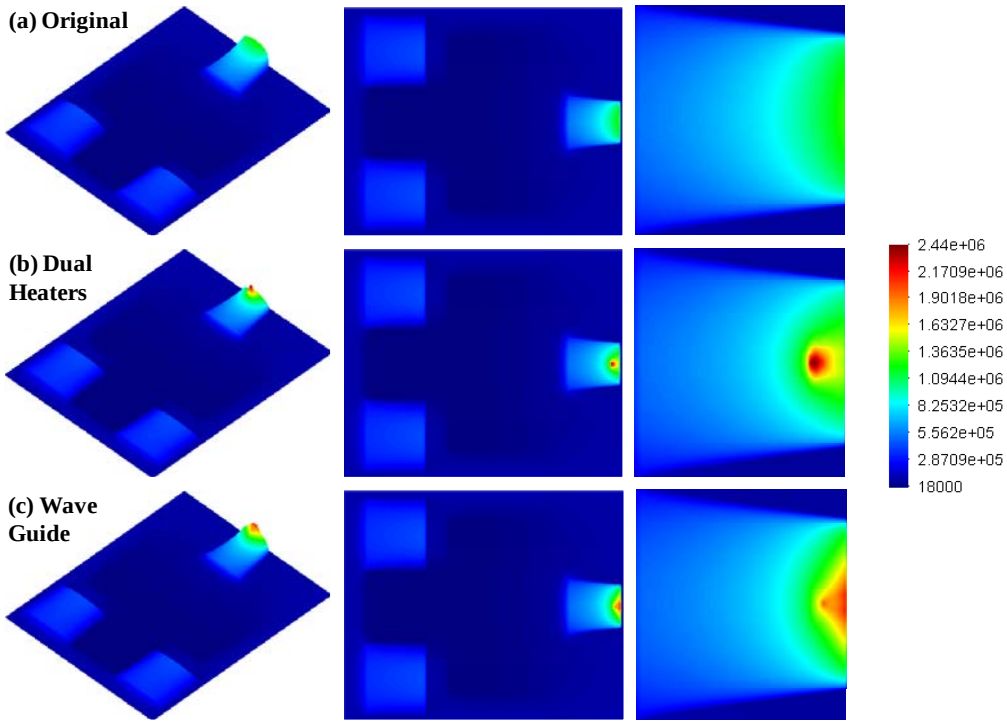

Figure 7.4 Pressure distribution at the air bearing surface for cases of (a) Original: slider without heat dissipation or heater activation (b) Dual Heaters: 32 mW power input to the dual heaters and (c) Wave Guide: 32 mW residual heat dissipation in the wave guide

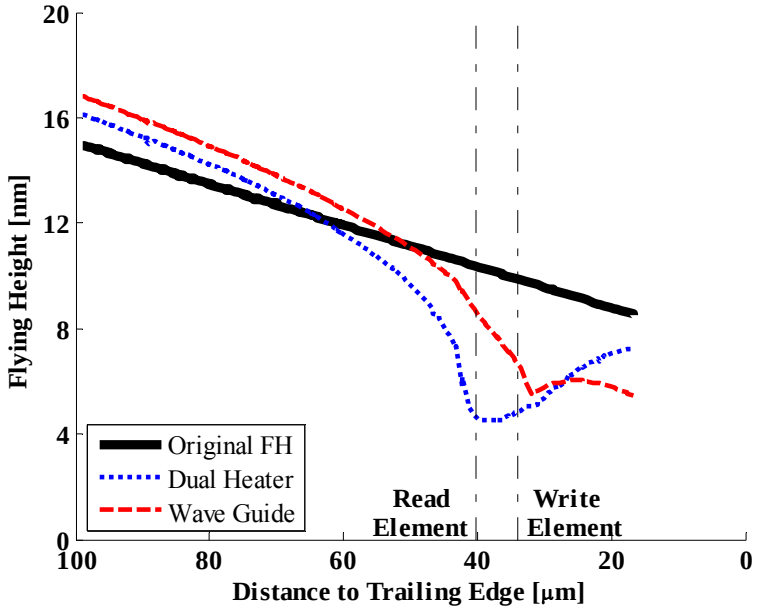

Figure 7.5 Flying height profile along the center line of slider

Figure 7.5 shows the flying height profiles along the center line of a HAMR-TFC slider for the three cases of (a) no heat input ("Original"), (b) "Dual Heaters" and (c) "Wave Guide". It can be seen that the dissipated heat in the wave guide has less effect on the flying height reduction at the read/write element than the power input to the heaters. However, the flying height difference between the read and write elements ($FH_{ReadElement} - FH_{WriteElement}$) is strongly affected by the dissipated energy in the wave guide. The flying height difference between the read and write elements is 2 nm for the case of the "Wave Guide", i.e., a value four times that of the original design (0.5 nm). In addition, it can be seen from Figure 7.5 that the minimum flying height occurs near the read and write elements (x = 37.067 μm) when the two heaters are operating ("Dual Heater"), while the minimum flying height is located at the trailing edge of the trailing pad (x = 16.731 μm) in the case of the "Wave Guide". Since the read/write elements should be as close as possible to the magnetic media, the flying height reduction at the trailing edge in the case of the "Wave Guide" will degrade the flying performance of the slider at the read/write element and may lead to contact between the slider and disk.

7.3.2 Effect of Dissipated Power in the Wave Guide

Increasing the efficiency of a heat assisted magnetic recording head is one of the most important considerations in the optimization of a heat assisted magnetic recording optical system. A reduction in the amount of dissipated energy in the wave guide is expected for future designs of the optical systems. Figure 7.6 and Figure 7.7 show the thermal protrusion and the flying height profiles along the center line of the

slider as a function of the dissipated energy in the wave guide for dissipated heat P_{WG} of 32 mW, 16 mW and 8 mW, respectively. We observe that the thermal deformation decreases as the dissipated energy in the wave guide decreases. The effect of dissipated energy in the wave guide on the flying height is greater at the write element than at the read element. As the heat dissipation decreases, the flying height difference between the read and write elements decreases from 2.0 nm to 0.9 nm. This is because the write element is positioned very close to the heat source. Therefore the write element is very sensitive to the heat dissipated in the wave guide.

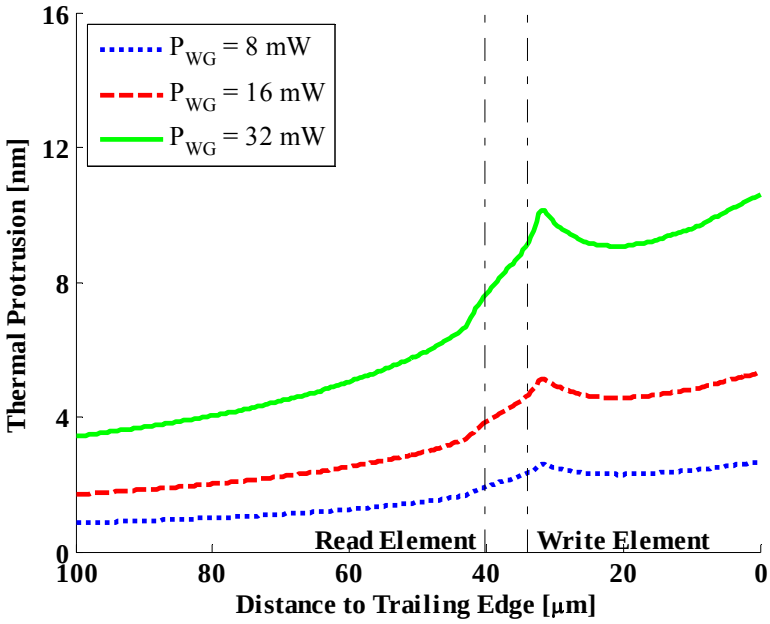

Figure 7.6 Thermal Protrusion profile along the center line of slider as a function of dissipated energy at the wave guide

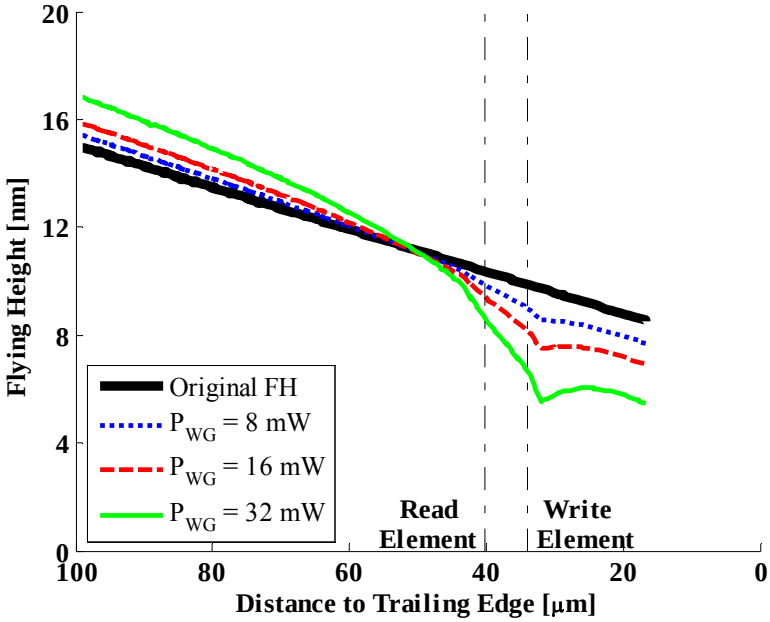

Figure 7.7 Flying height profile along the center line of slider as a function of dissipated energy in the wave guide

7.3.3 Effect of Power Input of the Heaters

Figure 7.8 shows the thermal protrusion profiles along the center line of the slider as a function of increasing the total power input of the dual heater P_H. The heat dissipation in the wave guide is assumed to be constant at 8 mW. We observe that the thermal protrusion increases with an increase of the heater power and becomes much larger than the thermal protrusion due to the heat dissipated in the wave guide. Figure 7.9 shows the corresponding flying height profiles for an increase in P_H. We observe that the minimum flying height moves from the trailing edge of the trailing pad (x = 16.731 μm) to the read/write elements (x = 37.067 μm) and that the flying height difference between the read and write elements decreases when the power input of the thermal flying height control heater increases. This indicates that the degradation of

flying characteristics at the read/write element caused by the dissipated energy in the wave guide can be compensated by the thermal flying height control heaters.

In Figures 7.10 to Figure 7.12, the effect of the power ratio between the two heaters on the flying performance of HAMR-TFC slider is investigated, keeping the total power input constant ($P_H = P_{H1} + P_{H2} = 32$ mW , $P_{WG} = 8$ mW). The power ratio of heater 1 to heater 2 ($P_{H1} : P_{H2}$) varies from 1:3 to 1:1 to 3:1. In addition, the two limiting cases with only one heater operating are shown, indicated as "Heater 1 Only" and "Heater 2 Only". The case of heat dissipation in the wave guide only, without activation of the thermal flying height control heaters ($P_H = 0$ mW , $P_{WG} = 8$ mW), is shown for comparison. This case is denoted as "Wave Guide Only". The flying height profiles at the read/write element are compared in Figure 7.12.

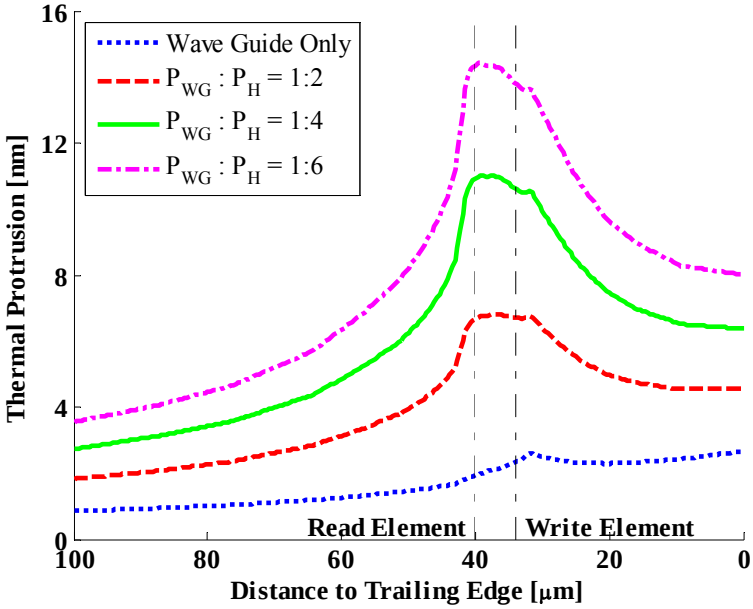

Figure 7.8 Thermal protrusion profile along the center line of slider as a function of increasing heater power

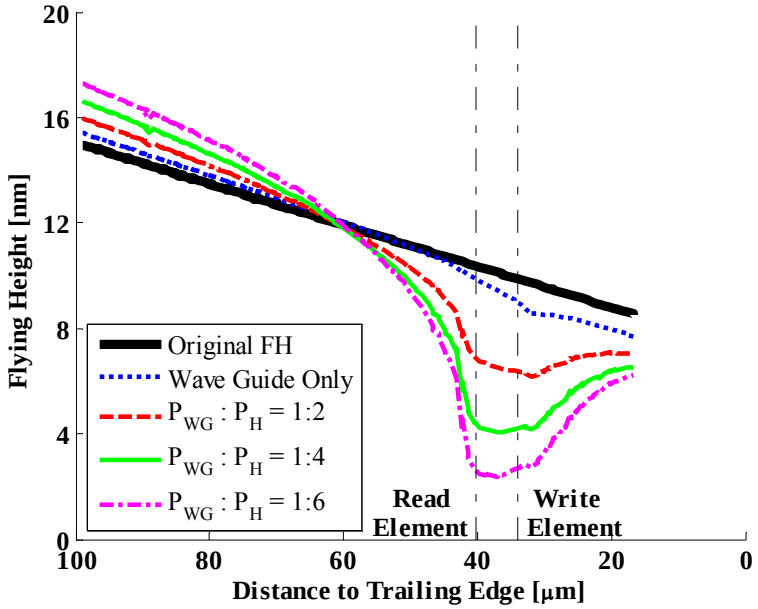

Figure 7.9 Flying height profile along the center line of slider as a function of increasing heater power

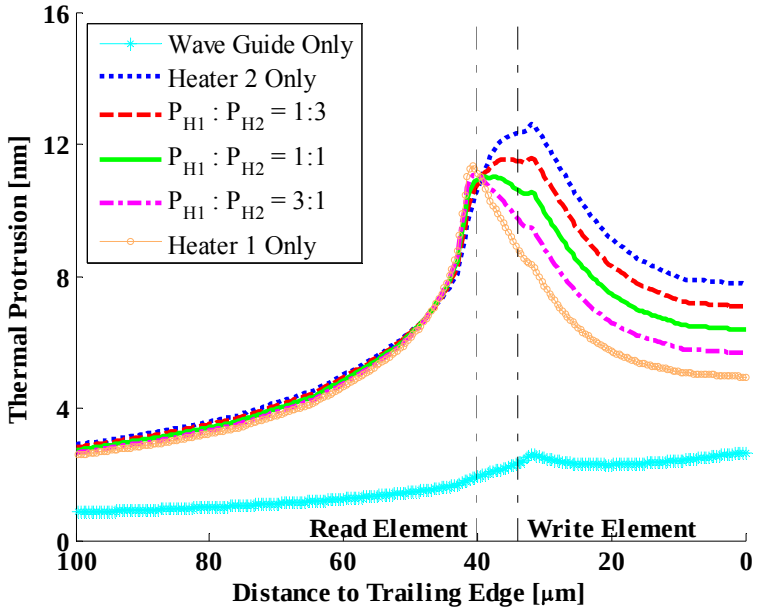

Figure 7.10 Thermal protrusion profile along the center line of slider as a function of the power ratio of heater 1 to heater 2, with P_{WG} = 8 mW

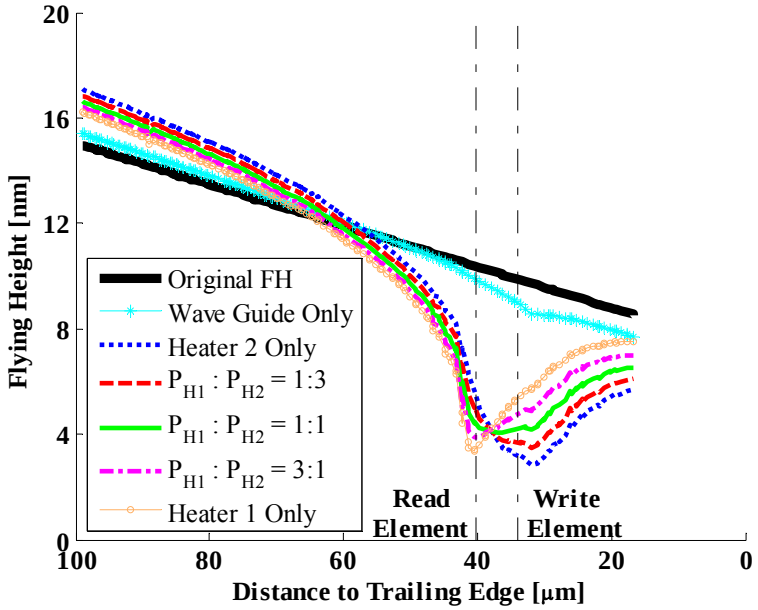

Figure 7.11 Flying height profile along the center line of slider as a function of the power ratio of heater 1 to heater 2, with P_{WG} = 8 mW

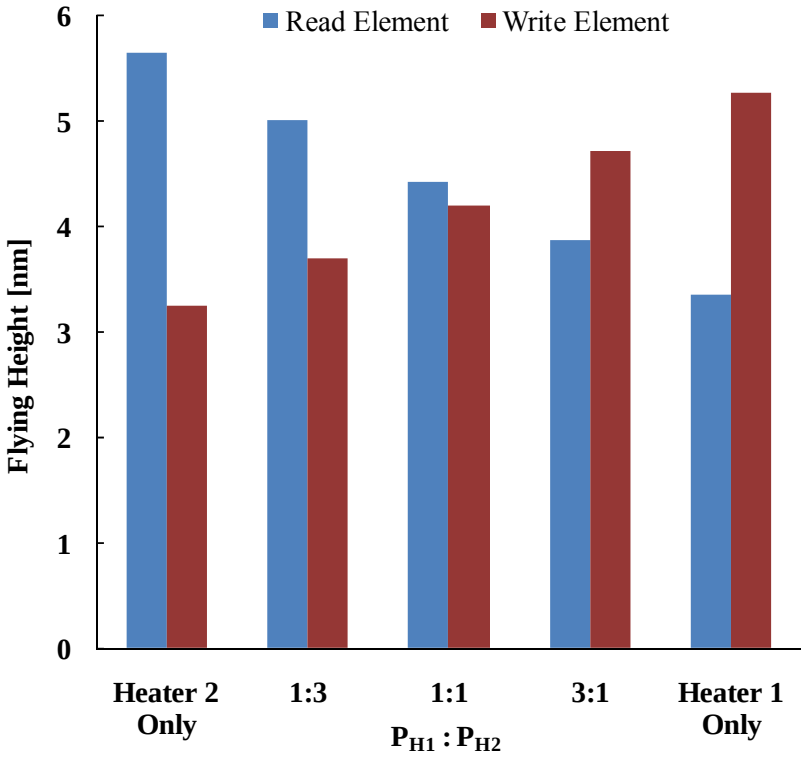

Figure 7.12 Flying height at the read and write elements

We observe that an increase of the power ratio of heater 1 to heater 2 reduces the effect of dissipated heat in the wave guide; however, this leads to a reduction in the thermal protrusion at the write element from 12.3 nm to 8.9 nm, and correspondingly, an increase in flying height from 3.2 nm to 5.3 nm. The thermal actuation efficiency (TAE), which is defined as the flying height reduction to the maximum thermal protrusion, is shown in Figure 7.13. As the heat input of heater 1 increases, the thermal actuation efficiency at the read element increases (from 38% to 62%) while a decrease of thermal actuation efficiency from 41% to 53% occurs at the write element due to the position of the heaters. Thus, we conclude that for the position of heaters 1 and 2 in our study, a variation of the power ratio from 3:1 to 1:1 can compensate the effect of dissipated heat in the wave guide while keeping a low flying height and high thermal actuation efficiency at the read and write elements. Clearly, the power ratio of the heaters is important to achieve optimal thermal flying height control slider performance.

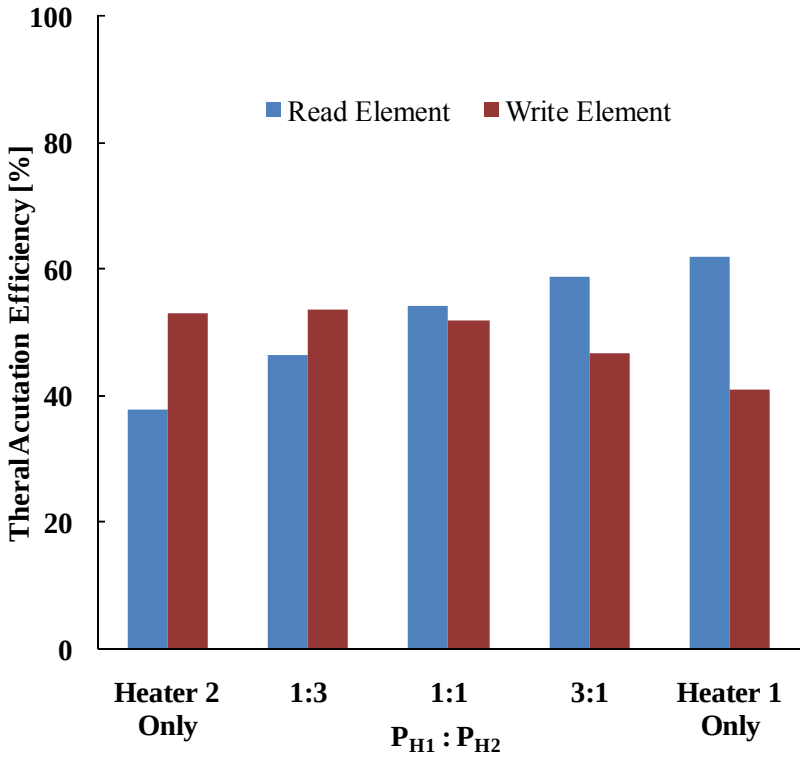

Figure 7.13 Thermal actuation efficiency at the read and write elements

7.3.4 Effect of Distance between the Heaters and the Air Bearing Surface

Investigations in Chapter 6 have shown that an increase in the distance between the heaters and the air bearing surface (ABS) reduces the effect of the heaters on the thermal protrusion and flying height. The thermal protrusion and flying height profiles along the center line of the slider are shown in Figure 7.14 and Figure 7.15, respectively, as a function of increasing distance between heater 1 and the air bearing surface, i.e., D_1 (from 12 μm to 24 μm). Again, the dissipated heat in the wave guide is assumed to be 8 mW. The thermal protrusion caused by the power input to the

heaters increases as heater 1 is positioned closer to the air bearing surface. The minimum flying height moves towards the read element (from x = 31.874 μm to x = 37.067 μm) with decreasing D_1. The change in the thermal protrusion and flying height at the write element (0.3 nm) is smaller than the change at the read element (2 nm). This is because heater 1 is located near the read element, i.e., heater 1 is more effective in changing the thermal protrusion and flying height at the read element than at the write element. Thermal actuation efficiency at the read element increases from 36% to 54% as the distance between thermal flying height control heater 1 and the air bearing surface decreases from 24 μm to 12 μm. The change of the thermal actuation efficiency at the write element is less than 4% as shown in Figure 7.16.

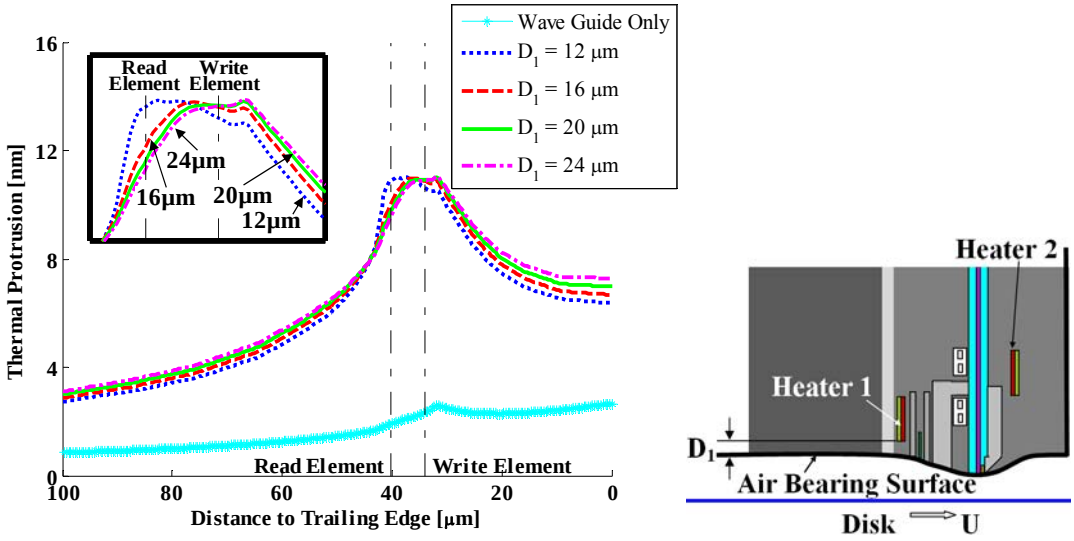

Figure 7.14 Thermal protrusion profile along the center line of slider as a function of increasing distance between heater 1 and air bearing surface (D_1)

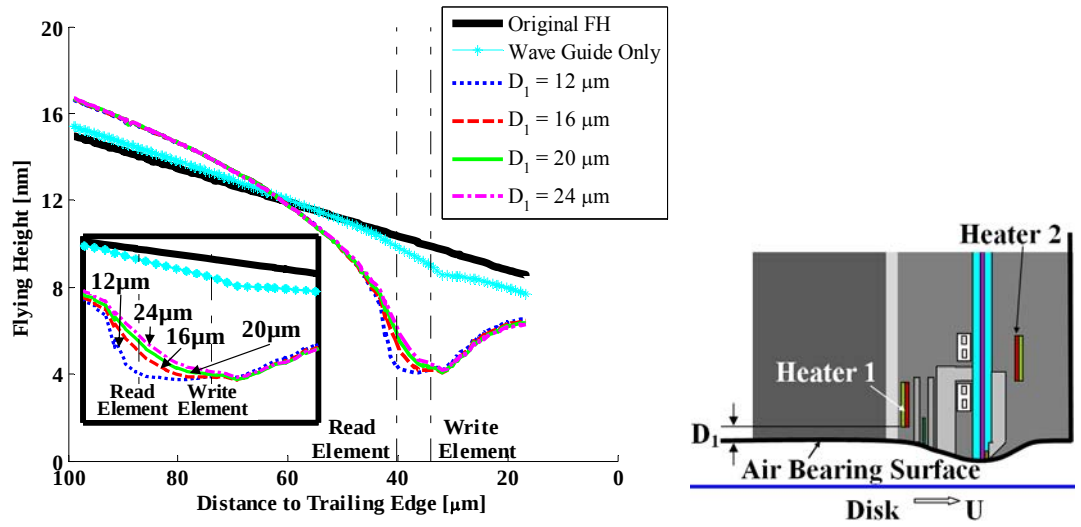

Figure 7.15 Flying height profile along the center line of slider as a function of increasing distance between heater 1 and air bearing surface (D_1)

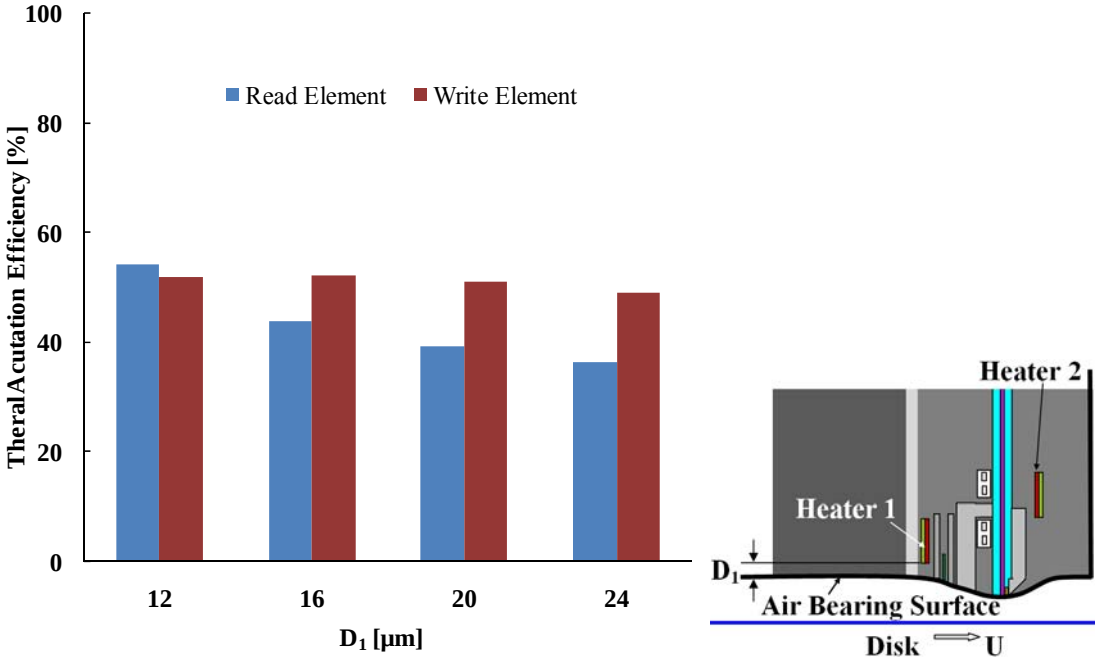

Figure 7.16 Thermal actuation efficiency at the read/write elements

Figure 7.17 and Figure 7.18 show the thermal protrusion and flying height profiles as a function of distance between heater 2 to the air bearing surface, i.e., D_2 .

Again, the heat dissipated in the wave guide is assumed to be 8 mW and is shown for comparison. We observe that the thermal protrusion induced by the power input to the heaters becomes larger than that caused by the dissipated energy in the wave guide and that the undesired flying height reduction occurred at the heat assisted magnetic recording optical system due to the heat dissipation in the wave guide is reduced if heater 2 is moved away from the air bearing surface. This leads to a low thermal flying height efficiency at both the read and write elements, as shown in Figure 7.19. Clearly, this is because thermal flying height control heater 2 is located near the wave guide and increases the effect of the wave guide. The effect increases further if heater 2 is positioned closer to the air bearing surface. Thus, a tradeoff exists between the effect of dissipated heat in the wave guide and thermal actuation efficiency of a HAMR-TFC slider as a function of D_2 .

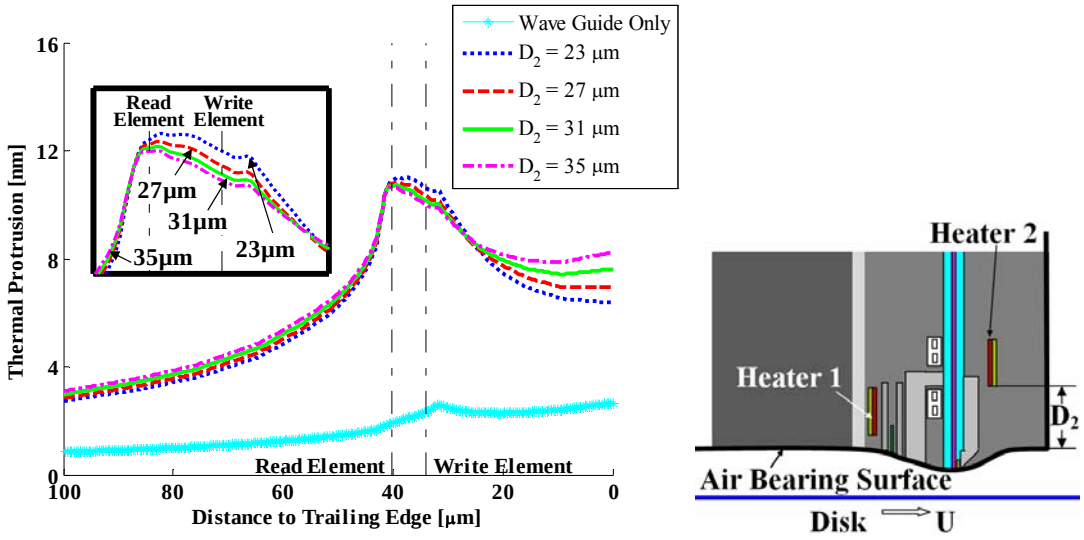

Figure 7.17 Thermal protrusion profile along the center line of slider as a function of increasing distance between heater 2 and air bearing surface (D_2)

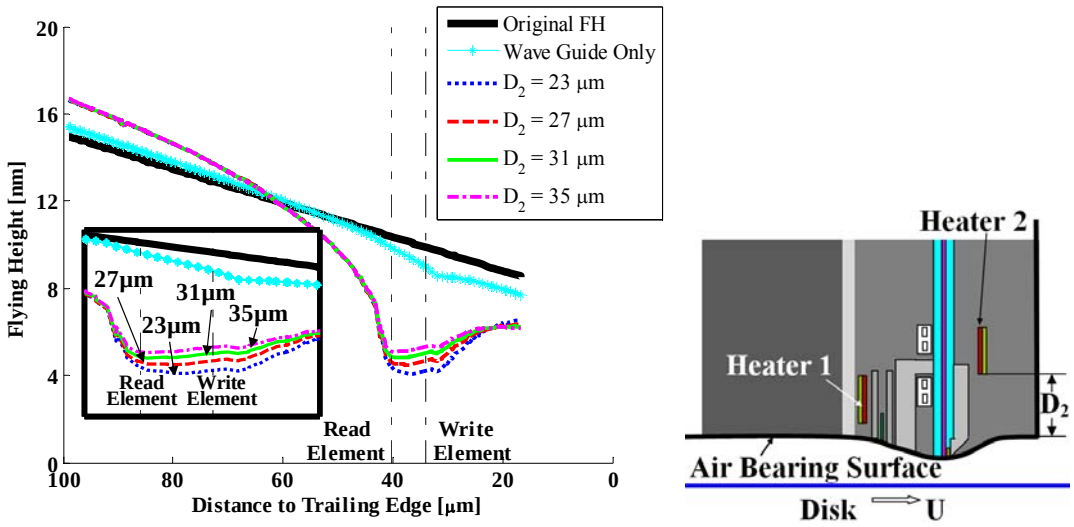

Figure 7.18 Flying height profile along the center line of slider as a function of increasing distance between heater 2 and air bearing surface (D_2)

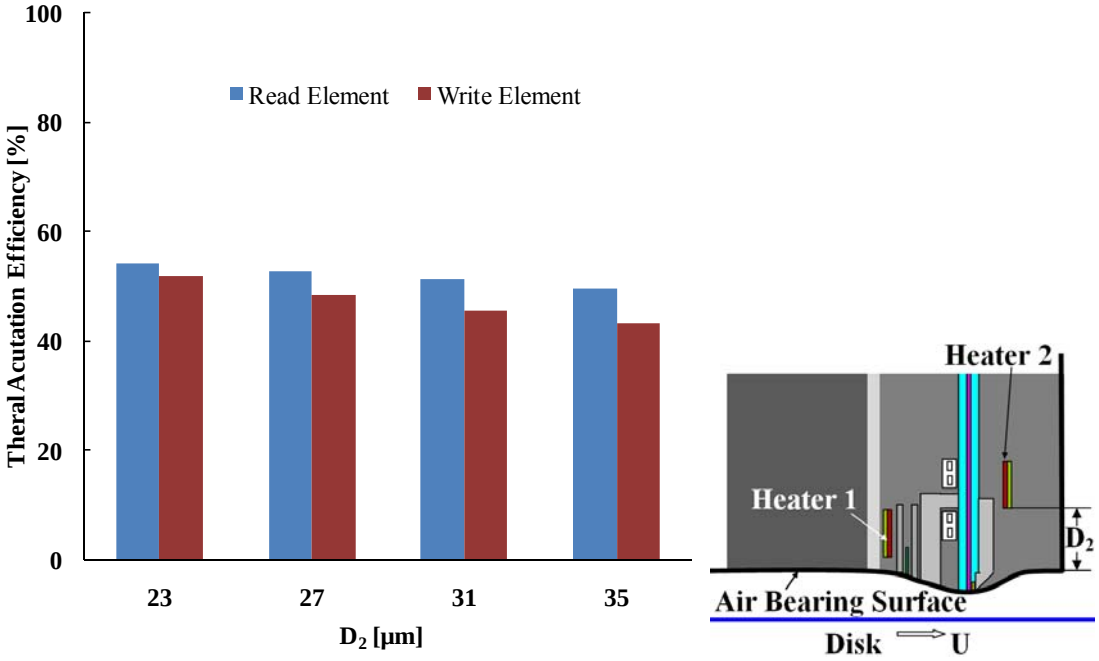

Figure 7.19 Thermal actuation efficiency at the read/write elements

7.4 Summary and Conclusions

A finite element model of a thermal flying height control slider with two heaters and a heat assisted magnetic recording optical system was developed to investigate the effect of dissipated heat in the wave guide on the flying characteristics of a HAMR-TFC slider. For the design investigated, the results show that the dissipated heat in the wave guide generates a thermal protrusion with smaller radius at the read/write element compared to that caused by an equal amount of heat input to the dual heaters. This is undesirable from a tribological point of view with respect to wear during slider/disk contacts. In addition, we observe that the minimum flying height occurs at the trailing edge of the slider in the case that heat is dissipated in the wave guide. Since the read/write elements should be as close as possible to the magnetic media, the flying height reduction at the trailing edge will degrade the flying performance of the slider at the read/write element and may lead to contact between the slider and disk. These effects increase as the dissipated heat increases. The heater can be used to modify the thermal deformation and flying height reduction at the trailing edge caused by heat dissipated in the wave guide, if the input power of the heater is larger than the dissipated energy in the wave guide. It should be noticed, however, that the additional flying height reduction at the read/write element used to compensate the flying characteristics degradation may lead to slider/disk contact with increasing power input to the heater. The power ratio (for a given position of heater 1 and heater 2) and the position of the two heaters must be carefully selected to achieve

low flying height, high thermal efficiency, and reduced dependence of the dissipated energy in the wave guide on spacing changes at the read/write elements.

7.5 Acknowledgement

Chapter 7, in part, is a reprint of the material as it appears in "Numerical simulation of thermal flying height control sliders in heat-assisted magnetic recording," Hao Zheng, Hui Li, and Frank E. Talke, submitted to Microsystem Technologies, 2011.

Chapter 8

Enhanced Photo-thermal Stability of Modified PFPE Lubricants under Laser Beam Exposure

Lubricant degradation caused by laser exposure is one of the critical issues in heat assisted magnetic recording (HAMR) systems. Advanced lubricants are needed that are resistant to the high temperatures generated by laser heating. The photo-thermal stability and tribological properties of modified perfluoropolyether (PFPE) lubricants under laser exposure are investigated in this chapter. The lubricants (Z-Dol) were modified by substituting the hydroxyl (OH) end groups with photo stabilizer end groups (benzophenone). The change in reflectance due to exposure of the modified PFPE lubricant films (HAMR-type lubricants) to laser light was measured using a surface reflectance analyzer (SRA). The friction force at the head/disk interface of sliders flying over modified Z-Dol films was measured on a spin stand. Modified PFPE films showed less reflectance change than conventional PFPE lubricants (pure Z-Dol). The photo-thermal stability was found to increase with higher substitution ratios. Under laser exposure, reflectance changes can be caused by lubricant depletion and/or changes in the optical properties of the lubricant. The normalized friction force

at the head/disk interface of sliders flying over modified Z-Dol remains constant under laser exposure. This is in contrast to the normalized friction force experienced by sliders flying over pure Z-Dol after laser heating. Modified PFPE lubricants are potential lubricants for application in future heat assisted magnetic recording systems.

8.1 Introduction

As introduced in chapter 7, heat assisted magnetic recording (HAMR) is one of the most promising technologies that can push areal density in magnetic disk drives beyond 1.6 Gb/mm² (1 Tb/inch²) [158][160][161]. In heat assisted magnetic recording systems, a laser beam is used during the writing process to heat up the magnetic media above its Curie temperature. This momentarily reduces the coercivity of the magnetic media and permits writing of information on the disk. The local heating of the magnetic material allows the use of magnetic media with high coercivity, thereby overcoming the super-paramagnetic limit [83][159]. However, high temperatures experienced by the magnetic media raise concerns about the stability and tribological properties of the lubricant layer on the disk surface. Lubricant depletion and lubricant degradation may occur under exposure to the laser [169]. Therefore, advanced lubricants (HAMR-type lubricants) with improved thermal stability are needed. An understanding of the effect of laser exposure on the performance of these lubricants is important to the future of heat assisted magnetic recording systems.

8.2 Lubricants in Hard Disk Drive

8.2.1 PFPE Lubricant

As the magnetic spacing between the slider and disk decreases, intermittent contacts between the slider and the disk are inevitable. Increasing demands are placed on the lubricants to reduce friction and wear due to the contact and to improve the durability of the head/disk interface [169]. The thickness of the lubricant films employed in current hard disk drives is on the order of one nanometer. The low film thickness affects material properties, such as viscosity and shear modulus [170].

Perfluoropolyether (PFPE) lubricants exhibit properties that are well suited for applications in hard disk drives [169][171]. The most favorable properties are low surface tension, low contact angle, hydrophobicity, non-toxicity, non-flammability, thermo-chemical stability at ambient conditions, and a good balance between mobility and affinity to the carbon overcoat. Lubricants must quickly flow over areas generated by head/disk contacts and must be resistant to spin off due to rotation of the disk. Typical PFPE lubricants that are commercially available are Fomblin Z, Fomblin Y, Krytox, and Demnum [172]. The representative chemical structure of PFPE lubricants is shown in Figure 8.1 [172].

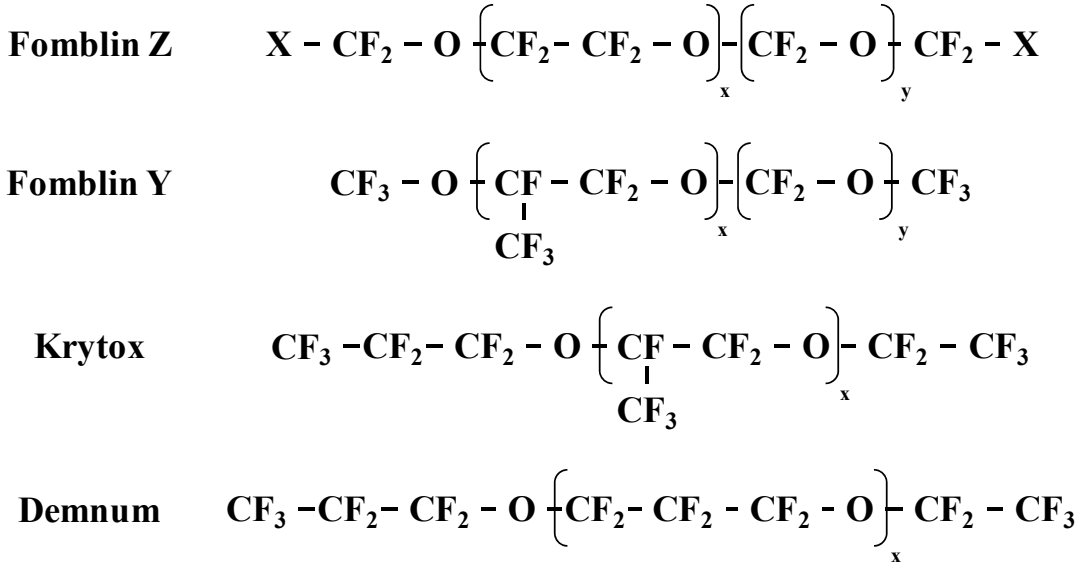

Figure 8.1 Typical chemical structure of PFPE lubricants

8.2.2 Lubricant Degradation

The decomposition of PFPE lubricants can be caused by thermal degradation, photo oxidation, and catalytic degradation.

Fomblin Z-Dol is one of the most widely employed lubricants in hard disk drives [171][173]. Waltman et al. [174] reported the loss of mobile lubricants during temperature increase due to evaporation. In addition, they have found that the hydroxyl end group of Z-Dol is critical in the interaction between Z-Dol and carbon overcoated surfaces [174]. Li et al. investigated the effect of molecular weight and terminal groups of Z-type PFPE lubricants on the weight loss due to temperature increase in the range of 200 ˚C to 500 ˚C. They found that the mechanism of temperature induced weight loss is primarily evaporation for low molecular weight lubricants and thermal oxidative decomposition for lubricants with high molecular

weight. Degradation of Z-Dol is initiated by the oxidation of hydroxyl end groups [172].

Zhao et al. observed lubricant decomposition at low temperatures in presence of ultraviolet (UV) light. The bonding of PFPE lubricants to the disk surface is improved by UV exposure. However, the low energy electrons produced by the UV light interact with the lubricant molecules and generate hydrogen radicals that accelerate the degradation of PFPE lubricant [175]. Weight loss of Z-Dol due to UV exposure was observed by Lee et al. The absorption of UV photons can cause the bonds to break in the lubricant. Chain scission due to the radicals originated from low energy electrons occurs in the methylene (fluorine) and the hydroxyl end chain [176][177].

Al_2O_3 is one of the main material components used in slider materials. It can convert to strong Lewis acids, such as AlF_3 and $AlCl_3$, at the surface of a slider [178]. Lewis acid acts as a catalyst and causes intramolecular reactions in the PFPE lubricant [175][179]. The $-OCF_2O-$ linkages in the PFPE decompose in the presence of Lewis acid and release COF_2 and fluorinated carbon compounds [175][179]. When catalytic Lewis acid degradation is initiated, chain breakage occurs in the methylene oxide and in the main chain of the ethylene oxide [177].

8.2.3 Lubricant Synthesis for Heat Assisted Magnetic Recording Application

During writing, the magnetic medium in heat assisted magnetic recording is exposed to an intense radiative field from a near-field transducer (NFT). The radiative energy is transferred to and dissipated in the magnetic medium. This heats the medium above its Curie temperature [83]. Advanced lubricants have to be resistant to high temperatures and high radiative energy from the laser light source while retaining good tribological properties. Zhu and Liew studied the effect of laser illumination on the molecular structure of PFPE lubricants and observed disk damage due to lubricant evaporation [180]. Tagawa et al. investigated laser heating induced lubricant depletion and its relationship to thickness, bonding ratio, molecular weight, and lubricant end groups. Degradation of PFPE lubricants under laser exposure due to molecular chain breakage and/or depletion has been observed [181-183].

The thermal and photo stability of PFPE lubricants may be enhanced by functionalizing the end groups or by increasing the molecular weight [181]. Zhang et al. developed lubricants that have demonstrated superior thermal stability and tribological properties when compared to commercially available lubricants such as Z-Dol, AM3001 and A20H [184]. Lee et al. have reduced the photo degradation of Z-Dol by using 2, 3, 4, 5, 6-pentafluorobenzophenone as UV-stabilizing additive. However, phase separation of the mixture has been observed over time due to the chemical incompatibility of Z-Dol and additive [176].

In this study, Fomblin Z-Dol® 2000, supplied by Solvay-Solexis [185], was chemically modified by the substitution of the hydroxyl end group with benzophenone (UVS) in order to improve its thermal and photo stability. The chemical structure of Z-Dol2000 is shown in Figure 8.2. The molecular weight affects both mechanical and chemical properties of PFPE lubricants. The molecular weight of Z-Dol2000 is 3.3×10^{-21} grams (2000 atomic mass unit). The diameter of the PFPE molecule is approximately 0.7 ~ 0.8 nm and the length is around 7 nm [185][186].

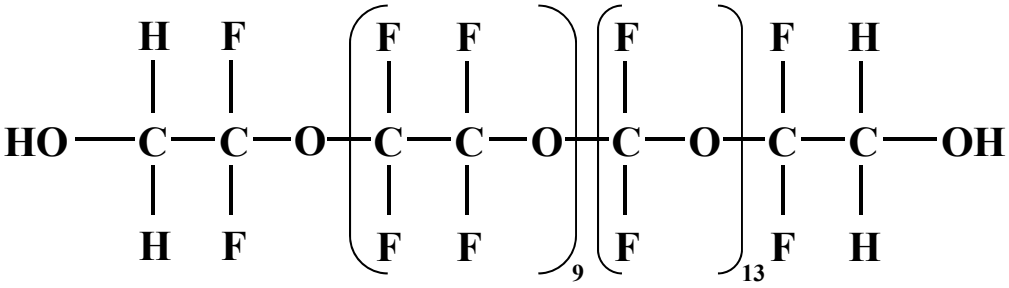

Figure 8.2 Chemical structure of perfluoropolyether

Figure 8.3 shows the molecular structure of 4-(bromomethyl) benzophenone. The procedure for the chemical modification of Z-Dol is shown in Figure 8.4 (after [165]). First, the hydroxyl end groups in Z-Dol are alkoxylated with a catalyst, such as sodium or potassium, at 40 ˚C in order to improve reactivity [187]. Then, benzophenone dissolved in HFE-7100 reacts with alkoxylated PFPE and replaces the ONa^+ (or OK^+) end groups. The hydroxyl terminal groups of Z-Dol can either be replaced by one UVS group (type 1), by two UVS groups (type 2), or remain unchanged (type 3). The substitution ratio of the benzophenone in PFPE can be controlled by various reaction parameters such as the amount of applied catalyst, reaction time, and mole ratio of reactants. The final products were analyzed by a 200

MHz Varian Zemine 2000 instrument for proton nuclear magnetic resonance (^{1}H NMR) measurements. Peak shifts corresponding to the hydrogen moieties (OH and CH_2) in the PFPE and peaks corresponding to the CH_2 in benzophenone were apparent in ^{1}H NMR spectrum. These peaks were used to determine the average substitution ratio in the three types of modified Z-Dol [187]. Z-Dol2000 lubricants with 22%, 48%, and 72% substitution ratios are investigated in our study and are referred to as $HAMR_{22\%}$, $HAMR_{48\%}$, and $HAMR_{72\%}$ respectively. The lubricant synthesis was performed in the laboratory of Professor Kang at the Dankook University, Korea.

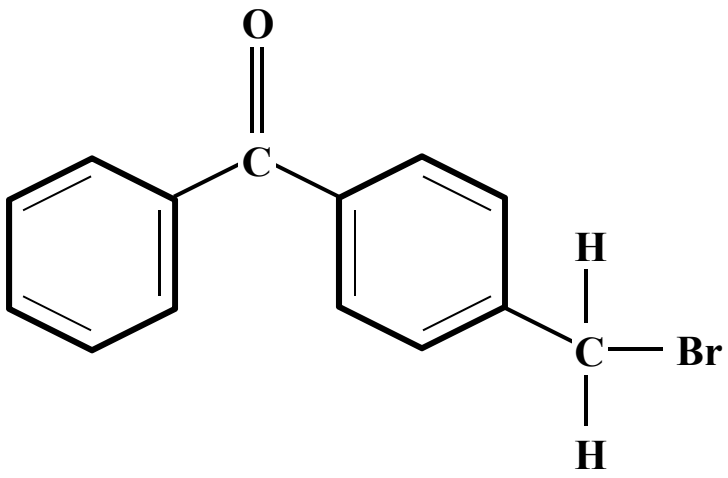

Figure 8.3 Chemical structure of 4-(bromomethyl) benzophenone

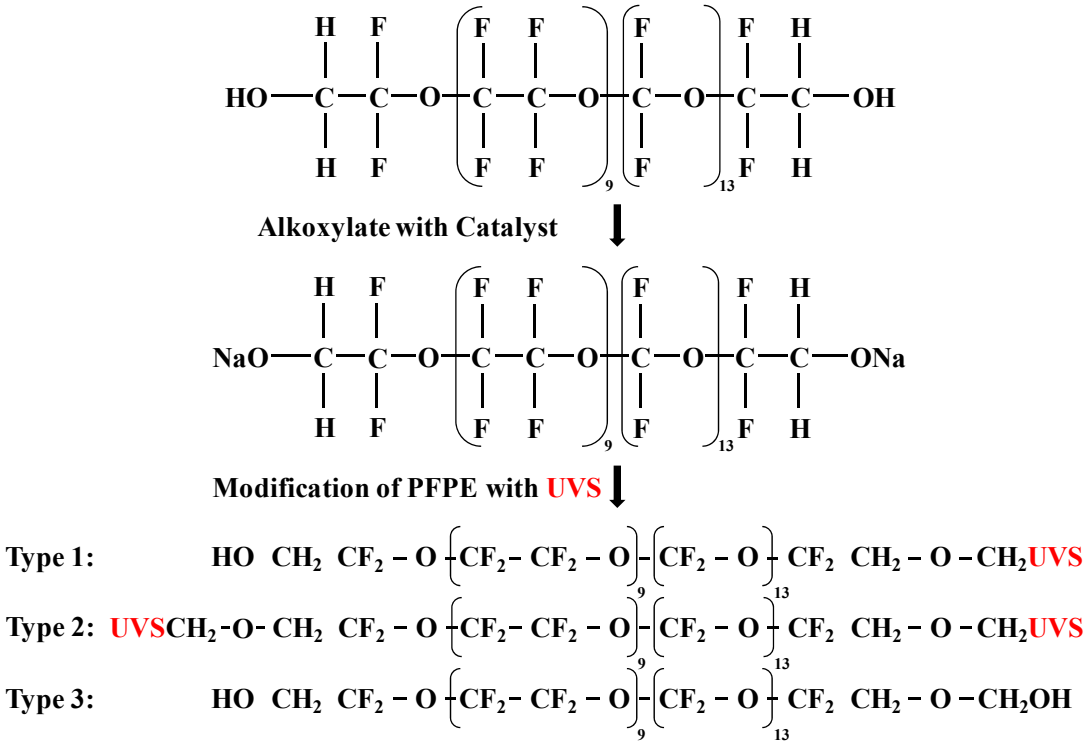

Figure 8.4 Chemical modification of PFPE with photo stabilizer (UVS)

8.3 Experimental Setup

The thermal stability of modified PFPE lubricants as a function of the substitution ratio was determined through thermo gravimetric analysis (TGA) using a Mettler TG15 analyzer. Weight loss due to thermal degradation in air was determined through dynamic scanning up to 700 ˚C with a scanning rate of 20 ˚C/min [176][187]. The disks used in this study were 64-mm (2.5-inch) diameter glass-substrate disks sputtered with perpendicular magnetic media and wear protective carbon overcoat. Pure lubricants were diluted with 3M's HFE-7100 solvent in order to create solutions that contained the lubricants at 0.1% by weight concentration. A dip-coater (Figure 8.5) was used to apply the lubricants onto the disk surface. Lubricant film thickness varied

from 1.5 nm to 2 nm, depending on the drain/withdraw speeds of the dip-coater [171][188]. The photo-thermal stability and tribological properties of $HAMR_{22\%}$ (containing 22% UVS), $HAMR_{48\%}$ (containing 48% UVS), and $HAMR_{72\%}$ (containing 72% UVS) were evaluated and compared with properties of pure Z-Dol. The lubricants were tested under identical laser irradiation. The laser diode was pulsed at 3 MHz and the pulse duration was approximately 200 ns. The wavelength of the laser used was 660 nm. The average power output used in this study was varied between 20 and 110 mW as measured with a power meter (Lasercheck, Coherent).

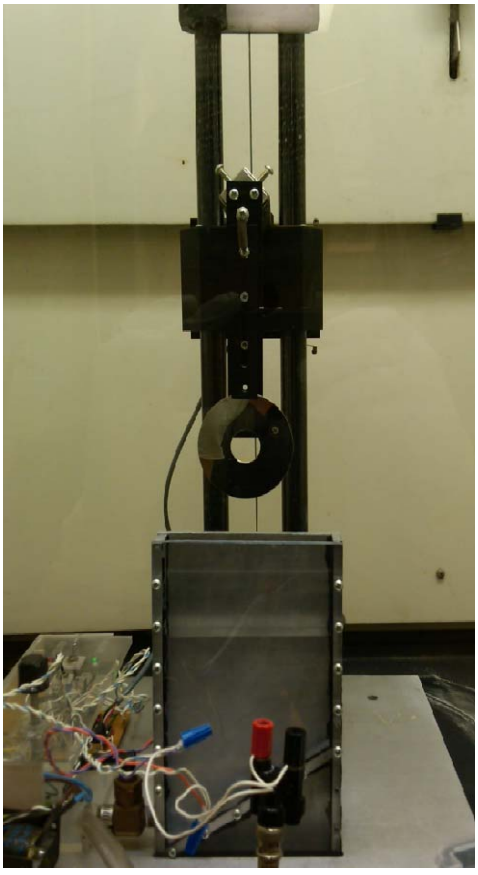

Figure 8.5 Dip-coater for deposition of lubricant onto disk surface

8.3.1 Modified Surface Reflectance Analyzer (SRA)

A commercially available surface reflectance analyzer (SRA) was modified in order to evaluate the thermo-photo stability of lubricants under laser exposure.

Surface reflectance analysis is an optical measurement technique used to determine the composition, thickness, uniformity, and cleanliness of thin film layers over planar surfaces [189-192]. A high resolution of less than 0.5 Å for typical overcoats and lubricants, and fast data acquisition speed of approximately 10 MHz enables the SRA to perform analyses of lubricant degradation in hard disk drives [190]. In addition, it can be used to detect carbon wear and contamination.

Surface reflectance analysis is based on the principles of ellipsometry [191]. The schematic of the optical system of a surface reflectance analyzer is shown in Figure 8.6. A laser source generates a stabilized monochromatic light beam. The laser light is circularly polarized by a linear polarizer and a quarter wave plate. The incident beam is split by the beam splitter and a fraction of the light is directed to a photo-diode in order to monitor the intensity of the laser beam. The light source controller uses a feedback system, based on the measured intensity, to control and stabilize the laser beam. The primary portion of the polarized light beam is focused on the sample surface, with an incident angle of 60˚ from the normal of the surface, by an objective. The scattered light is collected by an integrating sphere. The properties of the reflected light are changed according to the optical properties and thickness of the measured surface. Detectors measure the intensity and the phase difference of the polarized light reflected from the substrate. Intensities of the spatially resolved s-polarized light (R_s),

p-polarized light (R_p), and phase contrast (R_{ph}) are simultaneously monitored. A resolution higher than 0.1 nm is typical and is used in the mapping of the sample surface [38].

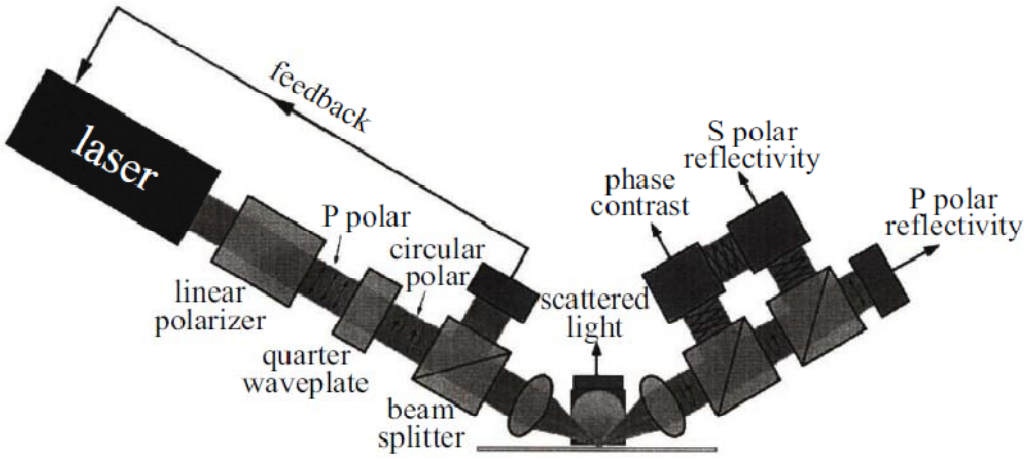

Figure 8.6 Schematic representation of SRA instrument (courtesy of [192])

Fresnel's equations are used to correlate parameters of the reflected light to the material properties of the measured surface [189]. The oblique reflection and transmission of plane waves at a planar surface are described in Figure 8.7 [193], where p and s are parallel and perpendicular axes to the plane of incidence. θ_i, θ_r, and θ_t are the incident, reflected and refracted angles, respectively. The refractive index of media 1 and 2 are denoted as n_1 and n_2, respectively.

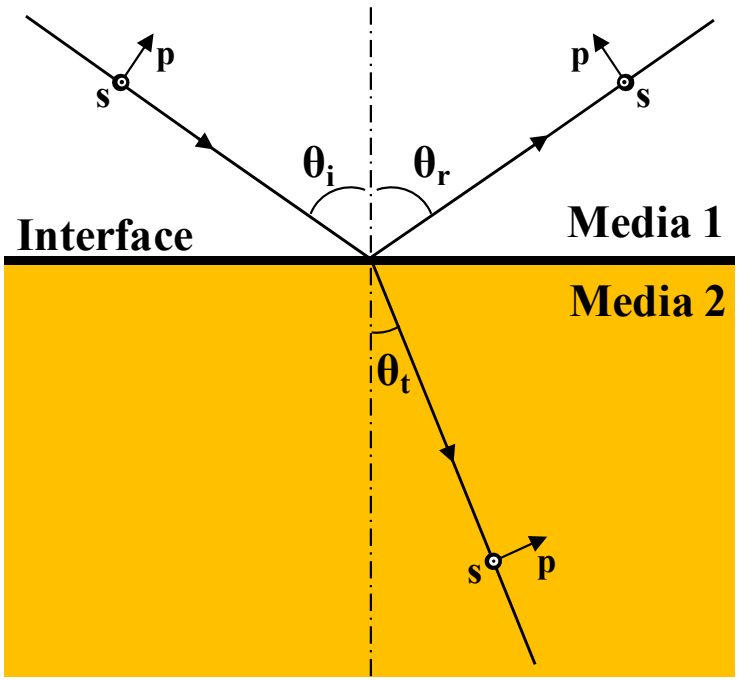

Figure 8.7 Oblique reflection and transmission of an optical plane wave at the planar interface (after [193])

The propagation of the light follows Snell's law ($n_1 \sin\theta_i = n_2 \sin\theta_t$). The Fresnel complex-amplitude reflection coefficients in the p- and s- directions are [193]:

$$r_p = \sqrt{R_p} e^{j\delta p} = \frac{\tan(\theta_i - \theta_t)}{\tan(\theta_i + \theta_t)} \tag{8.1}$$

$$r_s = \sqrt{R_s} e^{j\delta s} = \frac{-\sin(\theta_i - \theta_t)}{\sin(\theta_i + \theta_t)} \tag{8.2}$$

where δ_p and δ_s are the phase shift of the reflected p- and s-polarized light from the sample surface, respectively. R_p and R_s are the theoretical values of the reflection coefficients for p-polarized and s-polarized light, respectively, and are given by [38][194]:

$$R_p = \left(\frac{n_1 \cos\theta_t - n_2 \cos\theta_i}{n_1 \cos\theta_t + n_2 \cos\theta_i} \right)^2 = \left[\frac{n_1 \sqrt{1 - \left(\frac{n_1}{n_2} \sin\theta_i \right)^2} - n_2 \cos\theta_i}{n_1 \sqrt{1 - \left(\frac{n_1}{n_2} \sin\theta_i \right)^2} + n_2 \cos\theta_i} \right]^2 \tag{8.3}$$

$$R_s = \left(\frac{n_1 \cos\theta_i - n_2 \cos\theta_t}{n_1 \cos\theta_i + n_2 \cos\theta_t} \right)^2 = \left[\frac{n_1 \cos\theta_i - n_2 \sqrt{1 - \left(\frac{n_1}{n_2} \sin\theta_i \right)^2}}{n_1 \cos\theta_i + n_2 \sqrt{1 - \left(\frac{n_1}{n_2} \sin\theta_i \right)^2}} \right]^2 \tag{8.4}$$

The intensity of the phase contrast is the reflectivity modulated by the phase shift between the p-polarized and s-polarized components and is given by [192]:

$$R_{ph} = \frac{1}{2}\left(\pm\sqrt{R_p R_s} \cos(\delta_p - \delta_s) + \left(R_p + R_s \right) / 2 \right) \tag{8.5}$$

The phase shift between the reflected p-polarized and s-polarized light from the sample surface, as defined in equation (8.5), exhibits higher sensitivity to properties of the lubricant film compared to the p- and s-polarized intensities R_p and R_s alone [190]. Therefore, the phase contrast intensity signal was used to quantify the effect of laser exposure on the lubricant film reflectance in our study.

The experimental setup using the surface reflectance analyzer (SRA) is shown in Figure 8.8. The setup consists of a spindle, a disk, and a linear motor with an attached laser diode. The laser beam is focused on the sample surface using a magnifying optical camera and has a spot size of about 1 μm. The disk is kept stationary. Using a linear actuator at a speed of 0.5 mm/s, the laser is translated

parallel to the disk surface along 5 mm tracks in the radial direction of the disk. The reflectance change of the disk surface as a function of laser exposure was evaluated by the SRA.

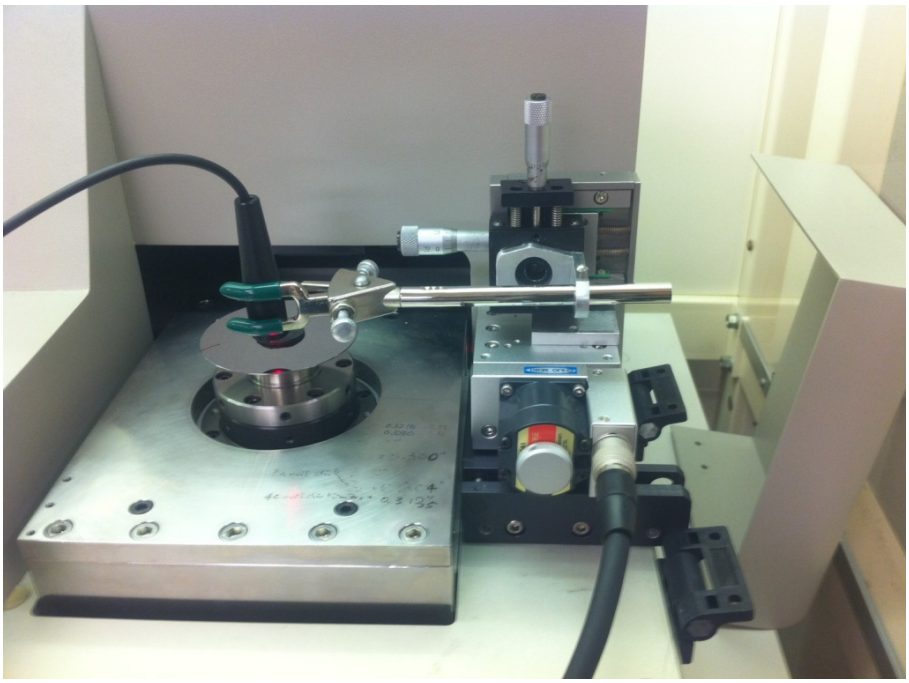

Figure 8.8 Experimental setup of modified surface reflectance analyzer (SRA) for studying the effect of laser light irradiation on the thickness variation of a modified Z-Dol thin film

8.3.2 Modified Contact Start-Stop (CSS) Tester

Drag tests were performed with a contact start-stop tester in order to evaluate the frictional properties of the lubricated disk after laser exposure [197]. The experimental setup is shown in Figure 8.9. The lubricated disks were first thermally treated at 90 ˚C for 24 hours in order to bond the lubricant to the carbon overcoat. The friction force at the interface between the rotating disk and the head/gimbal assembly

(HGA) was measured by a load cell (Figure 8.9). The slider was positioned with zero skew angle relative to the circumferential direction of the disk. The friction force was sampled at 12.8 kHz and the normal load was fixed at 25 mN. The disk was rotated at a constant speed of 1 m/s while the slider was dragged on the disk. The laser beam was directed onto the disk, in the area of the "wear track" of the slider, through a hole in the suspension. The friction force was measured as a function of laser exposure. For the different lubricants investigated, the collected data was normalized by the friction force measured for a slider over Z-Dol2000 without laser irradiation. The normalized friction force obtained with modified Z-Dol lubricants was compared with the friction force for pure Z-Dol before and after laser irradiation.

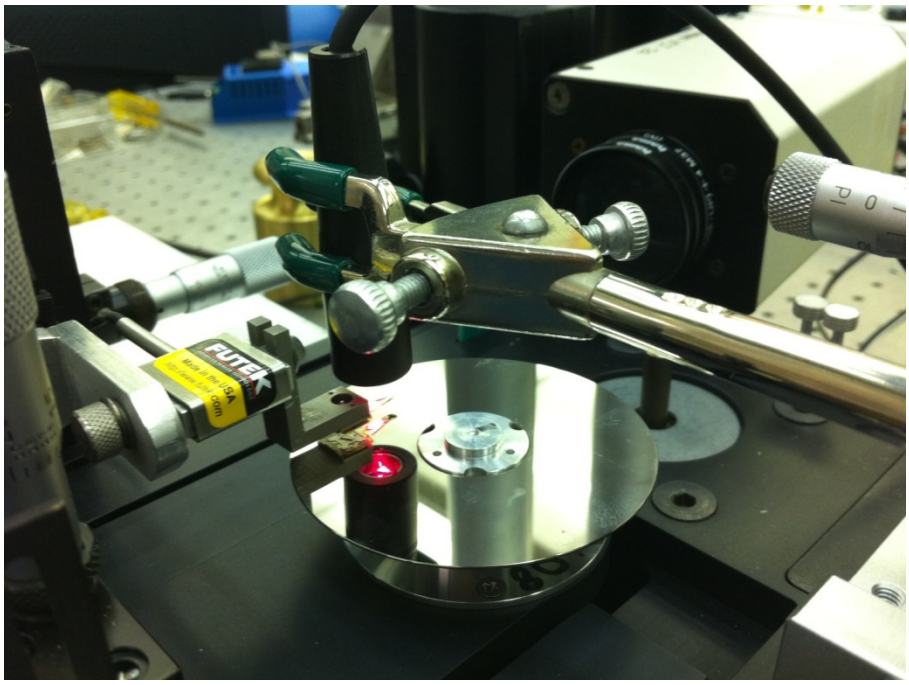

Figure 8.9 Experimental setup of modified Contact-Start-Stop (CSS) tester for drag tests for studying the effect of laser light irradiation on friction force of a modified Z-Dol thin film

8.4 Experimental Results

8.4.1 Thermal Stability of Bulk Lubricants

Figure 8.10 shows the effect of temperature on the weight loss of modified Z-Dol bulk lubricants as a function of the substitution ratio of UV-Stabilizer terminal groups ([162]). Thermal degradation of Z-Dol begins at 210 ˚C due to molecular dissociation of PFPE [187]. We observe that the weight loss curves of modified Z-Dol lubricants lie to the right of the weight loss curve of the pure Z-Dol2000, i.e., the initial degradation temperature of modified PFPE lubricants is higher than that of Z-Dol2000. This indicates that modified PFPE lubricants exhibit improved thermal stability. Furthermore, we note that the weight loss curves move further to the right as the substitution ratio increases. The highest thermal stability is observed for a substitution ratio of 100 percent. Thus, the thermal stability of modified Z-Dol improves with a higher content of benzophenone. This is due to the rigid chemical structure of the aromatic ring of the substituted benzophenone.

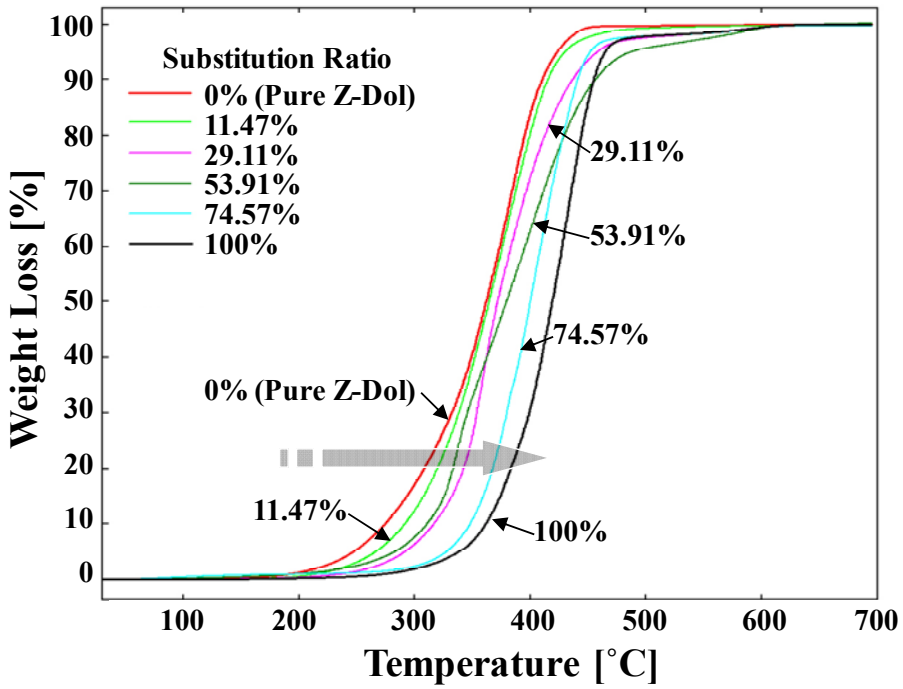

Figure 8.10 Thermal stability of modified Z-Dol lubricants as a function of substitution ratios of UVS end groups ([162])

8.4.2 Reflectance Change of Thin Lubricant Films under Laser Beam Exposure

The effect of laser beam irradiation on thin lubricant films is a function of film thickness [184]. Thus, the thickness should be taken into consideration when dealing with the effect of laser beam exposure on the reflectance properties of different lubricants. Modified lubricants with different substitution ratios of UV-Stabilizer are likely to have different optical properties and initial coating thickness compared to Z-Dol2000. While determination of a full set of optical and thermo-optical constant is beyond the scope of this work, we are using normalized reflectance values to evaluate

the photo-stability of different lubricants under laser beam irradiation independently of their initial thickness or optical properties.

The difference of reflectance (ΔR) between the non-irradiated (R_L) and irradiated lubricant surfaces (R_I), i.e., $\Delta R = R_L - R_I$, is evaluated for varying laser exposure times and average output power. ΔR is normalized by the initial difference in reflectance (ΔR_0) between the lubricant film (R_L) and the unlubricated surfaces (R_C), defined as $\Delta R_0 = R_L - R_C$.

Figure 8.11 shows the normalized reflectance change as a function of the average output power of the laser beam over a constant irradiation time of 400 seconds. It can be seen that $\Delta R/\Delta R_0$ increases with increasing output power for all lubricants investigated. In addition we observe that $HAMR_{48\%}$ and $HAMR_{72\%}$ exhibit less reflectance variation compared to pure Z-Dol and $HAMR_{22\%}$. The rate of reflectance change decreases as the UV-Stabilizer substitution ratio increases, under identical laser exposure conditions.

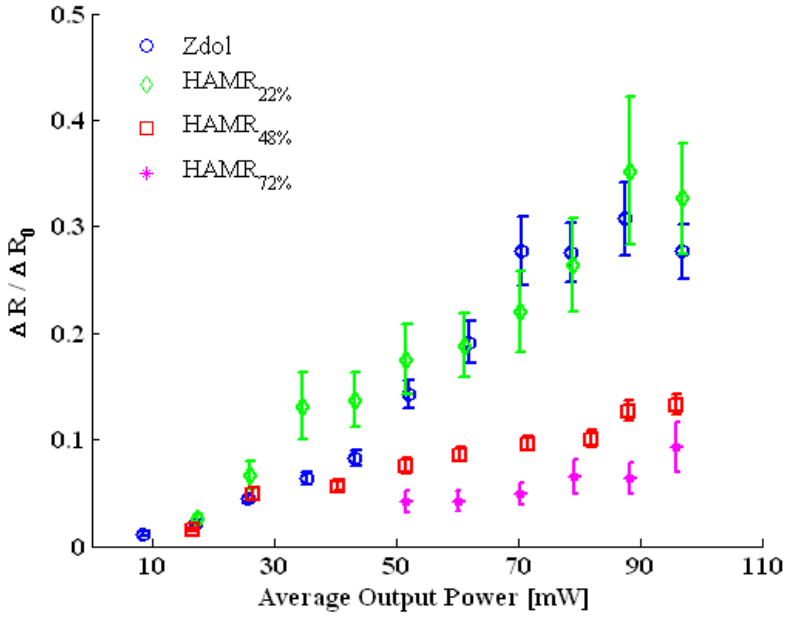

Figure 8.11 Normalized reflectance change as a function of average laser power at constant illumination time 400s

The evolution of the normalized reflectance change $\Delta R/\Delta R_0$ of Z-Dol2000, $HAMR_{22\%}$, $HAMR_{48\%}$, and $HAMR_{72\%}$ lubricants as a function of irradiation time is shown in Figure 8.12. A constant average output power of laser beam equal to 107 mW is used for all the cases. It can be observed that $\Delta R/\Delta R_0$ of Z-Dol2000, $HAMR_{22\%}$, $HAMR_{48\%}$, and $HAMR_{72\%}$ films increases as the irradiation time increases. Again a smaller variation of $\Delta R/\Delta R_0$ is exhibited for $HAMR_{48\%}$ and $HAMR_{72\%}$, compared to that of Z-Dol and $HAMR_{22\%}$. Thus, the normalized reflectance change of modified PFPE lubricants decreases with an increasing substitution ratio of UVS compound.

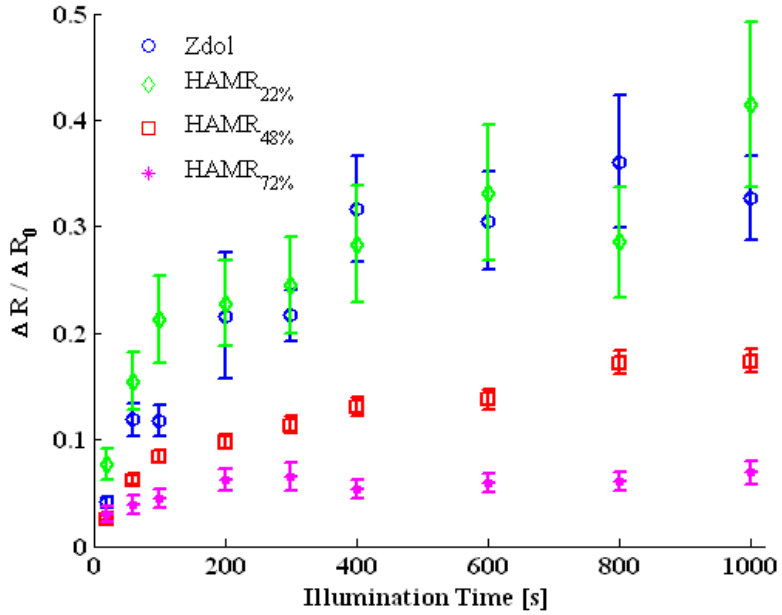

Figure 8.12 Normalized reflectance change as a function of laser illumination power at constant laser power P = 107 mW

The results shown in Figures 8.11 and 8.12 indicate clearly that the thermal stability of modified PFPE lubricants under laser beam exposure is improved compared to pure Z-Dol2000.

The observed reflectance change of the lubricant film can be due to the change in the thickness and/or a change in the optical properties of the lubricant. A theoretical model based on equation (8.5) was developed in order to relate the variations of the reflectance to the change in the thickness and optical properties of lubricants. A positive sign was employed in equation (8.5) as the convention in the following sections. Isotropic properties were assumed for the lubricant and unlubricated layers.

Optical constants described by Johnson et al. [195] and Chia et al. [196] were used for the calculation.

Figure 8.13 (a) and Figure 8.13 (b) represents the calculated normalized reflectance change of Z-Dol2000 as a function of film thickness for a constant index $n_0 = 1.31$, and of the refractive index of lubricant for a given thickness of $d_0 = 1.8$ nm, respectively. The cases that $d_0 = 1.8$ nm for Figure 8.13 (a) and $n_0 = 1.31$ for Figure 8.13 (b) corresponds to the initial "as-coated" values for $\Delta R/\Delta R_0 = 0$. It can be observed that an increase in $\Delta R/\Delta R_0$ can be caused by a decreased thickness or a reduced refractive index of the lubricant. The measured $\Delta R/\Delta R_0$ for Z-Dol2000 is about 0.3 at an average output power of 107 mW. We observe from Figure 8.13 (a) that the change of $\Delta R/\Delta R_0 = 0.3$ would correspond to a reduction of lubricant thickness from 1.8 nm to 1.2 nm, assuming only lubricant depletion occurred. This is consistent with the results of Tagawa et al. [182]. On the other hand, assuming that the normalized reflectance change is only due to a variation in the optical properties of the lubricant, a change of $\Delta R/\Delta R_0$ equal to 0.3 requires a reduction in the refractive index from 1.3 to 0.9, as shown in Figure 8.13 (b). Although a refractive index $n < n_{air} = 1$ is unlikely for the lubricants in current use, it is possible that a combination of both lubricant depletion and modification of the lubricant optical properties under laser exposure is responsible for the change of reflectance.

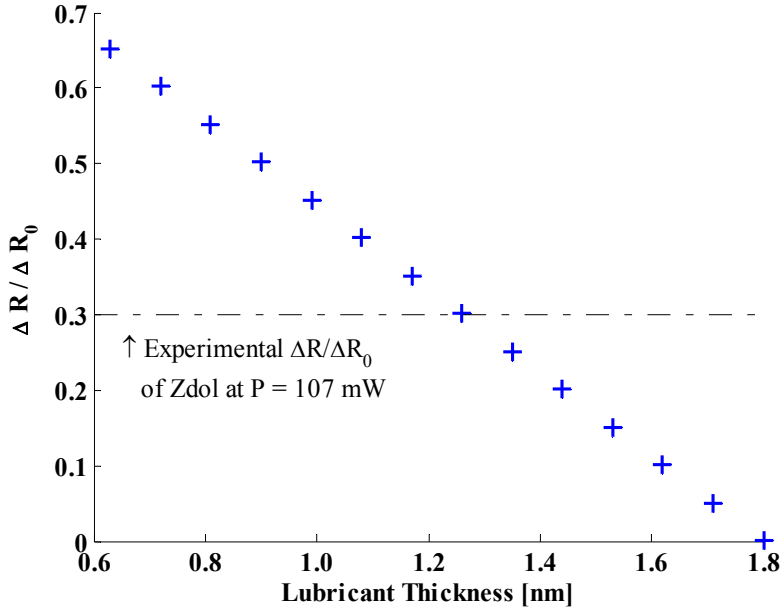

(a)

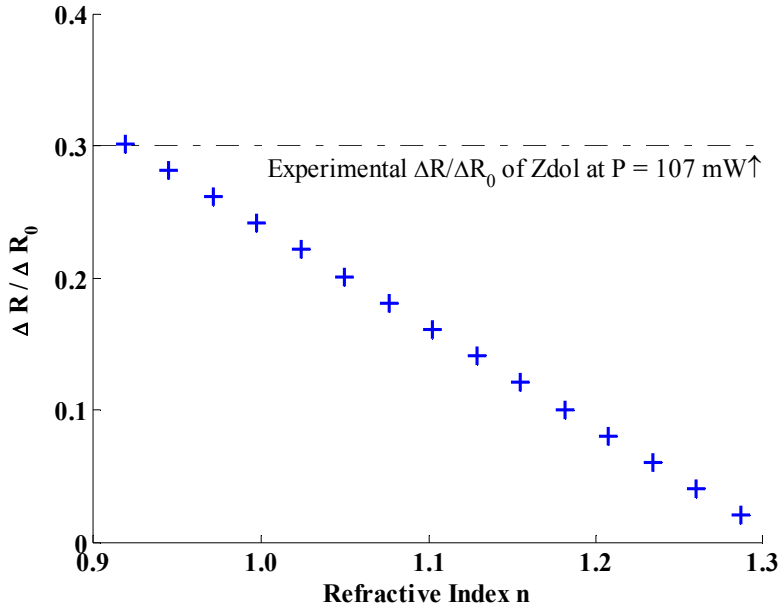

(b)

Figure 8.13 Theoretical normalized reflectance change as a function of (a) lubricant thickness and (b) refractive index of Z-Dol2000. The horizontal dashed line illustrates the experimental value of $\Delta R/\Delta R_0$ of Z-Dol2000 at an average power of 107 mW

The dependence of lubricant degradation due to laser beam exposure as a function of the substitution ratio of benzophenone end groups is well correlated to the thermal stability of bulk lubricant as shown in Figure 8.10, i.e., the thermal stability increases as the substitution ratio increases. Thus, it is justifiable to conclude that the photo-thermal stability of PFPE lubricant is enhanced by functionalizing the terminal groups using benzophenone.

8.4.3 Frictional Properties of Thin Lubricant Films under Laser Beam Exposure

Figure 8.14 shows the normalized friction force measured before and after laser beam exposure (indicated as "laser off" and "laser on", respectively) experienced by sliders flying over disk coated with Z-Dol2000, $HAMR_{22\%}$, $HAMR_{48\%}$, and $HAMR_{72\%}$, lubricants. The disk is rotating at a constant velocity of 1 m/s. At that speed, the asperities on the slider and the disk are in contact with each other, i.e., the air bearing force separating the slider from the disk is negligible. Thus, the friction force at the head/disk interface depends on the interactions of the slider with the lubricant film on the disk. In Figure 8.14 we compare the frictional forces at the head/disk interface for different lubricants by normalizing the friction force to that of Z-Dol2000 prior to laser beam exposure. We observe that the normalized friction force obtained with $HAMR_{22\%}$ and $HAMR_{48\%}$ before laser heating is slightly higher than that of Z-Dol. In addition, the normalized friction force at the head/disk interface of sliders flying over $HAMR_{72\%}$ is the lowest among all lubricants evaluated. This is likely because as the amount of benzophenone increases, the number of hydroxyl end

groups responsible for bonding the lubricant to the disk surface is reduced, leading to lower friction force obtained with highly substituted PFPEs in comparison to Z-Dol2000.

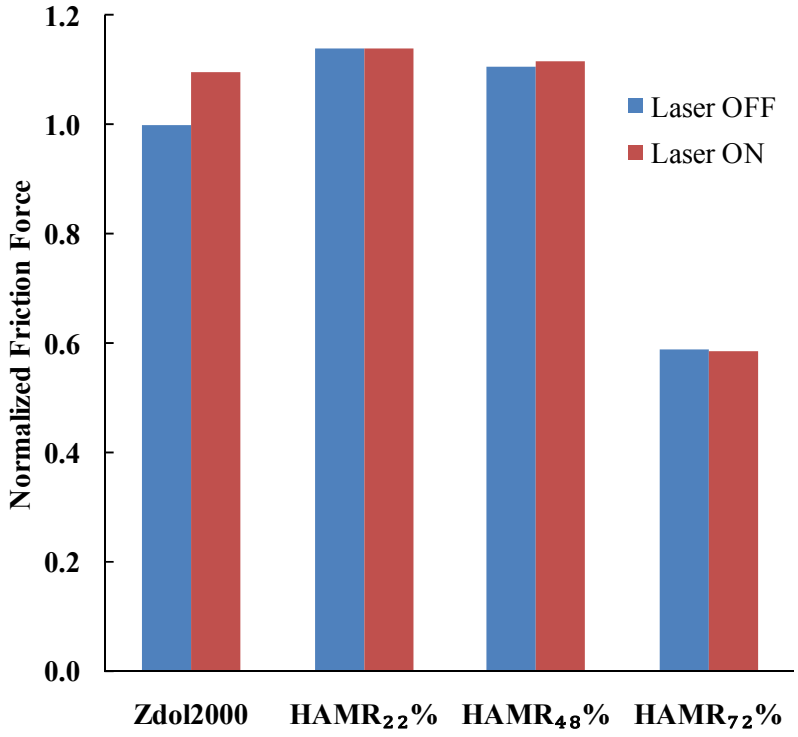

Figure 8.14 Normalized friction force of Z-Dol2000, $HAMR_{22\%}$, $HAMR_{48\%}$, and $HAMR_{72\%}$, at constant velocity of 1 m/s, before ("laser off") and after ("laser on") laser beam exposure of the wear track.

In the case of Z-Dol, a 10% increase of the normalized friction force after laser beam exposure is observed, compared to the normalized friction force prior to laser beam exposure. On the other hand, the normalized friction forces experienced by sliders flying over $HAMR_{22\%}$, $HAMR_{48\%}$, and $HAMR_{72\%}$, remains unchanged after laser beam exposure.

8.5 Discussion

In this work, the photo-thermal stability and the tribological properties of modified PFPE lubricants were investigated with different benzophenone end group substitution ratio under laser beam irradiation. Experimental results indicate that the substitution of Z-Dol2000 hydroxyl end groups by benzophenone moieties improves the photo and thermal stability, as well as the tribological properties of the lubricant under laser beam exposure compared to the pure Z-Dol.

The test condition used in our study is 3 MHz laser beam exposure at low power density between 10 and 100 mW/μm². The disk was kept stationary for the reflectance change measurement and was rotating at very low speed (1m/s) for the evaluation of tribological performance. Several differences exist between our experiments and a heat assisted magnetic recording system. In particular, in a heat assisted magnetic recording disk system, the laser beam is applied to a fast rotating disk. The laser beam is pulsed with a duration on the order of nanoseconds and the power density that could be reached is several $W/\mu m^2$ [160][161]. Thus, the question arises as to whether the present long-time laser exposure experiment can predict the performance of a lubricant in a heat assisted magnetic recording system where thermal stress is very different from our steady-state experiments. Even though our experimental setup does not reproduce conditions of a heat assisted magnetic recording system, we have developed an experimental method aiming at investigating photo-thermal and tribological properties of modified PFPE lubricants relative to pure PFPE lubricant, under laser irradiation. As a proof of principle, we have shown that

the substitution of Z-Dol2000 hydroxyl end groups by benzophenone species leads to improved photo-thermal stability and tribological performance under laser beam exposure compared to Z-Dol2000. This trend is well correlated to the thermal stability of bulk modified Z-Dol2000 lubricants.

8.6 Summary and Conclusions

Modified PFPE lubricant films with different substitution ratios were investigated under laser beam exposure. The normalized reflectance change of modified PFPE films was found to be sensitive to laser beam exposure and was interpreted as a result of lubricant depletion in the region exposed to the laser beam. Modified Z-Dol films show less reflectance change than pure Z-Dol2000, indicating higher stability under the same illumination condition. Photo-thermal stability of modified Z-Dol films under laser beam exposure increases with an increase of the substitution ratio. This result correlates well with the bulk thermal stability of modified Z-Dol lubricant as a function of the substitution ratio. A substantial increase of the normalized friction force of pure Z-Dol was observed after the wear track on the disk was exposed to a laser beam, while the friction force obtained with modified Z-Dol lubricants was less sensitive under laser beam exposure and remained constant. Based on these results, we can conclude that PFPE molecules modified with benzophenone compounds are potential candidates applicable to heat assisted magnetic recording systems.

8.7 Acknowledgement

Chapter 8, in part, is a reprint of the material as it appears in "Enhanced photo-thermal stability of modified PFPE lubricants under laser beam exposure," Melanie Gauvin, Hao Zheng, Benjamin Suen, Ho-Jong Kang, Jihye Lee, and Frank E. Talke, IEEE Transactions on Magnetics, Vol. 46, No. 7, Jul. 2011, pp. 1849 – 1854. The dissertation author was one the investigators and coauthors of this paper.

Chapter 9

Summary and Conclusions

With the continuous adoption of innovations, magnetic hard disk drives have changed dramatically since the first hard disk drive in RAMAC was introduced in 1956. The areal density of state-of-the-art hard disk drives is more than 370-million times that of the RAMAC. In contrast to the expensive cost of the RAMAC of tens of thousands of dollars per megabyte, the cost of storage in a modern drive is on the order of less than 5 cents per gigabyte.

The “magnetic recording trilemma” caused by the tradeoff among signal-to-noise ratio, write capability and thermal stability constrains the increase of areal density in magnetic hard disk drives. Perpendicular recording technology can greatly increase the areal density of disks but will reach its ceiling at an areal density around 1.6 – 2.3 Gb/mm^2 (1 – 1.5 Tb/in^2). New techniques are being investigated in order to push the areal density beyond the limits.

Bit patterned media (BPM) is one of these promising technologies. By using disks with physically separated magnetic patterns instead of conventional continuous recoding media, bit patterned media avoid magnetic interference between adjacent bits, improves the thermal stability of the media, and increase the areal density to above 1.6 Gb/mm^2 (1 Tb/in^2). In bit patterned media, bits are contained within individual island-like protrusions on the disk surface. This adds complexity in the manufacturing

process and causes changes in the flying behaviors of a slider. A finite-element based air bearing simulator was used to investigate the steady-state characteristics of femto and spherical-pad sliders flying over bit patterned media. The discrete bits were modeled as isolated islands on the disk surface. Peaks in the air bearing pressure distribution over each island were obtained. When a spherical-pad slider is used, the maximum pressure shifts towards the spherical pad of the slider. The flying characteristics of both the femto and spherical-pad sliders on bit patterned media are different from sliders flying over conventional smooth disks. The flying height of the slider is related to the design parameters of bit patterned media. These parameters include the bit height, the ratio of bit diameter to bit pitch, and the bit shape. The flying height decreases linearly with increasing bit height. A larger ratio of flying height reduction to bit height ratio is observed at the head/disk interface for bit patterned media than that for discrete track media. In addition, we observe that the flying height of a femto slider becomes more sensitive to skew angle as the bit height increases. On the other hand, the flying height of a spherical-pad slider is less sensitive to skew angle than a femto slider. The flying height of a spherical-pad slider decreases linearly with an increase in the height of the spherical pad. However, the ratio of flying height reduction to bit height is similar regardless of the height of the spherical pad. In addition, we observe that the flying height of a spherical-pad slider is not sensitive to the radius of the spherical pad.

In order to maintain an ultra-low yet stable head/disk interface, thermal flying height control (TFC) sliders are presently in use. A thermal resistor is integrated into

the slider and is located near the read/write element. When the heater is energized, thermal deformation occurs that moves the read and write element towards the disk, thereby reducing the local flying height at the read/write element.

An integrated simulator combining air bearing simulation and thermo-mechanical analysis of the slider was developed to numerically investigate the thermal protrusion and flying height characteristics of thermal flying height control sliders. The effect of radiation on thermal flying height control sliders was investigated for typical values of the near-field heat transfer coefficient. Numerical results show that the effect of radiation due to near-field effects is negligible for head/disk interfaces in present use.

The performance of thermal flying height control slider featuring two separate heaters and two individual insulator elements was investigated and was compared with thermal flying height control slider using a single heater. We observed that the flying height reduction at the read/write element of a dual TFC slider is larger than that obtained for a single TFC slider. In addition, the thermal actuation efficiency is found to be improved. When the write element is operating, a write-induced thermal protrusion is observed. We have found that the write current changes the flying height at the read element less than at the write element. The power ratio and the placement of the individual heaters must be carefully selected in order to reduce the flying height, improve the thermal actuation efficiency and minimize the dependence of the write current on spacing changes at the read/write elements.

Heat assisted magnetic recording (HAMR) has been introduced to address the difficulty of writing information on small and tight-packed bits of high coercivity media. In heat assisted magnetic recording systems, a laser beam is integrated into the write head in order to heat up the magnetic media above its Curie temperature. During writing, the magnetic medium is exposed to a highly concentrated radiative field delivered by the near-field transducer (NFT). The radiative energy is transferred to and dissipated in the magnetic medium. The local heating of the magnetic material reduces the coercivity momentarily and permits writing of information on the disk. This allows the use of magnetic media with high coercivity, thereby overcoming the superparamagnetic limit.

A finite element model of a thermal flying height control slider with two heaters and a heat assisted magnetic recording optical system was developed to investigate the effect of heat dissipated in the wave guide on the flying characteristics of a HAMR-TFC slider. For the design investigated, the results show that the heat dissipated in the wave guide generates a thermal protrusion with small radius at the read/write element and a large thermal deformation at the trailing surface compared to the thermal deformation profile due to an equal power input to the heaters. Both effects adversely affect the flying performance of a HAMR-TFC slider. These effects increase as the dissipated heat increases. If the input power of the heater is larger than the dissipated energy in the wave guide, a dual TFC heater can be used to compensate the effect of the undesired thermal deformation and flying height reduction at the trailing edge caused by the heat dissipated in the wave guide. Again, the design of the

two heaters must be carefully chosen to achieve optimal performance of a HAMR-TFC slider.

Another critical issue in heat assisted magnetic recording is lubricant degradation caused by laser exposure. The local heating of magnetic material allows the use of magnetic media with high coercivity. High temperatures experienced by the magnetic media, however, raise concerns about the stability and tribological properties of the lubricant layer on the disk. Photo-thermal stability and tribological properties of perfluoropolyether (PFPE) lubricants, modified by photo stabilizers, were investigated under laser beam exposure. The change of reflectance of modified PFPE lubricant films induced by laser exposure was measured using a surface reflectance analyzer. The friction force experienced by sliders flying over modified PFPE lubricant films was measured at the head/disk interface on a spin stand. Modified PFPE films show less reflectance change than conventional PFPE lubricants. The photo-thermal stability under laser beam exposure increases with an increase of the substitution ratio. A reflectance change can be caused by depletion of lubricant and/or modification of the lubricant optical properties under laser beam exposure. The normalized friction force obtained with modified PFPE lubricants remains constant under laser beam exposure. This is in contrast to the normalized friction force observed by sliders flying over pure Zdol after laser heating. Modified PFPE lubricants are potential disk lubricants for application in future heat assisted magnetic recording systems.

Appendix A

Newton-Raphson Approach to Steady-State Air Bearing Simulation

The CMRR/Talke Lab air bearing simulator uses the Newton-Raphson scheme to obtain the finite element solution of the generalized Reynolds equation and the slider equilibrium equations. The Newton-Raphson scheme is a powerful numerical scheme to find successively improved approximations of the roots of a real-valued function with second-order accuracy [110].

The generalized Reynolds equation and the equilibrium equations of the slider are functions of the slider position $\boldsymbol{\varepsilon}$ and the air bearing pressure p. They can be written as:

$$\mathbf{R}\left(\boldsymbol{\varepsilon}, p\left(\boldsymbol{\varepsilon}\right)\right) = 0 \tag{A.1}$$

$$\mathbf{F}_{air}\left(p\left(\boldsymbol{\varepsilon}\right)\right) - \mathbf{F}_{ext} - \mathbf{K}_s d\boldsymbol{\varepsilon} = 0 \tag{A.2}$$

The Newton-Raphson scheme of Equation (A.1) and (A.2) can be written as:

$$\mathbf{R}^{k+1}\left(\boldsymbol{\varepsilon}, p\right) = \mathbf{R}^{k} + \frac{\partial \mathbf{R}^{k}}{\partial p} dp + \frac{\partial \mathbf{R}^{k}}{\partial \boldsymbol{\varepsilon}} d\boldsymbol{\varepsilon} = 0 \tag{A.3}$$

$$\mathbf{F}_{air}^{k+1}\left(p\right) - \mathbf{F}_{ext} - \mathbf{K}_s d\boldsymbol{\varepsilon} = \mathbf{F}_{air}^{k} + \frac{\partial \mathbf{F}_{air}^{k}}{\partial p} dp - \mathbf{F}_{ext} - \mathbf{K}_s d\boldsymbol{\varepsilon} = 0 \tag{A.4}$$

with the pressure and the position of the slider independent of each other.

The matrix form of Equation (A.3) and (A.4) is:

$$\begin{bmatrix} \dfrac{\partial \mathbf{R}^k}{\partial p} & \dfrac{\partial \mathbf{R}^k}{\partial \boldsymbol{\varepsilon}} \\ \dfrac{\partial \mathbf{F}_{air}^k}{\partial p} & \mathbf{K}_s \end{bmatrix} \begin{Bmatrix} dp \\ d\boldsymbol{\varepsilon} \end{Bmatrix} = \begin{Bmatrix} -\mathbf{R}^k \\ \mathbf{F}_{air}^k - \mathbf{F}_{ext} \end{Bmatrix} \tag{A.5}$$

A similar procedure as shown in chapter 2.3 can be followed to obtain the finite element formulation of Equation (A.5).

The Newton-Raphson algorithm starts with an initial guess and improves the solution iteratively. However, when the initial guess is far from the solution, convergence difficulties may be encountered [110]. In order to choose a reasonable initial guess, the pressure distribution is first calculated from an initial position. Then the Newton Raphson scheme (Equation (A.5)) is used to obtain updates of the pressure and slider position until the convergence criteria is satisfied.

Appendix B

Order of Magnitude Analysis of Energy Equation

For steady-state conditions, the energy equation for a Newtonian fluid is:

$$\rho c_p \mathbf{u} \cdot \nabla T = k_{air} \nabla^2 T + \mathbf{u} \cdot \nabla p + \phi \tag{B.1}$$

where ρ is the air density, $\mathbf{u}$ is the velocity of air flow as defined in Chapter 2, c_p is the specific heat at constant pressure, T is the temperature of the air, k_{air} is the thermal conductivity of air, and p is the pressure. ϕ is the viscous dissipation function defined as [135]:

$$\begin{aligned} \phi = 2\mu & \left[\left(\frac{\partial u}{\partial x} \right)^2 + \left(\frac{\partial v}{\partial y} \right)^2 + \left(\frac{\partial w}{\partial z} \right)^2 - \frac{1}{3} \left(\nabla \cdot \mathbf{u} \right)^2 \right] \\ & + \mu \left[\left(\frac{\partial u}{\partial y} + \frac{\partial v}{\partial x} \right)^2 + \left(\frac{\partial v}{\partial z} + \frac{\partial w}{\partial y} \right)^2 + \left(\frac{\partial u}{\partial z} + \frac{\partial w}{\partial x} \right)^2 \right] \end{aligned} \tag{B.2}$$

The relevant terms in Equation (B.1) and (B.2) can be determined following an "order-of-magnitude" analysis similar to the one described in Section 2.1. The dimensionless variables defined in Section 2.1 are:

$$x^* = \frac{x}{B}, y^* = \frac{y}{L}, z^* = \frac{z}{h_{\min}}$$
$$u^* = \frac{u}{U}, v^* = \frac{v}{V}, w^* = \frac{w}{W} \tag{B.3}$$
$$\rho^* = \frac{\rho}{\rho_a}, p^* = \frac{p}{P}$$

where B and L are the width and length of the slider, respectively. $h_{\min}$ is the minimum head/disk spacing. $h_{\min} << B, L$. $W = \frac{h_{\min}}{B}U = \frac{h_{\min}}{L}V$ is the velocity scale in the z direction. ρ_a is the ambient density of the air. $P = \frac{\mu UB}{h_{\min}^2}$ is the viscous pressure scale. The temperature can be normalized by the temperature difference between the slider and the disk surfaces $\Delta T \equiv T_s - T_d$, i.e., $T^* = \frac{T}{\Delta T}$ [106].

Substituting the dimensionless terms into Equation (B.1) and (B.2), we obtain:

$$\begin{aligned}
&\mathrm{Re}^* c_p \Delta T \left[\rho^* \left(u^* \frac{\partial T^*}{\partial x^*} + v^* \frac{\partial T^*}{\partial y^*} + w^* \frac{\partial T^*}{\partial z^*} \right) \right] \\
&= \frac{k_{air}\Delta T}{\mu} \left[\left(\frac{h_{\min}}{B} \right)^2 \frac{\partial^2 T^*}{\partial x^{*2}} + \left(\frac{h_{\min}}{L} \right)^2 \frac{\partial^2 T^*}{\partial y^{*2}} + \frac{\partial^2 T^*}{\partial z^{*2}} \right] \\
&+ U^2 \left(u^* \frac{\partial p^*}{\partial x^*} + v^* \frac{\partial p^*}{\partial y^*} + w^* \frac{\partial p^*}{\partial z^*} \right) \\
&+ 2\left(\frac{h_{\min}}{B} \right)^2 U^2 \left[\left(\frac{\partial u^*}{\partial x^*} \right)^2 + \left(\frac{\partial v^*}{\partial y^*} \right)^2 + \left(\frac{\partial w^*}{\partial z^*} \right)^2 - \frac{1}{3}\left(\frac{\partial u^*}{\partial x^*} + \frac{\partial v^*}{\partial y^*} + \frac{\partial w^*}{\partial z^*} \right)^2 \right] \\
&+ \left(\frac{h_{\min}}{B} \right)^2 \left(\frac{U^2}{V} \frac{\partial u^*}{\partial y^*} + V \frac{\partial v^*}{\partial x^*} \right)^2 + V^2 \left(\frac{\partial v^*}{\partial z^*} + \left(\frac{h_{\min}}{L} \right)^2 \frac{\partial w^*}{\partial y^*} \right)^2 + U^2 \left(\frac{\partial u^*}{\partial z^*} + \left(\frac{h_{\min}}{B} \right)^2 \frac{\partial w^*}{\partial x^*} \right)^2
\end{aligned} \tag{B.4}$$

where $\mathrm{Re}^* \equiv \frac{\rho_a UB}{\mu}\left(\frac{h_{\min}}{B}\right)^2 = \mathrm{Re}\left(\frac{h_{\min}}{B}\right)^2$ is the modified Reynolds number. For our problem Re^* is on the order of 10^{-8} (Chapter 2). Since $h_{\min} << B, L$ and the pressure is constant across the thickness of the fluid film, i.e., $\frac{\partial p^*}{\partial z^*} = 0$, Equation (B.4) can be simplified as:

$$\frac{k_{air}\Delta T}{\mu}\frac{\partial^2 T^*}{\partial z^{*2}} + U^2\left(u^*\frac{\partial p^*}{\partial x^*} + v^*\frac{\partial p^*}{\partial y^*}\right) + V^2\left(\frac{\partial v^*}{\partial z^*}\right)^2 + U^2\left(\frac{\partial u^*}{\partial z^*}\right)^2 = 0 \qquad \text{(B.5)}$$

Writing Equation (B.5) in dimensional form yields:

$$k_{air}\frac{\partial^2 T}{\partial z^2} + u\frac{\partial p}{\partial x} + v\frac{\partial p}{\partial y} + \mu\left(\frac{\partial v}{\partial z}\right)^2 + \mu\left(\frac{\partial u}{\partial z}\right)^2 = 0 \qquad \text{(B.6)}$$

Appendix C

Interpolation Module

The meshed air bearing surface used for the air bearing simulation is discretized into extremely refined elements to account for the small features in the air bearing surface design. On the other hand, the discretization of the air bearing surface for the thermo-mechanical model is relatively coarse because the details of the air bearing surface design are not included in the model. The discretizations of the air bearing surface for the air bearing simulation (CMRR/Talke Lab air bearing simulator) and the thermo-mechanical modeling (ANSYS) are shown in Figure C.1.

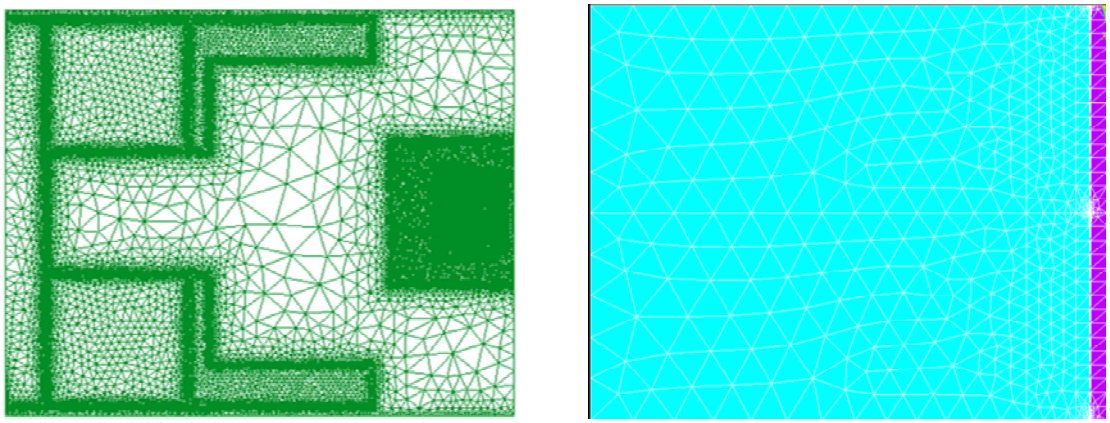

Air Bearing Simulation (Number of Node = 171999)

Thermo-Mechanical Modeling (Number of Node = 1420)

Figure C.1 Discretization of air bearing surface for air bearing simulation (CMRR/Talke Lab air bearing simulator) and thermo-mechanical modeling (ANSYS)

The thermal protrusion on the air bearing surface obtained from the thermo-mechanical modeling (ANSYS) alters the original air bearing surface design. A new air bearing calculation (CMRR/Talke Lab air bearing simulator) is needed to determine the updated pressure distribution and flying height. The interpolation module is used to map the thermal protrusion obtained from the thermo-mechanical modeling onto the meshed surface used for the air bearing simulation.

The principle of the interpolation algorithm is similar to the idea of shape function used in finite element method. The nodes used for the air bearing simulation are called "destination nodes" (○). The protrusion is mapped from the so-called "source nodes" (●), which is used in the thermo-mechanical modeling. When the destination node is lying in line with two nearest source nodes (Figure C.2), the thermal protrusion is calculated as:

$$z_0 = \begin{bmatrix} 1-\frac{x}{L} & \frac{x}{L} \end{bmatrix} \begin{Bmatrix} z_1 \\ z_2 \end{Bmatrix} \tag{C.1}$$

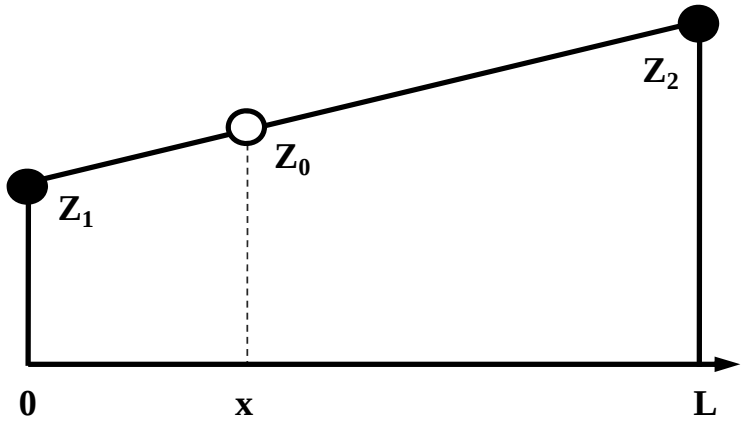

Figure C.2 Calculation of the thermal protrusion of the destination node for CMRR/Talke Lab air bearing simulator

When the destination node and the source nodes are not in line, the thermal protrusion is first calculated at the temporary points Z_t ($\otimes$). Z_t is the cross section between the line formed by the destination node and one of the nearest source points (Line Z_0Z_1), and the line formed by the other two nearest source nodes (Line Z_2Z_3). Z_t is then given by:

$$z_t = \begin{bmatrix} \frac{L}{L-x} & \frac{x}{L-x} \end{bmatrix} \begin{Bmatrix} z_2 \\ z_3 \end{Bmatrix} \tag{C.2}$$

Then the thermal protrusion at the destination points is calculated in the same way shown in Equation (C.1)

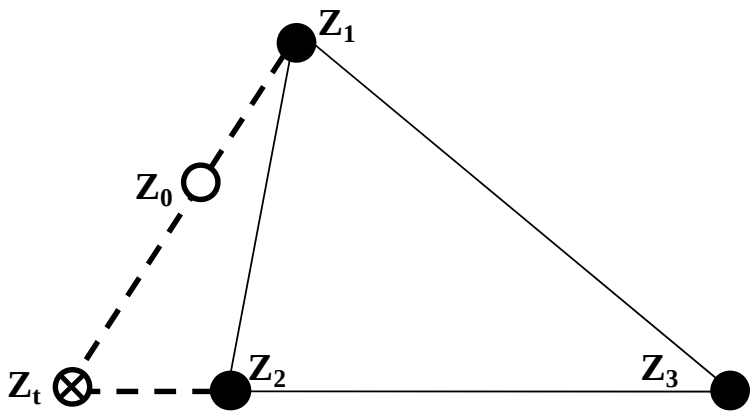

Figure C.3 Definition of temporary points in the interpolation of thermal protrusion

The final result of the interpolated thermal protrusion profile is demonstrated in Figure C.4, which exhibits a smooth thermal protrusion on the air bearing surface.

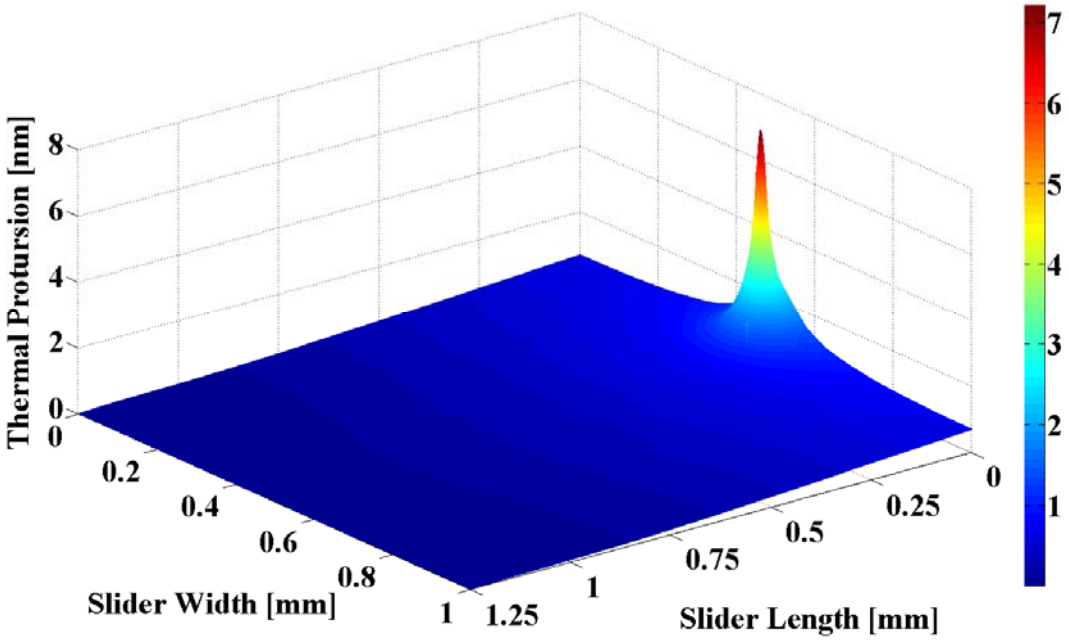

Figure C.4 Thermal protrusion interpolated onto the meshed surface for the air bearing calculation

Bibliography

[1] "It's happening now: This is the Tera Era," Hitachi Global Storage Technologies. [http://www.hitachigst.com/tech/techlib.nsf/techdocs/2981DFBB7F54012286257481 0012A04D/$file/TeraEra_WP.pdf].

[2] J. F. Gantz, C. Chute, A. Manfrediz, S. Minton, D. Reinsel, W. Schlichting, and A. Toncheva, "The diverse and exploding digital universe – An updated forecast of worldwide information growth through 2011," An IDC White Paper, Mar. 2008.

[3] R. E. Bohn and J. E. Short, "How much information? 2009 report on American consumers," Global Information Industry Center, University of California, San Diego, Dec. 2009.

[4] J. E. Short, R. E. Bohn, and C. Baru, "How much information? 2010 report on enterprise server information," Global Information Industry Center, University of California, San Diego, Jan. 2011.

[5] "Disk storage device," Wikipedia. [http://en.wikipedia.org/wiki/Data_storage_device].

[6] R. E. Rottmayer, S. Batra, Dorothea Buechel, W. A. Challener, J. Hohlfeld, Y. Kubota, L. Li, B. Lu, C. Mihalcea, K. Mountfield, K. Pelhos, C. Peng, T. Rausch, M. A. Seigler, D. Weller, and X.-M. Yang, "Heat-assisted magnetic recording," IEEE Transactions on magnetic, Vol. 42, No. 10, Oct. 2006, pp. 2417 – 2421.

[7] F. K. Engel, "Oberlin Smith and the invention of magnetic sound recording," An appreciation on the 150th anniversary of the inventor's birth, revised on Jul. 2006. [http://www.richardhess.com/tape/history/Engel--Oberlin_Smith_2006.pdf].

[8] Oberlin Smith, "Some possible forms of phonograph," The Electrical World, Sep. 8, 1888, pp.116 – 117.

[9] F. Engel and P. Hammer, "A selected history of magnetic recording," additional edited by R. L. Hess. [http://www.richardhess.com/tape/history/Engel_Hammar--Magnetic_Tape_ History.pdf].

[10] S. J. Begun, "Magnetic recording," History of magnetic recording, Murray Hill Books, New York, 1949.

[11] "Valdemar Poulsen," Wikipedia. [http://en.wikipedia.org/wiki/Valdemar_Poulsen].

[12] V. Poulsen, "Method of recording and reproducing sounds or signals," U. S. Patent 661,619, Nov. 13, 1900.

[13] "1935 AEG Magnetophon tape recorder," Mix, Sep. 1, 2006. [http://www.mixonline.com/TECnology-Hall-of-Fame/aeg-magnetophone-recorder-090106/].

[14] E. D. Daniel, C. D. Mee, and M. H. Clark, "Magnetic recording: the first 100 years," IEEE Press, New York, 1999.

[15] "Magnetic recording," Encyclopedia Britannica. [http://www.britannica.com/EBchecked/topic/357264/magnetic-recording].

[16] W. R. Qualls, "The future of tape technology," 2007 Imation End User Council (EUC) Symposium, Mar. 24 – 28, 2007, Marina del Ray, CA. [http://www.imation.com/euc/pdfs/EUC_07_Qualls.pdf].

[17] "Made in IBM labs: IBM research sets new record in magnetic tape data density," IBM Research – Zurich, Jan. 22, 2010. [http://www.zurich.ibm.com/news/10/storage.html].

[18] M. Ferelli, "In the tape vs. disk war, think tape and disk," Enterprise Systems, Feb. 17, 2009. [http://esj.com/Articles/2009/02/17/In-the-Tape-vs-Disk-War-Think-Tape-AND-Disk.aspx?Page=3].

[19] "IBM 305 RAMAC," Wikipedia. [http://en.wikipedia.org/wiki/IBM_305_RAMAC].

[20] "Storage product profiles," IBM Archive. [http://www-03.ibm.com/ibm/history/exhibits/storage/storage_profile.html].

[21] "The IBM 350 RAMAC disk file," Designated an international historic landmark by the American Society of Mechanical Engineers, Feb. 27, 1984. [http://files.asme.org/asmeorg/Communities/History/Landmarks/5573.pdf].

[22] "Main timeline of significant events and products", Computer History Museum Hard Disk Drive Events. [http://chmhdd.wetpaint.com/page/Main+Timeline+of+Significant+Events+and+Products#fbid=T9O2fHFJlfD].

[23] "Details of IBM 1311 disk storage drive," Computer History Museum. [http://www.computerhistory.org/collections/accession/X1395.97].

[24] Adam Oester, "The history of hard drives," [http://www.ehow.com/about_5366633_history-hard-drives.html].

[25] "Amazing facts and figures about evolution of hard disk drives," Pingdom. [http://royal.pingdom.com/2010/02/18/amazing-facts-and-figures-about-the-evolution-of-hard-disk-drives/]

[26] "1.8-inch hard disk drives," Toshiba. [http://sdd.toshiba.com/main.aspx?Path=storagesolutions/1.8-inchharddiskdrives/].

[27] D. Szabados, "Future storage technology: How to store the entire U.S. Library of Congress on a coin," Seagate Enterprise: Inside IT Storage. [http://enterprise.media.seagate.com/2010/12/inside-it-storage/future-storage-technology-how-to-store-the-entire-u-s-library-of-congress-on-a-coin/].

[28] "Memory storage density," Wikipedia. [http://en.wikipedia.org/wiki/Memory_storage_density].

[29] "5,400 rpm 2.5-inch SATA hard disk drives," Capacity & power efficiency for data-intensive & energy-sensitive applications, Toshiba. [http://sdd.toshiba.com/techdocs/MQ01ABDxxx.pdf].

[30] J.-J. Maleval, "HDD technology trends," Storage Newsletter, Jul. 2011. [http://www.storagenewsletter.com/news/disk/hdd-technology-trends-ibm].

[31] C. H. Bajorek, "Trends in recording and control technologies and evolution of subsystem architectures for data storage," Proceedings on VLSI and Computer Peripherals: VLSI and Microelectronic Applications in Intelligent Peripherals and their Interconnection Networks (CompEuro 89), Hamburg, West Germany, May 8 – 12, 1989, DOI: 10.1109/CMPEUR.1989.93329.

[32] Shuzhu Cheng (程守洙), Zhiyong Jiang (江之永), Panxin Hu (胡盘新), Yujun Tang (汤毓骏), and Kaixin Song (宋开欣), "College physics (普通物理学)," 5th ed, Vol. 2, Higher Education Press (高等教育出版社), Beijing, 1998.

[33] HyperPhysics. [http://hyperphysics.phy-astr.gsu.edu/hbase/solids/magpr.html#c1].

[34] "Diamagnetism," Wikipedia. [http://en.wikipedia.org/WIKI/Diamagnetism#Diamagnetic_materials].

[35] "Ferromagnetism,"Wikipedia. [http://en.wikipedia.org/wiki/ferromagnetism].

[36] B. D. Cullity and C. D. Graham, "Introduction to magnetic materials," *Ferromagnetism*, 2nd edition, IEEE Press/Wiley, Hoboken, NJ, 2009, pp. 116 – 117.

[37] H. N. Bertram, "Theory of magnetic recording," Cambridge University Press, Cambridge; New York, 1994.

[38] R. Brunner, “Properties of carbon overcoats and perfluoro-polyether lubricants in hard disk drives,” Ph.D. Dissertation, Department of Mechanical and Aerospace Engineering, University of California, San Diego, CA, 2009.

[39] S. Khizroev, Y. Liu, K. Mountfield, M. H. Kryder and D. Litvinov, “Physics of perpendicular magnetic recording: writing process,” Journal of Magnetism and Magnetic Materials, Vol. 246, 2002, pp. 335 – 344.

[40] J. N. Zhou, B. R. Acharya, P. Gill, E. N. Abarra, M. Zheng and G. Choe, “The role of underlayer permeability in wide area track erasure in high-density perpendicular recording,” Digests of the IEEE International Magnetics Conference, Apr. 2005, pp. 1335 – 1336. DOI: 10.1109/INTMAG.2005.1464097

[41] E. Grochowski, “Evolution of magnetic read/write sensors,” Hitachi Global Storage Technologies. [https://www1.hitachigst.com/hdd/hddpdf/tech/hdd_technology2003.pdf].

[42] “Magnetic recording theory.” [https://ccrma.stanford.edu/courses/192a/6-Magnetic_Recording.pdf].

[43] N. Smith, “Reciprocity principles for magnetic recording theory,” IEEE Transactions on Magnetics, Vol. MAG-23, No. 4, Jul. 1987, pp. 1995 – 2002.

[44] “Karlqvist head field,” IEEE Magnetics Wiki. [http://www.dev.hershberg.com/ieee/wiki/index.php?title=Karlqvist_Head_Field].

[45] R. L. Wallace, “The reproduction of magnetically recorded signals,” The Bell System Technical Journal, Oct, 1951, pp. 1145 – 1173.

[46] “Disk read-and-write head,” Wikipedia. [http://en.wikipedia.org/wiki/Disk_read-and-write_head].

[47] J. Belleson and E. Grochowski, “The era of giant magnetoresistive heads,” Hitachi Global Storage Technologies. [https://www1.hitachigst.com/hdd/technolo/gmr/gmr.htm].

[48] R. New, “The future of magnetic recording technology,” Hitachi Global Storage Technologies, Apr. 11, 2008. [http://asia.stanford.edu/events/spring08/slides402S/0410-Dasher.pdf].

[49] Bestofmedia Team, “Read/write heads designs: Magneto-resistive heads,” Tom’s Hardware. [http://www.tomshardware.com/reviews/hard-drive-magnetic-storage-hdd,3005-3.html].

[50] R. Lawrence-Comstock, “Introduction to magnetism and magnetic recording,” John Wiley & Sons, 1999.

[51] "The giant magnetoresistive head: A giant leap for IBM research," IBM Reasearch. [http://researchweb.watson.ibm.com/research/gmr.html].

[52] "Tunnel magnetoresistance," Wikipedia. [http://en.wikipedia.org/wiki/magnetic_tunnel_effect].

[53] "Recording head/Head materials," Hitachi Global Storage Technologies. [https://www1.hitachigst.com/hdd/research/recording_head/headmaterials/index.html].

[54] "Storage solutions guide," Barracuda® XT, Seagate, Oct. 2010. [http://www.seagate.com/docs/pdf/whitepaper/storage_solutions_guide.pdf].

[55] M. Duwensee, "Numerical and experimental investigations of the head/disk interface," Ph.D. Dissertation, Department of Mechanical and Aerospace Engineering, University of California, San Diego, CA, 2007.

[56] "Recording head/ADV. Head processing," Hitachi Global Storage Technologies. [https://www1.hitachigst.com/hdd/research/recording_head/headprocessing/index.html].

[57] N. Liu and D. B. Bogy, "Air-bearing shear force in the head-disk interface of hard disk," Tribology Letter, 2009, Vol. 35, pp. 121 – 125.

[58] "Head-disk interface," Hitachi Global Storage Technologies. [https://www1.hitachigst.com/hdd/research/storage/hdi/index.html].

[59] Bestofmedia Team, "Head sliders," Tom's Hardware. [http://www.tomshardware.com/reviews/hard-drive-magnetic-storage-hdd,3005-4.html].

[60] L. K. Dorius and L.S. Samuelson (To International Business Machines Corporation), "Negative pressure slider with optimized leading pocket for profile control," U. S. Patent 5,583,722, Dec. 10, 1996.

[61] "Disk technology," Hitachi Global Storage Technologies. [https://www1.hitachigst.com/hdd/research/storage/adt/index.html].

[62] L. Wu and F. E. Talke, "Modeling laser induced lubricant depletion in heat-assisted-magnetic recording systems using a multiple-layered disk structure," Microsystem Technologies, Vol. 17, 2011, pp. 1109 – 1114.

[63] R. Wood, "The feasibility of magnetic recording at 1 Terabit per square inch," IEEE Transaction on Magnetics, Vol. 36, No. 1, Jan. 2000, pp. 36 – 42.

[64] S. H. Charap, P.-L. Lu and Y. H, "Thermal stability of recorded information at high densities," IEEE Transactions on Magnetics, Vol. 33, No. 1, Jan. 1997, 978 – 983.

[65] J. C. Mallinson, “On extremely high density digital recording,” IEEE Transactions on Magnetics, Vol. 10, No. 2, Jun. 1974, pp. 368 – 373.

[66] E. Grochowski and D. A. Thompson, “Outlook for maintain areal density growth in magnetic recording,” IEEE Transactions on Magnetics, Vol. 30, No. 6, Nov. 1994, pp. 3797 – 3800.

[67] “Definition: What is the superparamagnetic effect?” http://www.dataclinic.co.uk/hard-disk-superparamagnetic-effect.htm

[68] R. Wood, M. Williams, A. Kavcic and J. Miles, “The feasibility of magnetic recording at 10 Terabits per square inch on conventional media,” IEEE Transaction on Magnetics, Vol. 45, No. 2, Feb. 2009, pp. 917 – 923.

[69] H. J. Richter and A. Yu. Dobin, “Angle effects at high-density magnetic recording,” Journal of Magnetism and Materials, Vol. 287, 2005, pp. 41 – 50.

[70] D. Weller and A. Moser, “Thermal effect limits in untrahihg-density magnetic recording,” IEEE Transactions on Magnetics, Vol. 35, No. 6, Nov. 1999, pp. 4423 – 4439.

[71] H. Kronmüller, K.-D. Durst and M. Sagawa, “Analysis of the magnetic hardening mechanism in Re-FeB Permanent magnets,” Journal of Magnetism and Magnetic Materials, Vol. 74, No. 3, Oct. 1988, pp. 291 – 302.

[72] F. G. Sánchez, “Modeling of field and thermal magnetization reversal in nanostructured magnetic materials,” Ph.D. Dissertation, Dpto de Física Teórica de la Materia Condensada, Universidad Autónoma de Madrid, Madrid, 2007.

[73] H. N. Bertram, H. Zhou and R. Gustafson, “Signal to noise ratio scaling and density limit estimates in longitudinal magnetic recording,” IEEE Transactions on Magnetics, Vol. 34, No. 4, Jul. 1998, pp. 1845 – 1874.

[74] K. Nguyen, “Perpendicular recording: A boom for consumer electronics,” Hitachi Global Storage Technologies. [https://www1.hitachigst.com/hdd/research/images/pr%20images/PerpRecWP.pdf].

[75] M. L. Plumer, J. V. Ek and W. C. Cain, “New paradigms in magnetic recording,” Physics in Canada (La Physique au Canada), Vol. 67, No. 1, 2011, pp. 25 – 29.].

[76] M. A. Samad, E. Rismani, H. Yang, S. K. Shiha and C. S. Bhatia, “Overcoat free magnetic media for lower magnetic spacing and improved tribological properties for higher areal density,” Tribology Letters, Vol. 43, No. 3, 2011, pp. 247 – 256.

[77] T. Imamura, M. Yamagishi M and S. Nishida S, “In situ measurements of temperature distribution of air-bearing surface using thermography,” IEEE Transactions on Magnetics, Vol. 38, No. 5, Sep. 2002, pp. 2147 – 2149.

[78] B. E. Schultz, “Thermal fly-height control (TFC) technology in Hitachi hard disk drives,” Apr. 2007. [http://www.hitachigst.com/tech/techlib.nsf/techdocs /98EE13311A54CAC886257171005E0F16].

[79] C. Mellor, “Raising the roof on the shingled write problem,” Sep. 27, 2010. [http://www.theregister.co.uk/2010/09/27/sw_tdmr/].

[80] Y. Shiroishi, K. Fukuda, I. Tagawa, H. Iwasaki, S. Takenoiri, H. Tanaka, H. Mutoh and N. Yoshikawa, “Future options for HDD storage,” IEEE Transactions on Magnetics, Vol. 45, No. 10, Oct. 2009, pp. 3816 – 3822.

[81] C. Mellor, “Hitachi GST plugs its areal hole with shingles,” Jul. 29, 2011. [http://www.channelregister.co.uk/2011/07/29/hgst_smr/].

[82] G. Gibson and M. Polte, “Directions for shingled-write and two dimensional magnetic recording system architectures: Synergies with solid-state disks (CMU-PDL-09-104),” Parallel Data Laboratory, 2009, Paper 7. [http://repository.cmu.edu/pdl/7].

[83] M. H. Kryder, E. C. Gage, T. W. McDaniel, W. A. Challener, R. E. Rottmayer, G. Ju, Y.-T. Hsia and M. F. Erden, “Heat assisted magnetic recording,” Proceedings of the IEEE, Vol. 96, No. 11, Nov. 2008, pp. 1810 – 1835.

[84] J.-G. Zhu, Xiaochun Zhu and Yuhui Tang, “Microwave assisted magnetic recording,” IEEE Transactions on Magnetics, Vol. 44, No. 1, Jan. 2008, pp. 125 – 131.

[85] S. Li, B. Livshitz, H. N. Bertram and E. E. Fullerton, “Microwave assisted magnetization reversal and multilevel recording in composite media.” [http://cem01.ucsd.edu/papers/JAP_2009_MAMR.pdf].

[86] J. K. W. Yang, Y. Chen, T. Huang, H. Duan, N. Thiyagarajah, H. K. Hui, S. H. Leong and V. Ng, “Fabrication and characterization of bit-patterned media beyond 1.5 Tbit/in^2,” Nanotechnology, Vol. 22, 2011, pp. 385301.

[87] B. D. Terris, T. Thomson and G. Hu, “Patterned media for future magnetic data storage,” Microsystem Technology, vol. 13, pp. 189 – 196, 2007.

[88] N. Robertson, “Magnetic data storage with patterned media,” Hitachi Global Storage Technologies. [http://www.nnin.org/doc/snmr10/Cornell_nanomanufacturing_2010.pdf].

[89] B. D. Terris, “Fabrication challenges for patterned recording media,” Journal of Magnetism and Magnetic Materials, Vol. 321, 2009, pp. 512 – 517.

[90] M. T. Moneck and J.-G. Zhu, “Challenges and promises in the fabrication of bit patterned media,” Proceedings on SPIE, Vol. 7823, 2010, 78232U. DOI:10.1117/12.875542

[91] I. M. Hutchings, “Tribology: Friction and wear of engineering materials,” Lubricants and lubrication, CRC Press, 1992, pp. 62 – 67.

[92] M. H. Wahl, “Numerical and experimental investigation of the head/disk interface,” Ph. D. Dissertation, Department of Mechanical and Aerospace Engineering, University of California, San Diego, 1994.

[93] Y. Hori, “Hydrodynamic lubrication,” Foundations of Hydrodynamic Lubrication, Springer, Verlag, Tokyo, 2006.

[94] P. K. Kundu and I. M. Cohen, “Fluid mechanics,” Conservation Laws, 4th ed., Academic Press, Burlington, MA, USA, 2008, pp.81 – 137.

[95] S. Nemat-Nasser and M. Hori, “Micromechanics: overall properties of heterogeneous materials,” 2nd revised ed., North Holland, Amsterdam, 1999, pp.140 - 161.

[96] “Divergence theorem,” Wikipedia. [http://en.wikipedia.org/wiki/Divergence_ theorem].

[97] G. Ramanaiah, “Influence of molecular mean free path in gas-lubricated thrust bearings,” Wear, Vol. 14, No. 3, Sep. 1968, pp. 193 – 198.

[98] N. Liu and E. Y.-K. Ng, “The posture effects of a slider air bearing on its performance with a direct simulation Monte Carlo method,” Journal of Micromechanics and Microengineering, Vol. 11, No. 5, pp. 463 – 473.

[99] A. Burgdorfer, “Influence of the mean free path on the performance of hydrodynamic gas lubricated bearings,” ASME Journal of Basic Engineering (Transaction ASME Series D), Vol. 81, 1989, pp. 84 – 100.

[100] W. Huang and D. B. Bogy, “The effect of the accommodation coefficient on slider air bearing simulation,” Journal of Tribology, Vol. 122, No. 2, Apr. 2000, pp. 427 – 435.

[101] Y.-T. Hsia and G. A. Domoto, “An experimental investigation of molecular rarefaction effects in gas lubricated bearings at ultra-low clearances,” ASME Journal of Tribology, Vol. 105, No. 1, Jan. 1983, pp. 120 – 130.

[102] R. F. Gans, “Lubrication theory at arbitrary Knudsen number,” Journal of Tribology, Vol. 107, No. 3, Jul. 1985, pp. 431 – 433.

[103] S. Fukuai and R. Kaneko, “Analysis of ultra-thin gas film lubrication based on linearized Boltzmann equation: First report – Derivation of a generalized lubrication equation including thermal creep flow,” Journal of Tribology, Vol. 110, No.2, Apr. 1988, pp. 253 – 261.

[104] “Finite element method,” Wikipedia. [http://en.wikipedia.org/wiki/Finite_ element_method].

[105] O. C. Zienkiewicz and R. L. Taylor, “The finite element method,” Steady-state field problems - heat conduction, electric and magnetic potential, fluid flow, etc., 5th ed., Vol. 1, Butterworth-Heinemann, Oxford, 2000, pp.140 – 161.

[106] S. Zhang and D. B. Bogy, “A heat transfer model for thermal fluctuations in a thin slider/disk air bearing,” International Journal of Heat and Mass Transfer, Vol. 42, 1999, pp. 1791 – 1800.

[107] “Air properties,” The Engineering ToolBox. [http://www.engineeringtoolbox. com/air-properties-d_156.html].

[108] T. J. R. Hughes, “The finite element method: Linear static and dynamic finite element analysis,” Dover, Mineola, NY, 2000.

[109] J. Fish and T. Belytschko, “A first course in finite element,” John Wiley and Sons, West Sussex, England, 2007.

[110] “Newton’s method,” Wikipeida. [http://en.wikipedia.org/wiki/Newton's_ method].

[111] T. Ishida, O. Morita, M. Noda, S. Seko, S. Tanaka and H. Ishioka, “Discrete-track magnetic disk using embossed substrate,” IEICE Transactions on Fundamentals of Electronics, Communications and Computer Sciences, Vol. E76 – A, No. 7, Jul. 1993, pp. 1161 – 1163.

[112] Y. Soeno, M. Moriya, K. Ito, K. Hattori, A. Kaizu, T. Aoyama, M. Matsuzaki and H. Sakai, “Feasibility of discrete track perpendicular media for high track density recording,” IEEE Transactions on Magnetics, Vol. 39, No. 4, Jul. 2003, pp. 1967 – 1971.

[113] D. Wachenschwanz, W. Jiang, E. Roddick, A. Homola, P. Dorsey, B. Harper, D. Treves and C. Bajorek, “Design of a manufacturable discrete track recording medium,” IEEE Transactions on Magnetics, Vol. 41, No. 2, Feb. 2005, pp. 670 – 675.

[114] Y. Soeno, M. Moriya, A. Kaizu and M. Takai, “Performance evaluation of discrete track perpendicular media for high recording density,” IEEE Transactions on Magnetics, Vol. 41, No. 10, Oct. 2005, pp. 3220 – 3222.

[115] K. Kawazoe, M. Yotsuya, T. Shimamura, and K. Okada, “Dynamics of flying head slider for grooved discrete track disk,” IEEE/ASME International Conference on Adavanced Intelligent, Tokyo, Japan, 1993, pp. 894 – 898.

[116] Y. Mitsuya, “A simulation method for hydrodynamic lubrication of surfaces with two-dimensional isotropic or anisotropic roughness using mixed average film thickness,” Bulletin of JSME, Vol. 27, No. 231, Sep. 1984, pp. 2036 – 2044.

[117] Y. Mitsuya, T. Ohkubo and H. Ota, “Averaged Reynolds equation extended to gas lubrication processing surface roughness in the slip flow regime: Approximate method and confirmation experiments,” ASME Journal of Tribology, Vol. 111, No. 3, Jul. 1989, pp. 495 – 503.

[118] Y. Mitsuya and T. Hayashi, “Transient response of head slider when flying over textured magnetic disk media,” in Proceedings of Japan International Tribology Conference, Maruzen, Tokyo, 1990, Vol. 3, pp. 1941 – 1946.

[119] T. Ohkubo and Y. Mitsuya, “An experimental investigation of the effect of moving two-dimensional roughness on thin film gas-lubrication for flying head slider,” in Proceedings of Japan International Tribology Conference, Maruzen, Tokyo, 1990, Vol. 3, pp. 1329 – 1332.

[120] N. Tagawa and D. B. Bogy, “Air film dynamics for micro-textured flying head slider bearings in magnetic hard disk drives,” ASME Journal of Tribology, Vol. 124, No. 3, Jul. 2002, pp. 568 – 574.

[121] A. N. Murthy, I. Etsion and F. E. Talke, “Analysis of surface textured air bearing sliders with rarefaction effects,” Tribology Letters, Vol. 28, No. 3, Dec. 2007, pp. 251 – 261.

[122] J. Li, J. Xu and Y. Shimizu, “Performance of sliders flying over discrete-track media,” ASME Journal of Tribology, Vol. 129, No. 4, Oct, 2007, pp. 712 – 719.

[123] M. Duwensee, S. Suzuki, J. Lin, D. Wachenschwanz and F. E. Talke, “Air bearing simulation of discrete track recording media,” IEEE Transactions on Magnetics, Vol. 42, No. 10, Oct. 2006, pp. 2489 – 2491.

[124] M. Duwensee, S. Suzuki, J. Lin, D. Wachenschwanz and F. E. Talke, “Simulation of the head disk interface for discrete track media,” Microsystem Technologies, Vol. 13, No. 8 – 10, 2007, pp. 1023 – 1030.

[125] J.-P. Peng, G. Wang, S. Thrivani, J. Chue, M. Nojaba and P. Thayamballi, “Numerical and experimental evaluation of discrete track recording technology,” IEEE Transactions on Magnetics, Vol. 42, No. 10, Oct. 2006, pp. 2462 – 2464.

[126] Y. Yoon and F. E. Talke, “Touch-down and take-off hysteresis of magnetic recording sliders on discrete track media,” Microsystem Technologies, Vol. 16, No. 1 – 2, 2010, pp. 273 – 278.

[127] S. Fukui and R. Kaneko, “Analysis of ultra-thin gas film lubrication based on linearized Boltzmann equation: First report – Derivation of a generalized lubrication equation including thermal creep flow,” ASME Journal of Tribology, Vol. 110, No. 2, Apr. 1988, pp. 253 – 261.

[128] M. Wahl, P. Lee and F. E. Talke, “An efficient finite element-based air bearing simulator for pivoted slider bearings using bi-conjugate gradient algorithms,” STLE Tribology Transactions, Vol. 39, No. 1, 1996, pp. 130 – 138.

[129] K. Ono, “Effect of van der Waals forces in a near contact head-disk interface,” IEEE Transactions on Magnetics, Vol. 44, No. 11, Nov. 2008, pp. 3675 – 3678.

[130] Y. Shimizu, K. Ono, J. G. Xu, R. Tsuchiyama and H. Anan, “Study of a spherical-pad head slider for stable low-clearance recording in near-contact regime,” Tribology Letters, Vol. 30, No. 30, 2008, pp. 161 – 167.

[131] H. Li, J. H. Li, J. G. Xu, Y. Shimizu, K. Ono and S. Yoshida, “Numerical simulation of touchdown/takeoff hysterisis of sphere-pad slider by considering the liquid bridge between the slider and lubricant-disk,” in Proceedings of STLE/ASME International Joint Tribology Conference (IJTC2008 – 71010), Oct. Miami, 2008, pp. 165 – 167.

[132] ANSYS, Inc., “ANSYS, Inc. Theory Reference,” Heat flow, ANSYS Release 9.0, Canonsburg, PA, 2006.

[133] P. Zeng (曾攀), W. Shi (石伟) and L. P. Lei (雷丽萍), “The finite element method in engineering (工程有限元方法),” Science Press (科学出版社), Beijing, 2010.

[134] ANSYS, Inc., “ANSYS coupled-field analysis guide,” Sequentially coupled physics analysis, ANSYS Release 10.0, Canonsburg, PA, 2005.

[135] H. H. Winter, “Viscous dissipation term in energy equations.” [http:// rheology.tripod.com/z07.13.pdf].

[136] “Prandtl number,” Wikipedia. [http://en.wikipedia.org/wiki/Prandtl_number].

[137] T. Imamura, M. Yamagishi M and S. Nishida S, “In situ measurements of temperature distribution of air-bearing surface using thermography,” IEEE Transactions on Magnetics, Vol. 38, No. 5, Sep. 2002, pp. 2147 – 2149.

[138] L. Pust, C. J. T Rea, and S. Gangopadhyay, “Thermomechanical head performance,” IEEE Transactions on Magnetics, Vol. 38, No. 1, Jan. 2002, pp. 101 – 106.

[139] H. Li, B. Liu B and T.-C. Chong, “Numerical simulation of slider temperature rise caused by read/write current,” Journal of Applied Physics, Vol. 97, No. 10, 2005, pp. 10P306.

[140] M. Kurita, J. Xu, M. Tokuyama, K. Nakamoto, S. Saegusa and Y. Maruyama, “Flying-height reduction of magnetic-head slider due to thermal protrusion,” IEEE Transactions on Magnetics, Vol. 41, No. 10, Oct. 2005, pp. 3007 – 3009.

[141] S. Song, L. Wang, V. Rudman, D. Fang, K. Stoev, J. Wang and B. Sun, “Finite element analysis of alternating write-current-induced pole tip protrusion in magnetic recording heads,” IEEE Transactions on Magnetics, Vol. 43, No. 6, Jun. 2007, pp. 2217 – 2219.

[142] S. Song, T. Pan, D. Fang, K. Stoev, M. Ho and S. Mao, “A comparative study of alternating write-current-induced pole tip protrusion in perpendicular and longitudinal recording heads,” Journal of Applied Physics, Vol. 103, No. 7, 2008, pp. 07F547.

[143] J. Xu, J. Kiely, Y.-T. Hsia and F. E. Talke, “Effect of thermal pole tip protrusion and disk roughness on slider disk contacts”, Microsystem Technologies, Vol. 15, No. 5, 2009, pp. 687 – 693.

[144] A. Dietzel, R. Berger, P. Machtle, M. Despont, W. Haberle, R. Stutz, G. K. Binnig and P. Vettiger, “In situ slider-to-disk spacing on a nanometer scale controlled by microheater-induced slider deformations,” Sensors and Actuators A: Physical, Vol. 100, No. 1, Aug. 2002, pp. 123 – 130.

[145] M. Suk, K. Miyake, M. Kurita, H. Tanaka, S. Saegusa and N. Robertson, “Verification of thermally induced nanometer actuation of magnetic recording transducer to overcome mechanical and magnetic spacing challenges,” IEEE Transactions on Magnetics, Vol. 41, No. 11, Nov. 2005, pp. 4350 – 4352.

[146] M. Kurita, T. Shiramatsu, K. Miyake, A. Kato, M. Soga, H. Tanaka, S. Saegusa and M. Suk, “Active flying-height control slider using MEMS thermal actuator,” Microsystem Technologies, Vol. 12, No. 4, 2007, pp. 369 – 375.

[147] J. Juang and D. B. Bogy, “Air-bearing effects on actuated thermal pole-tip protrusion for hard disk drives,” ASME Journal of Tribology, Vol. 129, No. 3, Jul. 2007, pp. 570 – 578.

[148] J. Fritzsche, H. Li, H. Zheng, K. Amemiya and F. E. Talke, “The effect of air bearing contour design on thermal pole-tip protrusion,” Microsystem Technologies, Vol. 17, No. 5 – 7, 2011, pp. 813 – 820.

[149] J. Liu, J. Li, J. Xu and S. Yoshida, “Optimization of micro-thermal actuator for flying height control,” Microsystem Technologies, Vol. 16, No. 1 – 2, 2010, pp. 249 – 255.

[150] H. Li, C.-T. Yin and F. E. Talke, “Thermal insulator design for optimizing the efficiency of thermal flying height control sliders,” Journal of Applied Physics, Vol. 105, No. 7, 2009, pp. 07C122.

[151] H. Li, M. Kurita, J. Xu and S. Yoshida, “Iteration method for analysis of write-current-induced thermal protrusion,” Microsystem Technologies, Vol. 16, No. 1 – 2, 2010, pp. 161 – 167.

[152] A. Narayanaswamy, S. Shen, L. Hu, X. Chen and G. Chen, “Breakdown of the Planck blackbody radiation law at nanoscale gaps,” Applied Physics A: Materials Science & Processing, Vol. 96, No. 2, 2009, pp. 357 – 362.

[153] S. Shen, A. Narayanaswamy and G. Chen, “Surface phonon polaritons mediated energy transfer between nanoscale gaps,” Nano Letters, Vol. 9, No. 8, 2009, pp. 2909 – 2913.

[154] S. Zhang and D. B. Bogy, “Variation of the heat flux between a slider and air bearing when the slider flies over an asperity,” IEEE Transactions on Magnetics, Vol. 34, No. 4, Jul. 1998, pp. 1705 – 1707.

[155] S. Zhang and D. B. Bogy, “A heat transfer model for thermal fluctuations in a thin slider/disk air bearing,” International Journal of Heat and Mass Transfer, Vol. 42, No. 10, May 1999, pp. 1791 – 1800.

[156] F. P. Incropera and D. P. DeWitt, “Fundamentals of heat and mass transfer,” Physical Origins and Rate Equations, 5th ed., John Wiley & Sons, Inc., New York, 2001, pp. 9 – 11.

[157] P. Kim and M. Suk, “Ramp load/unload technology in hard disk drives,” Hitachi Global Storage Technologies. [http://www.hitachigst.com/tech/techlib.nsf/techdocs/9076679E3EE4003E86256FAB005825FB/$file/LoadUnload_white_paper_FINAL.pdf].

[158] K. Matsumoto, A. Inomata and S. Hasegawa S, “Thermally assisted magnetic recording,” Jun. 2005. [http://www.fujitsu.com/downloads/MAG/vol42-1/paper18.pdf].

[159] L. Pan and D. B. Bogy, “Data storage: Heat-assisted magnetic recording,” Nature Photonics, Vol. 3, 2009, pp. 189 – 190.

[160] W. A. Challener, C. Peng, A. V. Itagi, D. Karns, W. Peng, Y. Peng, X. Yang, X. Zhu, N. J. Gokemeijer, Y. – T. Hsia, G. Ju, R. E. Rottmayer, M. A. Seigler and E. C. Gage, "Heat-assisted magnetic recording by a near-field transducer with efficient optical energy transfer," Nature Photonics, Vol. 3, 2009, pp. 220 – 224.

[161] B. C. Stipe, T. C. Strand, C. C. Poon, H. Balamane, T. D. Boone, J. A. Katine, J. – L. Li, V. Rawat, H. Nemoto, A. Hirotsune, O. Hellwig, R. Ruiz, E. Dobisz, D. S. Kercher, N. Robertson, T. R. Albrecht and B. D. Terris, "Magnetic recording at 1.5 Pb m^{-2} using an integrated plasmonic antenna," Nature Photonics, Vol. 4, Jun. 2010, pp. 484 – 488.

[162] W. Peng, Y.-T. Hsia, K. Sendur and T. McDaniel T, "Thermo-magneto-mechanical analysis of head-disk interface in heat assisted magnetic recording," Tribology International, Vol. 38, 2005, pp. 588-593.

[163] H. Li, B. Liu, H. Ye and T.-C. Chong, "Thermally induced stability issues of head-disk interface in heat-assisted magnetic recording systems," Japan Journal of Applied Physics, Vol. 44, No. 11, 2005, pp. 7950 – 7953.

[164] M. F. Erden, P. D. Mathur, W. A. Challener, E. C. Gage, W. Peng and T. W. McDaniel (To Seagate Technology LLC.), "Compensating the effects of static head-media spacing variations and nonlinear transition shift in heat assisted magnetic recording," U. S. Patent US 2007/0230012 A1, Oct. 4, 2007.

[165] M. Gauvin, H. Zheng, B. Suen, J. Lee, H. J. Kang and F. E. Talke, "Enhanced photo-thermal stability of modified PFPE lubricants under laser beam exposure," IEEE Transactions on Magnetics, Vol. 47, No. 7, Jul. 2011, pp. 1849 – 1854.

[166] T. W. McDaniel, W. A. Challener and K. Sendur, "Issues in heat-assisted perpendicular recording," IEEE Transactions on Magnetics, Vol. 39, No. 4, Jul. 2003, pp. 1972 – 1979.

[167] S. V. Canchi and D. B. Bogy, "Thermal fly-height control slider instability and dynamics at touchdown: Explanations using nonlinear systems theory," Journal of Tribology, Vol. 133, No. 2, Apr. 2011, pp. 021902-1 – 13.

[168] B. Liu, S. K. Yu, W. D. Zhou, C. H, Wong, and W. Hua, "Low flying-height slider with high thermal actuation efficiency and small flying-height modulation caused by disk waviness," IEEE Transactions on Magnetics, Vol. 44, No. 1, Jan. 2008, pp. 145 – 150.

[169] J. Gellman, "Lubricants and overcoats for magnetic storage media," Current Opinion in Colloid and Interface Science, Vol. 3, No. 4, Aug. 1998, pp. 368 – 372.

[170] S. J. Hirz, A. M. Homola, G. Hadziioannou and C. W. Frank, “Effect of substrate on shearing properties of ultratin polymer fims,” Langmuir, Vol. 8, No. 1, Jan. 1992, pp. 328 – 333.

[171] H. Liu and B. Bhushan, “Nanotribological characterization of molecularly thick lubricant films for applications to MEMS/NEMS by AFM,” Ultramicroscopy, Vol. 97, No. 1 – 4, Oct. – Nov. 2003, pp. 321 – 340.

[172] L. Li, P. M. Jones and Y.-T. Hsia, “Effect of chemical structure and molecular weight on high-temperature stability of some Fomblin Z-type lubricants,” Tribology Letters, Vol. 16, No. 1 – 2, Feb. 2004, pp. 21 – 27.

[173] C. M. Mate, Q. Dai, R. N. Payne, B. E. Knigge and P. Baumgart, “Will the numbers add up for sub-7-nm magnetic spacings? Future metrology issues for disk drive lubricants, overcoats, and topographies,” IEEE Transactions on Magnetics, Vol. 41, No. 2, Feb. 2005, pp. 626 – 631.

[174] R. J. Waltman, D. J. Pocker and G. W. Tyndall, “Studies on the interactions between ZDOL perfluoropolyether lubricant and the carbon overcoat of rigid magnetic media,” Tribology Letters, Vol. 4, No. 3 – 4, 1998, pp. 267 – 275.

[175] X. Zhao, B. Bhushan and C. Kajdas, “Lubricant studies of head-disk interfaces in a controlled environment. Part 2: degradation mechanisms of perfluoropolyether lubricants,” Proceedings of the Institution of Mechanical Engineers, Part J: Journal of Engineering Tribology, Vol. 214, No. 6, Jun. 2000, pp. 547 – 559.

[176] J. Lee, S.-W. Chun, H.-J. Kang and F. E. Talke, “The effect of UV stabilizer on photo degradation of perfluoropolyether lubricants used in hard disk,” Tribology Letters, Vol. 28, No. 2, 2007, pp. 117 – 121.

[177] J. Lee, S.-W. Chun, H.-J. Kang and F. E. Talke, “Photo oxidative degradation of perfluoropolyether lubricant for data storage,” Macromolecular Research, Vol. 19, No. 6, 2011, pp. 582 – 588.

[178] A. J. Gellman, “Lubricants and overcoats for magnetic storage media,” Current Opinion in Colloid & Interface Science, Vol. 3, No. 4, Aug. 1998, pp. 368 – 372.

[179] P. H. Kasai, “Perfluoropolyethers: Intramolecular disproportionation,” Macromolecules, Vol. 25, 1992, pp. 6791 – 6799.

[180] L. Zhu and T. Liew, “Spectral characterization of perfluoropolyethers lubricant irradiated by laser light,” Applied Surface Science, Vol. 203 -204, Jan. 2003, pp. 871 – 874.

[181] N. Tagawa, R. Kakitani, H. Tani, N. Iketani and I. Nakano, “Study of lubricant depletion induced by laser heating in thermally assisted magnetic

recording systems – effect of lubricant film materials," IEEE Transactions on Magnetics, Vol. 45, No. 2, Feb. 2009, pp. 877 – 882.

[182] N. Tagawa, H. Andoh and H. Tani, "Study on lubricant depletion induced by laser heating in thermally assisted magnetic recording systems: Effect of lubricant thickness and bonding ratio," Tribology Letters, Vol. 37, No. 2, 2010, pp. 411 – 418.

[183] N. Tagawa and H. Tani, "Lubricant depletion characteristics induced by rapid laser heating in thermally assisted magnetic recording," IEEE Transactions on Magnetics, Vol. 47, No. 1, Jan. 2011, pp. 105 – 110.

[184] J. Zhang, R. Ji, J. W. Xu, J. K. P. Ng, B. X. Xu, S. B. Hu, H. X. Yuan and S. N. Piramanayagam, "Lubricant for heat-assisted magnetic recording," IEEE Transaction on Matnetics, Vol. 42, No. 10, Oct. 2006, pp. 2546 – 2548.

[185] "Fomblin Z derivatives product data sheet," Solvay Solexis. [http://www. solvaysemiconductor.com/static/wma/pdf/1/7/3/4/fomblin_thin.pdf].

[186] G. W. Tyndall, P. B. Leezenberg, R. J. Waltman and J. Castenada, "Interfacial interactions of perfluoropolyether lubricants with magnetic recording media," Tribology Letters, Vol. 4, No. 2, 1998, pp. 103 – 108.

[187] J. Rhew, H. Kim, H. Zheng, H. – J. Kang and F. E. Talke, "Thermal stability of modified perfluoropolyether lubricants for application in heat assisted magnetic recording," Proceedings of the ASME/STLE International Joint Tribology Conference, Los Angeles, California, USA, Oct. 23 – 26, 2011.

[188] C. Gao, Y. C. Lee, J. Chao and M. Russak, "Dip-coating of ultra-thin liquid lubricant and its control for thin-film magnetic hard disks," IEEE Transactions on Magnetics, Vol. 31, No. 6, Nov. 1995, pp. 2982 – 2984.

[189] G. H. Vurens and D. L. Klein, "Composition and thickness distribution of carbon overcoat films on thin film magnetic disks studied with surface reflectance analyzers," Proceedings of SPIE, Vol. 3619, Jan. 1999, pp. 27 – 34.

[190] D. L. Klein and G. H. Vurens, "Measurements of thin film disks by surface reflectance analysis," Proceedings of SPIE, Vol. 3619, Jan. 1999, pp. 18 – 26.

[191] D. L. Klein and G. H. Vurens (to HDI Instrumentation), "Optical measurement system using polarized light," U. S. Patent US 6,134,011, Oct. 17, 2000.

[192] G. H. Vurens, D. L. Klein, W. Gan and T. Ultican, "Tribology applications of surface reflectance analyzer: optical characterization of the head disk interface," Tribology International, Vol. 33, 2000, pp. 647 – 653.

[193] R. M. A. Azzam and N. M. Bashara, “Ellipsometry and polarized light,” North-Holland, Amsterdam, The Netherlands, 1989.

[194] “Fresnel equations,” Wikipedia. [http://en.wikipedia.org/wiki/Fresnel_equations].

[195] P. B. Johnson and R. W. Christy, “Optical constants of transition metals: Ti, V, Cr, Mn, Fe, Co, Ni, and Pd,” Physical Review B, Vol. 9, No. 12, Jun. 1974, pp. 5056 – 5070.

[196] R. W.-J. Chia, E. Li, S. Sugi, G. G. Li, H. Zhu, A. R. Forouhi and I. Bloomer, “Optical characterization of nitrogenated carbon overcoats,” Thin Solid Films, Vol. 308 – 309, Oct. 1997, pp. 284 – 288.

[197] Y. Yoon, “Nano-tribology of discrete track recording media,” Ph.D. Dissertation, Department of Mechanical and Aerospace Engineering, University of California, San Diego, CA, 2010.

[198] F. Cain, “How far is Neptune from Earth,” Universe Today, Nov. 28, 2008. [http://www.universetoday.com/21628/how-far-is-neptune-from-earth/].

[199] “Avogadro constant,” Wikipedia. [http://en.wikipedia.org/wiki/Avogadro_constant# cite_note-SI-4].

[200] R. Fox and T. Hill, “An exact value for Avogadro’s number,” American Scientist, Vol. 95, No. 2, Mar. – Apr. 2007, pp. 104 – 107.

[201] W. Boettcher, H. Li, R. A. de Callafon, and F. E. Talke, “Dynamic flying height adjustment in hard disk drives through feedforward control,” IEEE Transactions on magnetic, Vol. 47, No. 7, Jul. 2011, pp. 1823 – 1829.

[202] D. Chen and D. B. Bogy, “Simulation of static flying attitudes with different heat transfer models for a flying-height control slider with thermal protrusion,” Tribology Letters, Vol. 40, No. 1, 2010, pp. 31 – 39.

[203] N. Liu, J. Zheng, and D. B. Bogy, “Thermo-mechanical aspects of thermal flying-height control sliders for hard disk drives,” Mathematics and Mechanics of Solids, Vol. 16, No. 7, 2011, pp. 694 – 705.

[204] L. Chen, D. B. Bogy, and B. Strom, “Thermal dependence of MR signal on slider flying state,” IEEE Transactions on Magnetics, Vol. 36, No. 5, Sep. 2000, pp. 2486 – 2489.

[205] S. A. Schaaf and P. L. Chambre, “Flow of rarefied gases,” Princeton University Press, Princeton, New Jersey, 1961.

[206] E. H. Kennard, “Kinetic theory of gases: With an introduction to statistic mechanics,” McGraw-Hill Book Company, Inc., New York and London, 1938.

[207] Gennadiy Nikishkov, “Programming finite element in JavaTM,” Springer, 1st edition, Jan. 12, 2010.

[208] U. Boettcher, C. A. Lacey, H. Li, K. Amemiya, R. A. de Callafon, and F. E. Talke, “Analytical read back signal modeling in magnetic recording,” Microsystem Technologies, Vol. 17, 2011, pp. 997 – 1002.

[209] H. J. Richter, “Recent advances in the recording physics of thin-film media,” Journal of Physics D: Applied Physics, Vol. 32, No. 21, 1999, pp. R147 – R168.

[210] H. J. Richter, “The transition from longitudinal to perpendicular recording,” Journal of Physics D: Applied Physics, Vol. 40, No. 9, 2007, pp. R149 – R177.

[211] J. A. Sievers, “Field symmetries and equivalence in longitudinal and perpendicular recording,” IEEE Transactions on Magnetics, Vol. MAG-19, No. 5, Sep. 1983, pp. 1745 – 1747.

[212] Y. Suzuki and Y. Nishida, “Exact calculation method for medium field from a perpendicular medium,” IEEE Transactions on Magnetics, Vol. 39, No. 5, Sep. 2003, pp. 2633 – 2635.

[213] B. Valcu, T. Roscamp, and H. N. Bertram, “Pulse shape, resolution, and signal-to-noise ratio in perpendicular recording,” IEEE Transactions on Magnetics, Vol. 38, No. 1, Jan. 2002, pp. 288 – 294.

[214] R. Brunner and F. E. Talke, “Tribological and mechanical characterization of carbon-coated sliders and disks,” Tribology Letter, 2010, Vol. 40, pp. 23 – 29.